Mechanochemically synthesized conversion electrodes and their application in sodium and lithium ion batteries with diglyme electrolytes

Dissertation
(kumulativ)

Zur Erlangung des akademischen Grades doctor rerum naturalium
(Dr. rer. nat)

vorgelegt dem Rat der Chemisch-Geowissenschaftlichen Fakultät der
Friedrich-Schiller-Universität Jena
von Wolfgang Brehm, M.Sc.
geboren am 14.03.1989 in Naumburg/Saale

Gutachter:

1. Prof. Dr. Philipp Adelhelm

2. Prof. Dr. Markus Rettenmayr

Tag der Verteidigung: 01.09.2021

Selbständigkeitserklärung

Ich erkläre, dass ich die vorliegende Arbeit selbständig und unter Verwendung der angegebenen Hilfsmittel, persönlichen Mitteilungen und Quellen angefertigt habe.

Ort, Datum   Unterschrift der Verfasserin/des Verfassers

Erklärung zu den Eigenanteilen der Promovendin/des Promovenden sowie der weiteren Doktorandinnen/Doktoranden als Co-Autorinnen/-Autoren an den Publikationen und Zweitpublikationsrechten bei einer kumulativen Dissertation

Für alle in dieser kumulativen Dissertation verwendeten Manuskripte liegen die notwendigen Genehmigungen der Verlage ("Reprint permissions") für die Zweitpublikation vor.

Die Co-Autorinnen/-Autoren der in dieser kumulativen Dissertation verwendeten Manuskripte sind sowohl über die Nutzung, als auch über die oben angegebenen Eigenanteile der weiteren Doktorandinnen/Doktoranden als Co-Autorinnen/-Autoren an den Publikationen und Zweitpublikationsrechten bei einer kumulativen Dissertation informiert und stimmen dem zu.

Die Anteile der Promovendin/des Promovenden sowie der weiteren Doktorandinnen/Doktoranden als Co-Autorinnen/Co-Autoren an den Publikationen und Zweitpublikationsrechten bei einer kumulativen Dissertation sind in der Anlage aufgeführt.

Name der Promovendin/	Datum	Ort	Unterschrift
des Promovenden: Wolfgang Brehm			

Ich bin mit der Abfassung der Dissertation als publikationsbasierte Dissertation, d.h. kumulativ, einverstanden und bestätige die vorstehenden Angaben.

Name Betreuerin/	Datum	Ort	Unterschrift
Betreuer: Prof. Dr. Philipp Adelhelm			

Declaration on authorship and copyright in this cumulative doctoral thesis

Publication #1 – *Reactive and non-reactive ball milling of tin-antimony (Sn-Sb) composites and their use as electrode for sodium-ion batteries with glyme electrolyte* (W. Brehm **[A1]**, J.R. Buchheim **[A2]**, P. Adelhelm **[CA]**, Energy Technol. 2019, 1900389) {CA: Corresponding author}			
Author	**A1**	**A2**	**CA**
Project idea	✓		✓
Conceptual research design	✓		✓
XRD measurements	✓	✓	
SEM and EDS measurements	✓		
Electrochemical measurements	✓		
In situ dilatometry studies	✓		
Combined data interpretation	✓		✓
Manuscript discussion	✓	✓	✓
Manuscript writing	✓	✓	✓
Suggested publication equivalence value	**1.0**		

Publication #2 – *Mechanochemically synthesized Cu₃P/C composites as a conversion electrode for Li-ion and Na-ion batteries in different electrolytes* (W. Brehm **[A1]**, S. Aggunda **[A2]**, Z.Zhang **[A3]**, C. Neumann **[A4]**, A. Turchanin **[A5]**, M. Seyring **[A6]**, M. Rettenmayr **[A7]**, J.R. Buchheim **[A8]**, P. Adelhelm **[CA]**, (Journal of Power Sources Advances 2020, 100031) {CA: Corresponding author}									
Author	**A1**	**A2**	**A3**	**A4**	**A5**	**A6**	**A7**	**A8**	**CA**
Project idea	✓	✓							
Conceptual research design	✓	✓	✓						
XRD measurements	✓							✓	
SEM and EDS measurements	✓								
TEM measurements						✓	✓		
Electrochemical measurements	✓								
XPS measurements				✓	✓				
Combined data interpretation	✓								✓
Manuscript discussion	✓	✓	✓	✓	✓	✓	✓	✓	✓
Manuscript writing	✓								✓
Suggested publication equivalence value	**1.0**								

Publication #3 – *Copper thiophosphate (Cu₃PS₄) as electrode for sodium-ion batteries with ether electrolyte* (W. Brehm **[A1]**, S. Aggunda **[A2]**, Z. Zhang **[A3]**, C. Neumann **[A4]**, A. Turchanin **[A5]**, A. Martin **[A6]**, N. Pinna **[A7]**, M. Seyring **[A8]**, M. Rettenmayr **[A9]**, J.R. Buchheim **[A10]**, P. Adelhelm **[CA]**, Adv. Funct. Mater. 2020, 1910583
{CA: Corresponding author}

author	A1	A2	A3	A4	A5	A6	A7	A8	A9	A10	CA
Project idea	✓	✓									
Conceptual research design	✓	✓	✓								
XRD measurements	✓									✓	
SEM and EDS measurements	✓										
TEM measurements						✓	✓	✓	✓		
Electrochemical measurements	✓										
In situ XRD measurements						✓	✓				
XPS measurements				✓	✓						
Combined data interpretation	✓										✓
Manuscript discussion	✓	✓	✓	✓	✓	✓	✓	✓	✓	✓	✓
Manuscript writing	✓										✓
Suggested publication equivalence value	**1.0**										

Acknowledgement

Content

List of Abbreviations

Abbreviation	Meaning
BM	Ball milling
CV	Cyclic voltammetry
EDS (EDX)	Energy dispersive X-ray spectroscopy
EIS	Electrochemical impedance spectroscopy
ECD	*in situ* electrochemical dilatometry
GCPL	Galavanostatic cycling with potential limitation
HEBM	High energy ball milling
ICE	Initial coulomb efficiency
LIBs	Lithium-ion batteries
PEIS	Potentiostatic electrochemical Impedance spectroscopy
PBM	Planetary ball mill
SBM	Swing ball mill
SAED	Small angle electron diffraction
SEM	Scanning electron microscopy
SEI	Solid electrolyte interphase
SIBs	Sodium-ion batteries
SSBs	Solid state batteries
TEM	Transmission electron microscopy
HRTEM	High resolution transmission electron microscopy
OCV	Open circuit voltage
XRD	X-ray diffraction
XPS	X-ray photoelectron spectroscopy

List of used chemicals

Chemical	Company	Purity [%]	Application as
Diglyme (2G)	Sigma Aldrich	99.5	Electrolyte solvent
Carbon black	Timcal		Conductive agent
Carboxymethylcellulose (CMC)	Alfa Aesar		Binder
Cu powder	Sigma Aldrich	99.5	Reactant
P_2S_5 (a)	Sigma Aldrich	99	Reactant
Sulfur (S)	Sigma Aldrich	99.5	Reactant
DMC (Dimethyl carbonate)	Sigma Aldrich		Electrolyte solvent
EC (Ethylene carbonate)	Sigma Aldrich		Electrolyte solvent
EC:DMC + 1M $LiPF_6$	Sigma Aldrich	>99.9	Electrolyte
$LiPF_6$	Sigma Aldrich		Conducting salt
LiTFSI	Sigma Aldrich	>98	Conducting salt
NaOTf (Sodium trifluoromethanesulfonate)	TCI Chemicals	98	Conducting salt
$NaPF_6$	Alfa Aesar	> 99	Conducting salt
NMP (N-methyl-2-pyrrolidone)	Sigma Aldrich		Slurry former
Red phosphorus (a)	Sigma Aldrich	99.8	Reactant
PVDF (Polyvinylidene fluoride)	MTI Corp.		Binder
Sn (tin, 325 mesh)	Alfa Aesar		Electrode material
Sb (antimony, 100 mesh)	Sigma Aldrich		Electrode material

List of used symbols

Symbol	Meaning	Unit
θ	Diffraction angle	$-$
φ	Phase angle	$-$
E	Applied potential	V
v	Scan rate	mV/s
E_0	Applied potential at t = 0	V
I	Current response	mA/cm^2
I_0	Current response at t = 0	mA/cm^2
$I_{p,a}$	Anodic current peak	mA/cm^2
$I_{p,c}$	Cathodic current peak	mA/cm^2
$E_{p,a}$	Potential at anodic current peak	V
$E_{p,c}$	Potential at cathodic current peak	V
$\Delta_R G$	Gibb's free energy	$\dfrac{kJ}{mol}$
$\Delta_R H$	Standard reaction enthalpy	$\dfrac{kJ}{mol}$
T	Temperature	K
ΔS	Reaction entropy	$\dfrac{J}{mol \cdot K}$
q	Specific capacity	$\dfrac{mAh}{g}$
OCV	Open circuit voltage	V
ω	Circular frequency	Hz
Z	Impedance	Ω
Z_0	Impedance at t = 0	Ω
n	Resonance order	$-$
λ	Wave length	nm
d	Lattice plane distance	nm

List of Figures

1. Summary (English)

The shift from fossil fuels to renewable energies is one of the most important discussed issues in the present time. Due to the increasing use of renewable energies, the demand of energy storage devices attracts enhanced interest in publicity, politics and in research. Hence, energy storage devices with very high efficiencies are required. Rechargeable batteries are reliable and highly efficient energy storage devices providing high energy density at high voltages with the lead of the Li-ion technology since the early 1990s. Because of the impressive reversibility of the redox reactions in the Li-ion technology, long cycle life of several thousand discharge/charge cycles may be enabled. Thus, electrical energy can be stored in case of oversupply and can be accessed if it is needed on demand. Despite these promising advantages, the strongly limited abundance of Li and also that of other elements contained in a Li-ion battery (LIB) leads to the thinking of low-cost and more abundant alternatives. Especially for stationary storage devices alternative battery technologies are required.

Sodium-ion batteries (SIBs) are a promising alternative, since Na cells show similar properties to the Li analogues in many cases, while they are based on more environmentally friendly and/or more abundant materials. SIBs often show slightly lower energy densities and cell voltages than those of LIBs, but they still provide significantly better values than lead-acid batteries, which are currently dominating the market in terms of annually manufactured capacity.

With view on commercially applicable electrode materials, intercalation compounds are mostly used so far due to their excellent cycle life, enabled by the low volume expansion during insertion/deinsertion of alkali-ions between the layers, but, however, the capacities are often below $250 \, \mathrm{mAh \, g^{-1}}$. Unfortunately, reversible capacities are even lower. Another option is the use of conversion electrodes. Conversion electrodes may be classified into alloys and transition metal compounds. They enable the transfer of several electrons per formula unit, resulting in large capacities. Accompanied with that, they suffer from the large volume expansion during discharge/charge cycles, which is still an issue for commercialization. Nevertheless, there are several approaches to mitigate this problem.

Tin (Sn) and its compounds are well investigated alloy electrodes for SIBs as tin provides a very high theoretical specific capacity of $847 \, \mathrm{mAh \, g^{-1}}$. Sn is an example that shows even better capacity retention when used in SIBs compared to its use in LIBs. Moreover, transition metal compounds containing phosphorus (P) and/or sulfur (S) are promising conversion electrodes as well, since these elements are well known to enable high specific volumetric and/or gravimetric capacities in LIBs and SIBs.

This cumulative Ph.D. thesis summarizes the research progress obtained during the last years on conversion electrodes for SIBs and LIBs.

The thesis is initiated with a brief discussion about renewable energy development and introduces the Li-ion battery concept and the use of sodium ion batteries as an alternative. The following part deals about the types of electrodes in a battery including the demonstration of typical examples. The subsequent part explains the research objectives and summarizes the main results accompanied with the approaches for reaching them.

The majority of the scientific work was conducted at the Friedrich-Schiller-University Jena within the research group of Prof. Philipp Adelhelm. Cooperation with other institutions was carried out in order to gain access to specific research instruments with regard to material characterization and thus deepen the scientific discussion.

The studies during the doctoral period are basically divided into two parts. On the one hand, an electrode made of a Sn-based alloy is studied and on the other hand, two copper-based transition metal compounds are discussed for their use in SIBs and LIBs.

The first publication (doi: 10.1002/ente.201900389) addresses the impact of reactive and non-reactive ball milling on the elements Sn and Sb including the composite formation with carbon. The fabricated electrodes are investigated in Na cells. Related to that, the voltage profiles are compared for these electrodes. As a result, it is found that Sb undergoes rapid capacity fading in cells containing diglyme as electrolyte solvent when Sb is not bound in an intermetallic phase. In case of the presence of the intermetallic phase β-SnSb, excellent capacities of more than $400\ \mathrm{mAh\ g^{-1}}$ are obtained after 190 cycles. Moreover, the height change of the electrodes, the so called "breathing", during discharge/charge is investigated by *in situ* dilatometry. Based on this method, it is found that composite formation with carbon by longer milling (6h vs. 1h) is the dominating condition over reactive or non-reactive ball milling between the elements Sn and Sb to enable enhanced cycle life.

The second publication (doi: 10.1016/j.powera.2020.100031) focuses on the comparison for the use of Cu_3P as transition metal compound based conversion electrode in Li and Na cells. Several carbonate and diglyme electrolytes are compared and studied related to their influence on cycle life and capacity. Cu_3P using 1M LiTFSI dissolved in diglyme as electrolyte is showing the overall best performance with the highest capacity and retention ($210\ \mathrm{mAh\ g^{-1}}$ after 120 cycles @ $36.6\ \mathrm{mA\ g^{-1}}$) for Li cells. Moreover, *in situ* dilatometry shows that breathing in the initial cycles is lower for the diglyme electrolytes in comparison to selected carbonate electrolytes for Li and for Na cells. However, strong capacity fading occurs for carbonate electrolytes and related to that, the breathing becomes lower upon cycling, while diglyme electrolytes enable almost constant breathing and a more stable cycle life.

In the third publication (doi: 10.1002/adfm.201910583), the combined use of a transition metal phosphide in combination with sulfur, this way forming a thiophosphate, is considered for its use as a conversion electrode in SIBs for the first time with Cu_3PS_4 as an example. It is found that the use of 1M $NaPF_6$ dissolved in diglyme shows the best performance. Hence, capacities of about 580 mAh g^{-1} are obtained after more than 200 cycles @120 mA g^{-1} and about 450 mAh g^{-1} after 1400 cycles @1 A g^{-1} in a voltage window between 0.01 and 2.5 V. Surprisingly, the capacity of Cu_3PS_4 in Li half cells is found to be smaller, showing only about 170 mAh g^{-1} after 200 cycles. The redox mechanism of the herein considered thiophosphate is discussed by the combined use of X-ray photoelectron spectroscopy (XPS) after galvanostatic discharge/charge, *in situ* X-ray diffraction (XRD) and galvanostatic cycling (GCPL) experiments. Based on these results, the redox mechanism is found to be controlled by sulfur, enabling reversible formation of Na_2S. Only in the initial cycle, copper (Cu^+) seems to be reduced to its elemental state and can act as polysulfide trap upon further cycling. The obtained results demonstrate that Cu_3PS_4 is an example for the use of a thiophosphate as an electrode to enable reversible charge storage with high capacity over several hundred cycles without notable capacity fading.

This thesis ends with an overview concluding the results from the publications and an outlook. Some comments are given to remaining scientific challenges in the research area of conversion electrodes for LIBs and SIBs. The results of this dissertation improve the understanding of using alloy and transition metal compound based conversion electrodes in diglyme electrolytes. While a couple of scientific questions could be answered, several questions and issues about conversion electrodes remain, being a motivation to still continue research on conversion electrodes for LIBs and SIBs in the future.

1. Zusammenfassung (German)

Die Umstellung von fossilen Brennstoffen auf erneuerbare Energien ist eines der wichtigsten Diskussionsthemen in der heutigen Zeit. Durch die zunehmende Nutzung erneuerbarer Energien zieht die Nachfrage nach Energiespeichern verstärktes Interesse in Öffentlichkeit, Politik und Forschung auf sich. Bei Energiespeichern sind sehr hohe Wirkungsgrade erforderlich. Wiederaufladbare Batterien sind zuverlässige, hocheffiziente Energiespeicher, die mit Einführung der Lithiumionentechnologie seit Anfang der 1990er Jahre besonders hohe Energiedichten und hohe Spannungen liefern. Aufgrund der beeindruckenden Reversibilität der Redoxreaktionen in der Li-Ionen-Technologie kann eine lange Lebensdauer von mehreren tausend Entlade-/Ladezyklen ermöglicht werden. So kann elektrische Energie bei einem Überangebot gespeichert und bei Bedarf abgerufen werden. Trotz dieser vielversprechenden Vorteile führt die stark begrenzte Menge an Li und auch an anderen Elementen, die in einer Li-Ionen-Batterie (LIB) enthalten sind, dazu über kostengünstige und reichhaltigere Alternativen nachzudenken. Insbesondere die stationäre Energiespeicherung erfordert alternative Batterietechnologien.

Natrium (Na)-Ionen-Batterien (SIBs) sind eine vielversprechende Alternative zu LIBs, da Na-Zellen in vielen Fällen ähnliche Eigenschaften wie Li-Zellen aufweisen, während sie auf umweltfreundlicheren Materialien und/oder deren größerem Vorkommen basieren. SIBs weisen häufig etwas niedrigere Energiedichten und Zellspannungen auf, welche aber immer noch deutlich höher als die von Bleibatterien sind, die den Markt in Bezug auf die jährlich genutzte Energiekapazität dominieren. SIBs eignen sich dabei besonders für Anwendungen, bei denen eine hohe Energiedichte auf Basis gut verfügbarer Elemente benötigt wird.

Interkalationsverbindungen ermöglichen aufgrund der geringen Volumenausdehnung bei der Ein-und auslagerung von Alkalimetallionen zwischen den Schichten eine hohe Zyklenstabilität, weisen aber generell theoretische Kapazitäten von unter $300\,\text{mAh}\,\text{g}^{-1}$ auf. Eine Option, höhere Kapazitäten zu erreichen, ist die Verwendung von Konversionselektroden. Konversionselektroden lassen sich in Legierungen und Übergangsmetallverbindungen unterscheiden. Sie ermöglichen die Übertragung mehrerer Elektronen pro Formeleinheit des Aktivmaterials, erfahren aber damit verbunden eine sehr große Volumenausdehnung während der Entladungs-/Ladungszyklen. Die daraus resultierende Dekontaktierung durch Pulverisierung geht dabei oftmals mit einem irreversiblen Kapazitätsverlust einher.

Zinn (Sn) und seine Verbindungen sind gut untersuchte Legierungselektroden für SIBs, da Sn eine sehr hohe Kapazität von $847\,\text{mAh}\,\text{g}^{-1}$ bietet. Sn zeigt bei der Verwendung in SIBs im Vergleich zu LIBs eine noch bessere Kapazitätserhaltung. Darüber hinaus sind phosphor- und/oder schwefelhaltige Übergangsmetallverbindungen ebenfalls vielversprechende Kandidaten zur Verwendung als

Konversionselektroden, da Phosphor und Schwefel hohe spezifische volumetrische und/oder gravimetrische Kapazitäten ermöglichen.

Diese kumulative Doktorarbeit fasst die in den letzten Jahren erzielten Forschungsergebnisse über die Untersuchung von ausgewählten Konversionselektroden für SIBs und LIBs zusammen.

Das Forschungsthema dieser Arbeit wird mit einer kurzen Diskussion der Entwicklung erneuerbarer Energien eingeleitet und stellt das Li-Ionen-Batteriekonzept mit Verbindung zur Verwendung von SIBs als Alternative vor. Anschließend werden die Elektrodentypen in einer Batterie einschließlich typischer Beispiele diskutiert. Darauffolgend werden Forschungsziele und deren Ansätze erläutert. Dabei werden die wichtigsten erzielten Ergebnisse zusammengefasst.

Der Großteil der wissenschaftlichen Arbeiten wurde an der Friedrich-Schiller-Universität Jena innerhalb der Forschungsgruppe von Prof. Philipp Adelhelm durchgeführt. Kooperationen mit anderen Institutionen wurden vorgenommen, um in Hinblick auf die Materialcharakterisierung Zugang zu spezifischen Forschungsinstrumenten zu erhalten und die wissenschaftliche Diskussion weiter zu vertiefen.

Diese Studie gliedert sich grundsätzlich in zwei Teile. Zum einen wird eine Legierungselektrode auf Zinnbasis untersucht und zum anderen werden zwei Übergangsmetallverbindungen auf Kupferbasis für den Einsatz in SIBs und LIBs diskutiert.

Die erste Veröffentlichung (doi: 10.1002/ente.201900389) befasst sich mit dem Einfluss der Kugelmahldauer auf das nicht-reaktive und reaktive Vermahlen von Zinn (Sn) und Antimon (Sb) für die Nutzung als Kompositelektrode mit Kohlenstoff unter Verwendung eines Diglyme basierten Elektrolyts. Der Einfluss von reaktivem und nicht-reaktivem Vermahlen der Elemente Sn und Sb wird mittels elektrochemischer Messungen untersucht. Dabei erfährt Sb einen ungewöhnlich schnellen Kapazitätsverlust, wenn es nicht als intermetallische Phase mit Zinn im Diglymeelektrolyten vorliegt. Im Falle der Verwendung der intermetallischen Phase β-SnSb werden nach 190 Zyklen hohe Kapazitäten von mehr als 400 mAh g^{-1} erreicht. Darüber hinaus zeigt eine *in situ*-Dilatometriestudie, dass die "Atmung" der Elektroden während der Entlade-/Ladezyklen durch die Kompositbildung mit Kohlenstoff und nicht durch das Vorliegen einer intermetallischen Phase bzw. einer einfachen Mischung aus den Elementen Sn und Sb dominiert wird.

In einer weiteren Studie (doi: 10.1016/j.powera.2020.100031) wird ein Vergleich für den Einsatz von Cu_3P als übergangsmetallbasierte Konversionselektrode in Li und Na-Halbzellen durchgeführt. Mehrere Elektrolyte werden untersucht und hinsichtlich ihres Einflusses auf die Lebensdauer, Überspannungen und Kapazität verglichen. Für Cu_3P wird in einer Li-Zelle unter Verwendung von 1M LiTFSI in Diglyme als Elektrolyt das insgesamt beste Ergebnis mit der höchsten Kapazität und Zyklenstabilität (210 mAh g^{-1} nach 120 Zyklen bei 36.6 mA g^{-1}) erhalten. Darüber hinaus wird mittels *in situ*-Dilatometriestudie gezeigt, dass die Atmung der Elektroden in den Initialzyklen bei

Verwendung der Diglymelektrolyte im Vergleich zu ausgewählten Carbonatelektrolyten für Li und für Na-Halbzellen geringer ist. Bei den Carbonat-Elektrolyten tritt jedoch mit steigender Zyklenzahl ein starker Kapazitätsschwund, mit einhergehender verringerter Elektrodenatmung auf, während die Diglymelektrolyte eine höhere Zyklenstabilität ermöglichen. Daher zeigt diese Studie, dass Diglyme ein besser geeignetes Elektrolytlösungsmittel für Cu_3P/C-Kompositelektroden in Li und Na-Halbzellen ist.

In der dritten Publikation (doi: 10.1002/adfm.201910583) wird erstmals ein Thiophosphat für seine Verwendung als Konversionselektrode für Übergangsmetallverbindungen mit Cu_3PS_4 als Beispiel für SIBs betrachtet. Der Redox-Mechanismus dieses Thiophosphats wird durch Röntgenphotoelektronenspektroskopie (XPS)- und *in situ* Röntgendiffraktometrie (XRD)-Studien nach galvanostatischer Ent- und Aufladung untersucht. Mittels dieser Methoden wird gezeigt, dass der Redox-Mechanismus unter der reversiblen Bildung von Na_2S von Schwefel dominiert wird. Nur im initialen Entladeschritt (Sodiierung) scheint Kupfer (Cu^+) in seinen elementaren Zustand reduziert zu werden, welches beim weiteren Zyklisieren als Schwefelfalle agieren kann. Die Verwendung von Cu_3PS_4 wird für ausgewählte diglyme- und carbonatbasierte Elektrolyte in Li- und Na-Halbzellen diskutiert. Dabei werden die besten Resultate mit 1M $NaPF_6$ in Diglyme als Elektrolyt erhalten. Auf diese Weise werden Kapazitäten von etwa 580 mAh g^{-1} nach mehr als 200 Zyklen bei einem Strom von 120 mA g^{-1} und etwa 450 mAh g^{-1} nach 1400 Zyklen bei einem Strom von 1 A g^{-1} erreicht. Überraschenderweise sind die erhaltenen Kapazitäten für Cu_3PS_4 in Li-Halbzellen deutlich kleiner und betragen nach 200 Zyklen nur etwa 170 mAh g^{-1}. Die erhaltenen Ergebnisse zeigen, dass Cu_3PS_4 ein Beispiel dafür ist, dass ein Thiophosphat eine sehr hohe Speicherkapazität über mehrere hundert Zyklen ohne nennenswerte Kapazitätsverluste in Na-Zellen ermöglichen kann.

Diese Arbeit schließt mit einer Zusammenfassung, welche die wichtigsten Resultate aus den Publikationen enthält und einen Ausblick auf mögliche weitere Untersuchungen gibt. Die Ergebnisse dieser Dissertation verbessern das Verständnis zur Verwendung von Konversionselektroden auf der Basis von Legierungen und Übergangsmetallverbindungen in Diglymeelektrolyten. Während einige wissenschaftliche Fragen beantwortet werden konnten, verbleiben dennoch einige offene Frage- und Problemstellungen, die dazu motivieren sollten, Konversionselektroden für LIBs und SIBs auch in Zukunft weiterhin zu untersuchen.

2. Introduction

The increasing energy need is one of the most important issues in world's economy and social life. Because of severe environmental problems caused by the use of fossil fuels, coal or nuclear power, there is a need of a change to renewables. In the last two decades, Germany for example, has already achieved a major increase in the use of renewable energies, enabling the switch to environmentally friendly green electricity, see **Figure 1.** [1] Hence, there is currently an urgent need for stationary storage devices taking up the electrical energy. Typically, energy stores are classified into mechanical, chemical, thermal, electrical and electrochemical energy stores. The important advantage of the latter mentioned kind of energy store over others is the low loss of energy to the environment during energy conversion. The optimization of the electrochemical storage devices related to their energy and power density thereby is of great relevance. The balance between both parameters can be illustrated in a Ragone plot, see **Figure 2**. [2] One could conclude from that plot that fuel cells are the best choice looking at their outperforming energy density values, but they also show the smallest power density. Moreover, it is worth to note that fuel cells are only energy converter and hence suffer from the permanent need of a hydrogen source and also show a lower degree of energy efficiency in comparison to the other devices. In addition, hydrogen storage and production are still issues. Thus, rechargeable batteries receive more and more attention, as they provide high capacities and energy densities together with moderate power densities, including the highly reversible transformation between chemical energy and electrical energy. Especially Li-ion batteries (LIBs) and Na-ion batteries (SIBs) deliver a very high energy density being caused by the large potential difference between positive and negative electrode. Li shows the most reductive potential within the standard electrochemical series and may therefore enable large voltage differences in combination with an appropriate positive electrode material. Because of these conditions and the permanent need of energy supply on demand in social and economic life being required for smart devices like mobile phones, tablets, cameras, notebooks, working tools and automobiles, batteries are ideal candidates.
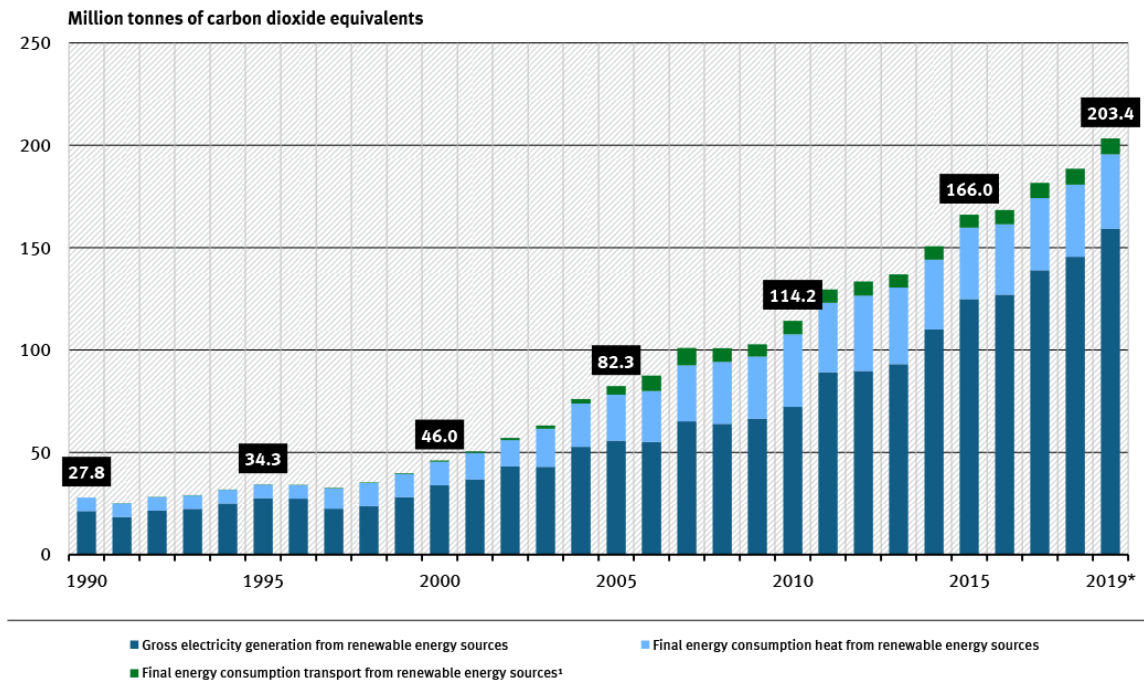
Figure 1: *The development of renewable energies in Germany since the past two decades. Source: German Environmental Agency using data from AGEE-Stat, as of 02/2020.* [1]
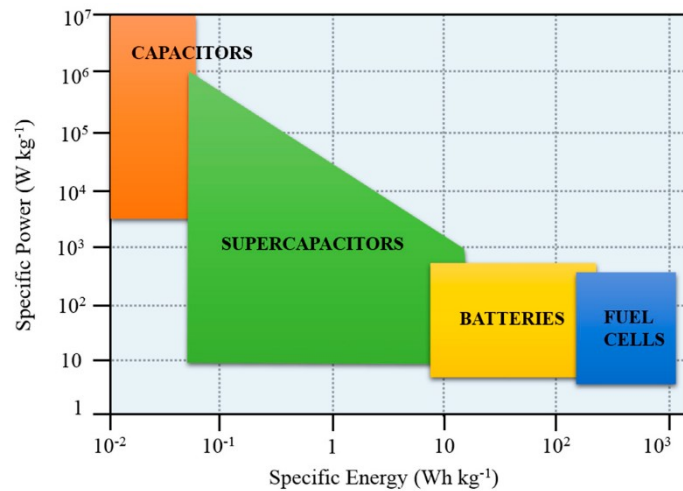
Figure 2: *Ragone plot for electrochemical storage devices and fuel cells as an energy converter.* [2]

2.1. Cell setup and working principle of a Li-ion battery

The general cell setup for a Li-ion battery can be seen in **Figure 3**. A single LIB cell consists of a positive and a negative electrode immersed in an electrolyte. The resulting potential difference between the electrodes drives a current when a load is applied. Because of this potential difference, redox reactions occur at each electrode, enabling simultaneously the electron transfer through the external circuit during discharge/charge. When discharging a battery, an electrochemical oxidation

$A \longrightarrow A^+ + e^-$ takes place at the negative electrode (anode). Typically, graphite is used as negative electrode material in commercial LIBs, since it provides a low potential vs. Li$^+$/Li and a moderate capacity accompanied with excellent cycle life. The reversible formation and decomposition of LiC$_6$ limits the specific capacity of graphite (372 mAh g^{-1}). In contrast to that, an electrochemical reduction occurs at the positive electrode (cathode) $B^+ + e^- \longrightarrow B$. Materials for the positive electrode are commonly layered oxides as they were found to provide high redox potentials and sufficient cycling stability. [3] Note that usually the positive electrode limits the specific capacity of the overall battery capacity, since reachable capacities are mostly below 250 mAh g^{-1}. [4] A typical example for a positive electrode is LiCoO$_2$ which was commercialized in the early 1990s for its use in LIBs. [4b, 4c] For this, the storage mechanism is based on the reversible intercalation/deintercalation of the Li-ions during discharge/charge cycles in the layered structures. The electrolyte between the electrodes serves thereby both as an ion conductor and as an electronic insulator. During the oxidation and reduction processes at the electrodes the electrolyte is partially decomposed at the electrode/electrolyte interface (especially on the negative electrode), this way forming a solid electrolyte interphase (SEI). The so called SEI model was firstly introduced by Peled *et al.* in 1979 for lithium electrodes. [5] The SEI is composed of organic and inorganic decomposition products being responsible for the passivation of the electrodes from degradation and is essential for the reversible transfer of Li-ions. [6]
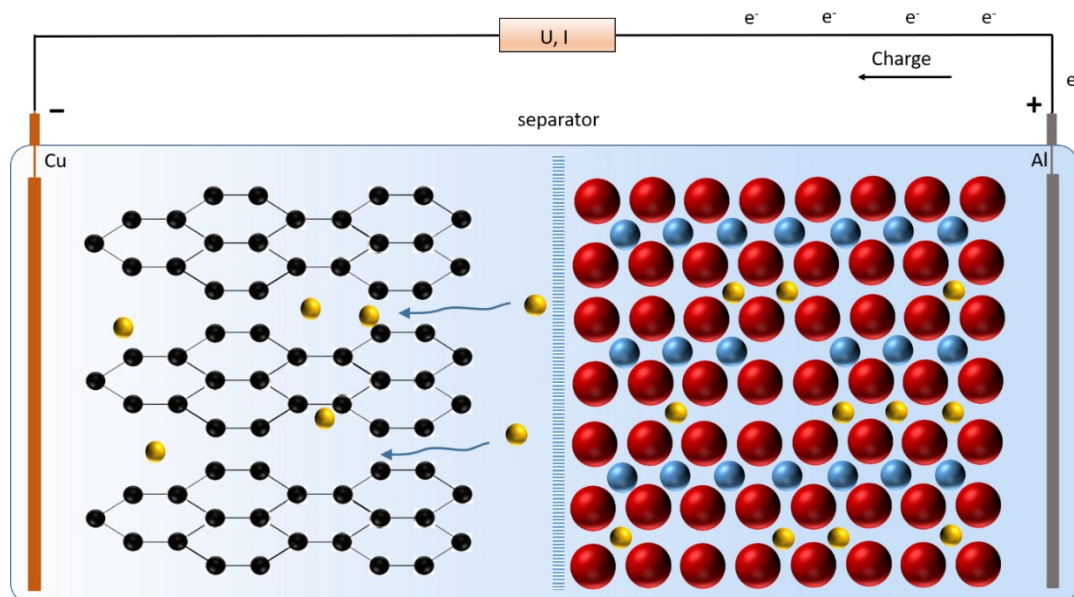
Figure 3*: General cell setup of a Lithium ion battery.*

2.2. Change to sodium ion batteries - a promising abundant and environmentally friendly alternative

The limited abundance of lithium and other elements typically used in LIBs such as Co or Ni may cause, together with geopolitical issues, restriction of the widespread use of LIBs in the future. For an electric vehicle for example, 7.5 kg Li, 65 kg Ni, Co, Mn, 55kg graphite, 48 kg copper and 30 kg of aluminum can be roughly assumed. [4c] On base on this estimation one can conclude that large scale production of electric vehicles can lead to depletion of resources in the closer future. Furthermore, electrochemical stationary storage based on Li-ion technology would lead to even more issues. Because of these conditions, there is a need for alternatives. Abundant, environmentally friendly and more cheap materials have to be used. A promising alternative to lithium is the use of sodium, as it demonstrates similar chemical properties. The current research progress and opportunities about sodium-ion batteries (SIBs) can be seen in several review articles. [4c, 7] However, despite the similarities of Li and Na, the redox chemistry of host materials for both is different in many cases. This might be due to the different ionic radius of sodium (r = 1.02 A, CN = 6) compared to lithium r = 0.59 A, CN = 4 [8]) and the less polarizing nature of Na^+ which influences the phase behavior (crystal structure, coordination number and lattice constants) and the diffusion properties as well. [4c] Calculations for several organic molecules have shown that the energy required for stripping the solvation shell from Na^+ is much smaller compared to Li^+.[9] Conclusively, the charge transfer resistance is expected to be smaller for Na^+ which may improve the electrode kinetics. Some differences between the use of lithium and sodium are discussed in the following. Graphite, for example, cannot be used as negative electrode, since sodium does not form Na-rich intercalation compounds with graphite. Nevertheless, it is possible to intercalate sodium via the co-intercalation mechanism together with solvent molecules, which was shown by Jache *et al.,* but this way only minor capacities of about 110 mAh g^{-1} can be achieved. [10] Moreover, sodium does not form alloys at low voltages with aluminum in contrast to lithium. This circumstance allows the use of the comparably cheap aluminum as current collector instead of copper also at the negative electrode, this way lowering the cost of the battery. Looking at the positive electrode, using the layered oxide $NaCoO_2$ as intercalation host material instead of $LiCoO_2$ that is popular in LIBs leads to a huge difference of the voltage profiles, see **Figure 4**. [4c, 7d] Thereby, the overpotentials drastically increase and several voltage steps can be observed, which is attributable to differences of phase transitions during charge and discharge, respectively. The multiple voltage drops make $NaCoO_2$ unattractive for application and consequently other compositions of layered composites are required. [11] Usually nickel-iron-manganese (NFM) compounds and polyanionic structures show promising electrochemical performance and competitive reversible capacities when being used as cathode materials for SIBs, for example. [4c, 7a, 7d, 12] A further advantage of latter mentioned cathode materials is the avoidance of the use of cobalt (Co), which is toxic and expensive. As shown in **Figure 4** the average discharge voltage of $LiCoO_2$ is larger than that from $NaCoO_2$. This shift to lower voltages in case of sodium is observed

for most of the electrode materials known. A schematic overview of potential shifts for selected compounds can be seen in **Figure 5**. [4c]

This phenomenon is due to the energetically less favorable Na^+ intercalation compared to Li^+ intercalation, but there are also exceptions for some conversion reactions, being discussed further below. [4c, 13]
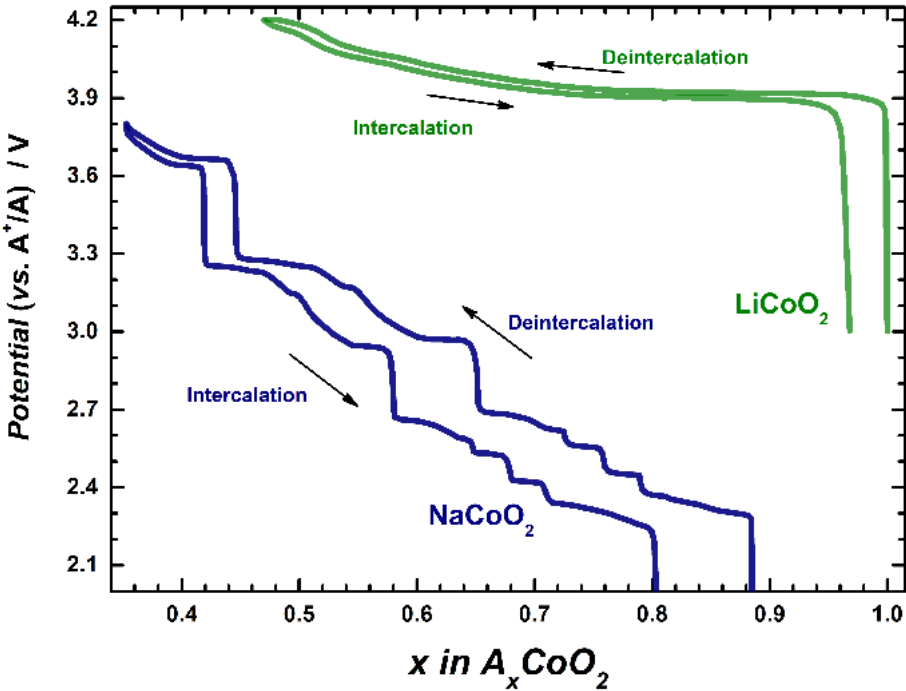
Figure 4: Comparison of the voltage profiles of LiCoO₂ and NaCoO₂ for their use in Li and Na half cells, respectively. Reprodcued with permission from Wiley. [4c]
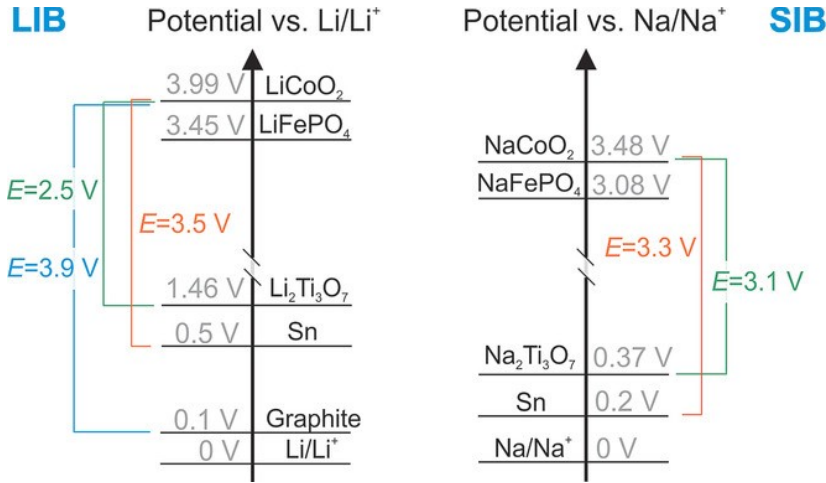
Figure 5: Schematic shift of cell potentials when switching from Li to Na analogues. Reproduced from with permission from Wiley. [4c]

3. State of the art: Electrode types

Electrode materials are generally classified in intercalation compounds and conversion electrodes. Latter mentioned electrodes can be either based on the use of metals/alloys or transition metal compounds. It is important to note that alloys are discussed as an extra type of reaction mechanism in many literature articles, but these can be counted to conversion electrodes as well since new phases form during the reaction, which is the main characteristic for this kind of electrodes. Nevertheless, often only transition metal compounds are classified as conversion electrodes. In view of the industrial use, electrodes based on the intercalation mechanism dominate the market so far because of their excellent cycle life accompanied with a small volume expansion during cycling. [3c-e, 14] Although the properties of the intercalation compounds appear promising, they suffer from their quite limited capacities. Thus, the use of conversion electrodes might be a promising option in order to enhance the capacities due to the transfer of several electrons per formula unit of the active material. Next to these advantages from conversion electrodes some challenges like large volume changes and overpotentials remain. A more detailed discussion of the electrode types is presented below.

3.1. Intercalation electrodes

Intercalation electrodes are used in most commcercialized LIBs as well as many SIB prototypes and lab cells. This is due to the highly reversible cell reaction as only small volume changes occur during the intercalation/deintercalation of alkali-ions between the layers, while the crystal structure is maintained. A schematic illustration of the intercalation mechanism can be seen in **Figure 6**. [15] During intercalation/deintercalation the chemical potential is continously changing due to the continous change of the alkali-ion concentration within the layered structure, resulting in a slope of the corresponding voltage profiles. Intercalation compounds provide only moderate energy densities and capacities, since intercalation electrodes are mostly limited to the transfer of only less than 1 e^- per formula unit. Layered oxides and polyanionic compounds are well known examples, as they provide often high voltages, thus making them attractive for application for their use as cathode materials. [4c, 7d, 12a, 15] While for LIBs only MO_6 edge sharing octahedra are observed, which are separated by lithium when occupying octahedral instional sites (O-type), different types are frequently observed for SIBs (O-type and P-type). [14b] This way, sodium layered oxides can adopt O3, O1, P2 or P3 crystal structures. [14c, 16] The number indicates the number of transition metal oxide (MO_2) layers per unit cell. Hence, O-type phases exhibit sodium in the octahedral sites and P-type phases exhibit sodium in prismatic sites within the crystal lattice. [16a] Numerous Na-layered oxides can provide specific energies from 400-600 Wh kg^{-1} for Na half cells. [4c, 7d, 14b] For the negative electrode, intercalation compounds can be used as well. Graphite is the material of choice for commercially available LIBs, in which usally 6 carbon atoms match with one lithium-ion, for example. [4c] Unfortunately, as already mentioned, sodium cannot be intercalated into graphite in the same manner as lithium. Though,

sodium can be reversibly intercalated together with its solvation shell as it was described by Jache *et al.* in 2014 for the first time. [10] Several studies followed related to that. [14d, 17] Nevertheless, minor capacities of just 110 mAh g^{-1} can be reached this way, thus research aims at developing alternatives with higher capacity. Other useful intercalation compounds for the negative electrode are diversified titanium oxides, for example, since titanium is a quite abundant element. However, the limited capacities below 200 mAh g^{-1} are still an issue for reaching high energy densities for a cell. [18]
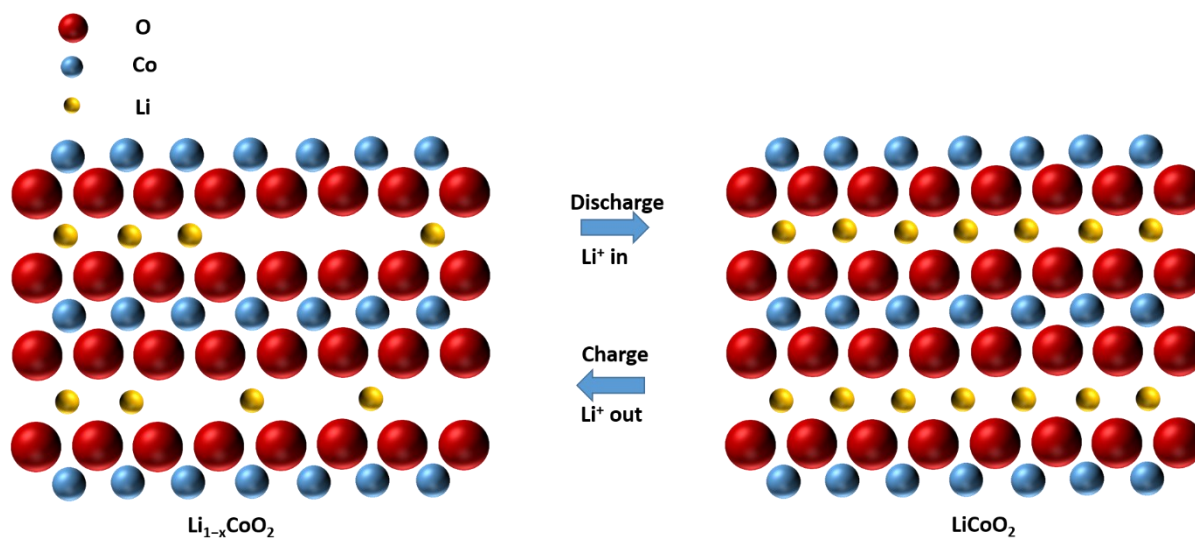
Figure 6: *Schematic drawing of the intercalation mechanism for LiCoO2 as an example for a layered oxide.*

3.2. Conversion electrodes

Conversion electrodes are the only option to reach significantly higher specific capacities on the materials level, as they can store several Li/Na atoms per formula unit. As already mentioned above, conversion electrodes are classified in alloys and transition metal compounds. The conversion types are discussed below.

3.2.1 Alloy electrodes

Alloy electrodes form intermetallic phases and/or compounds with Li and Na when being cycled. Thus, they can form solid solutions as well as defined stoichiometric compounds during discharge/charge. Phase transitions during the cell reaction often correlate with the predicted phase transition from the corresponding phase diagrams. Hence, voltage steps occur when forming a new phase upon discharge/charge. At the same time, also the formation of metastable or amorphous phases is often observed, i.e. the phase diagram is only useful for providing a first hint on what specific reactions will take place. When reaching one-phase regions of a phase diagram upon discharge/charge, solid solution behavior takes place being indicated by a continous change of the cell voltage. Alloy electrodes may enable extraordinary high capacities, but unfortunately, this advantage causes huge volume changes of several hundred percent. This issue can be alleviated by nanostructuring or the embedment of the active material in a carbon matrix as it was shown in previous studies. [19]

Silicon (Si) is the electrode material providing the highest storage capacity of all known electrode materials as it forms $Li_{3.75}Si$ enabling ~3590 mAh g^{-1} at state of full lithitation. [19a] However, the use of Si in Na cells is rather difficult as simulations from Jung *et al.* have shown that the electrochemical formation of a Na_xSi alloy is dependent on the crystallinity of Si. They found that amorphous Si can electrochemically uptake 0.76 Na when using amorphous Si corresponding to a capacity of 725 mAh g^{-1}. In contrast to that, the formation enthalpy for $Na_{0.76}Si$ using crystalline Si is positive (+0.18 eV), which means that the formation of $Na_{0.76}Si$ being energetically unfavorable. But, however, the formation enthalpy is −0.15 eV for the use of amorphous Si, enabling the formation of the intermetallic phase. [20] An experimental study from Lim *et al.* showed that the practical capacity of a-Si is rather low and can be only enhanced when being used in compounds. [21] More promising candidates for SIBs are tin (Sn), antimony (Sb) and lead (Pb) for example, since these elements show very high theoretical capacities at reasonably low redox potentials thereby providing good cycle life. [7d, 19c, 22] In this thesis, one publication is based on the consideration of the reversible sodiation/desodiation of a Sn based compound/mixture with Sb. Electrochemical properties of Sn, Sb and the intermetallic phase SnSb for the use in Na cells are discussed in the subsequent subchapters.

3.2.1.1 Tin

The advantage of tin in comparison to other electrode materials is due to environmental friendly applicability, the quite low redox potential and the high theoretical capacity of 847 mAh g^{-1} including the formation of Na$_{3.75}$Sn. [19c, 23] Unfortunately, tin undergoes a volume expansion of ca. 420% [19c, 22f] during sodiation/desodiation cycles. Despite the large volume expansion caused by the larger size of the sodium ions, the capacity retention is even better in case of Na in comparison to Li, because of the higher structural stability during cycling. Related to that, Wang *et al.* found based on an X-ray nanotomographic study that lithiation of tin results only in microsctructural damage, but delithiation leads to large pulverization among the formation of pores. Using Sn in Na cells instead, large volume changes occur upon sodiation, but desodiation induces only volume contraction with negligible pulverization, while maintaining the microstructural integrity. [24] The alloy formation of Sn with Na with its voltage profile is shown in **Figure 7**. [22a] From that one can see that not all phase transitions known from the phase diagram cause a voltage step with view on the voltage profile inlay. This fact indicates that kinetical limitations hinder the transitions in several thermodynamically stable phases.

The sodiation of Sn proceeds over four steps undergoing crystalline as well as amorphous intermediate phase transitions. Ellis *et al.* summarized the cell reaction as follows with 'a' stating the intermetallic phase being amorphous and '*' stating an unexpected crystalline phase. [4c, 22b, 25]

Plateau 1: $Na + Sn \longrightarrow NaSn_3 *$ (eq. 1)

Plateau 2: $Na + NaSn_3 * \longrightarrow a - NaSn$ (eq. 2)

Plateau 3: $5Na + 4(a - NaSn) \longrightarrow Na_9Sn_4 *$ (eq. 3)

Plateau 4: $6Na + Na_9Sn_4 * \longrightarrow Na_{15}Sn_4$ (eq. 4)
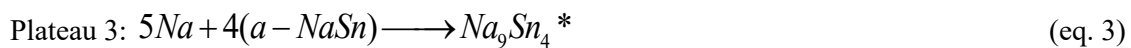
DFT calculations about the phase transitions were performed by Chevrier and Ceder and they found similar results. [22f] Slightly different phase transitions were also found by Wang *et al.* [26], which implies that the sodiation of Sn is not clearly understood yet and appears rather complex. [4c] Especially during charging, the phase transitions can be linked to four clearly observable distinct voltage plateaus. [22a, 25, 27] The overall best performance of Sn/C electrodes after their synthesis by ball milling was shown by Zhang *et al.* as they used a diglyme electrolyte instead of conventional carbonate electrolytes (NaPF$_6$ in diglyme). This way, a capacity of 768 mAh g^{-1} after 100 cycles was retained. [19c] The average redox potential of Sn is about 0.2 V vs. Na$^+$/Na, which is appealing for application.
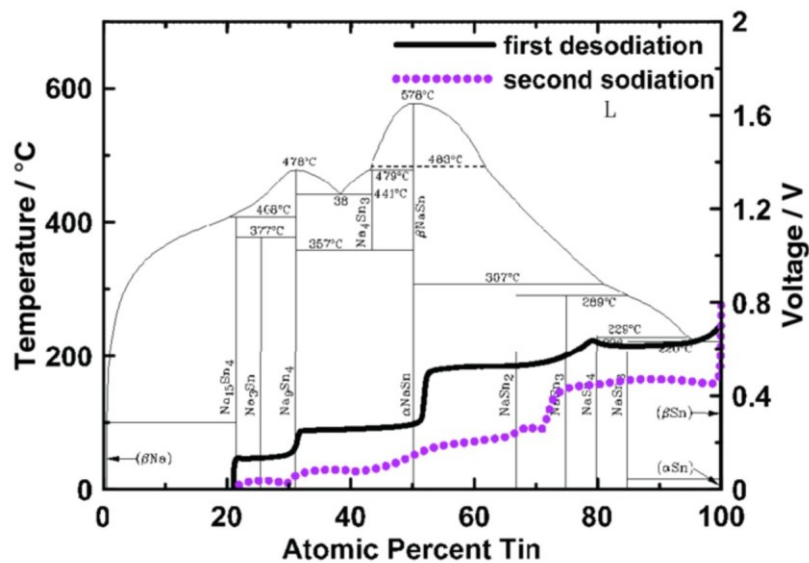
eq

Figure 7: Na-Sn phase diagram and the corresponding voltage profile for the electrochemical sodiation/desodiation of tin. Reproduced from with permission from Elsevier. [22a]

3.2.1.2 Antimony

Another attractive anode material for SIBs is antimony. It shows a high theoretical capacity of (660 mAh g^{-1} with formation of Na$_3$Sb) and usually enables a comparably better capacity retention and a smaller volume change (~390%) in comparison to tin. [22f, 28] A further advantage is the cheap price of Sb, which is rather low (about only 7 $ kg) making it attractive for its use. [22] But unfortunately, Sb suffers from its toxic properties. Nevertheless, however, it might be used in minor content or as additive in applications. The Na-Sb phase diagram is shown in **Figure 8**. The phase transitions in the voltage profile for the sodiation of Sb are hardly visible as compared to those of tin. However, sodiation of Sb takes place at an average value of about 0.6 V and typically occurs within three steps after the initial sodiation/desodiation cycle: Amorphous Sb transforms into a-Na$_3$Sb, subsequently into hexagonal/cubic Na$_3$Sb and finally in pure hexagonal Na$_3$Sb after full sodiation. Based on this reaction mechanism the cycle life is very stable. [19d, 29] Sb can even enable good cycle life when using it as bulk electrode. Darwiche *et al.* obtained this way 580 mAhg^{-1} after 160 cycles at a current rate of 55 mA g^{-1} for Na half cells. [30]
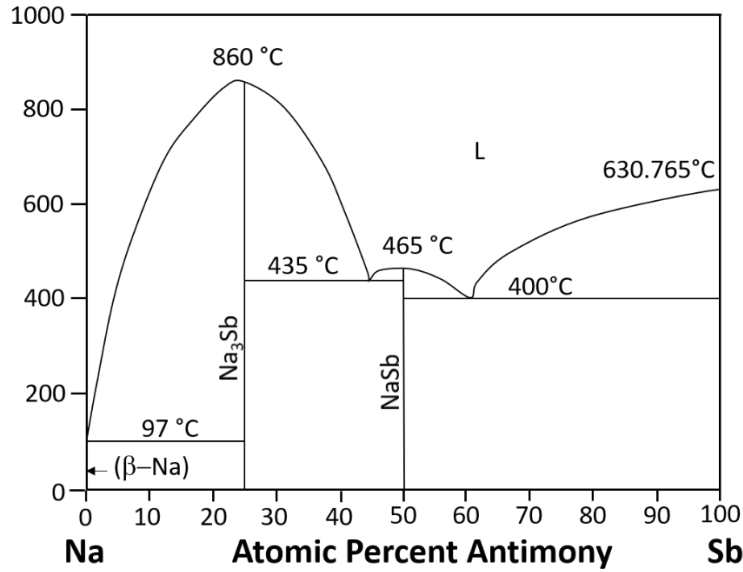
Figure 8: Na-Sb phase diagram. Redrawn from reference [31].

3.2.1.3 Stistaite – SnSb

Another option to enhance the cycle life is the use of binary or ternary intermetallic phase systems instead of pure metals. However, the sodiation of SnSb is known to be more complex in comparison to the sodiation of its constituents. SnSb undergoes a couple of (amorphous) phase transitions during sodiation. [22d, 22g, 32] Thus, electrochemical reaction with Na results in a different voltage profile. The phase diagram of Sn-Sb shows that the stoichiometric ratio can slightly vary at the 1:1 ratio due to solid solution behavior over a small range (2 at%), see **Figure 9.** The simplified reaction equations for the stepwise sodiation of SnSb can be illustrated as shown in eq. 5, eq. 6.

$$SnSb + 3Na^+ + 3e^- \rightleftharpoons Na_3Sb + Sn \qquad\qquad E > 0.4 \text{ V vs. Na}^+/\text{Na} \quad \text{(eq. 5)}$$

$$Na_3Sb + Sn + 3.75Na^+ + 3.75e^- \rightleftharpoons Na_3Sb + Na_{3.75}Sn \qquad E < 0.4 \text{ V vs. Na}^+/\text{Na} \quad \text{(eq. 6)}$$
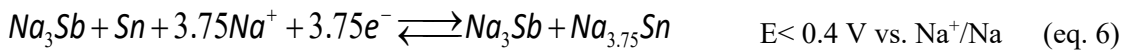
The overall reaction can be summarized as

$$SnSb + 6.75Na^+ + 6.75e^- \rightleftharpoons Na_3Sb + Na_{3.75}Sn \qquad\qquad\qquad \text{(eq. 7)}$$
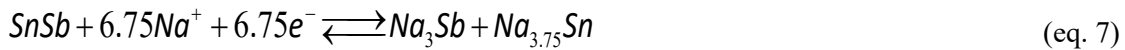
With view on eq. 7 one obtains an overall theoretical capacity of 754 mAh g^{-1} for the sodiation of SnSb. Note that Sb becomes inactive when reaching voltages < 0.4 V. After charging, SnSb is reformed again. [22d] This multistep reaction might enable a self-supporting network, which buffers the volume change and enhance electronic conductivity. [22d] The sodiation of SnSb was firstly investigated by Xiao *et al.* as they synthesized SnSb by simple reactive ball milling (BM) and used a carbonate electrolyte for their cells. [22d] They found a good cycle life enabled by the synergic properties of the elements Sn and Sb as they retained 435 mAh g^{-1} after 50 cycles, which is about 80%

of the initial capacity (544 mAh g^{-1})), being a good motivation for further studies on SnSb as an electrode.
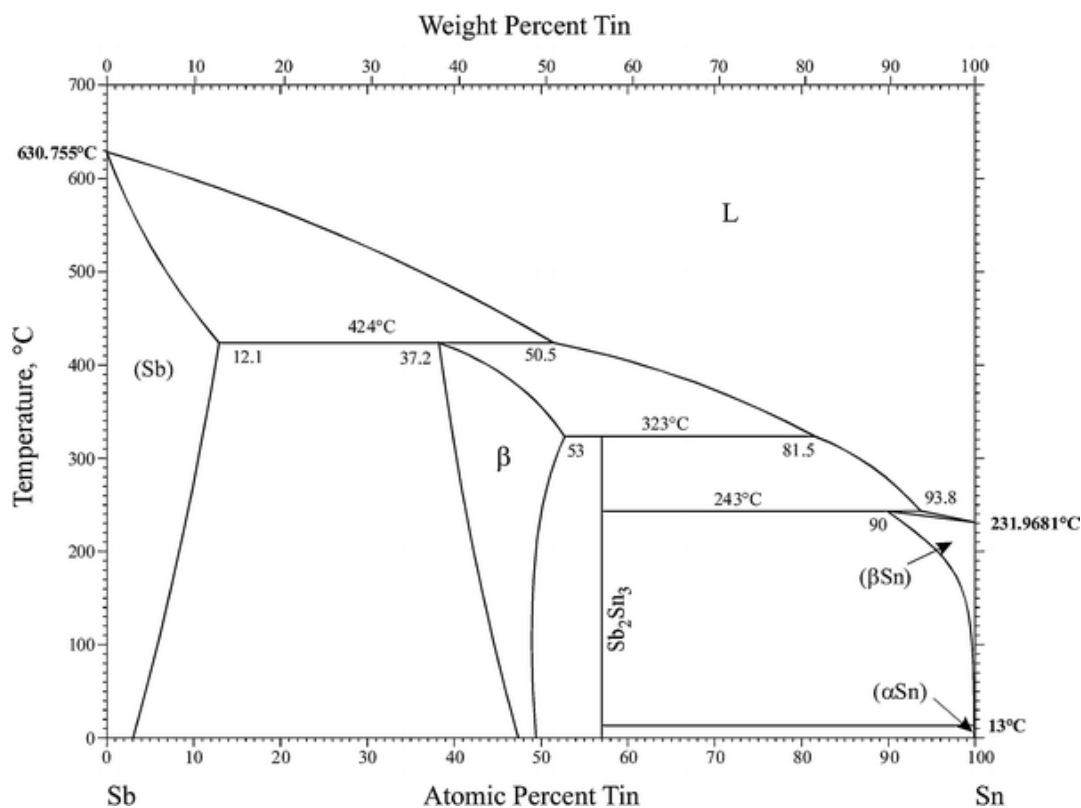
Figure 9*: Sn-Sb phase diagram. Reproduced with permission from Springer.* [33]

3.2.2. Transition metal compounds

Another promising option to obtain high capacities is the use of transition metal compounds as conversion electrodes. [13, 34]
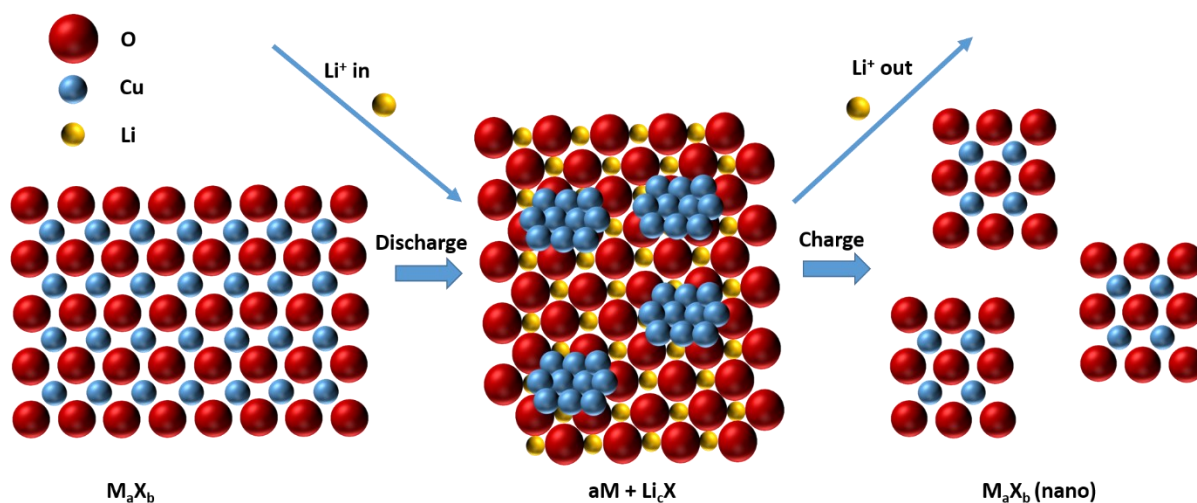
Figure 10*: Schematic view of a conversion reaction based on a transition metal compound.*

Transition metal compounds as conversion electrodes are indicated by the formation of stoichiometric defined compounds during cycling. The schematic reaction mechanism for these type of conversion electrodes is visualized in **Figure 10**. Hence, the general conversion reaction for lithium can be simply written as

$$M_a X_b + (bc)Li \underset{\text{charge}}{\overset{\text{discharge}}{\rightleftharpoons}} aM + bLi_c X \qquad \text{(eq. 8)}$$

M thereby represents a transition metal and X the anionic species initially bond with the transition metal, while a, b and c are constants. The described reaction leads to a constant chemical potential during the cell reaction, since the concentration of the alkali-ions in the host lattice is constant during conversion as only the amounts of charge and discharge products are changing. This phenomenon typically results in a horizontal voltage plateau upon discharge/charge when looking at the corresponding voltage profile. However, in many cases, voltage plateaus are non-ideal because of changes being caused by decomposition reactions on the electrode surface or the formation of amorphous phases and intermediates for example. Transition metal chalcogenides or halogenides basically undergo a complete reduction of a transition metal to its elemental state. That is why a transfer of several electrons accompanied with high specific capacities of several hundred mAh g^{-1} is possible.

However, several issues have to be considered for conversion reactions. Due to volume changes of several hundred percent for an electrode during conversion including the formation of a nanoscopic structure lead to contact losses and pulverization of the electrodes, resulting in rapid capacity fading. Moreover, large overpotentials assigned by a voltage hysteresis occur during discharge/charge. During the initial lithiation/sodiation process a kind of nanocomposite is formed, the structure of which is maintained upon cycling. [13, 34b, 35] The huge irreversible structural change in the initial cycle results commonly in a low initial coulomb efficiency (ICE) value. In order to buffer the volume changes, conversion materials can be embedded in a carbon matrix, reducing the volume changes and providing enhanced electronic conductivity within the electrode, for example. The benefit of these carbon composites was already studied in several research publications. [11b, 13, 22b, 22c, 36] Further options to circumvent structural instabilities due to volume changes and resulting capacity losses are the use of nanostructures or thin films. [7h, 34b, 34c, 37]

With view on application, conversion electrodes can be either used as cathode or anode material, since a wide range of materials with different operative voltages exists. Related to that, Klein *et al.* have shown that the voltages undergo a constant voltage shift when switching from LIBs to SIBs depending on the anion. [13] An overview about the voltage shift for several compounds can be seen in **Figure 11**. From this one can recognize that dependent on the anion, the voltages can be even higher in Na cells as compared to Li cells when using transition metal bromides or iodides, for example. [13] Thus, the redox voltage is simply tunable by substitution of the anion.
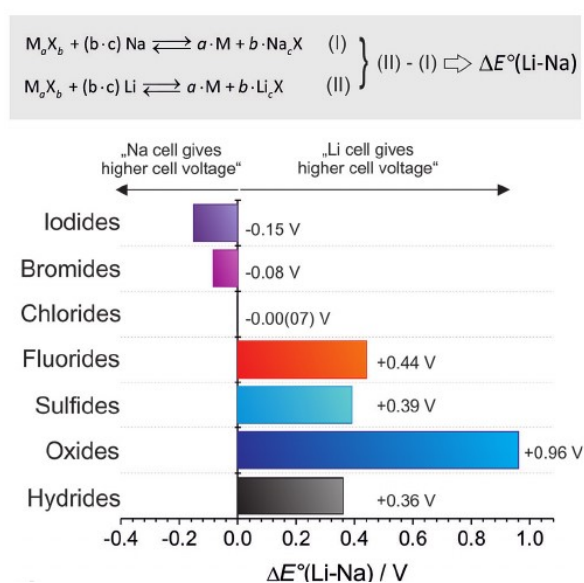
Figure 11: *The substitution of lithium by sodium results in a constant voltage shift of the cell voltages for different transition metal compounds, here presented with chalcogenides or halogenides. The Li cell provides higher voltages for fluorides, sulfides, oxides and hydrides. However, for bromides and iodides the cell voltages are even higher in Na cells. Conversion reactions with chlorides lead to nearly identical cell voltages in Li- and Na-cells. Reproduced with permission from Wiley.* [4c]

4. Aim of the thesis and approach

The use of three different conversion type electrodes for Li and Na cells is discussed within the thesis. A variety of analysis methods and electrochemical investigations was applied in order to study the cell reaction mechanisms for each considered electrode material. Hence, voltage profiles, phase transitions and cycle life have been analyzed. The materials were characterized before and after sodiation/desodiation and lithiation/delithiation, respectively. Partially, *in situ* measurements were performed in order to obtain information about structural changes during cycling. Within all herein presented studies, the electrodes were prepared by ball milling. A schematic overview of the research objectives is presented in **Figure 12**.

Herein, on the one hand, an alloy as electrode material was investigated with the aim to study the influence of ball milling time onto structural changes and the electrochemical performance for a mixture between the elements Sn and Sb and the intermetallic phase SnSb emebedded in a carbon matrix (publication 1). On the other hand, the electrochemical behavior of two transition metal compounds was studied. Related to that, Cu_3P was compared between its use in Li and Na cells in terms of voltage profiles, phase behavior and cycle life in different electrolytes under the same synthesis conditions (publication 2). In another study, the redox activity of a thiophosphate was investigated by using Cu_3PS_4 as a conversion electrode in Li and mainly in Na cells (publication 3).

Most of the herein considered studies were performed at the Friedrich-Schiller-University Jena within the Research group of Prof. Adelhelm. However, some measurements were conducted by cooperation partners in order to study the electrode properties after discharging/charging. TEM measurements were carried out in cooperation with the research group of Prof. Rettenmayr (Friedrich-Schiller-University Jena, Germany). XPS measurements were done by the research group of Prof. Turchanin (Friedrich-Schiller-University Jena, Germany). *In situ* XRD and additional TEM measurements were performed in cooperation with the research group of Prof. Pinna (Humboldt-University Berlin, Germany).
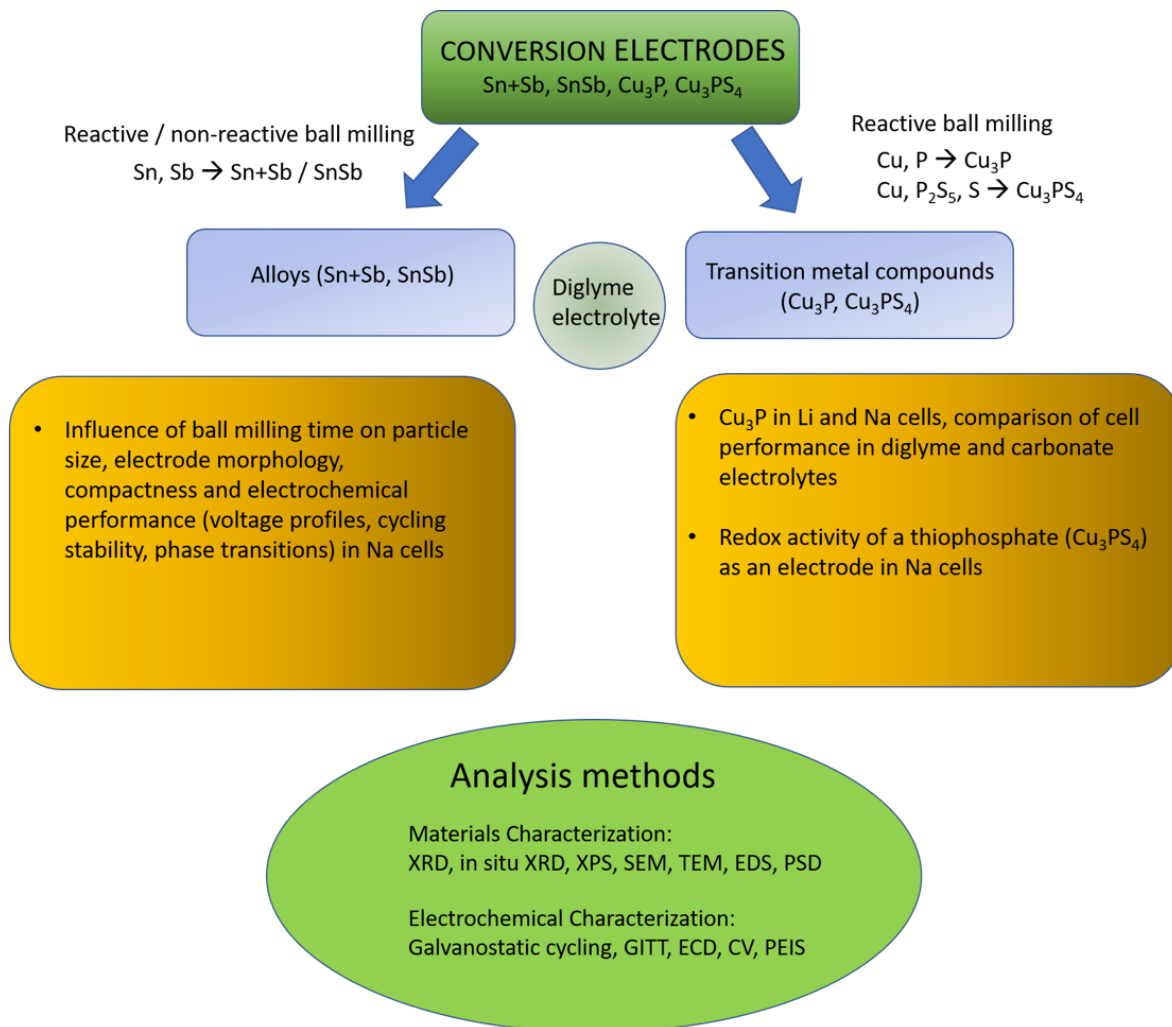
Figure 12: *Schematic overview of the research objectives. Alloys and transition metal compounds as electrodes were fabricated by ball milling. The investigations were done mainly using diglyme based electrolytes.*

4.1. The influence of the ball milling time on structural changes, phase behavior and electrochemical properties for an alloy electrode

An efficient synthesis of electrode materials is crucial considering their use in practical devices. In addition, energy consumption should be minimized for environmentally friendly production. A cost-effective and simple method to synthesize electrode materials is the use of high energy ball milling (HEBM). [22b, 22d, 38]

Herein, the applicability of the high energy ball milling synthesis method and its effects on structural changes are considered for a SnSb and Sn+Sb alloy electrode. The following questions are discussed.

- **Q1**: How does the ball milling time influence crystal structure, lattice parameters, particle size and distribution of the elements Sn and Sb when being milled together with carbon?
- **Q2**: Does reactive ball milling of the elements Sn and Sb (formation of SnSb intermetallic phase) lead to differences in the voltage profiles and cycle life in comparison to the use of non-reactive ball milling (formation of Sn+Sb mixture)?
- **Q3**: What is the impact of ball milling time in a swing ball mill (SBM) onto the electrochemical performance for both, when Sn+Sb and SnSb being milled with carbon?
- **Q4**: Which role plays the electrolyte?
- **Q5**: How does the ball milling time influence the composite formation and the electrode thickness change? Is there any relationship between thickness change and capacitiy accompanied with its retention?

Q1: In order to prove the influence of time ball milling time on crystal structure, lattice parameters, particle size and the distribution of the elements Sn and Sb, X-ray diffraction (XRD) and scanning electron microscopy (SEM) combined with energy dispersive X-ray spectroscopy (EDS) were performed. For the determination of changes in the crystal structure and the lattice parameters, diffraction patterns for different milling times were recorded. **Figure 13** shows the XRD pattern of the Sn+Sb mixture with time dependency of the ball milling time using a swing ball mill (SBM). The lattice parameters can be obtained by applying a Rietveld Refinement, (see SI publication 1: Figure S1).
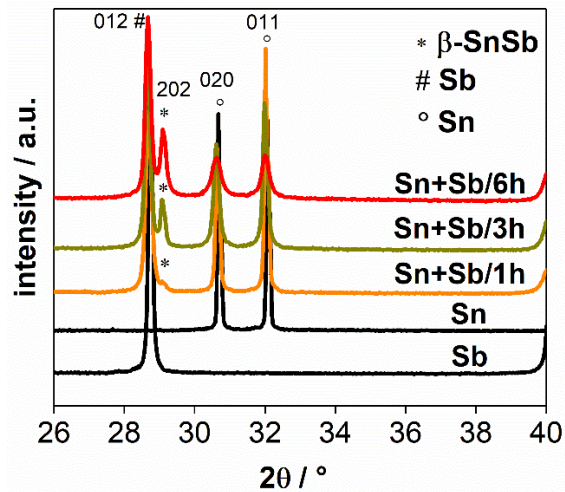
Figure 13: Diffraction patterns of Sn, Sb and the 1:1 mixtures after ball milling for 1h, 3h and 6h. Reproduced with permission from Wiley. [22b]

SEM combined with EDS are appropriate methods in order to detect morphological changes after ball milling. **Figure 14** shows the EDS and SEM images for the Sn+Sb mixture and the SnSb intermetallic phase after milling in a SBM for 1h and 6h. **Figure 14**a demonstrates the EDS and SEM images of the mixture of Sn+Sb. EDS shows that ball milling Sn and Sb for only 1h, leads to an inhomogenous distribution of both elements, while the SEM images show that the particles exceed sizes of even 50 μm. In contrast to that, the EDS and SEM images in **Figure 14**b show a homogenous distribution of the elements Sn and Sb for the intermetallic phase SnSb synthesized by reactive ball milling in an initial ball milling step in a planetary ball mill (PBM). Furthermore, particle sizes are found to decrease to below less than 10 μm.
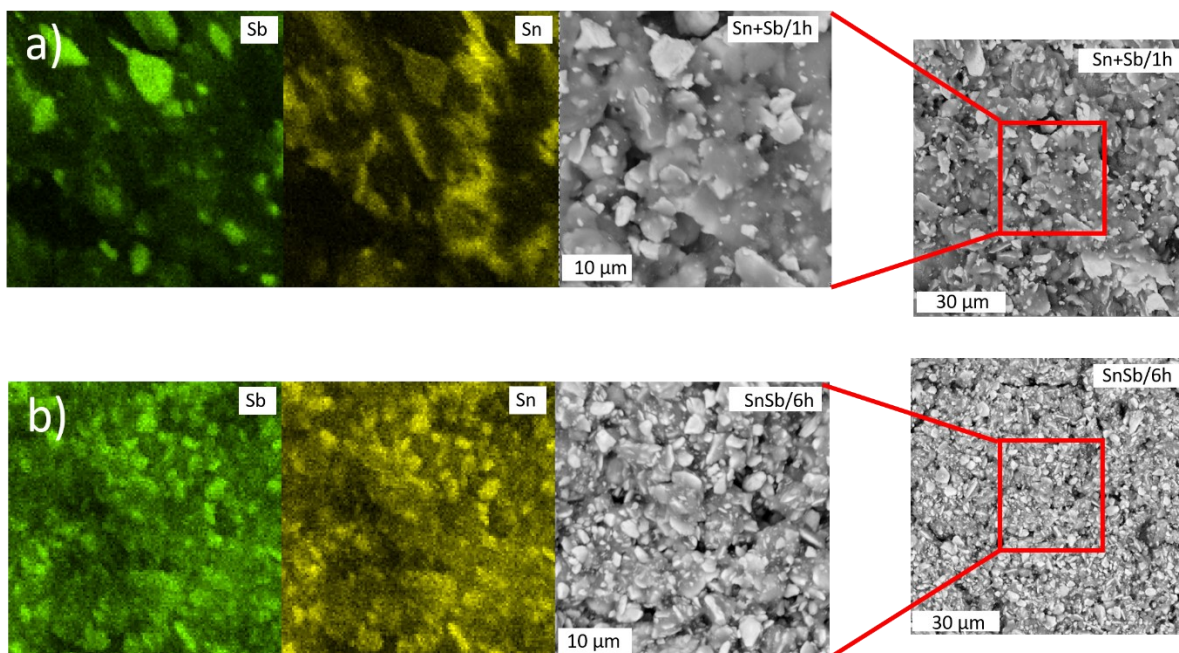
Figure 14: SEM images of Sn+Sb mixtures and the SnSb intermetallic phase after ball milling for a) 1h, and b) 6h with carbon. Reproduced with permission from Wiley. [22b]

Q2: Galvanostatic cycling with potential limitation (GCPL) can be used in order to investigate achievable capacities and cycle life of an electrode material. This method also provides an insight about how phase transformations occur during discharge/charge cycles with view on the voltage profiles. Herein, all measurements were performed using a diglyme electrolyte (1 M $NaPF_6$ in diglyme).

The question about the influence of reactive ball milling in comparison to non-reactive ball milling of the elemental components Sn and Sb onto the electrochemical performance can basically discussed by the sole use of GCPL.

Related to that, voltage profiles and a cycle life test of the intermetallic phase SnSb and the mixture of its constituents can be seen in **Figure 15**a,b.

The voltage profile for the Sn+Sb mixture, prepared by non-reactive ball milling, is found to be largely dominated by the redox activity of Sn, which can be explained by the redox inactivity of Sb in diglyme electrolytes, being discussed in detail in **Q4**. Moreover, the formation of SnSb by reactive ball milling leads to a smoothened two plateaus containing voltage profile. SnSb is undergoing a transition over a couple of intermediates upon sodiation/desodiation. [22b, 22d, 22g, 32]

Q3: The influence of ball milling time with carbon onto the electrochemical performance is discussed using GCPL when comparing the cycle life for different milling times (6h vs. 1h). For that, discharge capacity is illustrated over cycle number. As a result, enhanced capacity retention is found for Sn+Sb and SnSb being milled for 6h, which can be explained by improved composite formation as can be further seen from **Figure 15**b.
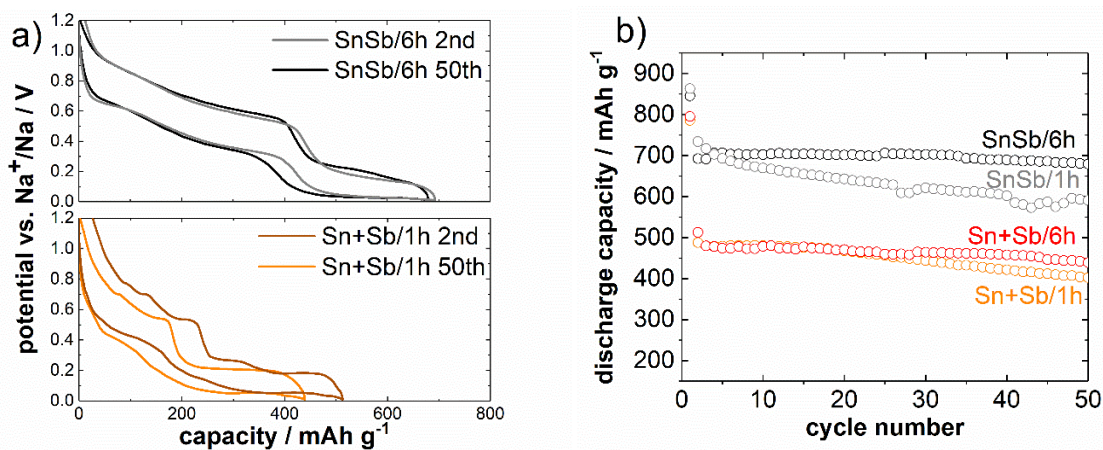
Figure 15: Galvanostatic cycling of SnSb and Sn+Sb electrodes (C-rate of 0.13 (100 mA g^{-1})) in a diglyme electrolyte (1M $NaPF_6$ in diglyme) in a voltage window of 0.01-1.2 V vs. Na^+/Na: a) Voltage profiles of Sn+Sb/1h and SnSb/6h; b) Discharge capacities of the first 50 cycles. Reproduced with permission from Wiley. [22b]

Q4: The influence of the electrolyte can be seen when comparing discharge capacities for Sn+Sb mixtures and the SnSb intermetallic phase. Capacities are observed to be much lower for the mixture when using diglyme electrolytes. In order to discover the origin of the much smaller capacities for the mixture in diglyme electrolytes, the constituents are compared for their application in both, diglyme and carbonate electrolytes. The results of the redox activity of Sb for both types of electrolytes are shown in

Figure 16a,b. However, in case of using diglyme electrolyte, large capacity fading of more than 75% occurs already in the 2nd cycle, while Sb cycled in a carbonate electrolyte delivers capacities of about 500 mAh g^{-1} even after 10 cycles. This observation leads to the conclusion that a thick passivation layer forms on the Sb electrode in diglyme electrolytes after the initial discharge/charge cycle, being impermeable for the Na-ions upon further cycling. In contrast, Sn is known to be largely redox active in diglyme electrolytes [19c] as can also be seen in **Figure 16c.** Consequently, this result indicates that the lower capacities of the Sn+Sb mixture in comparison to the SnSb intermetallic phase originate from the redox inactivity of elemental Sb in diglyme electrolytes after the initial cycle.
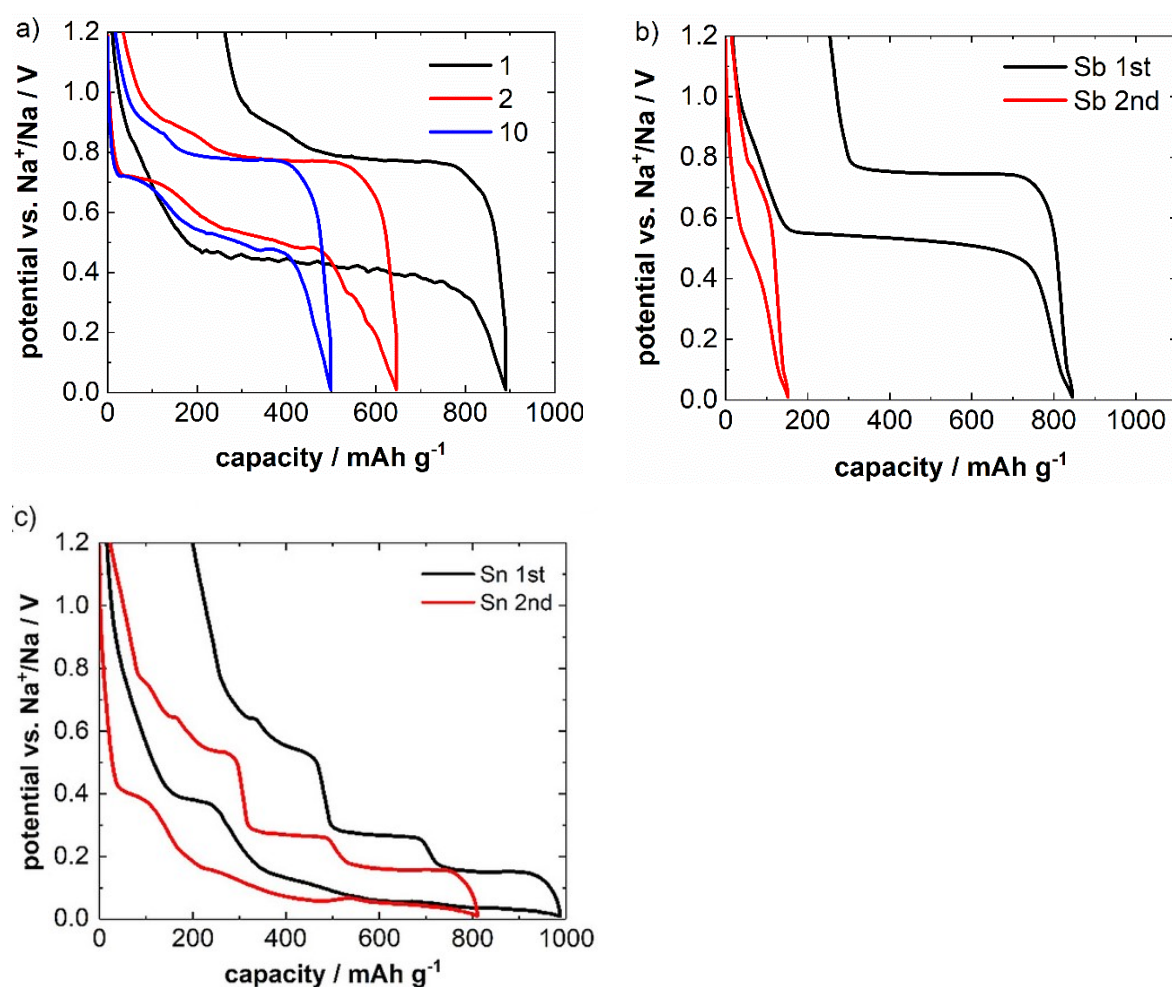
Figure 16: *Voltage profiles of a) Sb/C in a carbonate electrolyte (1M NaPF$_6$ in EC:DMC(1:1v)+FEC(2vol%)); b) Sb/C and c) Sn/C in a diglyme electrolyte (1M NaPF$_6$ in diglyme). Cycling was performed in a voltage range of 0.01-1.2 V vs. Na$^+$/Na at 100 mA g^{-1}. Reproduced with permission from Wiley. [22b]*

Q5: In order to investigate the thickness changes mentioned related to, *in situ* dilatometry (ECD) is performed. During a conversion reaction, the electrode undergoes a huge volume change due to changes of the crystal structure and the formation of a nanoscopic structure within the initial discharge process. This usually leads to contact losses resulting in rapid capacity fading. However, to circumvent this issue, particles of active material may be embedded in a carbon matrix which makes it impossible to determine the overall volume change by standard methods like *in situ* X-ray diffraction. Nevertheless, the shrinking and expansion of the whole electrode can be directly reliable measured and described by *in situ* dilatometry. Therefore, a sensor is fixed on the top of the electrode moving up and down with the electrode surface during the cell reaction, this way recording the electrode height change during cycling, which in the battery community is typically named as electrode "breathing".

Herein, *in situ* dilatometry was applied in order to find a correlation between electrode thickness changes and capacity retention in dependency of the ball milling time for SnSb and Sn+Sb with carbon. This method can consequently be used to assess whether composite formation or reactive ball milling of the metallic components is the most important factor in achieving improved capacity maintenance. The considered dilatometry studies are shown in **Figure 17**. Since the mass loadings are quite similar (1.18-1.44 mg cm^{-2}) and thus well comparable, the influence of ball milling on the compactness of the composites can also be discussed. Interestingly, the initial electrode thickness at longer ball milling times (6h vs. 1h) is smaller for both the mixture and the intermetallic phase, which is an indication of a higher compactness. Obviously, the height changes during cycling are also smaller and similar for SnSb and Sn+Sb electrodes for those that are subjected to a longer milling process together with carbon, resulting in improved capacity retention. Thus, one can link the enhanced capacity retention to reduced electrode breathing by a more compact embedment of the metallic particles in the carbon matrix enabled by longer milling. A more detailed view on **Figure 17** leads to the conclusion that composite formation with carbon by prolonged milling is the predominant process over alloying/mixing of the metallic components Sn and Sb to achieve reduced breathing accompanied with enhanced cycle life.
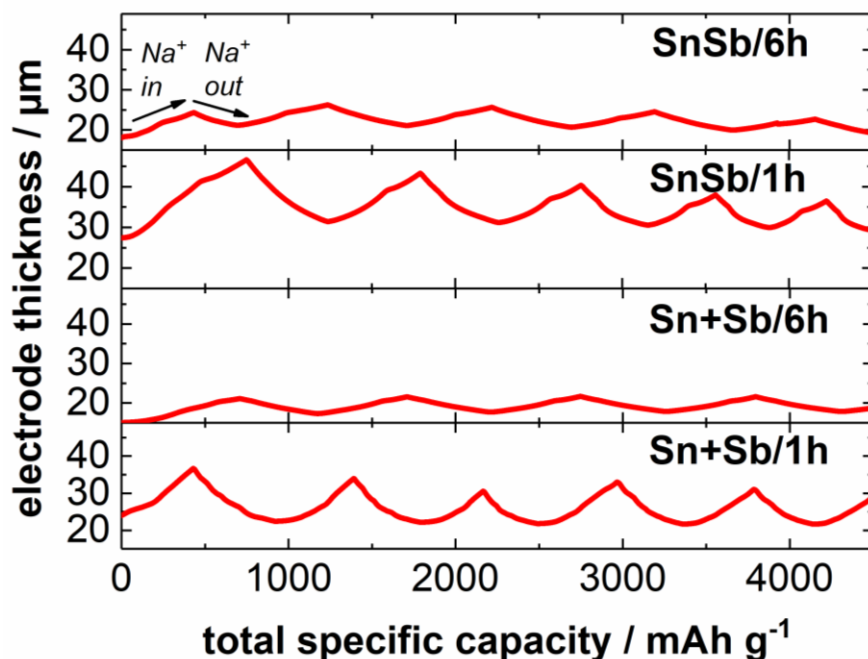
Figure 17: *Electrode thicknesses change during sodiation/desodiation of Sn+Sb and SnSb with varying ball milling times measured by ECD at 0.13 C (100 mA g^{-1}). Reproduced with permission from Wiley.* [22b]

4.2. Transition metal (copper) compounds
4.2.1 Li vs. Na comparison for a copper based conversion electrode (Cu₃P)

The use of copper rich copper phosphide (Cu$_3$P) in Li and Na cells is compared within this section for the use in combination with different types of electrolytes. Differences and correlations between electrode breathing, cycle life, capacity and voltage profiles are discussed. Following questions were aimed to be clarified.

- **Q1**: What is the difference in storage behavior between the use of Cu$_3$P in Li cells and Na cells?
- **Q2**: Which role plays the use of different electrolytes on the electrochemical performance with respect to voltage profiles, capacity retention, cycle life and rate performance?
- **Q3**: How much charge is stored in the carbon matrix?
- **Q4**: What is the difference in electrode thickness change when using Cu$_3$P as electrode material in Li cells compared to Na cells?

Q1: Best electrochemical results were achieved by using diglyme electrolytes containing large anions in the conducting salts (LiTFSI in Li cells and NaOTf in Na cells). To clarify the difference in storage behavior, these electrolytes are used in Li and Na cells. The difference in storage behavior can be determined by GCPL analyzing the voltage profiles for both cells, see **Figure 18**. In fact, one can observe a multistep reaction mechanism for lithium while for sodium only one large sloping plateau can be observed. One can see that the use of Li leads to larger capacities (210 mAh g^{-1} after 100

cycles in a voltage window of 0.5-2 V) compared to the use of Na (120 mAh g^{-1} after 100 cycles in a voltage window of 0.01-2 V) despite of the smaller applied voltage window at the same current density. One can also recognize that the use of Li leads to smaller overpotentials although the obtained discharge capacities after 100 cycles being higher compared to the Na cells, see **Figure 18**f).

Q2: In order to clarify the role of the different electrolytes, the use of carbonate and ether (diglyme) electrolytes is directly compared in terms of effects on overpotentials, cycle life and achievable capacities. Unfortunately, the dissolution of small anions like PF_6^- and ClO_4^- is not possible in diglyme, since these anions form immobile solid salt-solvent complexes with digylme in Li cells. [39] Thus, herein a smaller matrix of electrolytes is considered than one could expect. However, one can observe rapid capacity fading and a fast increase of overpotentials when using carbonate electrolytes upon cycling (see **Figure 18**b,d and **Figure 19**). Illustrating capacities vs. cycle number (see **Figure 19**) shows that the use of diglyme based electrolytes results in higher capacity retention, and if **Figure 18**a,c,e, is examined more closely, also in lower overpotentials for both, Li and Na cells.
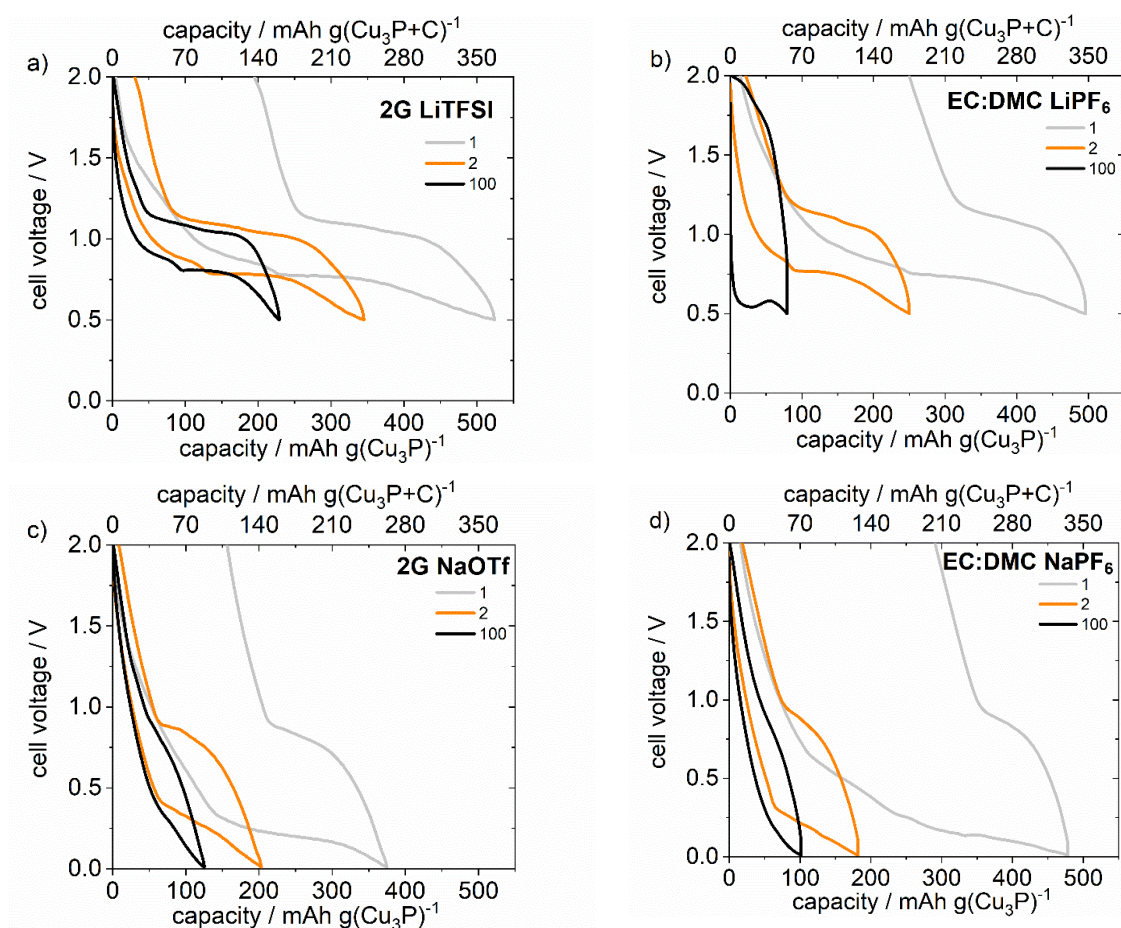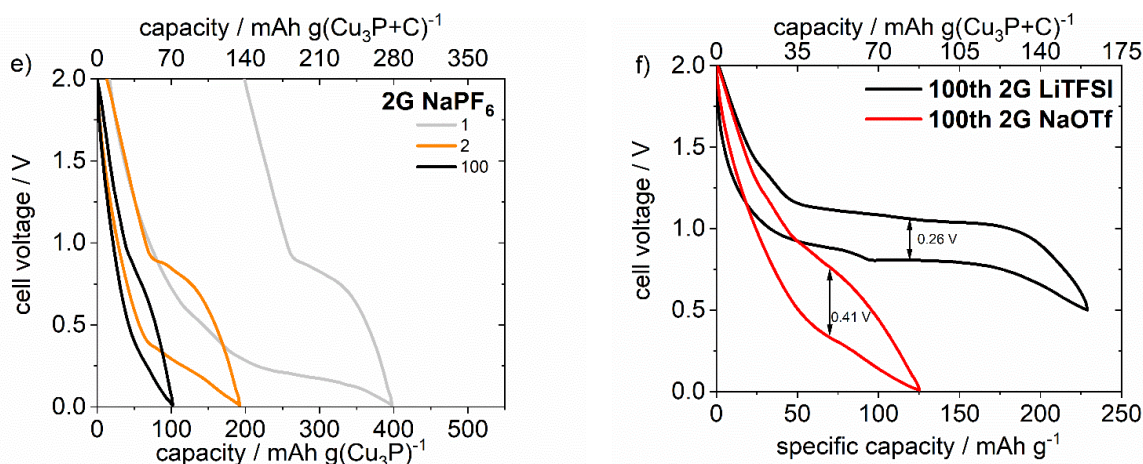
Figure 18: *Galvanostatic discharge/charge curves for Cu₃P/C electrodes in Li- and Na-half cells (two-electrode geometry with Li/Na as counter electrode) for different electrolyte solutions a) Voltage profiles of the 1ˢᵗ , 2ⁿᵈ and 100ᵗʰ cycle for a) 2G LiTFSI; b) EC:DMC LiPF₆; c) 2G NaOTf; d) EC:DMC NaPF₆; e) 2G NaPF₆; f) Voltage profiles of the 100ᵗʰ cycle for Li (2G LiTFSI electrolyte) and Na (2G NaOtf electrolyte) in comparison. Arrows indicate the combined overpotentials for both cells. Cycling was performed with a current rate of 0.1 C (36.6 mA g⁻¹) in a voltage window of 0.5-2.5 V in Li cells and 0.01 -2.5 V in Na cells. Reproduced with permission from Wiley. [36d]*
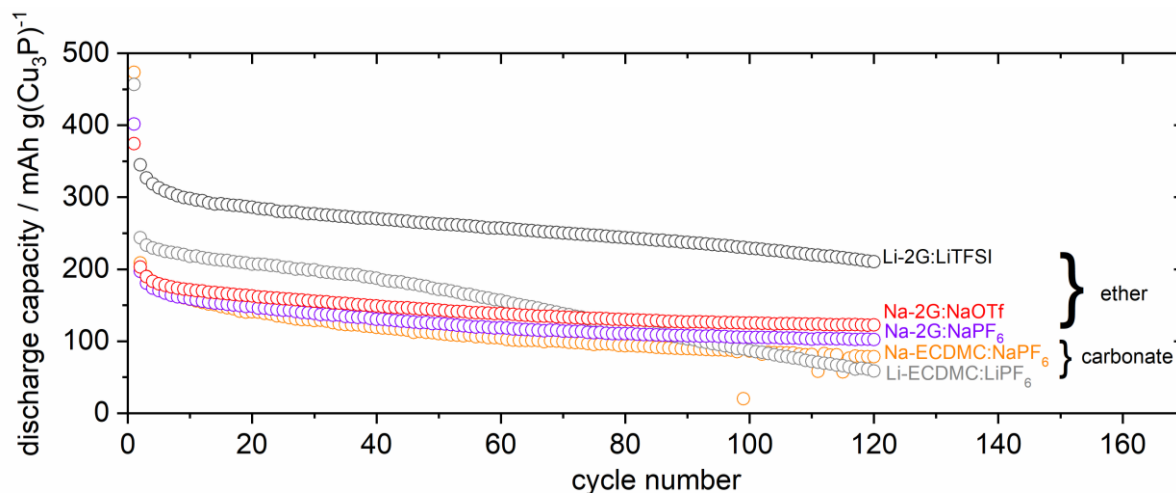
Figure 19: *Discharge capacities vs. cycle number for Cu₃P/C electrodes in Li and Na half cells (two electrode geometry) for different electrolytes. Cycling was performed with a current rate of 0.1 C (36.6 mA g⁻¹) in a voltage window of 0.5-2.5 V (Li cells) and 0.01 -2.5 V (Na cells). Reproduced with permission from Wiley. [36d]*

Since diglyme electrolytes containing large anions (TFSI⁻, OTf⁻) provided the best results, GCPL rate performance tests were were conducted with these electrolytes in order to receive information about the reaction kinetics (see **Figure 20**). Therefore, the applied current was increased every five cycles to higher C-rates and finally reduced to the initially applied C-rate. However, a larger capacity of about 300 mAh g(Cu₃P)⁻¹ was retained for Li (85% of the capacity of the 2ⁿᵈ cycle) as compared to 170 mAh g(Cu₃P)⁻¹ for the use of Na (71% of the capacity of the 2ⁿᵈ cycle), implying better reaction kinetics for Li cells.
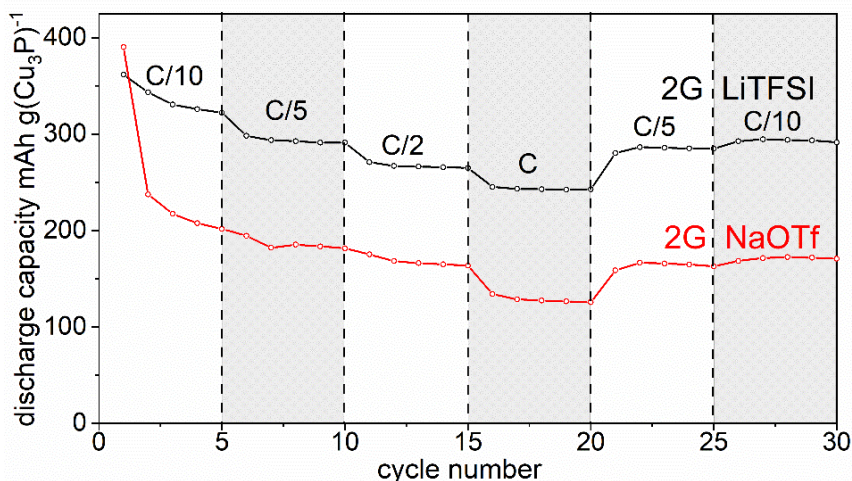
Figure 20: *Rate capability test for five different C-rates for Cu$_3$P/C electrodes in Li and Na half cells (two electrode geometry, 1C = 363 mA g^{-1}) in a voltage window of 0.5-2.5 V (Li cells) and 0.01 -2.5 V (Na cells). Reproduced with permission from Wiley.* [36d]

Q3: The carbon black contained in the electrode (30 wt%) enables extra capacity, thus capacity values are given per gram and per gram Cu$_3$P/C in the voltage profiles. To determine the contribution of carbon to the overall capacity, voltage profiles of the carbon black conducting agent were recorded at 36 mA g^{-1} for different electrolytes, as can be seen in **Figure 21**. The capacity contribution of carbon black in the case of Li is about 70 mAh g^{-1} after around 20 cycles with use of the electrolytes 2G LiTFSI and EC:DMC LiPF$_6$, see **Figure 21**a,b. These values remain almost constant upon cycling. The carbon content results in a capacity contribution of about 21 mAh g^{-1} to the overall capacity of Cu$_3$P in Li half cells which is only about 7% of the overall theoretical capacity of Cu$_3$P. The capacity contribution of carbon black in Na cells can be seen in **Figure 21**c-e. A reversible capacity of about 150 mAh g^{-1} is found for carbon black using 2G NaPF$_6$ and EC:DMC NaPF$_6$ within a voltage window of 0.01 V-2 V vs. Na$^+$/Na, which leads to a storage contribution of 45 mAh g^{-1} (12% of the theoretical capacity of Cu$_3$P) to the overall capacity of the Cu$_3$P/C electrodes. Because of the much smaller practical capacities in case of using Cu$_3$P in Na cells, the capacity contribution of carbon black can amount up to 38%, while for Li a capacity contribution of 10% is not exceeded.
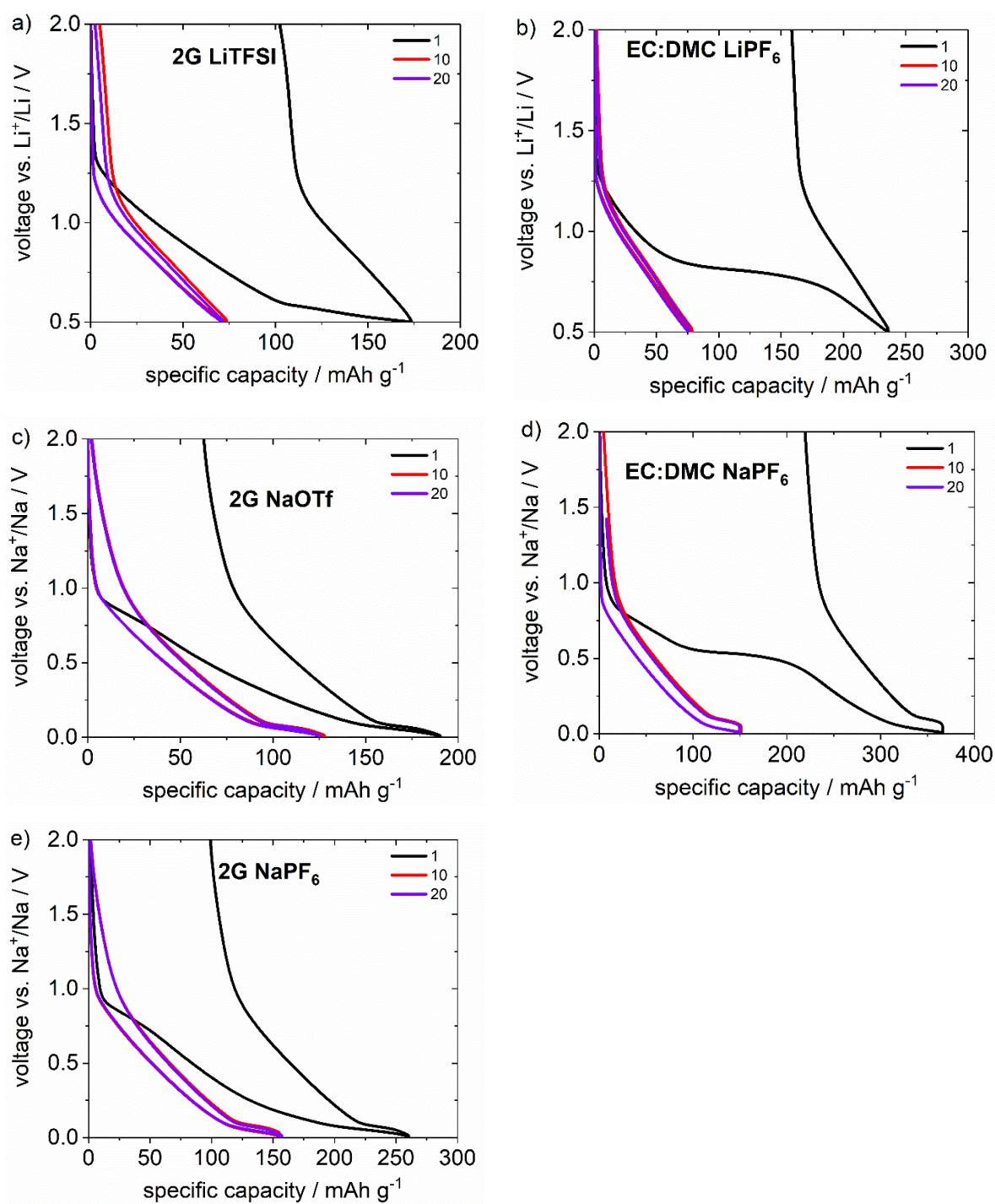
Figure 21*: Voltage profiles of carbon black at 36 mA g⁻¹ for different electrolytes. It is of note, however, that the preparation of carbon black electrodes is difficult as the material is very fluffy, which causes problems during electrode preparation. The mass loadings are typically very small (in our case about 0.7-1.0 mg cm⁻²). Overall, an exact deconvolution of the individual contributions of Cu₃P and carbon black to the capacity of the Cu₃P electrode is not possible, but the contribution of carbon black is discussed in the main manuscript. The herein used carbon black was carbon Super P. Reproduced with permission from Wiley.* [36d]

Q4: *In situ* dilatometry experiments were performed in order to investigate the influence of the alkali-ion on the electrode thickness change upon cycling. **Figure 22** shows the electrode thickness change for the lithium cell (LiTFSI in 2G) and the Na cell (NaOTf in 2G) within the intial five cycles. The considered electrodes are well comparable as mass loading and initial height are quite similar (36 vs. 39 µm) and (3.49 vs. 3.23 mg cm^{-2}). In the initial cycle, a larger height change for the sodium cell has been observed, which might be explained by the larger radius of the Na-ion, resulting in a higher volume expansion and a more excessive SEI formation. Upon consecutive cycling, height changes are larger in the lithium cell. This result is expected to be caused by the higher practical storage capacity of Cu$_3$P in the lithium cell, which usually leads to larger volume changes. The use of carbonate electrolytes shows analogue behavior and leads to a more rapid decrease of electrode breathing, being discussed more in detail in publication 2.
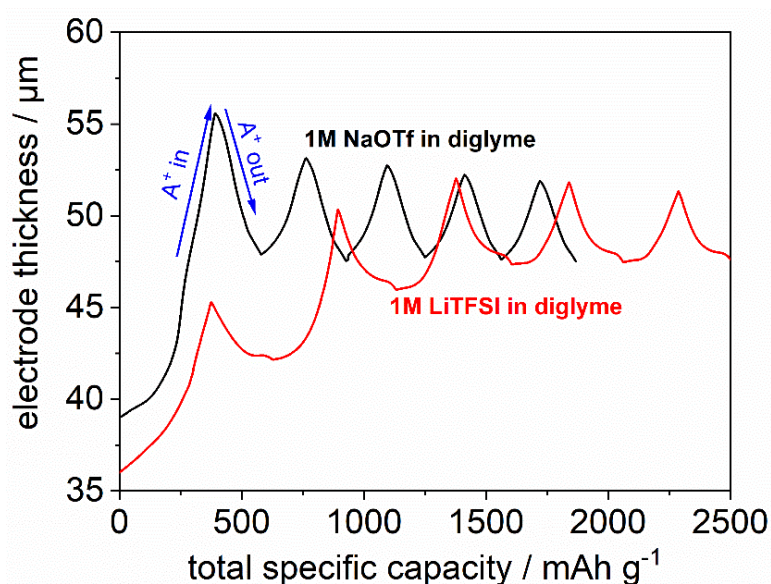
Figure 22*: In situ dilatometry studies of Cu₃P in Li and Na half cells with diglyme electrolytes for 1M LiTFSI in diglyme (red); and 1M NaOTf (black) in diglyme. Cycling was performed with a current rate of 0.1 C (36.6 mA g⁻¹) in a voltage window of 0.5-2.5 V vs. Li⁺/Li for the use of Li and 0.01 -2.5 V vs. Na⁺/Na for the use of Na. Reproduced with permission from Wiley. [36d]*

4.2.2 Redox activity of copper thiophosphate Cu₃PS₄

Within this chapter a novel transition metal based conversion electrode is basically discussed for its use in SIBs and partially for LIBs. Redox activity of Cu_3PS_4 is unknown so far, but a variety of thiophosphates was previously studied related to their use as solid electrolytes in solid state batteries (SSBs). [40] Following questions were aimed to be answered.

- **Q1**: Is it possible to synthesize pure phase Cu_3PS_4 by reactive ball milling of the raw materials Cu, P_2S_5 and S in appropriate stoichiometric amount, analogue to lithium/sodium thiophosphate Li_3PS_4, Na_3PS_4?

- **Q2**: What is the capacity and its retention over large cycle numbers? What are the advantages over copper sulfides and copper phosphides?

- **Q3**: Which alkali metal leads to better performance, Li or Na?

- **Q4**: Which elements are redox active? Are there differences and similarites in comparison to decomposition products when thiophosphates being used as electrolytes in SSBs?

Q1: The presence of Cu_3PS_4 after reactive ball milling of Cu, P_2S_5 and S was proven by XRD, see **Figure 23**. In order to check the presence of Cu_3PS_4 and its lattice structure in a local area, the crystals were visualized with transmission electron microscopy (TEM), as it is a powerful imaging method for illustrating nanosized particles and lattice planes on atomic level, see **Figure 24**. Based on these analysis tools, phase pure Cu_3PS_4 was found to crystallize in an orthorhombic crystal structure (P m n 21 space group). Informations about lattice parameters and particle size, determined by XRD are discussed in detail in publication 3.
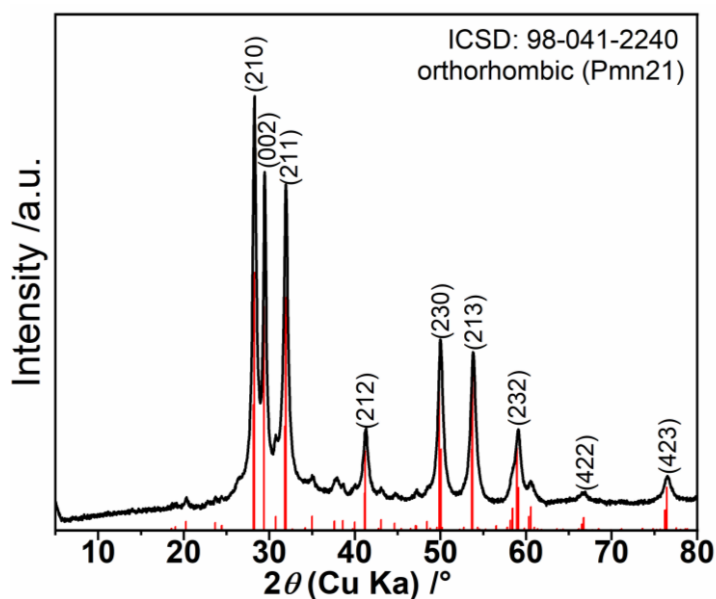
Figure 23: *X-ray diffraction pattern of Cu₃PS₄ powder synthesized by high energy ball milling for 24 h in a planetary ball mill (ICSD: 98-041-2240). The obtained pattern corresponds to an orthorhombic crystal lattice of the P m n 21 space group. Reproduced with permission from Wiley.* [11b]
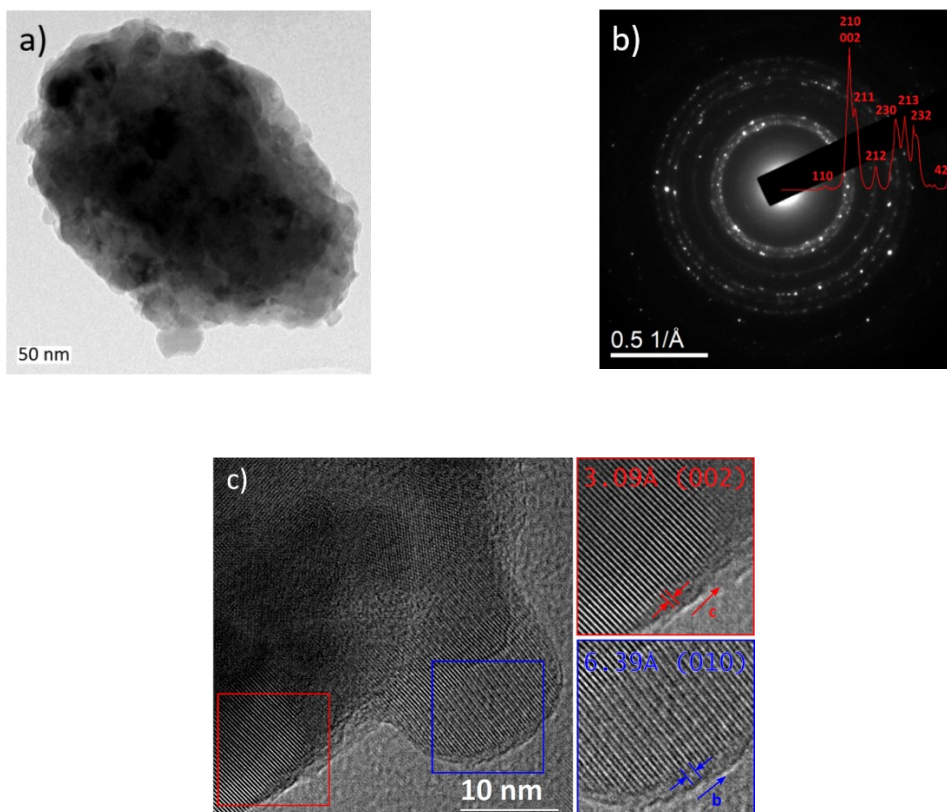
Figure 24: *TEM analysis of the Cu₃PS₄ powder after synthesis by reactive ball milling of Cu, P₂S₅ and S: a) single particle image; b) TEM/SAED pattern; c) HRTEM images of agglomerated Cu₃PS₄ crystals. Reproduced with permission from Wiley.* [11b]

Q2: In this study, electrochemical experiments were conducted using a diglyme electrolyte for Li and mainly Na half cells. Galvanostatic cycling was performed to get an insight in which extend Cu_3PS_4 contributes to the overall capacity and moreover, the reaction kinetics and mechanism. With view on **Figure 25**, the voltage profiles show that Cu_3PS_4 undergoes an activation process during cycling, since the capacities are increasing until up ~ 200 cycles at 120 mA g^{-1}, reaching values of about more than 580 mAh g^{-1}. Hence, Cu_3PS_4 enables even higher capacities and cycle life than what has been reported for copper sulfides and copper phosphides. [12b, 18, 30]
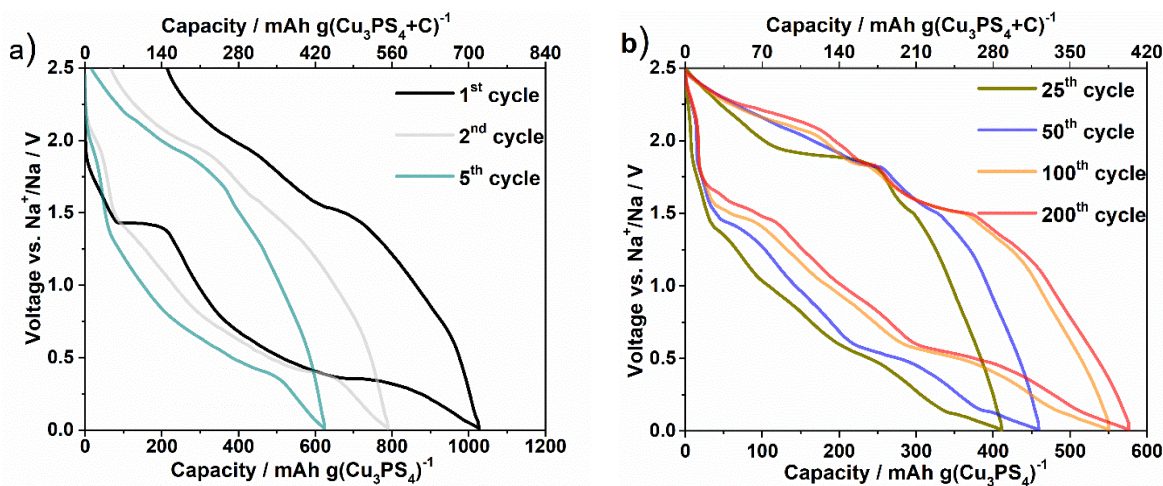
Figure 25*: a) Voltage profiles of the 1ˢᵗ, 2ⁿᵈ and 5ᵗʰ cycle. Cycling was performed with 1 M NaPF₆ in diglyme as electrolyte within a voltage window of 0.01 – 2.5 V vs. Na⁺/Na with a current density of 120 mA g⁻¹; b) voltage profiles of the 25ᵗʰ, 50ᵗʰ, 100ᵗʰ and 200ᵗʰ cycle. Reproduced with permission from Wiley.* [11b]

Q3: The cycle life of Cu_3PS_4 in Li and Na cells is compared in **Figure 26**a,b using diglyme electrolytes. Using $NaPF_6$ in diglyme as electrolyte was showing the overall best result (>600 mAh g⁻¹ after ~70 cycles @ 50 mA g⁻¹ and 580 mAh g⁻¹ @ 120 mA g⁻¹ after 200 cycles). In contrast, the use of a large anion (OTf⁻) resulted in rapid capacity fading in case of Na. For the use of Cu_3PS_4 in Li cells, only minor capacities of about 200 mAh g⁻¹ after 200 cycles @ 50 mA g⁻¹ were obtained (170 mAh g⁻¹ after 200 cycles @120 mA g⁻¹).
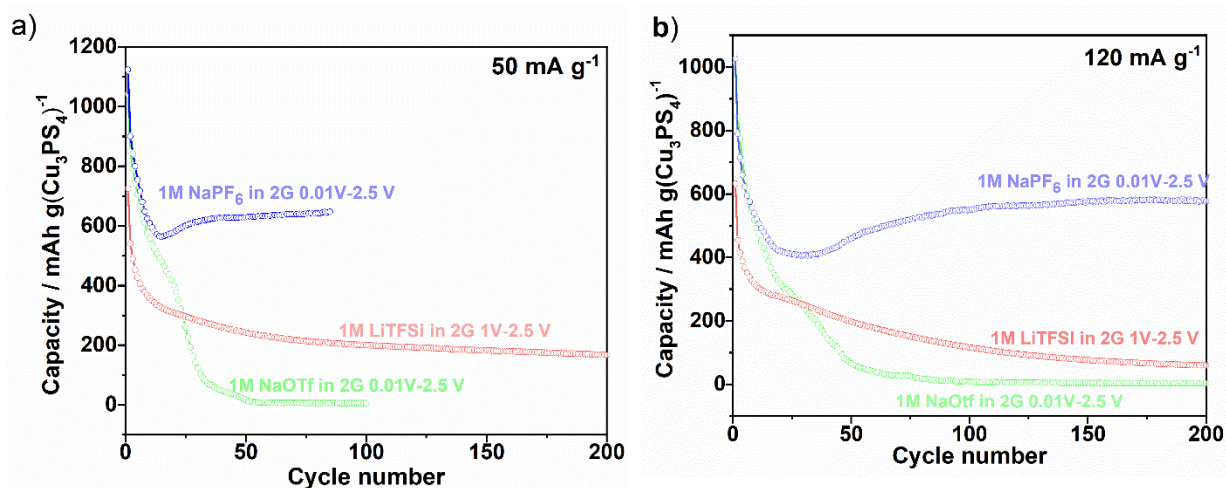
Figure 26*: Discharge capacities vs. cycle number with a current rate of a) 50 mA g⁻¹ and b) 120 mA g⁻¹ for Na and Li with different electrolytes using diglyme (abbreviation 2G) as a solvent. Reproduced with permission from Wiley.* [11b]

Q4: The redox behavior of Cu_3PS_4 was investigated in Na cells via the combined use of galvanostatic cycling, *in situ* XRD and X-ray photon spectroscopy (XPS). XPS allows to determine binding energies on a small local surface area in nanometer scale. Herein, this method was used in order to determine charge and discharge products after the 50th cycle. As a reference, the S 2p and P 2p signals of the pristine electrodes are shown in **Figure 27**a,b. Next to Cu_3PS_4 some P-S bondings and/or sulfur signals can be observed. After cycling, Na_2S was found in the fully sodiated state as S $2p_{3/2}$ and S $2p_{1/2}$ peaks at 161.6 and 162.8 eV have been observed, see **Figure 27**c,d. [41] With view on **Figure 27**e,f, one can recognize that residues of Na_2S remain inactive after subsequent desodiation. Moreover, more sodium polysulfides and/or possibly Cu_2S might be formed.

When using thiophosphates typically as solid electrolytes for solid state batteries (SSBs), for example, the use of Li_3PS_4 in Li cell leads to extra capacity, if the electrochemical stability window $>= 2$ V vs. Li^+/Li is exceeded. [40d] During oxidation, the formation of elemental sulfur S(0), P_2S_5 or phospho sulfidic anions then is likely. [42] These decomposition products can further react to $Li_4P_2S_6$ or Li_3P and Li_2S when reaching voltages < 1.5 V. [40d, 42] In the analogue case of using Na_3PS_4 as an electrolyte, Na_3P and Na_2S and P-S as well as P-S-Na bonds were found as decomposition products. [40f] Comparing with our results, not any prove for Na_3P, but the presence of Na_2S as an analogue decomposition product is found. Furthermore, next to Na_2S, P-S bindings are found to be present in minor content as can be concluded from the associated consideration of the capacities after sodiation and desodiation, respectively, see **Figure 27**d,f.
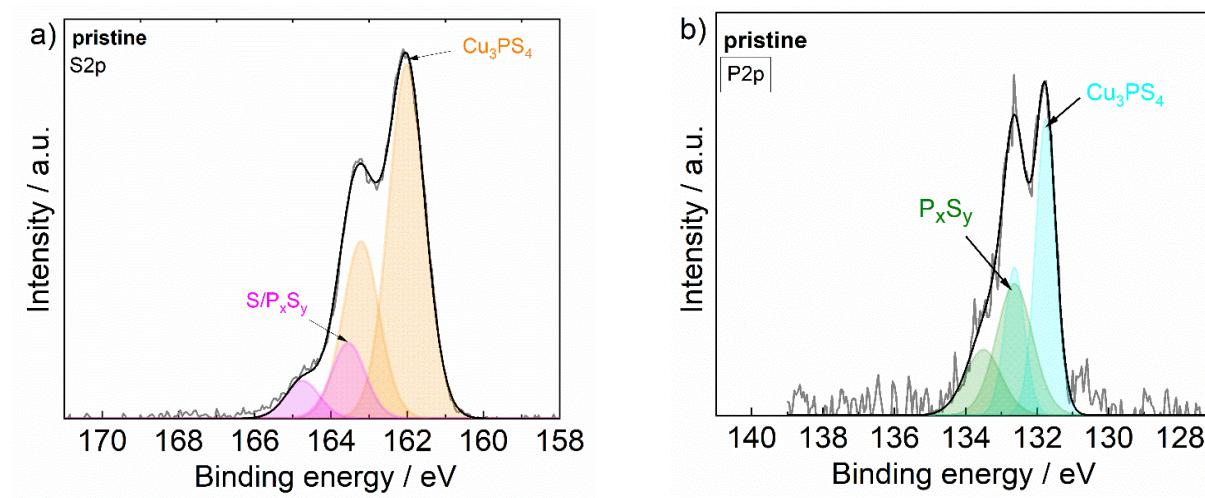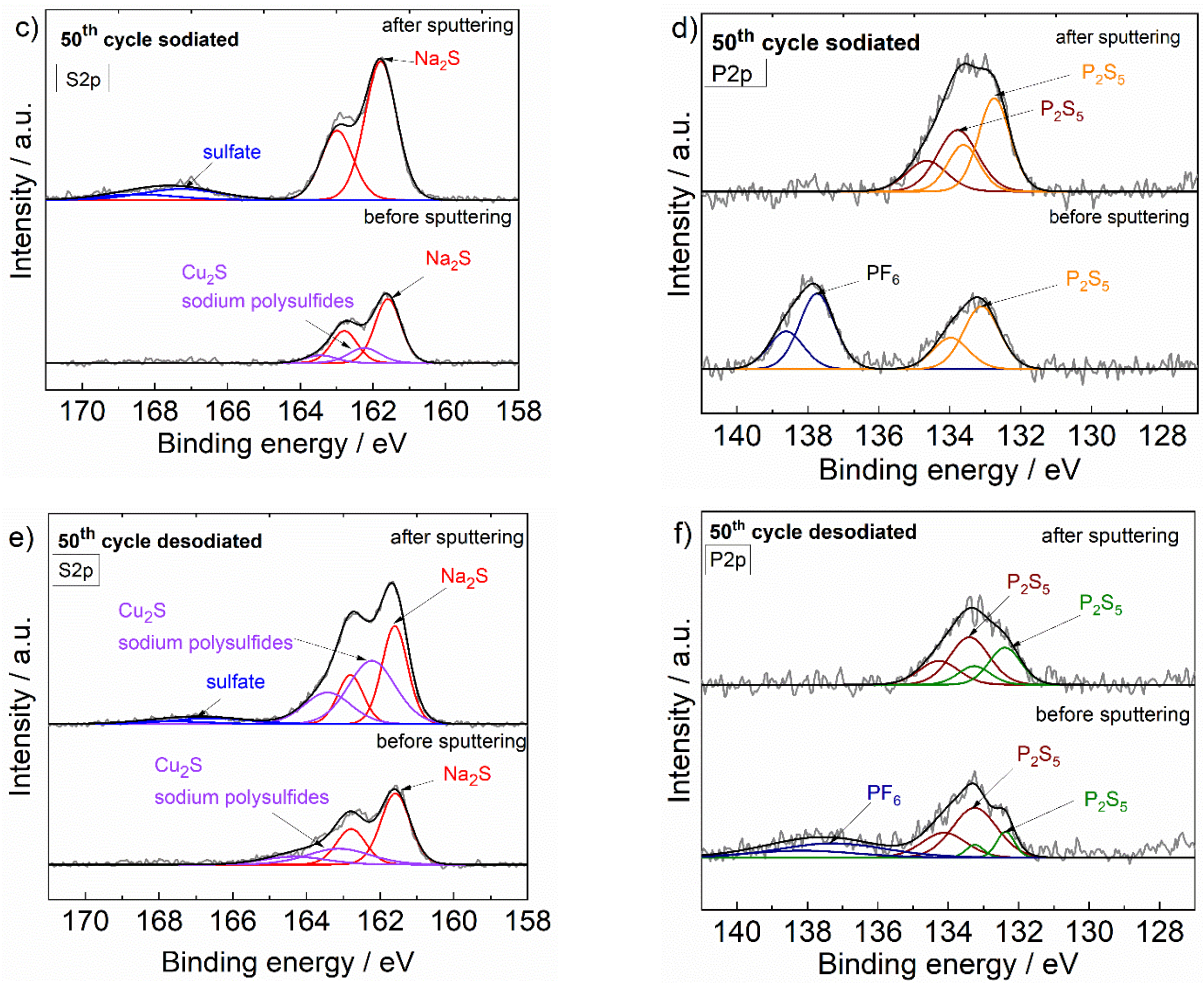
Figure 27*: XPS analysis of the S 2p signal for a) pristine Cu₃PS₄; c) the sodiated state of the 50ᵗʰ cycle; e) the desodiated state of the 50ᵗʰ cycle. The corresponding P 2p signals are shown in b,d,f). The sputtering time was 30 min. Cycling was performed at 120 mA g⁻¹ in a voltage window of 0.01-2.5 V vs. Na⁺/Na using 1 M NaPF₆ in diglyme as electrolyte. Reproduced with permission from Wiley.* [11b]

It is difficult to identify the redox activity of Cu via XPS since signals for Cu(0) and Cu(I) are very close to each other. Thus, *in situ* XRD was performed. *In situ* XRD is an useful analysis tool in order to record crystalline phases during a running cell reaction. Herein, copper was found to be only redox active within the initial sodiation step as the intensity of the Cu signal was found to undergo a large intensity change in comparison to the subsequent charge step and the complete following cycle, see **Figure 28**a,b. Furthermore, the experimentally determined capacities of about 580 mAh g^{-1} are close to the theoretical value of solely sulfur redox activity between S^{2-} and S^0 in Cu$_3$PS$_4$ (613 mAh g^{-1}). From these observations it can be concluded that the redox activity of sulfur is dominating the capacity contribution. Moreover, it is worth to note that with view on the long cycle life, dissolution of the electrode components does not take place. Further details related to the reaction mechanism are discussed in publication 3. By linking the results from GCPL, XRD and XPS one can conclude that Cu is only redox active during the initial discharge. Upon further cycling, the redox activity of sulfur was found to be dominating the cell reaction based on the reversible formation of Na$_2$S. However, the role of phosphorus remains unclear, hence further investigations like the use of NMR studies are required.
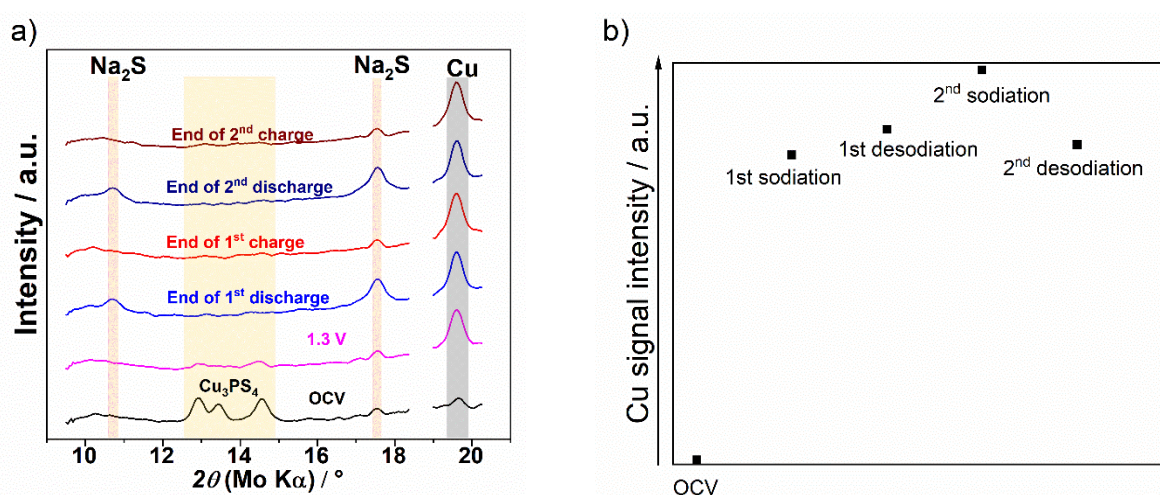
Figure 28: *a) In situ XRD analysis after the initial sodiation and desodiation step; b) Cu signal intensity change measured by in situ XRD before and after the first two sodiation and desodiation cycles. The crystalline nature of Cu$_3$PS$_4$ vanishes and Cu as well as Na$_2$S signals increase during sodiation. Cycling was performed at 120 mA g^{-1} in a voltage window of 0.01-2.5 V vs. Na$^+$/Na using 1 M NaPF$_6$ in diglyme as electrolyte. Reproduced with permission from Wiley.* [11b]

5. Results and discussion – publications

Publication 1: Reactive and non-reactive ball milling of tin-antimony (Sn-Sb) composites and their use as electrode for sodium-ion batteries with glyme electrolyte

Conversion electrodes are well known to enable high theoretical capacities. Related to that, Sn and its compounds are attractive for their use as electrode material in SIBs as Sn shows a theoretical capacity of 847 mAh g^{-1}. But, however, a couple of fabrication methods for electrodes is quite complex and expensive. Thus, in Publication 1 a very simple and cheap method for electrode fabrication is considered, which is simple ball milling. Especially up to the begin of this Ph.D. project, no systematic study about the influence of the ball milling time onto the electrochemical performance for Sn based electrodes was performed before publication. Therefore, a mixture between Sn and Sb (Sn+Sb), prepared by non-reactive ball milling, and the intermetallic phase[1] (SnSb), prepared by reactive ball milling, are compared in regard to their electrochemical behavior. Moreover, as conversion electrodes suffer from huge volume changes and often large overpotentials during phase conversion, the active material may be embedded in a carbon matrix in order to minimize these problems. Therefore, the influence of the ball milling time onto cycle life is discussed. Voltage profiles and cycle life tests reveal that the intermetallic phase shows larger capacities (680 mAh g^{-1} vs. 440 mAh g^{-1} after 50 cycles @ 100 mA g^{-1}). Ball milling of the active material together with carbon in a swing ball mill (SBM) for longer times is found to lead to enhanced cycle life because of a more stable composite formation. Further, the redox activity of the constituents is investigated in diglyme and it is found that Sb is largely redox inactive in diglyme electrolyte in contrast to its use in carbonate electrolytes. Surprisingly, however, Sb is largely redox active in diglyme electrolyte when being bond as intermetallic phase with Sn. *In situ* dilatometry reveals that composite formation with carbon is dominant over reactive and non-reactive ball milling of the active material components to enable enhanced cycle life. The results of these findings are published in the journal of *Energy Technology* with the title "Reactive and non-reactive ball milling of tin-antimony (Sn-Sb) composites and their use as electrode for sodium-ion batteries with glyme electrolyte" (doi: 10.1002/ente.201900389). The authors are Wolfgang Brehm, Johannes R. Buchheim and Philipp Adelhelm.

For this publication, XRD studies were performed by Johannes R. Buchheim. SEM, ECD, GCPL, particle size distribution (PSD) measurements, post mortem XRD as well as data analysis and further calculations were conducted and evaluated by the first author. The paper was written by the first author and edited by Philipp Adelhelm. This is an open access article distributed under the terms of the Creative Commons CC BY license, which permits unrestricted use, distribution, and reproduction in any medium, provided the original work is properly cited.

---

[1] In this publication the intermetallic phase SnSb is named as intermetallic compound

Reactive and Nonreactive Ball Milling of Tin-Antimony (Sn-Sb) Composites and Their Use as Electrodes for Sodium-Ion Batteries with Glyme Electrolyte

Wolfgang Brehm, Johannes Rolf Buchheim, and Philipp Adelhelm*

Tin (Sn), antimony (Sb), as well as their intermetallic compound SnSb are potential high-capacity negative electrodes for lithium- or sodium-ion batteries. Starting from bulk Sn and Sb, the effect of ball milling in sodium-ion half cells with a diglyme-based electrolyte is studied. Nonreactive ball milling of Sn, Sb, and carbon leads to intimately mixed but largely phase-separated composites (Sn + Sb) with electrochemical sodiation behavior being the sum of the individual phases. Thereby, Sb shows an unusual and rapid capacity fade in the chosen electrolyte which is unexpected, considering the usually excellent compatibility of diglyme-based electrolytes with negative electrodes. Reactive ball milling of Sn and Sb using a planetary ball mill leads to the phase-pure intermetallic compound β-SnSb. Compared with Sn + Sb, SnSb shows excellent performance with a specific capacity exceeding 400 mAh g^{-1} after 190 cycles and a high rate capability (around 400 mAh g^{-1} at 5 C). Hence, herein, Sb is largely inactive as a pure phase but active when bound in the β-SnSb intermetallic compound. Using in situ electrochemical dilatometry, the "breathing" of the electrodes during charging/discharging is minimized by optimizing ball-milling time, which improves cycle life.

1. Introduction

Sodium-ion batteries (SIBs) are considered as attractive future energy stores which could complement the more mature Li-ion and lead-acid technologies.[1–5] Considering potential negative electrodes, the use of graphite is not straightforward in SIBs due to the lack of sodium-rich NaC_x compounds. This can be circumvented by use of solvent cointercalation reactions though the obtainable capacity of about 110 mAh g^{-1} is still limited.[6–9] The use of hard carbon is one promising option with capacities up to about 400 mAh g^{-1},[10] but the partly extremely low redox potential versus Na$^+$/Na might easily lead to dendrite formation

during charging. In view of these challenges, the use of metals (or metalloids) appears attractive which typically provide high capacities at attractive redox potentials. However, the use of silicon, which is widely studied for lithium-ion batteries (LIBs), also has failed in SIBs so far. For this reason, a lot of interest is currently devoted to the use of tin (Sn) and antimony (Sb).[11–17] In both cases, the redox reaction involves several phase transitions and therefore the potential curve has a more stepped shape. The major redox potentials of Sn and respectively Sb in sodium cells are at about 0.2 and 0.6 V versus Na$^+$/Na, which makes their use very appealing. In lithium cells, the redox potentials are about 0.5 and 0.9 V versus Li$^+$/Li. Moreover, when comparing the sodiation/lithiation of Sn and Sb in SIBs and LIBs, it is quite interesting to note that structural stability was found to be better for the case of sodium, despite its larger atom/ion size.[18,19] This indicates that the difference between analogue reactions for "lithium" and "sodium" can be also counterintuitive.[1,9]

Advantages of Sn are its environmental friendliness, the attractive redox potential, and the high theoretical capacity, 847 mAh g^{-1}, for the formation of Na$_{3.75}$Sn.[11,14,20] On the downside, the volume expansion is, just as for all alloying reactions, very large. Sodiation of Sn to Na$_{3.75}$Sn is accompanied by a crystallographic volume expansion of 420%[14,21], for example. The theoretical capacity of Sb is somewhat lower (660 mAh g^{-1}, the formation of Na$_3$Sb with a volume expansion of 390%[21,22]) but its cycling stability is usually better as compared with Sn. Sb shows even stable cycling when used as bulk material. Related to that, Darwiche et al. obtained a specific capacity of 580 mAh g^{-1} after 160 cycles at a current rate of 55 mA g^{-1}, using half cells with sodium as the counter electrode.[19] A drawback is the toxicity of many Sb compounds as well as its limited abundance in the Earth's crust. This restricts the practical use of Sb but it may be suitable when used in smaller amounts or as an additive. The costs of Sn and Sb are currently in the range of 20–7 $ per kg which is in the same range or lower compared with other metals used in LIBs such as cobalt (40–100 $ kg^{-1}), nickel (10–15 $ kg^{-1}), or copper (7 $ kg^{-1}).[23]

The cycle life for both Sn and Sb can be also improved by embedding them as nano- or microparticles in a carbon matrix

W. Brehm, Dr. J. R. Buchheim, Prof. P. Adelhelm
Institute of Technical Chemistry and Environmental Chemistry
Friedrich Schiller University Jena
Philosophenweg 7a, Jena 07743, Germany
E-mail: philipp.adelhelm@uni-jena.de

W. Brehm, Dr. J. R. Buchheim, Prof. P. Adelhelm
Center for Energy and Environmental Chemistry (CEEC Jena)
Friedrich Schiller University Jena
Philosophenweg 7a, Jena 07743, Germany

The ORCID identification number(s) for the author(s) of this article can be found under https://doi.org/10.1002/ente.201900389.

ADVANCED
SCIENCE NEWS _____
www.advancedsciencenews.com

Energy Technology
Generation, Conversion, Storage, Distribution
www.entechnol.de

by, e.g., high-energy ball milling (HEBM), which overall improves the mechanical stability of the electrode during cycling.[13,20] The size reduction not only improves cycle life but also increases electrode utilization and rate capability. The trade-off of using a porous matrix as a support is a decrease in electrode density and a weight penalty which decreases the energy density of the cell. A careful balance between advantages and disadvantages is therefore needed. Note that also the carbon matrix contributes to charge storage.

It has been also reported that the cycle life can be further improved by using binary or ternary intermetallic phase systems instead of pure metals.[15,16] Xiao et al. explained the better stability of a binary intermetallic phase of the active materials Sn and Sb by the unique structural confinement during galvanostatic cycling in comparison with a single metal.[15] Park et al. observed these improvements for SnSb/C nanocomposites in LIBs as well.[24] The use of SnSb results in a theoretical capacity of 754 mAh g^{-1}. In general, the sodiation process of SnSb is complex, involving the formation of several (amorphous) intermediates. In a simplified way, however, the reaction shows two steps, see Xiao et al.[15,25]

$$SnSb + 3Na^+ + 3e^- \rightleftarrows Na_3Sb + Sn \; E > 0.4 \, V vs. Na^+/Na \quad (1)$$
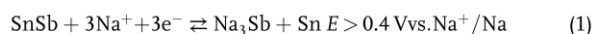
Theoretical capacity per g of Sb: 660 mAh g^{-1}.

$$Na_3Sb + Sn + 3.75Na^+ + 3.75e^- \rightleftarrows$$
$$Na_3Sb + Na_{3.75}Sn \; E < 0.4 V vs. Na^+/Na \quad (2)$$
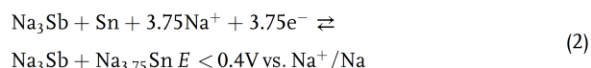
Theoretical capacity per g of Sn: 847 mAh g^{-1}.

The overall reaction for the sodiation of SnSb can be described as

$$SnSb + 6.75Na^+ + 6.75e^- \rightleftarrows Na_3Sb + Na_{3.75}Sn \quad (3)$$
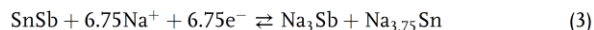
Theoretical capacity per g of SnSb: 754 mAh g^{-1}.

The sodiated Sb phase is inactive when discharged below 0.4 V. When recharged, SnSb is ideally fully reformed. Whereas it is difficult to explain the overall improved behavior, it has been suggested that the use of SnSb is advantageous because the multistep reaction creates a self-supporting network which improves structural stability and conductivity.[15]

Another approach to improve cycle life is to change the electrolyte composition. Tarascon et al. showed that the performance of Sn/C electrodes can be improved by replacing conventional carbonate-based electrolytes by glyme-based electrolytes. Using NaPF$_6$ in diglyme, the capacity reached was 768 mAh g^{-1} after 100 cycles.[14] Glyme-based electrolytes are recently reconsidered for a variety of electrode reactions.[26,27] In our previous studies diglyme showed preferable properties in Na-O$_2$ batteries,[28] CuS electrodes[29], or graphite electrodes,[30] for example. A recent review summarizes latest progress in the use of glymes for rechargeable batteries.[27] However, carbonate-based electrolytes remain the ones most frequently used in the literature. In these cases, the use of fluoroethylene carbonate (FEC) as additive has been shown to be beneficial for creating a stable solid electrolyte

interphase (SEI), thereby minimizing catalytic decomposition processes of the main solvents of the electrolyte.[14,22]

Despite the overall promising results on Sn, Sb, and SnSb-based electrodes, there is still a lack of understanding on how the preparation parameters influence the electrochemical performance, whether the SnSb intermetallic phase behaves better than the 1:1 stoichiometric mixture of the elements, and whether electrochemical alloying of Sn + Sb during cycling takes place. Moreover, the use of glyme electrolytes in combination with Sb electrodes has never been reported.

In this study, we therefore systematically analyze how milling conditions affect the structural properties of the composites and whether reactive ball milling leads to better electrochemical performance than conventional (i.e., nonreactive) ball milling. Several Sn + Sb composites (with carbon as the additive) are prepared by a swing ball mill (SBM) using different milling times. Using the same starting materials, we prepare the SnSb intermetallic compound by reactive ball milling using a high-energy planetary ball mill (PBM). We discuss particle and crystallite sizes of Sn + Sb and SnSb, homogeneity of the composite, cycle life, potential profiles, and phase behavior. For comparison, we also study the behavior of the pure metals Sn and Sb. Electrochemical measurements are done using glyme-based electrolytes (1 M NaPF$_6$ in diglyme). Finally, we perform in situ electrochemical dilatometry (ECD) to study the change in electrode thickness during cycling.

2. Results and Discussion

Figure 1 shows an overview of the produced samples. The composites from Sn and Sb were prepared in an SBM using 1:1 stoichiometric amounts and 30 wt% of carbon additive (carbon black, C65). The ball-to-powder weight ratio was 10:1 and the milling time varied from 1 to 6 h (batch size 1 g). The SnSb intermetallic phase was prepared by reactive ball milling of Sn and Sb for 24 h in a PBM under protective atmosphere (batch size: 5 g). SnSb was then further milled with carbon black in the SBM. Samples based on the 1:1 element mixtures and the intermetallic compound are denoted as Sn + Sb and SnSb, respectively.

2.1. Characterization of the Materials

Figure 2 shows the diffraction patterns of the starting materials (Sn, Sb) and the 1:1 mixtures after ball milling for 1, 3, and 6 h. In line with the phase diagram, we find Sn, Sb, and the intermetallic phase SnSb.[31] Note that SnSb and Sb show an extended homogeneity range of 2 at% at room temperature. The results show that Sn and Sb remain the major components of the samples although the content of β-SnSb increases with ball-milling time, i.e., the related (202) reflex at $2\theta = 29.1°$ increases.

After 6 h the content of β-SnSb is around 20 wt%, as determined by the Rietveld refinement. The contribution of the carbon additive to the diffraction pattern is negligible due to its disordered structure. The related structure refinement is summarized in Table S1, Supporting Information. An increase in milling time leads to a small expansion of the a and c lattice
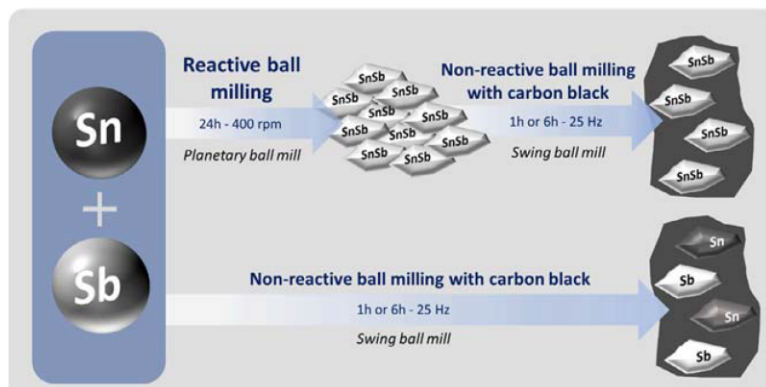
Figure 1. Ball-milling conditions for the preparation of SnSb/C and (Sn + Sb)/C composites from bulk Sn and Sb and carbon black. The carbon content for all samples was 30 wt%. Reactive ball milling was conducted in an Ar-flooded ball-milling jar.
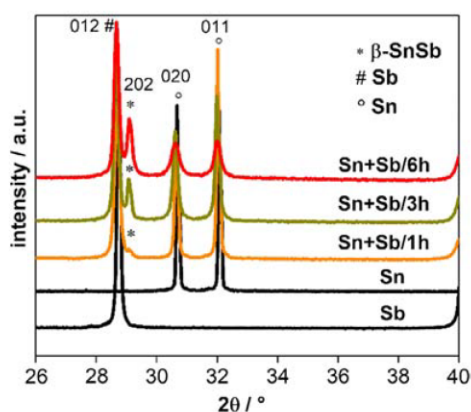
Figure 2. Diffraction patterns of Sn, Sb, and 1:1 mixtures after ball milling for 1, 3, and 6 h.

parameters of Sn, Sb, and SnSb, respectively. For all samples, the increase by ball milling over 6 h is in the range of about 0.2–0.7% in the a direction and 0.4%–0.6% in the c direction, see Figure S1, Supporting Information. We attribute this increase to the lattice distortion induced by plastic deformation. This effect has been also found for other metals such as Cu[32,33] and Al,[34] for example. We also note that solid solution formation could affect the lattice parameters. In this case, however, the expected changes would be much larger. For example, a change of 3.4% for the a parameter was found when ball milling Fe/Ni mixtures along with solid solution formation.[35]

The diffraction pattern of the Sn + Sb mixture after reactive ball milling for 24 h is shown in **Figure 3**. The formed SnSb phase exhibits a hexagonal structure with the lattice parameters $a = 4.32$ Å and $c = 5.34$ Å (see also Table S2, Supporting Information). The average crystallite size obtained from Rietveld refinement was determined to $D = 50$ nm. The difference in (202) reflex intensity between the experiment and refinement is caused by the preferred orientation of the crystals.

Scanning electron microscopy (SEM) combined with energy dispersive X-ray spectroscopy (EDX) was used to study particle size and homogeneity of the samples, see **Figure 4**. Ball milling reduced the particle sizes in all cases. For the shortest ball-milling time of 1 h, the sample (Sn + Sb/1 h) contained still quite large particles, some even exceeding 50 μm in diameter, see Figure 4 top image. The biphasic nature of the sample can be also easily seen from EDX mapping. A much more homogenous particle size and elemental distribution was found for the sample containing the SnSb intermetallic phase. Particle sizes were below about 10 μm. It is of note that the milling process was likely also aided by the higher hardness of the intermetallic phase. The EDX analysis of the investigated electrodes in Figure 4 shows a complete homogeneous distribution of both elements, well in line with the X-ray diffraction (XRD) results.

As SEM is a quite local method, we further used light scattering for determining the particle size distributions (PSDs) of the powders, see Figure S2, Supporting Information. Although the expected trend of decreasing particle sizes with increasing milling times could be observed, it is of note that only a qualitative correlation should be made. The distributions are very broad and multimodal in all cases which is likely because of the carbon additive that is highly absorbing and forms agglomerates. Nevertheless, the measurements confirm that the particle sizes shift to smaller values for longer ball-milling times.

2.2. Electrochemical Studies

Results from galvanostatic charge/discharge experiments are shown in **Figure 5**. All investigated electrodes were prepared based on a metal-to-carbon black weight ratio of 7:3 with 10 wt% carboxy methyl cellulose (CMC) binder and exhibited an active mass loading of 1.2–1.3 mg cm^{-2} (without carbon black). The CMC binder was used because it allows aqueous processing of the electrodes which is, in view of application, a better choice compared with using N-methyl-2-pyrrolidone (NMP) solvent that is required for polyvinylidine fluoride (PVDF) binders. Moreover, the use of CMC binders has been
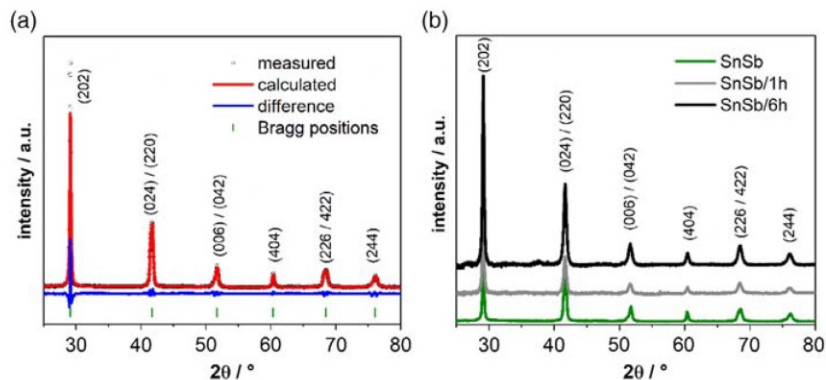
Figure 3. a) Diffraction pattern and refinement of β–SnSb prepared by reactive ball milling from Sn and Sb powders (SnSb ICSD 98-005-2294). b) Diffraction pattern of SnSb samples after subsequent ball milling with carbon black C65 for 1 and 6 h.
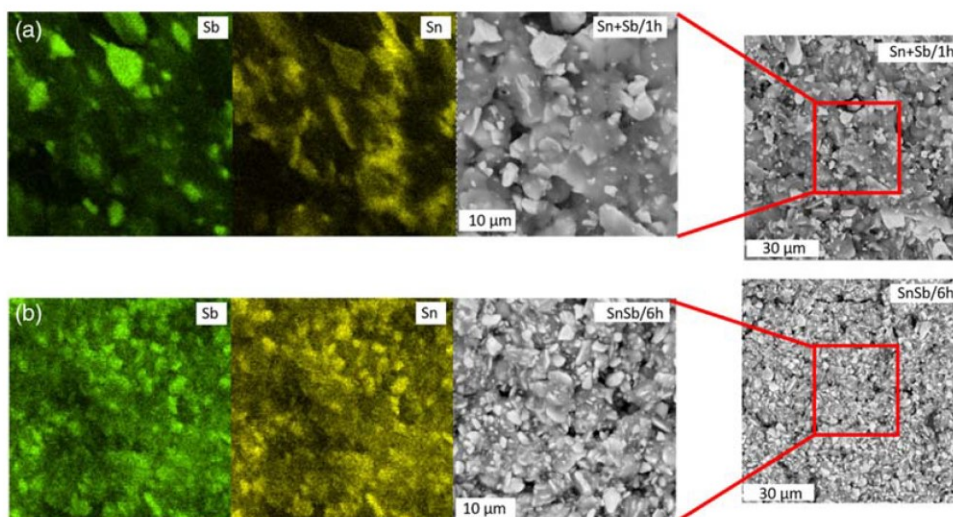
Figure 4. SEM/EDX analysis of a) Sn + Sb/1 h and b) SnSb/6 h electrodes.

shown as effective in improving the capacity and cycle life of Sn electrodes. This has been explained by the strong interaction between Sn and the CMC binder due to its carboxylic groups.[36,37] The initial electrode thicknesses (without the current collector) were around 15–18 μm for the samples ball milled for 6 h and 23–28 μm for the samples ball milled for 1 h. All experiments were performed with a current of $100\,mA\,g^{-1}$ (0.13 C related to the theoretical capacity of SnSb). Capacity values are normalized to the metal content of the electrode. Galvanostatic discharge/charge and cycle life measurements for the electrodes Sn + Sb/1 h and SnSb/6 h are shown in Figure 5a,b. These electrodes show the largest difference in the electrochemical properties of all samples. In both cases, the initial discharge capacity slightly exceeds the theoretical capacity of $754\,mAh\,g^{-1}$ by about 4% (Sn + Sb/1 h) and 12% (SnSb/6 h), which is due to SEI formation and excess storage capacity of carbon (see the following section for further details).

The initial coulombic efficiency (ICE) is similar, 78% for Sn + Sb/1 h and 79% for SnSb/6 h, but the capacity drops after the initial cycle, reaching $487\,mAh\,g^{-1}$ for Sn + Sb/1 h and $692\,mAh\,g^{-1}$ for SnSb/6 h (the latter value corresponds to $0.88\,mAh\,cm^{-2}$). Cycle life for all electrodes is compared in Figure 5b. As shown, all Sn + Sb electrodes show a strong capacity loss in the first two cycles, reaching about $500\,mAh\,g^{-1}$. Further cycling shows that longer ball milling leads to a more stable cycle life. The average capacity loss per cycle between the 2nd and 50th cycle is $7.68\,mAh\,g^{-1}$ for Sn + Sb/1 h and $3.28\,mAh\,g^{-1}$ for Sn + Sb/6 h. Notably, the capacity is much higher for the SnSb electrodes, showing that initially starting with the intermetallic phase is beneficial for achieving high capacity over many cycles. Around $680\,mAh\,g^{-1}$ ($0.24\,mAh\,g^{-1}$ of average capacity loss per cycle between the 2nd and 50th cycle) is obtained in case of SnSb/6 h after 50 cycles. Before concluding further, it is important to note that the carbon additive also

**ADVANCED
SCIENCE NEWS**
www.advancedsciencenews.com

Energy Technology
Generation, Conversion, Storage, Distribution
www.entechnol.de
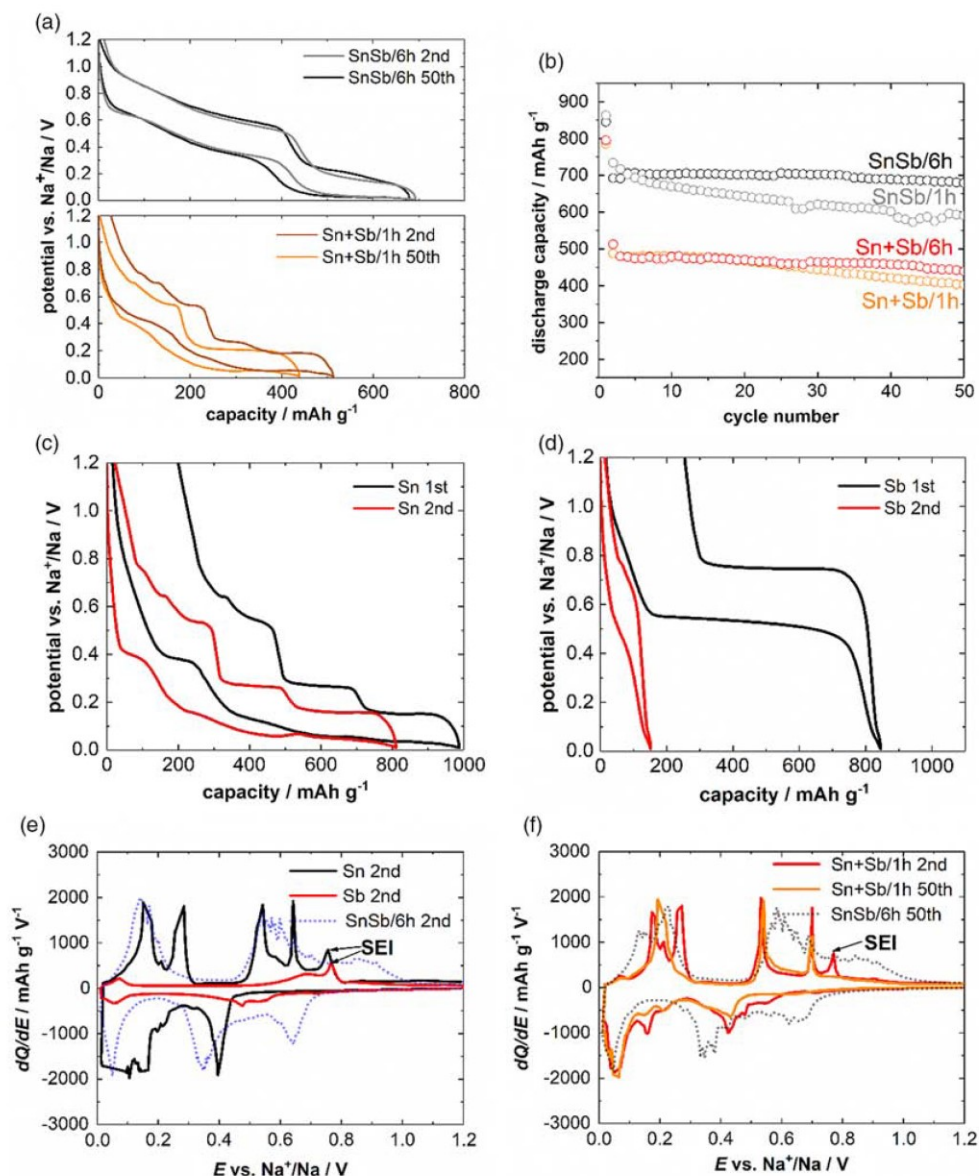
Figure 5. Galvanostatic cycling of the different electrodes (C-rate of 0.13 (100 mA g^{-1})): a) Voltage profiles of Sn + Sb/1 h and SnSb/6 h; b) discharge capacities of the first 50 cycles; c,d) voltage profiles of the first two cycles of Sn/C and Sb/C; e) 6 h capacity derivatives of the second cycles of Sn/C, Sb/C, and SnSb/6 h; and f) derivative plots of the 2nd and 50th cycle of Sn + Sb/1 h and the 50th cycle of SnSb/6 h.

contributes to sodium storage capacity. The maximum capacity for used carbon black is about 220 mAh g^{-1} using NaPF$_6$ (1 M) in diglyme as the electrolyte, see Figure S3, Supporting Information. It is generally difficult to get reliable data on the storage capacity of carbon black as the material is a very fluffy powder and active mass loadings will become comparably small (about 0.5 mg cm^{-2}). This likely also explains the deviation from the 155 mAh g^{-1} obtained in the study by Zhang et al. under similar conditions.[14] Considering a maximum capacity of 220 mAh g^{-1},

the contribution of carbon black to the composite will amount to 66 mAh g^{-1}.

From these results, one can overall conclude that 1) the use of SnSb instead of Sn + Sb mixtures is beneficial for achieving higher capacity and 2) longer milling times are achieved with carbon.

A closer look at the voltage profile reveals that both electrodes show a characteristic multistep behavior which is due to the reaction over several consecutive phases. To understand the behavior,

**ADVANCED
SCIENCE NEWS**
www.advancedsciencenews.com

Energy Technology
Generation, Conversion, Storage, Distribution
www.entechnol.de

it is important to note a difference between Sn, Sb, and SnSb. The sodiation of Sn has been described to proceed over several steps, undergoing a couple of crystalline and amorphous intermediate phases. Ellis et al. observed that the sodiation of tin occurs within four steps with "a" stating that the intermetallic compound is amorphous and "*" stating an unexpected crystalline phase.[1,38]

Plateau region 1: $Na + Sn \rightarrow NaSn_3*$
Plateau region 2: $Na + NaSn_3* \rightarrow a\text{-}NaSn$
Plateau region 3: $5\ Na + 4(a\text{-}NaSn) \rightarrow Na_9Sn_4*$
Plateau region 4: $6\ Na + Na_9Sn_4* \rightarrow Na_{15}Sn_4$

The detected phases are similar (but not identical) but not in coherence with the density functional theory (DFT) calculations of Chevrier and Ceder.[39] Slightly different experimental results were also discussed by Wang et al.,[40] showing that the sodiation mechanism of Sn is not clearly understood and rather complex.[1]

Especially during charging, the phase transitions can be clearly observed.[38,41,42] We also find this behavior for a Sn/C reference cell (the same electrolyte was used), see Figure 5c. While for Sn, plateaus in the potential profile are commonly clearly visible (at least during desodiation), they are hardly observed for Sb. After the initial sodiation/desodiation cycle of crystalline Sb, it stays amorphous. Mainly three voltage plateaus are observed in the subsequent cycles during sodiation, correlated with the following three sodiation steps: Amorphous Sb reacts to a-Na_3Sb, which then transforms into hexagonal/cubic Na_3Sb and finally a Na_3Sb hexagonal pure phase after full sodiation. After the activation cycle, the cycle life is very stable.[13,43] We prepared Sb/C reference cells, see Figure 5d, but found a different behavior. For the diglyme electrolyte, only the first cycle shows an appreciable capacity and a defined redox plateau. Notable is the rapid capacity loss of more than 75% in the second cycle. This is rather unexpected, considering the previously reported excellent stability for Sb[19] and the generally better stability of glymes at lower redox potentials. Sb therefore seems an unusual case where the replacement of carbonates by diglymes leads to a clear loss in electrode stability.

The significantly better cycling stability of Sb with a carbonate electrolyte, is confirmed by using $NaPF_6$ (1 M) EC:DEC (3:7) with addition of FEC (5%) for stabilizing the SEI, see Figure S4, Supporting Information. Even after ten cycles we still obtained around 500 mAh g^{-1}. Impedance data for the Sb/C electrode are shown in Figure S5, Supporting Information. Spectra were collected after sodiation and desodiation (first cycle) and after second sodiation. From this, one can observe that the transfer resistance becomes smaller after first sodiation and remains constant after first desodiation and the subsequent sodiation step. This observation can be explained by the poor activity of Sb in the diglyme electrolyte after the first cycle. After the first cycle, the conducting carbon matrix dominates the Na storage behavior and also impedance spectra (with comparably small resistance values).

In contrast, the reversibility of the SnSb electrode is very high, indicating that a reversible storage of Na ions by Sb only takes place when being bound in an intermetallic phase. Recently, Fehse et al. experimentally investigated the sodiation/desodiation behavior and detected the occurrence of an amorphous α-Sn phase and Na_3Sb on the higher voltage plateau. In the lower

voltage plateau the amorphous tin phase was observed to react to pure $Na_{3.75}Sn$.[25] The voltage profile also smoothens in case of SnSb. The unexpected inactivity of Sb in diglyme might be due to excessive SEI formation, leading to passivation of the electrode. A hint on side reactions can be discerned from the derivative plots shown in Figure 5f, showing an extra maximum at around 0.77 V during charging only for metals but not for the intermetallic phase. It can be also seen that Sn changes its charging behavior during cycling as a maximum at around 0.28 V disappears over cycling (comparing the 2nd and 50th cycle). This indicates that behavior during cycling is dynamic and the sodiation/desodiation mechanisms stabilize only after several cycles. Figure S6, Supporting Information, shows that this situation is reached after about 15 cycles. When further looking at Figure 5f, it is worth mentioning that the derivative curve of Sn + Sb/1 h of its second cycle is approximately identical with that of Sn, indicating the inactivity of Sb in the Sn + Sb electrode. In contrast to Sn + Sb, the behavior of the SnSb electrode is comparable for the 2nd and 50th cycle, see Figure 5a and Figure 5e,f. The extra maximum at 0.77 V which is present for Sn and Sb is also absent. Comparing the results for the Sn, Sb, Sn + Sb, and the SnSb electrode, it also becomes evident that no electrochemical (de-) alloying between the components takes place. In other words, Sn + Sb mixtures do not form SnSb during cycling, and SnSb does not phase separate to its constituents.

Further evidence for these conclusions was obtained by XRD measurements, demonstrated in **Figure 6**. For this, cells were dismantled in the desodiated state after 50 cycles. For the Sn + Sb/1 h electrode, crystalline Sn was detected, indicating that Sb remains amorphous after the first cycle. For the SnSb/6 h electrode, neither Sn, Sb, nor SnSb signals could be detected after 50 cycles. As the voltage profile did not change within 50 cycles, one can conclude that amorphization of SnSb took place. Both electrodes, however, contain unknown reflexes at about 6 h at around $2\theta = 29°$ and $36°$. The origin is unknown so far but they could be due to a decomposition product that forms during cycling or due to unknown metastable phases. The amorphization of SnSb during cycling is in line with results from Darwiche et al.[44] Although we did not observe any drying out of the cells, the appearance of these reflexes may indicate side reactions that require further studies.

Rate capability measurements for the electrode with the best performance (SnSb/6 h) are shown in **Figure 7**. Even at higher C rates of 5 C (3.7 A g^{-1}) still values at around 400 mAh g^{-1} are achieved, indicating excellent kinetics. Values for coulombic efficiencies η_C are close to 100%. After reapplying a rate of C/10, the capacity largely recovered, indicating an overall satisfying structural stability of the electrode. For the same sample, results for 190 consecutive cycles at 0.13 C are shown in **Figure 8**. It can be seen that accelerated aging of the electrode starts at about 50–60 cycles; nevertheless, about 400 mAh g^{-1} are still obtained at the end of the experiment with coulombic efficiencies close to 100%, demonstrating the excellent reversibility of the electrode reaction after many cycles. Only the initial cycle shows a higher value which is expected, and is a result of SEI formation.

Although further improvement is necessary, these results are better compared with what is commonly achieved for carbonated-based electrolytes. A comparison with literature results is shown in Table S3, Supporting Information. Overall, the comparison

**ADVANCED
SCIENCE NEWS**

www.advancedsciencenews.com

Energy Technology
Generation, Conversion, Storage, Distribution

www.entechnol.de
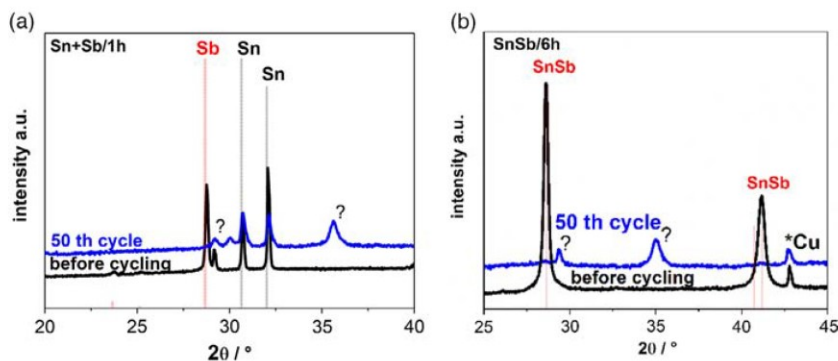
Figure 6. XRD analysis for Sn + Sb/1 h and SnSb/6 h before cycling and after the 50th cycle in the desodiated state (Sn: ICSD 98-004-0037; Sb: ICSD 98-000-9859; SnSb: ICSD 98-005-2294).
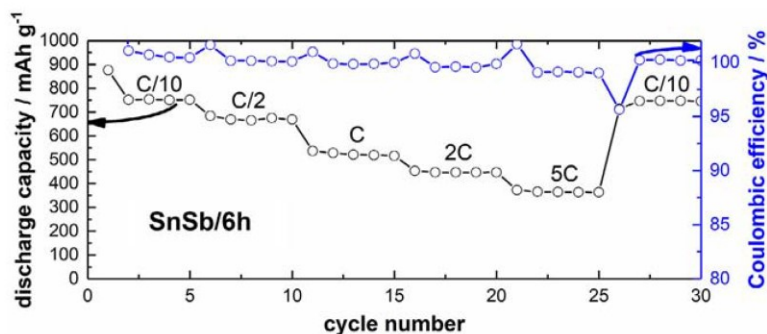
Figure 7. Rate capability test of an SnSb/6 h electrode at different C rates. (1C = 754 mA g^{-1}). Coulombic efficiencies η_C are calculated as $\eta_C = (Q_{Na_{in}}/Q_{Na_{out}}) \times 100\%$.
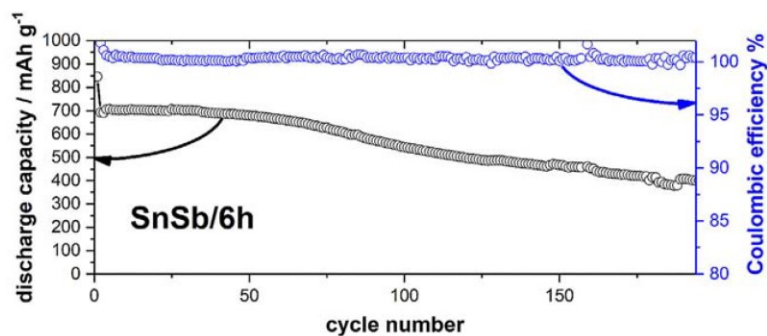
Figure 8. Cycle life test at 0.13 C for the SnSb/6 h electrode.

clearly indicates that the use of diglyme as the electrolyte is preferable for achieving a longer cycle life. Likely, this is related with the better behavior of ether electrolytes at low potentials in general combined with a more uniform SEI for Na-ion batteries as compared with carbonate-based electrolytes,[14,45] – Sb being an exception as shown in this work. The better performance for Sn/C electrodes within the first 100 cycles, reported by Zhang et al.,[14] might be explained by the better compatibility of

diglyme with Sn compared with Sb (see Figure 5d) and additionally by the applied smaller voltage window, as the influence of capacity fading by the applied upper cut-off voltage can be seen in Figure S7, Supporting Information. However, adding Sb leads to a smoothening of the voltage profile which is preferable.

Finally, we applied in situ ECD to study the electrode dynamics, i.e., the change in electrode thickness during cycling. Whereas the volume changes in Sn (420%, sodiation) and Sb

**ADVANCED
SCIENCE NEWS**
www.advancedsciencenews.com

Energy Technology
Generation, Conversion, Storage, Distribution
www.entechnol.de

(390%, sodiation) during cycling are very large, buffering those is an urgent matter related to application. Despite these large values, the effective change in electrode thickness might be much smaller, depending on the ability of the electrode to compensate for the volume change. In situ ECD is a useful method to probe the effective change in the electrodes during ion insertion/deinsertion. For example, Cámer et al. analyzed the influence of electrode binder materials via dilatometry studies for a graphite/Si electrode, revealing that the large capacity fading can be mitigated by using a cross-linked binder.[46] Jeong et al. demonstrated by dilatometry studies that a poly(methyl methacrylate) (PMMA) treatment improves the dimensional reversibility in coherence with improved capacity retention for a porous (Si/Fe)-based composite electrode.[47] In another study by Goktas et al., intercalation of solvated ions into graphite could be monitored, showing that capacity fading can be small even for very large changes in electrode thickness. Moreover, the change in electrode thickness might be far from linear during galvanostatic cycling.[8] However, no literature related to in situ ECD for Sn + Sb and SnSb electrodes for LIBs and SIBs is published yet.

Results for the "breathing" of different electrodes over 4–5 cycles are compared in **Figure 9**. The initial thicknesses and porosities of the electrodes are summarized in **Table 1**. The porosity P was determined by the quotient of the bulk volume V_b and the apparent electrode volume V_{el} based on the real electrode dimensions. The electrode porosity in percent is then $P = \left[1 - \frac{V_b}{V_{el}}\right] \cdot 100\%$. The values demonstrate that longer ball milling also leads to a more compact electrode, considering the

corresponding decreasing porosities for the mixture as well as for the intermetallic phase. In addition, the SnSb electrodes ($P = 67\%$ for 6 h ball milling) are less compact than the Sn + Sb electrodes ($P = 64\%$ for 6 h ball milling) for the same ball-milling times. The lower porosities for the 6 h ball-milled samples result in higher theoretical volumetric capacities compared with 1 h ball-milled samples. The obtained values respond to around 52%–78% of the bulk values (864 mAh cm^{-3} for SnSb electrodes and 866 mAh cm^{-3} for Sn + Sb electrodes, calculated with the densities of the electrode components). A theoretical gravimetrical capacity of 220 mAh g^{-1} was assumed for the calculation of the carbon black contribution to the volumetric capacities. Higher values could be obtained by calendering. An overview on volumetric capacities of several metals and alloys in combination with lithium is given by Obrovac and Chevrier.[48]

During initial sodiation the relative change in thickness is surprisingly smaller for the more compact electrodes (33% and 40% for SnSb/6 h and Sn + Sb/6 h) compared with the less packed ones (48% and 74%) for Sn + Sb/1 h and SnSb/1 h. Because of the similarity of the height changes between SnSb/6 h and Sn + Sb/6 h, the "breathing" of the electrode seems dominated by the ball-milling time with the carbon additive. Longer mixing times with carbon black seem to reduce the changes in electrode thickness during cycling. This observation underlines that embedment of the active material in the carbon matrix is important for buffering volume changes. Identifying such correlations can help further optimize electrode stability during cycling. The results also show that the "breathing" of the electrodes over cycling is much more constant for the electrode from mixtures that have been milled for 6 h. Electrodes from mixtures milled for only 1 h show a larger change upon cycling, indicating structural changes and contact losses. As a result, these electrodes age faster as also seen in Figure 5b. Overall, in situ ECD is an effective tool that can help to understand the fading of electrodes with identical composition but different preparation strategies.

3. Conclusions

The influence of ball-milling conditions on the performance of Sn- and Sb-containing electrodes for SIBs was evaluated in diglyme-based electrolytes. For this, electrodes from Sn, Sb, Sn + Sb mixtures, and SnSb were systematically compared. Sn, Sb, and Sn + Sb electrodes were prepared in a one-step ball-milling process using 30 wt% of the carbon additive. Mixing times
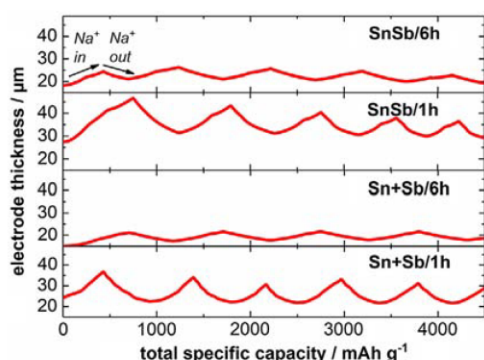
Figure 9. Electrode thicknesses change during sodiation/desodiation measured by ECD at 0.13 C.

Table 1. Electrode thicknesses and the height change during the first sodiation measured by ECD at 0.13 C. The porosity P was calculated based on the real electrode volume and the volume of the components with their crystalline densities. The following density values were used: $\rho_{SnSb} = 7.0$ g cm^{-3} (space group R-3 m, hexagonal), $\rho_{Sb} = 6.70$ g cm^{-3} (space group R-3 m, hexagonal), $\rho_{Sn} = 7.3$ g cm^{-3} (space group I4$_1$/amd, tetragonal), $\rho_{(carbon\ black,\ estimated)} = 2.0$ g cm^{-3}, $\rho_{(CMC\ binder)} = 1.6$ g cm^{-3}. $q_{th,vol}$ and $q_{th,areal}$ are the theoretical volumetric and areal capacities of the electrode including the porosity.

Electrode	Initial electrode thickness [μm]	Metal loading [mg cm^{-2}]	$q_{th,areal}$ [mAh cm^{-2}]	P [%]	$q_{th,vol}$ [mAh cm^{-3}]	Height change during first sodiation [μm]	Height change during first sodiation [%]
SnSb/6 h	18	1.29	1.39	67	605	6	33
SnSb/1 h	27	1.44	1.55	74	452	20	74
Sn + Sb/6 h	15	1.18	1.62	64	672	6	40
Sn + Sb/1 h	25	1.44	1.55	74	490	12	48

ADVANCED
SCIENCE NEWS
www.advancedsciencenews.com

Energy Technology
Generation, Conversion, Storage, Distribution
www.entechnol.de

were 1 and 6 h. SnSb was prepared by reactive ball milling using a PBM and then further treated with carbon black in the same way as the other materials. Important conclusions are summarized as follows: 1) Sb shows unexpected and very poor stability in the diglyme-based electrolyte. This is different from many other negative electrodes for which diglyme has been recently identified as a promising solvent. However, Sb reversibly stores sodium ions when bound in a SnSb intermetallic phase. 2) The electrochemical activity of electrodes from Sn and Sb mixtures (Sn + Sb) is largely dominated by Sn. Electrochemical results indicate that the sodiation/desodiation mechanism stabilizes after around 15 cycles. This stabilization can be seen from a change in the voltage profile. Electrochemical alloying of both elements during cycling does not take place. 3) The performance of SnSb electrodes is superior to Sn + Sb mixtures. SnSb electrodes show high specific capacity, of about 680 mAh g^{-1}, within the first 50 cycles, along with good cycle life (>400 mAh g^{-1} after 190 cycles). SnSb becomes amorphous during cycling with no obvious changes in the voltage profile. Compared with Sn, the use of SnSb leads to a smoothening of the voltage profile. 4) Longer milling (6 vs 1 h) has only a minor influence on the initial capacity, but it significantly improves cycle life stability. These results can be well understood from in situ ECD measurements which show that long milling times reduce the "breathing" of the electrodes during cycling (despite the fact that the electrodes are also more compact).

4. Experimental Section

Ball milling of SnSb/C; Sn + Sb/C; Sn/C, and Sb/C: Commercial Sn particles from Alfa (325 mesh) and Sb particles (100 mesh) from Sigma Aldrich were used as active materials. Sn and Sb were put into zirconia jars with a molar ratio of 1:1. For reactive ball milling (synthesis of β-SnSb), a 5 g batch of stoichiometric amounts of Sn and Sb was ball milled for 24 h at 400 rpm in a PBM (PBM, Fritsch Pulverisette 7) with a jar volume of 80 ml. For creating the composites, 1 g batch of the raw materials was ball milled together with carbon black, C65, in a metal-to-carbon weight ratio of 7:3 (IMERYS Graphite&Carbon) in an SBM with a frequency of 25 Hz in a jar volume of 10 ml (SBM, Retsch MM 400). All materials were ball milled in a ball-to-powder ratio of 10:1 for both types of ball mills.

Slurry and Electrode Preparation: An aqueous slurry was prepared containing 10 wt% CMC related to the total weight of SnSb/C, Sn + Sb/C, Sn/C, and Sb/C powder. The slurry was cast onto a copper foil and the electrodes were cut into disks (12 mm in diameter) followed by drying under vacuum at 60 °C overnight. The active mass loading was around 1.2 mg cm^{-2}.

Characterization Methods: XRD analysis was performed on a Bruker D2 Phaser diffractometer using Cu Kα radiation ($\lambda_{K\alpha} = 1.54184$ Å). A Fritsch Analysette 22 Microtec plus measuring unit with wet dispersion was used to determine PSD.

Electrochemical Tests: A 1 M concentrated electrolyte solution was prepared from NaPF$_6$ purity >99% (Alfa Aesar) and diglyme (Sigma Aldrich). Diglyme was dried in a molecular sieve (4 Angstrom, Sigma Aldrich) to ensure that the water content was lower than 10 ppm, confirmed by Karl-Fischer titration. The reference measurement for Sb/C with the carbonate electrolyte was performed with NaPF$_6$ (1 M) in EC:DEC (3:7) with the addition of FEC (5%). The electrochemical tests were performed in coin cells in the C2032 format, using two pieces of Whatman separators (glass microfiber filters GF/A) and Na metal (provided by BASF SE) as the counter electrode. The cells were cycled using multichannel cyclers from Biologic (BCS, MPG2) and an SP150 galvanostat/potentiostat.

Dilatometer Measurement: For dilatometer measurements, a dilatometer ECD-3-nano from EL-CELL was used for measuring the expansion and shrinking of the electrodes. Herein, the used electrodes exhibited a diameter of 10 mm.

Supporting Information

Supporting Information is available from the Wiley Online Library or from the author.

Conflict of Interest

The authors declare no conflict of interest.

[1] P. K. Nayak, L. Yang, W. Brehm, P. Adelhelm, *Angew. Chem., Int. Ed.* **2018**, *57*, 102.

[2] N. Yabuuchi, K. Kubota, M. Dahbi, S. Komaba, *Chem. Rev.* **2014**, *114*, 11636.

[3] M. D. Slater, D. Kim, E. Lee, C. S. Johnson, *Adv. Funct. Mater.* **2013**, *23*, 947.

[4] D. Kundu, E. Talaie, V. Duffort, L. F. Nazar, *Angew. Chem., Int. Ed.* **2015**, *54*, 3431.

[5] S.-W. Kim, D.-H. Seo, X. Ma, G. Ceder, K. Kang, *Adv. Energy Mater.* **2012**, *2*, 710.

[6] B. Jache, P. Adelhelm, *Angew. Chem. Int. Ed.* **2014**, *53*, 10169.

[7] H. Kim, J. Hong, Y.-U. Park, J. Kim, I. Hwang, K. Kang, *Adv. Funct. Mater.* **2015**, *25*, 534.

[8] M. Goktas, C. Bolli, E. J. Berg, P. Novák, K. Pollok, F. Langenhorst, M. V. Roeder, O. Lenchuk, D. Mollenhauer, P. Adelhelm, *Adv. Energy Mater.* **2018**, *8*, 1702724.

[9] DOI: 10.1039/C9CS00162J.

[10] C. Zhao, Q. Wang, Y. Lu, B. Li, L. Chen, Y.-S. Hu, *Sci. Bull.* **2018**, *63*, 1125.

[11] M. Lao, Y. Zhang, W. Luo, Q. Yan, W. Sun, S. X. Dou, *Adv. Mater.* **2017**, *29*, 1700622.

[12] H. Ying, W. Q. Han, *Adv. Sci.* **2017**, *4*, 1700298.

[13] G. Wang, X. Xiong, Z. Lin, C. Yang, Z. Lin, M. Liu, *Electrochim. Acta* **2017**, *242*, 159.

[14] B. Zhang, G. Rousse, D. Foix, R. Dugas, D. A. Corte, J. M. Tarascon, *Adv. Mater.* **2016**, *28*, 9824.

[15] L. Xiao, Y. Cao, J. Xiao, W. Wang, L. Kovarik, J. Nie, J. Liu, *Chem. Commun.* **2012**, *48*, 3321.

[16] W. Zhang, J. Mao, W. K. Pang, Z. Guo, Z. Chen, *Electrochim. Acta* **2017**, *235*, 107.

**ADVANCED
SCIENCE NEWS**
www.advancedsciencenews.com

Energy Technology
Generation, Conversion, Storage, Distribution
www.entechnol.de

[17] H. Tan, D. Chen, X. Rui, Y. Yu, *Adv. Funct. Mater.* **2019**, *29*, 1808745.

[18] J. Wang, C. Eng, Y. C. Chen-Wiegart, J. Wang, *Nat. Commun.* **2015**, *6*, 7496.

[19] A. Darwiche, C. Marino, M. T. Sougrati, B. Fraisse, L. Stievano, L. Monconduit, *J. Am. Chem. Soc.* **2012**, *134*, 20805.

[20] T. Palaniselvam, M. Goktas, B. Anothumakkool, Y.-N. Sun, R. Schmuch, L. Zhao, B.-H. Han, M. Winter, P. Adelhelm, *Adv. Funct. Mater.* **2019**, 1900790.

[21] V. L. Chevrier, G. Ceder, *J. Electrochem. Soc.* **2011**, *158*, A1011.

[22] J. Qian, Y. Chen, L. Wu, Y. Cao, X. Ai, H. Yang, *Chem. Commun.* **2012**, *48*, 7070.

[23] Preistrendmonitor, https://www.deutsche-rohstoffagentur.de/DERA/DE/Rohstoffinformationen/Rohstoffpreise/Preistrendmonitor/preistrendmonitor_node.html (accessed: February 2019).

[24] C. M. Park, K. J. Jeon, *Chem. Commun.* **2011**, *47*, 2122.

[25] M. Fehse, M. T. Sougrati, A. Darwiche, V. Gabaudan, C. La Fontaine, L. Monconduit, L. Stievano, *J. Mater. Chem. A* **2018**, *6*, 8724.

[26] K. Westman, R. Dugas, P. Jankowski, W. Wieczorek, G. Gachot, M. Morcrette, E. Irisarri, A. Ponrouch, M. R. Palacín, J. M. Tarascon, P. Johansson, *ACS Appl. Energy Mater.* **2018**, *1*, 2671.

[27] J. Zhang, D.-W. Wang, W. Lv, L. Qin, S. Niu, S. Zhang, T. Cao, F. Kang, Q.-H. Yang, *Adv. Energy Mater.* **2018**, *8*, 1801361.

[28] P. Hartmann, C. L. Bender, M. Vračar, A. K. Dürr, A. Garsuch, J. Janek, P. Adelhelm, *Nat. Mater.* **2012**, *12*, 228.

[29] B. Jache, B. Mogwitz, F. Klein, P. Adelhelm, *J. Power Sources* **2014**, *247*, 703.

[30] M. Goktas, B. Akduman, P. Huang, A. Balducci, P. Adelhelm, *J. Phys. Chem. C* **2018**, *122*, 26816.

[31] H. Okamoto, *J. Phase Equilib. Diffus.* **2012**, *33*, 347.

[32] E. Purushotham, *J. Eng. Sci. Technol. Rev.* **2013**, *6*, 83.

[33] J. Y. Huang, Y. K. Wu, H. Q. Ye, *Mater. Sci. Eng.* **1995**, *A199* 165.

[34] M. Toozandehjani, K. A. Matori, F. Ostovan, S. Abdul Aziz, M. S. Mamat, *Materials (Basel)* **2017**, 10.

[35] K. Gheisari, S. Javadpour, J. T. Oh, M. Ghaffari, *J. Alloys Compd.* **2009**, *472*, 416.

[36] Y.-X. Wang, Y. Xu, Q. Meng, S.-L. Chou, J. Ma, Y.-M. Kang, H.-K. Liu, *Adv. Mater. Interfaces* **2016**, *3*, 1600662.

[37] J. S. Bridel, T. Azaïs, M. Morcrette, J. M. Tarascon, D. Larcher, *Chem. Mater.* **2010**, *22*, 1229.

[38] L. D. Ellis, T. D. Hatchard, M. N. Obrovac, *J. Electrochem. Soc.* **2012**, *159*, A1801.

[39] V. L. Chevrier, G. Ceder, *J. Electrochem. Soc.* **2011**, *158*, A1011.

[40] J. W. Wang, X. H. Liu, S. X. Mao, J. Y. Huang, *Nano Lett.* **2012**, *12*, 5897.

[41] L. D. Ellis, T. D. Hatchard, M. N. Obrovac, *J. Electrochem. Soc.* **2012**, *159*, A1801.

[42] J. M. Stratford, M. Mayo, P. K. Allan, O. Pecher, O. J. Borkiewicz, K. M. Wiaderek, K. W. Chapman, C. J. Pickard, A. J. Morris, C. P. Grey, *J. Am. Chem. Soc.* **2017**, *139*, 7273.

[43] P. K. Allan, J. M. Griffin, A. Darwiche, O. J. Borkiewicz, K. M. Wiaderek, K. W. Chapman, A. J. Morris, P. J. Chupas, L. Monconduit, C. P. Grey, *J. Am. Chem. Soc.* **2016**, *138*, 2352.

[44] A. Darwiche, M. T. Sougrati, B. Fraisse, L. Stievano, L. Monconduit, *Electrochem. Commun.* **2013**, *32*, 18.

[45] J. Zhang, D.-W. Wang, W. Lv, L. Qin, S. Niu, S. Zhang, T. Cao, F. Kang, Q.-H. Yang, *Adv. Energy Mater.* **2018**, *8*, 1801361.

[46] J. L. Gómez-Cámer, C. Bünzli, M. M. Hantel, T. Poux, P. Novák, *Carbon* **2016**, *105*, 42.

[47] G. Jeong, S. M. Lee, N. S. Choi, Y.-U. Kim, C. K. Lee, *Electrochim. Acta* **2011**, *56*, 5095.

[48] M. N. Obrovac, V. L. Chevrier, *Chem. Rev.* **2014**, *114*, 11444.

Publication 2: Mechanochemically synthesized Cu₃P/C composites as a conversion electrode for Li-ion and Na-ion batteries in different electrolytes

Transition metal compounds as conversion electrodes show commonalities and differences for their use in LIBs and SIBs as discussed by Klein *et al*. for several examples. This study continues such considerations for a transition metal phosphide conversion electrode due to its very high specific gravimetric and/or volumetric capacities. Copper rich copper phosphide (Cu_3P) for example, shows a theoretical capacity of 363 mAh g^{-1} being on one level with that of graphite but its volumetric capacity is about three times higher (2664 Ah l^{-1} vs. 780 Ah l^{-1}). However, before publication, a detailed comparison of Cu_3P as electrode material for its use in Li cells and Na cells was missing so far. Thus, herein, electrochemical studies are performed for the use of Cu_3P as electrode material for Li and Na cells under same fabrication conditions. Moreover, the influence of the electrolyte is thereby considered as well. Voltage profiles and cycle life experiments show larger capacities in case of Li as well as better capacity retention compared to the Na analogues for both, ether and carbonate electrolytes. The capacity contribution of carbon is thereby found to be larger in case of Na as compared to Li. Furthermore, the use of ether (glyme) electrolytes results in outperforming properties over the use of carbonate electrolytes, like enhanced capacity retention and smaller overpotentials, for example. In a final consideration, an *in situ* dilatometry study shows that breathing of the electrodes is larger in Li cells than for Na cells with link to a higher storage capacity of Cu_3P in Li cells. Glyme electrolytes demonstrate quite constant breathing in contrast to the carbonate electrolytes.

The authors are Wolfgang Brehm, Aggunda L. Santhosha, Zhenggang Zhang, Christof Neumann, Andrey Turchanin, Martin Seyring, Markus Rettenmayr, Johannes R. Buchheim and Philipp Adelhelm.

For this paper, XRD studies were performed by Johannes R. Buchheim. TEM measurements were conducted and analyzed by Martin Seyring and Markus Rettenmayr. Further, XPS post mortem studies were carried out and analyzed by Christof Neumann and Andrey Turchanin. SEM, ECD, GCPL, PEIS, GITT and post mortem XRD as well as the corresponding data analysis and further calculations were performed by the first author. The paper was written by the first author and edited by Philipp Adelhelm.

Mechanochemically synthesized Cu₃P/C composites as a conversion electrode for Li-ion and Na-ion batteries in different electrolytes

Wolfgang Brehm [a], Aggunda L. Santhosha [a,c], Zhenggang Zhang [a,c], Christof Neumann [b], Andrey Turchanin [b], Martin Seyring [d], Markus Rettenmayr [a,d], Johannes R. Buchheim [a], Philipp Adelhelm [a,c,*]

[a] Institute of Technical Chemistry and Environmental Chemistry, CEEC Jena, Friedrich Schiller University Jena, Philosophenweg 7a, 07743, Jena, Germany
[b] Institute of Physical Chemistry, CEEC Jena, Friedrich Schiller University Jena, Lessingstraße 10, 07743, Jena, Germany
[c] Department of Chemistry, Humboldt-University Berlin, Brook-Taylor-Str. 2, 12489, Berlin, Germany
[d] Otto-Schott-Institute of Materials Research, Friedrich Schiller University Jena, Löbdergraben 32, 07743, Jena, Germany

ARTICLE INFO

ABSTRACT

Copper phosphide (Cu₃P) is a potentially high volumetric capacity conversion electrode for the use in Li-ion as well as in Na-ion batteries. Here, we study the lithium and sodium storage properties of Cu₃P/Carbon (Cu₃P/C) composites containing 70 wt% Cu₃P and 30 wt% carbon black. Cu₃P is prepared by reactive ball milling from the elements while in a second step Cu₃P is mixed with carbon black by non-reactive ball milling. Structure and morphology are characterized by X-ray diffraction (XRD) as well as scanning and transmission electron microscopy (SEM, TEM). The electrochemical properties are studied in Li and Na half cells with different types of electrolytes based on carbonates (EC:DMC mixture) or diglyme, with the latter clearly leading to better results such as higher capacity, better cycle life and smaller polarization. After 120 cycles, the Li-cell showed a capacity of 210 mAh g⁻¹ while around 120 mAh g⁻¹ were found for the Na cell. The contribution of the carbon black is negligible in case of the Li cell while it becomes an important factor in the Na cell. Electrode expansion/shrinkage of the electrode during cycling ("breathing") as determined by in situ dilatometry is fairly constant in diglyme electrolytes while rapid fading is observed in carbonate electrolytes.

1. Introduction

An important challenge for current battery technologies is to reduce the amount of expensive and non-abundant elements in order to further reduce cost and to avoid possible supply risks. This is especially a target for lithium-ion battery (LIB) as well as for the more recent sodium-ion battery (NIB) technology [1–10]. An approach to fulfill these requirements are conversion electrodes. Conversion electrodes based on transition metal compounds enable the transfer of several electrons per formula unit, this way leading to high capacities and energy densities when being used as a cathode or anode material. The reaction equation can be generalized as follows

$$M_aX_b + (bc)Li \underset{charge}{\overset{discharge}{\rightleftarrows}} aM + bLi_cX \qquad \text{eq 1}$$
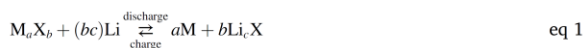
General challenges related to conversion reactions are the large

volume changes that occur during cycling and strong polarization leading to a large voltage hysteresis. Many compounds, like transition metal oxides, nitrides, fluorides, sulfides and phosphides are considered as potential electrode materials for LIBs and NIBs [1,2,11–13]. For these series of compounds Klein et al. discussed the shift in cell voltage when replacing lithium by sodium. The difference depends on the anion which amounts to 0.96 V for oxides (lithium cell shows higher voltages than sodium cells), for example. For chlorides, the voltage is almost identical while conversion reactions with e.g. iodides would lead to a higher voltage in case of sodium [12]. From the large number of conversion electrodes, recently copper phosphides attracted attention because of their very high theoretical volumetric and/or gravimetric capacities [14–18]. Elemental phosphorus shows a theoretical capacity as high as 2596 mAh g⁻¹ (based on formation of Na₃P), which is, besides Na metal, the material with the highest capacity for NIB anodes [19,20]. Phosphorous is a comparably abundant element, though natural sources of

phosphorous are largely minerals. A direct consequence of the large capacity of elemental phosphorous is that large volume changes take place during battery cycling which is a severe challenge. The formation of Na_3P from P comes along with a volume change of about 490%, resulting in electrode degradation and hence poor cycle life [21]. The volume expansion in case of phosphorus is even higher compared alloy electrodes such as the well investigated Sn (420%), Sb (390%), and also amorphous Si (282%) electrodes for example [22–26]. In view of these challenges for elemental phosphorous and metals, the use of phosphides becomes interesting. For Cu_3P, the volume expansion on the materials level during sodiation is 164%. This also requires nanosizing but the issue is less severe compared to elemental phosphorous and the above-mentioned metals. The ideal electrode reactions of Cu_3P with lithium/sodium as counter electrode are

$$3 \cdot A + Cu_3P \underset{charge}{\overset{discharge}{\rightleftarrows}} 3 \cdot Cu + A_3P \ (A = Li, \ Na\ ) \qquad\qquad eq\ 2$$
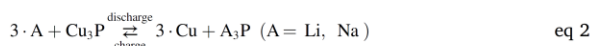
The theoretical capacity of Cu_3P (363 mAh g^{-1}) is close to that of graphite (372 mAh g^{-1}), but it exhibits a theoretical volumetric capacity of 2664 A h l^{-1}, being about three times larger compared to graphite (~780 A h l^{-1}) [27]. Additionally, transition metal phosphides are generally known to be electronically conductive if there is an appropriate difference in electronegativity and atomic ratio of metal and P, so that they are advantageous for application compared to the well investigated copper oxides, for example [28]. Moreover, sodiation of Cu_3P leads to the formation of highly conductive Cu which may improve the electronic wiring also in the sodiated state, this way mitigating contact losses. It is also worth mentioning CuP_2 as another candidate [29]. The larger phosphorous content provides a higher theoretical capacity, but on the other hand the volume expansion becomes much larger again (462%) and the conductivity is lower.

Studies on the use of Cu_3P in LIBs so far showed that, according to eq. (2), Li_3P and Cu form as discharge products [30,31]. Stan et al. used wet ball milling for the synthesis of a Cu_3P/C composite and found that the cycling performance was strongly depending on the applied voltage window [32]. Using a carbonate-based electrolyte, the best capacity retention was obtained when cycling between 0.5 and 2 V maintaining 220 mAh g^{-1} after 50 lithiation/delithiation cycles. The use of Cu_3P as electrode for NIBs is not well investigated so far. Only two studies have been published so far [17,33]. In line with eq. (2), sodiation of Cu_3P should lead to the formation of Na_3P and Cu. Clear evidence for Na_3P formation by XRD is, however, missing so far. Using X-ray photoelectron spectroscopy, Fan et al. at least could show that phosphidic bonds with Na develop during sodiation [33]. In contrast, the reversible formation of elemental Cu could be verified via XRD. Zhu et al. very recently studied $Cu_3P@C$ nanosheets being synthesized by a temperature induced synthesis and compared the electrochemical performance with that of using other synthesis methods creating Cu_3P/C composites [17]. They reached an excellent cycling stability and retained a capacity of 286 mAh g^{-1} at 0.1 A g^{-1} after 300 cycles with the temperature induced method. Fan et al. obtained similar capacities after more than 50 cycles for Cu_3P nanowire structures [33].

Although the nanostructuring approach leads to better performance, a simpler synthesis method is desirable. There are several methods to synthesize Cu_3P. For example, thermal synthesis in a quartz tube, wet ball milling, *in situ* growth of $Cu(OH)_2$ nanowires, followed by a phosphidation reaction as well as solvothermal methods have been used [17,27,33,34]. A simpler method is the use of (dry) high energy ball milling. The method also is convenient for adding carbon which acts as a support for the active material. The embedment of active materials as nano- or microparticles in a carbon matrix generally improves the cycle life [23,35–37]. In a previous study on such composites, we showed for Sn, Sb and C that the ball milling time has a major influence on the composite formation and consequently on the electrode properties. Also the degree of electrode "breathing" (electrode expansion/shrinkage during cell

cycling) was influenced as proven by *in situ* dilatometry studies [36]. While the use of carbon as matrix is quite effective in buffering volume changes and improving the electronic wiring, the trade-off is the additional weight and volume which reduces the energy density of a cell. A careful balance in properties is therefore required.

It is also widely known that the cycle life of electrodes is strongly influenced by the electrolyte composition [1,36–40]. Carbonate-based electrolytes are used in commercial LIBs and hence also in most research studies for conversion electrodes [11–13]. Compared to ether electrolytes, carbonate electrolytes generally show the advantages of higher relative permittivity and better oxidative stability while ethers can have a wider temperature window and show a better reductive stability [41]. The latter property can also lead to favorable SEI formation and hence longer cycle life as shown for various cases [1,8,35,36,38–41]. The use of an ether-based electrolyte for Cu_3P as electrode material has not been reported yet, however. Moreover, a direct comparison between lithium and sodium storage in Cu_3P electrodes is still lacking in literature.

Here, we report on the lithium and sodium storage in Cu_3P/C composites in half cells using different electrolytes (ether-based and carbonate-based). We also discuss the storage capacity of carbon black which contributes to the storage capacity of the electrodes to different degrees in Li- and Na-cells. Further analysis was done using X-ray diffraction (XRD), scanning/transmission electron microscopy with elemental mapping (SEM, TEM) and X-ray photoelectron spectroscopy (XPS).

2. Results and discussion

2.1. Cell reaction and physicochemical properties

Properties of the ideal cell reactions of Cu_3P in Li and Na cells are compared in Table 1. The larger size of the sodium ion causes a larger volume expansion during discharge (261% for Na compared to 190% for Li). Considering the cell level, the difference is much less drastic (−22.3% for Na vs. −17.1% for Li) which is due to the lower density of lithium metal (0.53 g cm^{-3}) compared to sodium (0.97 g cm^{-3}). Herein, the volume expansions were simply determined by the densities and molecular weights of the expected charge and discharge products. In Fig. S1 GITT measurements give an estimate about the average voltages for lithiation and sodiation of Cu_3P. Obviously, the discharge voltage in case of lithium (~0.8 V vs. Li^+/Li) is larger compared to sodium (~0.3 vs. Na^+/Na).

Table 1
Properties for the reaction of Cu_3P with lithium and sodium (298 K). Due to lack of tabulated data, the cell voltage E could only be calculated for the reaction with sodium ($E = -\Delta G/zF$, neglecting the contribution of ΔS). The formation enthalpy from Cu_3P was taken from Ref. [42] and that of Na_3P from Ref. [43]. The densities for the calculation were taken from Refs. [44] for Na_3P [45], for Li_3P, and [46] for Cu_3P, respectively. Note that Cu_3P can adopt different crystal structures and hence different densities are reported in literature. As commonly reported for conversion electrodes, values for q_{th} (mAh g^{-1}) refer to the active material, i.e. Cu_3P. Including the mass of Li and Na gives values of $q_{th,Cu3P+Li} = 331$ mAh g^{-1} and $q_{th,Cu3P+Na} = 277$ mAh g^{-1}.

Cell reaction	$3Na + Cu_3P \rightarrow Na_3P + 3Cu$	$3Li + Cu_3P \rightarrow Li_3P + 3Cu$
number of transferred e$^-$	3	3
Cell voltage E/V	0.34	–
q_{th} (Cu_3P)/mAh cm^{-3}	2664	2664
q_{th} (Cu_3P)/mAh g^{-1}	363	363
volume expansion electrode reaction/%	261	190
volume expansion cell reaction/%	−22.3	−17.1

2.2. Materials characterization

Fig. 1a shows the X-ray diffraction (XRD) pattern of the Cu_3P powder after its synthesis by reactive ball milling in a PBM. The pattern corresponds to the expected hexagonal crystal structure (space group: P 63 c m). An average crystallite size of about 17 nm was determined by Rietveld analysis, see Fig. S2a. The lattice parameters were determined to $a = 6.970 (6)$ Å and $c = 7.153 (6)$ Å and are well in line with the previous results from Bichat et al. and Stan et al. [32,47]. The not specified small reflection at $2\theta = 30.6°$ might be a phosphidic intermediate impurity which, however, is not detectable anymore after the subsequent ball milling step in the swing ball mill, see Fig. S2b.

Further information on the synthesized Cu_3P was obtained from transmission electron microscopy (TEM) measurements. The TEM selected area electron diffraction (SAED) pattern of the particle in Fig. 1b confirms formation of Cu_3P. Related to that, the high-resolution TEM image in Fig. 1c shows the (112) lattice plane of a Cu_3P crystal with an interplanar spacing 2.55 Å. Scanning electron microscopy (SEM) with elemental mapping (energy dispersive X-ray spectroscopy, EDS) was used to study the morphology and homogeneity of the sample, see Fig. 1d. Particles were generally smaller than 5 μm and the clearly overlapping signals from Cu and P indicate, in line with XRD measurements, complete reaction between Cu and P throughout the sample.

2.3. Electrochemical characterization of Cu_3P/C

Galvanostatic discharge/charge experiments are shown in Fig. 2a–g. All experiments shown in this manuscript were performed with a current density of 36.3 mA g^{-1} (corresponding to a C-rate of 0.1 related to q_{th} (Cu_3P) = 363 mAh g^{-1}). The voltage windows were 0.5–2 V for the Li-half cells and 0.01–2 V for the Na-half cells. Electrolytes based on diglyme (2G) or a 1:1 vol mixture of ethylene carbonate (EC) with dimethyl carbonate (DMC) were used using Li/Na salts with different

anions, i.e. OTf$^-$ (triflate), TFSI$^-$ (bis(trifluoromethanesulfonyl)imide) and PF$_6^-$ (hexafluorophosphate). The experimental matrix, however, is smaller than one would expect at first. One reason is that we were not successful in preparing glyme electrolyte solutions with the salts LiPF$_6$ and LiClO$_4$. This is because these salts form solid complexes with diglyme molecules [48]. On the other hand, NaTFSI cannot be used in sodium half cells due to rapid corrosion [40]. Overall five different electrolyte compositions were compared and abbreviated as follows EC:DMC LiPF$_6$, EC:DMC NaPF$_6$, 2G LiTFSI, 2G NaOTf, 2G NaPF$_6$. The electrolyte concentration was 1 M in all cases.

As the carbon black (30 wt%) contributes to the overall electrode capacity, capacity values are stated form gram of Cu_3P and per gram of Cu_3P/C in the related figures. Note that the storage capacity provided by the carbon black depends on the used electrolytes and the type of ion (Li, Na). Moreover, the voltage windows are necessarily different in both half cells. Fig. S3 shows the capacity contribution of carbon black for Li and Na for the different electrolytes. For example, the capacity contribution of carbon black in the case of Li is about 70 mAh g^{-1} after around 20 cycles using for 2G NaPF$_6$ and EC:DMC LiPF$_6$ and remains almost constant within the subsequent cycles, see Figs. S3a and b. This results in a contribution of about 21 mAh g^{-1} to the overall capacity of Cu_3P in Li half cells which is only about 7% of the overall theoretical capacity. The capacity contribution of carbon black in case of Na can be seen in Figs. S3c–e. A reversible capacity of about 150 mAh g^{-1} for carbon black was measured for 2G NaPF$_6$ and EC:DMC NaPF$_6$ within a voltage window of 0.01 V–2 V vs. Na$^+$/Na, which results in a storage contribution of 45 mAh g^{-1} to the overall capacity of the Cu_3P/C electrodes. This amounts to about 12% of the theoretical capacity of Cu_3P. The effect on the practical capacities is discussed further below. Note that the storage capacity of carbon black is slightly influenced by the chosen conducting salt, therefore the use of 2G NaOTf results in a reversible capacity of about only 120 mAh g^{-1}, for example.

In case of Li, the initial cycle shows a discharge capacity of about
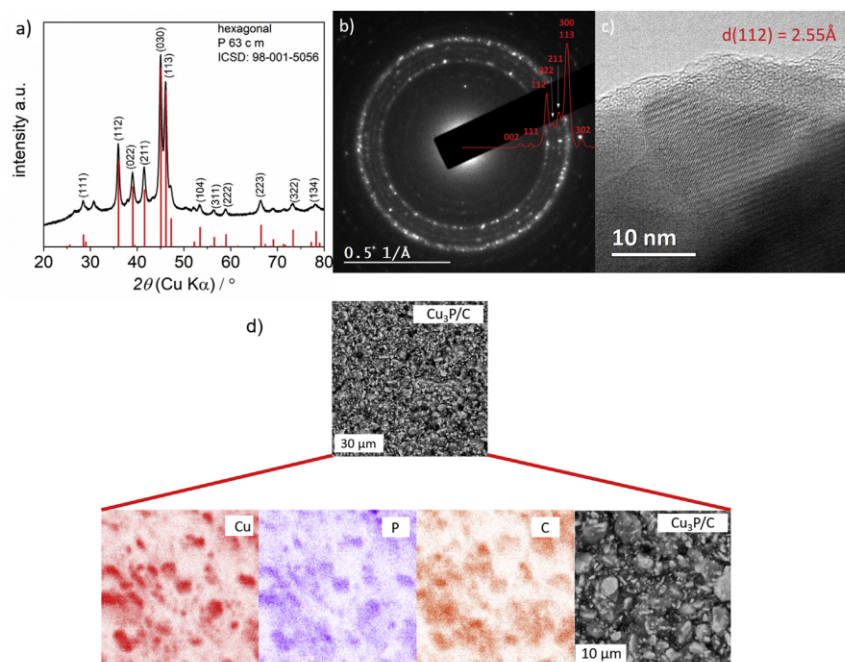
Fig. 1. a) XRD analysis of Cu_3P after reactive ball milling of Cu and P with a planetary ball mill (Reference: ICSD: 98-001-5056); b) SAED pattern of a Cu_3P particle; c) High resolution TEM image of Cu_3P after high energy ball milling for 24 h @ 400 rpm in a planetary ball mill; d) SEM analysis of Cu_3P/C composite electrodes with elemental mapping by EDX.
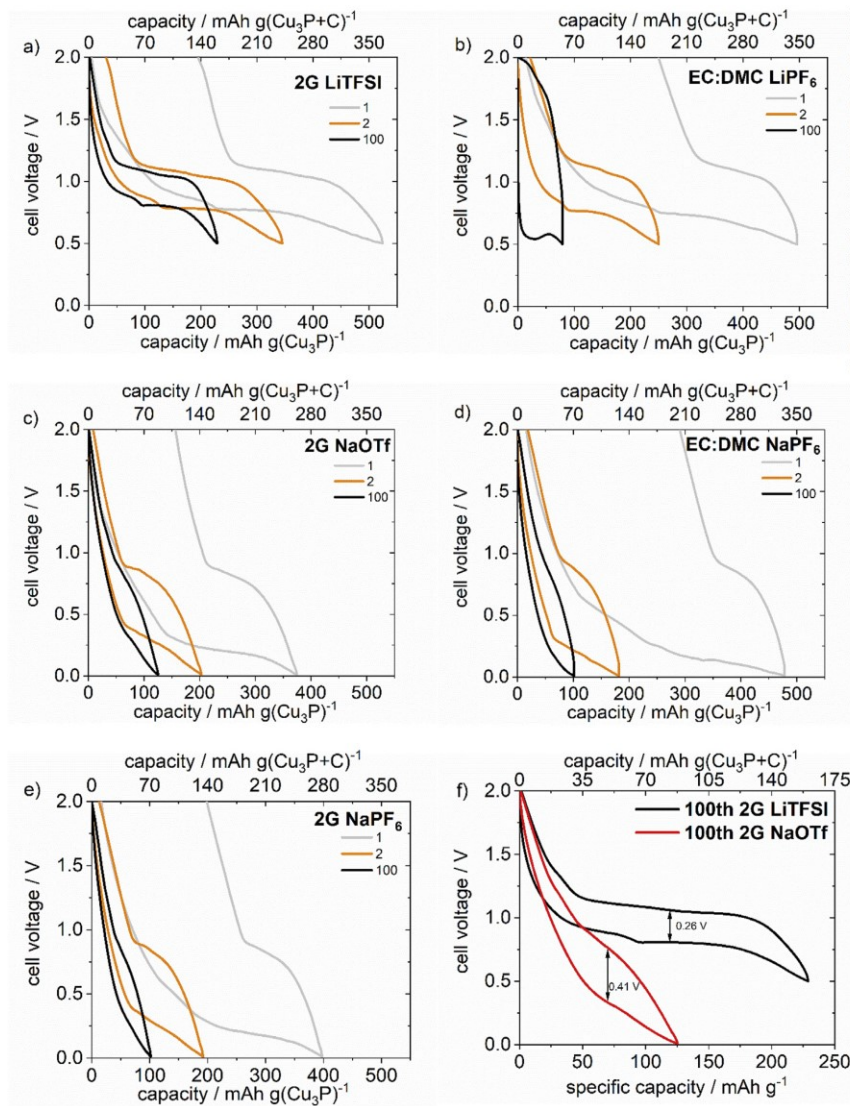
Fig. 2. Galvanostatic discharge/charge curves for Cu_3P/C electrodes in Li- and Na-half cells (two-electrode geometry with Li/Na as counter electrode). Cycling was performed with a current rate of 0.1 C (36.6 mA g^{-1}) in a voltage window of 0.5–2.5 V in Li cells and 0.01–2.5 V in Na cells for different electrolyte solutions. Voltage profiles are shown of the 1st, 2nd and 100th cycle for a) 2G LiTFSI; b) EC:DMC LiPF$_6$; c) 2G NaOTf; d) EC:DMC NaPF$_6$; e) 2G NaPF$_6$; f) Voltage profiles of the 100th cycle for Li (2G LiTFSI electrolyte) and Na (2G NaOTf electrolyte) in comparison. Arrows indicate the combined overpotentials for both cells; g) Discharge capacities vs. cycle number for Cu_3P/C electrodes h); Rate capability test for five different C-rates for Cu_3P/C electrodes in Li and Na half cells (1C = 363 mA g^{-1}).

500 mAh g $(Cu_3P)^{-1}$ for both, carbonate and diglyme electrolytes, exceeding the theoretical capacity of 363 mAh g^{-1}. For 2G LiTFSI the initial discharge capacity was 523 mAh g $(Cu_3P)^{-1}$, see Fig. 2a. The initial Coulomb efficiency (ICE) was about 63% with an accompanied charge capacity of 329 mAh g $(Cu_3P)^{-1}$. Herein, Coulomb efficiencies were calculated based on $\eta_C = \frac{Q_{out}}{Q_{in}} \cdot 100\%$. Sloping voltages and a large plateau region are observed, being typical for conversion reactions. However, the obtained overpotentials of about 0.2 V are comparably small to that what has been typically observed for other conversion reactions, e.g. CuO or CoS (0.6 V–1.0 V) [12,13,33,49]. In contrast to that, the use of the carbonate electrolyte EC:DMC LiPF$_6$ leads to an initial discharge capacity of 496 mAh g $(Cu_3P)^{-1}$ and an initial charge capacity of 245 mAh g $(Cu_3P)^{-1}$. The resulting ICE is only 50% accompanied with larger overpotentials in the first cycle.

The excess capacity ($q > q_{th}$) and the large capacity loss in the first cycle are due to excessive electrolyte decomposition (SEI formation) along with the formation of a nanoscopic structure typical for conversion reactions [12,13]. A similar behavior is found in case of sodium, see Fig. 2c,d,e. The ICE value is higher for the ether electrolyte (2G NaPF$_6$, 50%) compared to the carbonate electrolyte (EC:DMC NaPF$_6$, 39%). The lower ICE for carbonate electrolytes is also in line with the larger polarization during charging. This suggests a much thicker SEI in case of carbonates. As both electrodes (working electrode and counter electrode) show an SEI, we conducted impedance measurements in a three electrode arrangement with Li as a reference and counter electrode. Results are shown in Fig. S4 and indicate a much less resistive SEI for the Cu_3P electrode in case of the diglyme electrolyte. Fig. 2g shows the discharge capacity for the different electrolytes over 120 cycles. Few cycles are needed in all cases to reach fairly stable capacity values after which slow

Fig. 2. (*continued*).

g)

h)
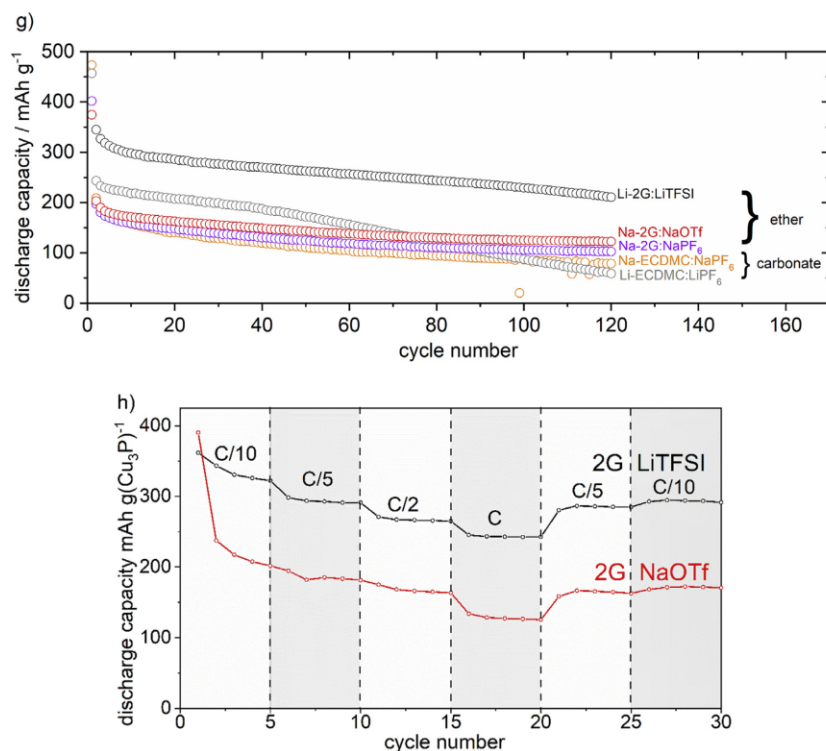
fading takes place.

For both cells (Li, Na), the capacity retention as well as the absolute capacity values are clearly better in case of the ether electrolyte indicating an overall better stability of the electrode. The use of large anions (TFSI$^-$ for Li and OTf$^-$ for Na) seems beneficial. For better comparison the voltage profiles using large anions in diglyme for Li and Na cells are shown in Fig. 2f. For Na and 2G NaOTf as electrolyte, the capacity after 120 cycles reaches 120 mAh g $(Cu_3P)^{-1}$, formally corresponding to 33% of the theoretical capacity. Unfortunately, the real values might be lower as the carbon black additive could contribute to the capacity as much as 38% (assuming that the carbon black provides 150 mAh g^{-1} also in the Cu_3P/C composite (carbon, 30 wt%). Higher capacity values are obtained in case of lithium, i.e. 210 mAh g $(Cu_3P)^{-1}$ after 120 cycles are retained when using the ether based electrolyte 2G LiTFSI. This value corresponds to 58% of the theoretical capacity (or 1.74 Li ions per formula unit). In this case, the capacity contribution of carbon black to the practical capacities does not exceed 10%. While improvements are needed, the use of glymes shows already superior performance compared to many previous studies in which always carbonate electrolytes were used [32,50]. A literature comparison is shown in Table S1. Note that in our study we chose for a simple ball milling synthesis based on bulk precursors. This shows that quite reasonable results can be already obtained with this straightforward preparation method.

A rate performance test of the electrodes in the diglyme electrolytes is shown in Fig. 2h. One can observe higher capacities for all current rates for Li. Even at a current rate of 1C (363 mA g $(Cu_3P)^{-1}$), a capacity of about 250 mAh g $(Cu_3P)^{-1}$ is retained compared to 130 mAh g $(Cu_3P)^{-1}$ for Na. The initial capacity drop is much larger for Na (391–235 mAh g $(Cu_3P)^{-1}$) compared to Li (359–343 mAh g $(Cu_3P)^{-1}$). With consecutive

cycling the voltage drops occur in similar extent, implying similar kinetics. When returning to C/10 a capacity of close to 300 mAh g $(Cu_3P)^{-1}$ for Li and around 170 mAh g $(Cu_3P)^{-1}$ for Na is recovered. Considering the Li case, 85% of the capacity obtained in the 2nd cycle are retained after completing the rate performance test when reapplying C/10. In contrast, only 71% for Na were retained. These results indicate that the overall rate performance of the lithium cell is better compared to the sodium cell. The observation that the storage capacity for Na is smaller compared to Li for the same conversion electrode is frequently reported in literature. This is typically explained with the larger ion radius of Na$^+$ which makes efficient diffusion more difficult. Given the complicated nanoscopic structure and the excessive SEI formation, however, a clear explanation is difficult. In some cases, conversion electrodes show a higher capacity for Na compared to Li when using transition metal carbodiimides such as CuNCN and ZnNCN, for example [51,52].

2.4. Post mortem analysis

Post mortem analysis was conducted in order study the electrodes after cycling. XRD patterns (measured under Ar atmosphere) after 5 cycles are shown in Fig. 3a and b. For lithium, Cu_3P reflections can be observed in the lithiated state, meaning that the conversion reaction was incomplete. However, the broadening of the signals might be a hint for a gradual loss in crystallinity (amorphization) during cycling. We could not find any evidence for Li_2CuP which was found by Bichat et al. in small amounts [47]. This might be also due to different experimental conditions (larger active mass loading), see Table S1. In case of Na, Cu_3P signals are visible in the sodiated state as well. Broadening of Cu_3P signals is more distinct and therefore a stronger loss in crystallinity may take

5

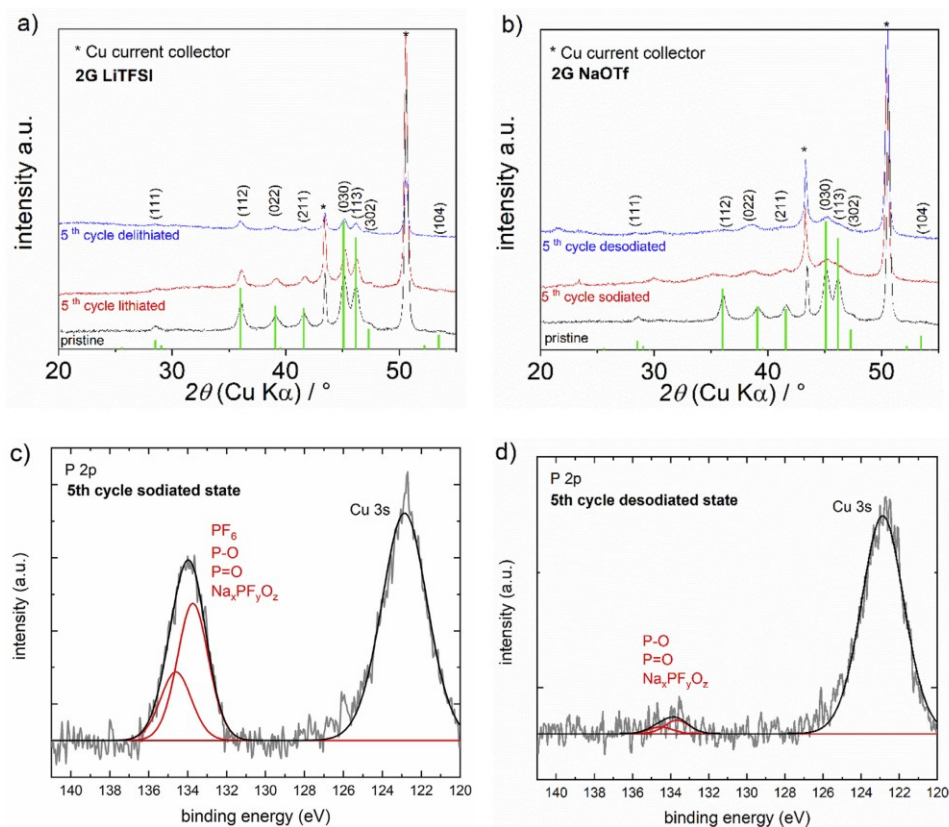**Fig. 3.** Post mortem XRD analysis of Cu_3P/C electrodes after 5 cycles a) in the lithiated/delithiated and b) sodiated/desodiated states. ICSD: 98-001-5056 was used as reference for Cu_3P. The '*' indicates the diffraction signals derived from the Cu current collector (ICSD: 98-005-3755). For XRD, cycling was performed with a current rate of 0.1 C (36.6 mA g^{-1}) in Li and Na half cells (two electrode geometry) in a voltage window of 0.5–2.5 V (Li cells) and 0.01–2.5 V (Na cells); XPS analysis of the P 2p signal is shown for c) the sodiated state of Cu_3P of the 5th cycle; d) the desodiated state of Cu_3P of the 5th cycle. For XPS, cycling was performed at 0.1 C (36.6 mA g^{-1}) within a voltage window of 0.01–2 V vs. Na^+/Na using 1 M NaOTf in diglyme as electrolyte.

place upon cycling. Overall, XRD did not provide evidence for the formation of Li_3P and respectively Na_3P. Note that the formation of copper as discharge product could not be analyzed as copper was used as current collector for the experiments.

For the Na-cell, further analysis on the possible discharge products was done using X-ray photoelectron spectroscopy (XPS). The results of the discharged and charged state after five cycles are shown in Fig. 3c and d. Note, the samples were pretreated by Ar^+-sputtering to remove the top surface layer (see experimental for details). In the sodiated state, hardly evidence was found for phosphidic species which show characteristic signals at binding energies (BE) between 123 and 126 eV, see Fig. 3c. However, the BE of phosphidic species is close to the Cu 3s signal from the collector at about 122 eV, which complicates the analysis. On the other hand, signals from phosphate species and other compounds containing oxidized phosphorous (for simplicity denoted as "P–O bonds" in the following) were clearly observed between 132 and 136 eV. The corresponding spectrum for the desodiated state is shown in Fig. 3d. Similarly, a signal at 132–136 eV can be observed, however, with much smaller intensity. These measurements are again an indication that the conversion reactions are chronically difficult to analyze. The rather unexpected observation of "P–O" bonds instead of the expected Cu_3P is a clear sign for side reactions with the electrolyte solution causing the low ICE value and a thick SEI. The presence of "P–O" bonds is in line with the observations of Fan et al. as they detected phosphate species next to phosphidic species as well [33]. The difficulty in analyzing the samples

can be understood from a previous study on CuO thin films (approx. 200 nm in thickness) where we found that the SEI can grow to a thickness of several μm during discharge but at the same time the surface layer partly disappears during charging [11]. The partial dissolution/decomposition of the SEI during charging could explain the reduced signal intensity for the "P–O" bonds in the desodiated state.

Overall, the results from XRD and XPS provided only limited information on the electrode reaction. Nevertheless, some conclusions can be drawn. (1) The XRD measurements indicate that the conversion reaction is incomplete and that amorphous phases form during cycling. (2) The XPS measurements show that the surface is rich in "P–O" compounds which likely result from side reactions with the electrolyte solution resulting in a thick SEI.

2.5. In situ electrochemical dilatometry (ECD)

In situ ECD provides information on the electrode thickness during charging/discharging ("breathing"), i.e. it is also sensitive to amorphous phases and SEI formation as long as there is a sufficiently large change in electrode thickness.

Fig. 4 shows the electrode thickness change for the lithium cell (1 M LiTFSI in 2G) and the sodium cell (1 M NaOTf in 2G). The presented samples are well comparable since mass loading and initial height are quite similar (36 vs. 39 μm) and (3.49 vs. 3.23 mg cm^{-2}). Both cells show a large increase in electrode thickness during the initial
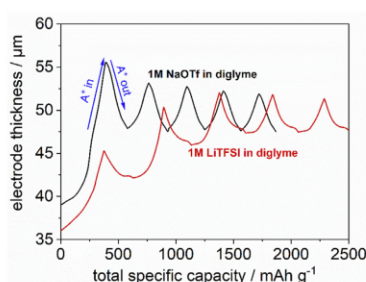
Fig. 4. In situ dilatometry studies of Cu_3P in Li and Na half cells with diglyme electrolytes a) 1 M LiTFSI in diglyme; b) 1 M NaOTf in diglyme. Cycling was performed with a current rate of 0.1 C ($36.6 \, mA \, g^{-1}$) in three-electrode geometry in a voltage window of 0.5–2.5 V vs. Li^+/Li and 0.01–2.5 V vs. Na^+/Na, respectively.

sodiation/lithiation. This has been observed for other measurements [36,53] and relates to restructuring of the electrode particles, combined with surface film formation (SEI formation). The larger thickness increase in case of sodium indicates a more excessive surface film formation and also results from the ion size effect (Na > Li) [11]. Upon further cycling, breathing becomes larger in the lithium cell, which can be explained by the higher specific capacity obtained in comparison to the sodium cell.

The use of carbonate electrolytes results in analogue behavior to the use of diglyme electrolytes but a stronger capacity decay occurs (see Fig. S5). Obviously, there is a larger thickness change in the initial cycles for both cases, Li (23 μm) and Na (20 μm) compared to when diglyme is used as electrolyte solvent (Li, 10 μm and Na, 17 μm), which might be a hint for intensified side reactions when carbonate electrolytes are used. Moreover, to begin of the intial discharging processes, the increase in electrode thickness in case of the carbonates is slower compared to that of diglyme electrolytes for both, Li and Na cells. While it is difficult to completely rationalize this, it may indicate a more excessive electrolyte decomposition before the desired cell reaction begins (see peak shape profile). This layer limits then the redox activity upon further cycling and hence a strong capacity fade occurs. These results are in line with the results from GCPL from Fig. 4 as an improved capacity retention was found for diglyme electrolytes in comparison to the carbonate electrolytes.

The theoretical volumetric capacities and porosities of the electrodes are summarized in Table S2 as they are important practical parameters. Porosity values P were calculated with $P = \left(1 - \frac{V_b}{V_{el}}\right) \cdot 100\%$. The calculation was based on the densities of the materials contained within the electrode with the carbon black contribution to the overall capacity being neglected. Herein, porosities range from 54% to 67% (see Table s2), which is in good accordance with the porosities obtained in our previous study on Sn + Sb and SnSb electrodes being prepared on the same synthesis route [36]. Related to that, the achievable theoretical volumetric capacities for the herein considered electrodes vary between 530 and 642 mAh cm^{-3}, which is about 64–78% of the theoretical volumetric bulk capacity of the overall electrode (826 mAh cm^{-3}). However, the practical volumetric capacity for 2G LiTFSI was somewhat lower, reaching 216 mAh cm^{-3} in the 5th lithiation cycle, which is 41% of the theoretical value. In case of Na, only 131 mAh cm^{-3} discharge capacity were obtained after five cycles corresponding to 23% of the theoretical value for 2G NaOTf. These values show that the volumetric capacities are smaller than that what is being found for graphite (~550 mAh cm^{-3}) which emphasizes the need for further optimization processes by e.g. calendering.

Overall, all electrodes showed large height changes in the first cycles which is typical for conversion electrodes. Breathing was found being

constant in case glyme electrolytes were used, while a rapid capacity decay was found for carbonate electrolytes. The breathing for the lithium cell was larger, in line with the significantly larger capacity.

3. Conclusion

Mechanochemically synthesized Cu_3P/C composites were studied for lithium and sodium storage in different electrolyte solutions. The most important results are concluded as follows.

1) For Li and Na cells, the use of diglyme leads to a much better capacity and cycle life compared to the carbonate electrolyte. The combined overpotentials are also larger for latter electrolyte, indicating a more resistive surface layer as a result of a more unfavorable electrolyte decomposition.

2) Despite the larger voltage window the sodium storage capacity of the electrodes is smaller. After 120 cycles, approx. 1 Na is stored per formula unit compared to 1.74 for Li.

3) Revealing the reaction mechanism was found to be very difficult. Post mortem XRD after discharging/charging reveals that Cu_3P is not fully utilized. Crystalline discharge products such as sodium or lithium phosphide could not be detected. Instead, amorphization takes place which seems stronger in case of Na. XPS measurements showed that the surface layers contain oxidized phosphorus species likely as a result of side reactions with the electrolyte solution. The first discharge capacity exceeds the theoretical capacity due to electrolyte decomposition/film formation.

4) Results from *in situ* electrochemical dilatometry studies corresponded well to the galvanostatic measurements. The diglyme electrolyte leads to more stable "breathing" while a rapid degradation is found for carbonate electrolytes. Carbonate electrolytes lead to a larger breathing during the initial discharge for both Li and Na, indicating more side reactions and hence a more unfavorable SEI formation which may cause the faster capacity fade for these electrolytes.

3.1. Experimental part

Materials synthesis: Commercial Cu particles (<425 μm, 99.5% purity) and phosphorus (99,8% purity) from Sigma Aldrich were used as active materials and were put in appropriate stoichiometric ratios into zirconia jars. 5 g of the raw materials were ball milled in a planetary ball mill (PBM, Fritsch Pulverisette 7) for 24 h at 400 rpm with a jar volume of 80 ml as well as in a subsequent step in a swing ball mill (SBM, Retsch MM 400) for 12 h with a jar volume of 10 ml applying a frequency of 25 Hz, in order to form a composite with carbon. Cu_3P to carbon weight ratio was set to 7:3. For the use of both ball mill machines, the ball to powder weight ratio was set to 10:1.

Characterization methods: XRD analysis of the Cu_3P electrodes and powders was performed with a Bruker Phaser D2 diffractometer using Cu Kα radiation (0.02° step width and 20 s step time). XPS of the Cu_3P/C electrodes was performed using a multiprobe system (Scienta Omicron) with a monochromatic X-ray source (Al K_α) and an electron analyzer (Argus CU) with 0.6 eV spectral energy resolution. The spectra were fitted using Voigt functions after background subtraction. In order to remove the thin surface layer, consisting of salt residuals and oxidized species, the samples were sputtered in the same multiprobe system using Ar^+-ions (FOCUS FDG150, 1 keV, 10 mA) for 30 min. This corresponds to an approximate sputter depth of 15 nm. Longer sputter times did not change the spectra. SEM images were obtained using a benchtop SEM machine (Phenom ProX) operating at 15 kV accelerating voltage. TEM specimens were prepared by dispersing the powder in ethanol in an ultrasonic bath and placing onto a holey carbon copper grid. The structural features of the Cu_3P nanoparticles were studied by high-resolution transmission electron microscopy (HRTEM) and selected area electron diffraction (SAED) in a JEOL JEM 3010HT operating at 300 kV that is

equipped with a LaB$_6$ filament and a 1 k x 1 k GATAN multi scan CCD-camera.

Electrode preparation: A slurry, using 5 wt% of PVDF binder related to the total weight of Cu$_3$P/C powder was prepared in an NMP solution in an MBraun Glovebox under Ar atmosphere. The slurry was casted with a doctor blade by hand onto a copper foil (Schlenk) under inert conditions. Electrodes were punched into round discs (12 mm diameter) and dried overnight in a vacuum oven (Büchi B-585) at 70 °C. The active mass loadings varied between 1.5 and 2.5 mg cm^{-2}. The initial electrode thickness (without current collector) of the electrodes varied between 20 and 40 μm.

Electrochemical tests: The diglyme electrolytes for Na cells were prepared by dissolving NaPF$_6$ (1 M) from Alfa Aesar and NaOTf (1 M) (TCI Chemicals, 98%). The carbonate electrolyte was prepared by dissolving NaPF$_6$ (1 M) in a EC:DMC (1:1) mixture (chemicals obtained from Sigma Aldrich). Diglyme and EC:DMC were dried over molecular sieves (4 Å, Sigma Aldrich). For the Li cells, the diglyme electrolyte was obtained by dissolving (1 M) LiTFSI (Sigma Aldrich). For the carbonate electrolyte, a commercial product of (1 M) LiPF$_6$ in EC:DMC (1:1) was purchased from Sigma Aldrich. Electrochemical investigations were performed in C2032 coin cells, using two pieces of glass microfiber filters (Whatman, GF/A) as separator and Na metal (BASF SE) as counter electrode. An electrolyte volume of 100 μl was used for each cell. Cycling was conducted using Biologic MPG2 and BCS instruments.

In situ dilatometry was performed using a three electrode setup of ECD-3-nano from EL-CELL for measuring the expansion and shrinking of the electrodes. Herein, the used electrodes exhibited a diameter of 10 mm.

Declaration of competing interest

The authors declare that they have no known competing financial interests or personal relationships that could have appeared to influence the work reported in this paper.

Acknowledgements

Appendix A. Supplementary data

Supplementary data to this article can be found online at https ://doi.org/10.1016/j.powera.2020.100031.

References

[1] P.K. Nayak, L. Yang, W. Brehm, P. Adelhelm, Angew Chem. Int. Ed. Engl. 57 (2018) 102–120.
[2] L. Chen, M. Fiore, J.E. Wang, R. Ruffo, D.-K. Kim, G. Longoni, Advanced Sustainable Systems 2 (2018) 1700153.
[3] M. Lao, Y. Zhang, W. Luo, Q. Yan, W. Sun, S.X. Dou, Adv Mater 29 (2017).
[4] D. Kundu, E. Talaie, V. Duffort, L.F. Nazar, Angew Chem. Int. Ed. Engl. 54 (2015) 3431–3448.
[5] N. Yabuuchi, K. Kubota, M. Dahbi, S. Komaba, Chem. Rev. 114 (2014) 11636–11682.
[6] H. Pan, Y.-S. Hu, L. Chen, Energy Environ. Sci. 6 (2013) 2338.
[7] M.H. Han, E. Gonzalo, G. Singh, T. Rojo, Energy Environ. Sci. 8 (2015) 81–102.
[8] L. Medenbach, P. Adelhelm, Top. Curr. Chem. 375 (2017) 81.
[9] Q. Liu, Z. Hu, M. Chen, C. Zou, H. Jin, S. Wang, S.L. Chou, Y. Liu, S.X. Dou, Adv. Funct. Mater. 30 (2020).
[10] G. Chang, Y. Zhao, L. Dong, D.P. Wilkinson, L. Zhang, Q. Shao, W. Yan, X. Sun, J. Zhang, J. Mater. Chem. 8 (2020) 4996–5048.
[11] F. Klein, R. Pinedo, P. Hering, A. Polity, J. Janek, P. Adelhelm, J. Phys. Chem. C 120 (2016) 1400–1414.
[12] F. Klein, B. Jache, A. Bhide, P. Adelhelm, Phys. Chem. Chem. Phys. 15 (2013) 15876–15887.
[13] J. Cabana, L. Monconduit, D. Larcher, M.R. Palacin, Adv Mater 22 (2010) E170–E192.
[14] C. Kim, H. Kim, Y. Choi, H.A. Lee, Y.S. Jung, J. Park, ACS Omega 3 (2018) 7655–7662.
[15] F. Zhao, N. Han, W. Huang, J. Li, H. Ye, F. Chen, Y. Li, J. Mater. Chem. 3 (2015) 21754–21759.
[16] S. Liu, X. He, J. Zhu, L. Xu, J. Tong, Sci. Rep. 6 (2016) 35189.
[17] J. Zhu, Q. He, Y. Liu, J. Key, S. Nie, M. Wu, P.K. Shen, J. Mater. Chem. 7 (2019) 16999–17007.
[18] E.J. Sheets, W.-C. Yang, R.B. Balow, Y. Wang, B.C. Walker, E.A. Stach, R. Agrawal, J. Mater. Res. 30 (2015) 3710–3716.
[19] J. Ni, L. Li, J. Lu, ACS Energy Letters 3 (2018) 1137–1144.
[20] F. Yang, H. Gao, J. Chen, Z. Guo, Small Methods 1 (2017) 1700216.
[21] J. Qian, X. Wu, Y. Cao, X. Ai, H. Yang, Angew Chem. Int. Ed. Engl. 52 (2013) 4633–4636.
[22] F. Legrain, O.I. Malyi, S. Manzhos, Comput. Mater. Sci. 94 (2014) 214–217.
[23] T. Palaniselvam, M. Goktas, B. Anothumakkool, Y.N. Sun, R. Schmuch, L. Zhao, B.H. Han, M. Winter, P. Adelhelm, Adv. Funct. Mater. 29 (2019) 1900790.
[24] H. Ying, W.Q. Han, Adv. Sci. 4 (2017) 1700298.
[25] G. Wang, X. Xiong, Z. Lin, C. Yang, Z. Lin, M. Liu, Electrochim. Acta 242 (2017) 159–164.
[26] V.L. Chevrier, G. Ceder, J. Electrochem. Soc. 158 (2011) A1011.
[27] H. Pfeiffer, F. Tancret, M.-P. Bichat, L. Monconduit, F. Favier, T. Brousse, Electrochem. Commun. 6 (2004) 263–267.
[28] Y. Shi, B. Zhang, Chem. Soc. Rev. 45 (2016) 1529–1541.
[29] S.O. Kim, A. Manthiram, ACS Appl. Mater. Interfaces 9 (2017) 16221–16227.
[30] F. Poli, J.S. Kshetrimayum, L. Monconduit, M. Letellier, Electrochem. Commun. 13 (2011) 1293–1295.
[31] F. Poli, A. Wong, J.S. Kshetrimayum, L. Monconduit, M. Letellier, Chem. Mater. 28 (2016) 1787–1793.
[32] M.C. Stan, R. Klöpsch, A. Bhaskar, J. Li, S. Passerini, M. Winter, Advanced Energy Materials 3 (2013) 231–238.
[33] M. Fan, Y. Chen, Y. Xie, T. Yang, X. Shen, N. Xu, H. Yu, C. Yan, Adv. Funct. Mater. 26 (2016) 5019–5027.
[34] S. Liu, Y. Qian, L. Xu, Solid State Commun. 149 (2009) 438–440.
[35] B. Zhang, G. Rousse, D. Foix, R. Dugas, D.A. Corte, J.M. Tarascon, Adv Mater 28 (2016) 9824–9830.
[36] W. Brehm, J.R. Buchheim, P. Adelhelm, Energy Technology, 2019, p. 1900389.
[37] W. Brehm, A.L. Santhosha, Z. Zhang, C. Neumann, A. Turchanin, A. Martin, N. Pinna, M. Seyring, M. Rettenmayr, J.R. Buchheim, P. Adelhelm, Advanced Functional Materials, 2020.
[38] J. Zhang, D.-W. Wang, W. Lv, S. Qin, S. Niu, S. Zhang, T. Cao, F. Kang, Q.-H. Yang, Advanced Energy Materials 8 (2018) 1801361.
[39] K. Westman, R. Dugas, P. Jankowski, W. Wieczorek, G. Gachot, M. Morcrette, E. Irisarri, A. Ponrouch, M.R. Palacín, J.M. Tarascon, P. Johansson, ACS Appl. Energy Mater. 1 (2018) 2671–2680.
[40] M. Goktas, C. Bolli, J. Buchheim, E.J. Berg, P. Novak, F. Bonilla, T. Rojo, S. Komaba, K. Kubota, P. Adelhelm, ACS Appl. Mater. Interfaces 11 (2019) 32844–32855.
[41] G.G. Eshetu, G.A. Elia, M. Armand, M. Forsyth, S. Komaba, T. Rojo, S. Passerini, Advanced Energy Materials, 2020.
[42] O.J.K. Steve Boone, Thermochim. Acta 202 (1992) 113–119.
[43] M.P. Morozova, G.A. Bol'shakova, N.L. Lukinykh, Enthalpy of Formation of Compounds of Sodium with Elements of the Main Subgroups of Group V, Zh. Obshch. Khim. 29 (1959) 3144–3145, in Russian; TR: J. Gen. Chem. USSR, 1959, 29, p 3112-3113 (Thermo; Experimental).
[44] https://materials.springer.com/isp/crystallographic/docs/sd_0458519 ((accessed May 2020)).
[45] https://materials.springer.com/isp/crystallographic/docs/sd_0458524 ((accessed May 2020)).
[46] https://materials.springer.com/isp/crystallographic/docs/sd_0528447 ((accessed May 2020)).
[47] M.P. Bichat, T. Politova, J.L. Pascal, F. Favier, L. Monconduit, J. Electrochem. Soc. 151 (2004) A2074.
[48] J. Grondin, Solid State Ionics 166 (2004) 441–452.
[49] J.Y. Park, S.J. Kim, J.H. Chang, H.K. Seo, J.Y. Lee, J.M. Yuk, Nat. Commun. 9 (2018) 922.
[50] M.-P. Bichat, T. Politova, H. Pfeiffer, F. Tancret, L. Monconduit, J.-L. Pascal, T. Brousse, F. Favier, J. Power Sources 136 (2004) 80–87.
[51] A. Eguía-Barrio, E. Castillo-Martínez, X. Liu, R. Dronskowski, M. Armand, T. Rojo, J. Mater. Chem. 4 (2016) 1608–1611.
[52] A. Eguia-Barrio, E. Castillo-Martínez, F. Klein, R. Pinedo, L. Lezama, J. Janek, P. Adelhelm, T. Rojo, J. Power Sources 367 (2017) 130–137.
[53] M. Goktas, C. Bolli, E.J. Berg, P. Novák, K. Pollok, F. Langenhorst, M.v. Roeder, O. Lenchuk, D. Mollenhauer, P. Adelhelm, Advanced Energy Materials 8 (2018) 1702724.

Publication 3: Copper thiophosphate (Cu$_3$PS$_4$) as electrode for sodium-ion batteries with ether electrolyte
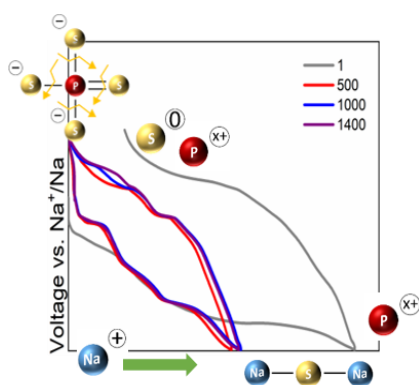
The application of a thiophosphate (Cu$_3$PS$_4$) as electrode material is demonstrated for sodium ion batteries in half cells. During cycling, redox activity of Cu$_3$PS$_4$ is found to be largely dominated by sulfur including the formation of Na$_2$S as a final discharge product. This way, Cu$_3$PS$_4$ shows excellent cycle life while reaching capacities of about 580 mAh g^{-1}.

Keyword: Thiophosphate electrodes.

In publication 3 the redox activity of a thiophosphate is considered for its use as electrode material for SIBs. Li/Na thiophosphates are often used as electrolytes in SSBs as they provide high ionic conductivities and structural integrity. Before this publication, there was only one study about using a thiophosphate (Li$_3$PS$_4$) in combined application as electrode and electrolyte for Li SSBs [43], but however, no study has been carried out for the use of a thiophosphate as an electrode in SIBs. This study aims at studying the redox activity of a thiophosphate in SIBs when being used only as an electrode at the example of copper thiophosphate (Cu$_3$PS$_4$). The synthesis of this thiophosphate is based on reactive ball milling of the raw materials S, P$_2$S$_5$ and Cu in powder form using appropriate stoichiometric ratios. The as-synthesized Cu$_3$PS$_4$ is characterized by XRD, TEM and SEM related to its crystal structure, morphology and particle size. Electrochemical investigations, *in situ* XRD[2] and XPS based post mortem studies reveal that Cu$_3$PS$_4$ undergoes a phase conversion with Na, based on the reversible formation of Na$_2$S, leading to capacities of about more than 580 mAh g^{-1} after 200 cycles @ 120 mAh g^{-1}. Furthermore, redox activity is dominated by sulfur. Interestingly, only during the initial discharge, copper (Cu) is the sole redox active element, while in the further cycles the redox inactive remaining Cu can act as polysulfide trap, avoiding dissolution effects and resulting in enhanced cycle life. However, the role of phosphorus remains unclear so far.

The authors of this publication are Wolfgang Brehm, Aggunda L. Santhosha, Zhenggang Zhang, Christof Neumann, Andrey Turchanin, Andréa Martin, Nicola Pinna, Martin Seyring, Markus Rettenmayr, Johannes R. Buchheim and Philipp Adelhelm.

The results of this study were published in *Advanced Functional Materials* under the title "Copper thiophosphate (Cu$_3$PS$_4$) as electrode for sodium-ion batteries with ether electrolyte" (doi: 10.1002/adfm.201910583).

---

[2] In the research community the terms *in situ* and *operando* are not consistently used. In cooporation with the coauthors, the designation *operando* XRD was used in publication 3.

For this paper, XRD studies were performed and analyzed by Johannes R. Buchheim and Wolfgang Brehm. TEM measurements were conducted and analyzed by Martin Seyring and Markus Rettenmayr. *In situ* XRD and some additional TEM imaging were carried out and discussed by Andrea Martin and Nicola Pinna (Humboldt-University Berlin). Further, XPS post mortem studies were performed and analyzed by Christof Neumann and Andrey Turchanin. Synthesis, SEM imaging, *in situ* dilatometry, GCPL, PEIS, post mortem XRD and overall data analysis as well as further calculations were performed by the first author. The paper was written by the first author and edited by Philipp Adelhelm.

Copper Thiophosphate (Cu₃PS₄) as Electrode for Sodium-Ion Batteries with Ether Electrolyte

Wolfgang Brehm, Aggunda L. Santhosha, Zhenggang Zhang, Christof Neumann, Andrey Turchanin, Andréa Martin, Nicola Pinna, Martin Seyring, Markus Rettenmayr, Johannes R. Buchheim, and Philipp Adelhelm*

Lithium and sodium thiophosphates (and related compounds) have recently attracted attention because of their potential use as solid electrolytes in solid-state batteries. These compounds, however, exhibit only limited stability in practice as they react with the electrodes. The decomposition products partially remain redox active hence leading to excess capacity. The redox activity of thiophosphates is explicitly used to act as electrode for sodium-ion batteries. Copper thiophosphate (Cu₃PS₄) is used as a model system. The storage behavior between 0.01 and 2.5 V versus Na⁺/Na is studied in half cells using different electrolytes with 1 M NaPF₆ in diglyme showing the best result. Cu₃PS₄ shows highly reversible charge storage with capacities of about 580 mAh g⁻¹ for more than 200 cycles @120 mA g⁻¹ and about 450 mAh g⁻¹ for 1400 cycles @1 A g⁻¹. The redox behavior is studied by operando X-ray diffraction and X-ray photoelectron spectroscopy. During initial sodiation, Cu₃PS₄ undergoes a conversion reaction including the formation of Cu and Na₂S. During cycling, the redox activity seems dominated by sulfur. Interestingly, the capacity of Cu₃PS₄ for lithium storage is smaller, leading to about 170 mAh g⁻¹ after 200 cycles. The results demonstrate that thiophosphates can lead to reversible charge storage over several hundred cycles without any notable capacity decay.

1. Introduction

Sodium-ion batteries (NIBs) are currently developed with the aim to provide an alternative to lead–acid and lithium-ion batteries that is based on more abundant and low-cost materials. The progress in the field is frequently summarized in literature.[1,2] For the positive electrodes, the field is especially profiting from the rich chemistry of layered oxides, polyanion compounds and Prussian blue analogues, which allows tuning of the electrode properties.[3] To reduce cost, compounds rich in abundant Mn and Fe are preferred over Co and Ni that dominate the cathode materials for most lithium-ion batteries (LIBs). The composition of the electrolyte solutions is largely adopted from LIBs with carbonates as solvents and NaPF₆ as conductive salt though also ethers are increasingly being studied as well as polymer and inorganic solid electrolytes.[4] Considering potential negative electrodes, however, the materials choice is presently rather limited. Graphite, being the standard material in lithium-ion batteries, can only be applied using solvent cointercalation phenomena in ether electrolytes.[5] The capacity, however, is limited to around 110 mAh g⁻¹ so far and the electrode undergoes large volume changes during cycling.[6] Higher capacities can be achieved in disordered carbons,[7] but much of the capacity is obtained at potentials likely too close to the sodium metal plating potential to enable safe operation. Various titanium oxides and related compounds are of interest too because titanium is quite abundant. The capacities, however, are often well below 200 mAh g⁻¹.[8] From the class of metals and metalloids, only Sn, Sb, and Pb show high storage capacities.[1e,9] While the volume expansion on the electrode level can be

W. Brehm, A. L. Santhosha, Z. Zhang, Dr. J. R. Buchheim,
Prof. P. Adelhelm
Institute of Technical Chemistry and Environmental Chemistry
Friedrich Schiller University Jena
Philosophenweg 7a, Jena 07743, Germany
E-mail: philipp.adelhelm@hu-berlin.de

A. L. Santhosha, Z. Zhang, A. Martin, Prof. N. Pinna, Prof. P. Adelhelm
Institut für Chemie
Humboldt-Universität zu Berlin
Brook-Taylor-Str. 2, Berlin 12489, Germany

C. Neumann, Prof. A. Turchanin
Institute of Physical Chemistry
Friedrich Schiller University Jena
Lessingstraße 10, Jena 07743, Germany

Prof. A. Turchanin, Prof. M. Rettenmayr, Prof. P. Adelhelm
Center for Energy and Environmental Chemistry Jena (CEEC Jena)
Philosophenweg 7a, Jena 07743, Germany

M. Seyring, Prof. M. Rettenmayr
Otto-Schott-Institute of Materials Research
Friedrich Schiller University Jena
Löbdergraben 32, Jena 07743, Germany

**ADVANCED
SCIENCE NEWS**

www.advancedsciencenews.com

**ADVANCED
FUNCTIONAL
MATERIALS**

www.afm-journal.de

effectively buffered by embedding the particles in a carbon matrix, the widespread use might be limited as these elements are not abundant. Moreover, Pb, Sb and their compounds are not environmentally friendly and/or toxic. For high capacity electrodes, this largely leaves conversion electrodes as options.[10] These are based on transition metal compounds, often oxides or sulfides. During sodiation/lithiation, the transition metal is fully reduced along with formation of sodium/lithium oxides or sulfides. Depending on the transition metal and the type of anion (oxides, sulfides, fluorides, ...) used, the properties of these electrodes can strongly vary. Common advantages are very high capacities easily reaching several hundred mAh g^{-1}, while common challenges are sluggish kinetics leading to large voltage hysteresis, volume expansion, and low initial coulombic efficiency (ICE). Moreover, the reaction mechanisms are often nonideal, include amorphous and intermediate phases along with side reactions, see, e.g., results on CuO.[10a,11]

Recently, copper phosphides were investigated because of their very high theoretical volumetric or gravimetric capacities.[12] For example, Zhao et al. reported that CuP$_2$ has a theoretical capacity of q_{th} = 1282 mAh g^{-1}. In Na half cells, the practical storage capacity at 150 mA g^{-1} was about 450 mAh g^{-1} between the 2nd and 30th cycle ($\approx$100% capacity retention). However, strong capacity fading occurred during prolonged cycling leaving only 170 mAh g^{-1} after 100 cycles.[12b] Cu$_3$P shows only a moderate theoretical capacity of 363 mAh g^{-1}, i.e., on par with graphite in lithium-ion batteries, but its volumetric capacity is approximately three times higher (2664 Ah l^{-1} vs 781 Ah l^{-1}). Stan et al. found stable cycling with 220 mAh g^{-1} after 50 cycles.[13]

Copper sulfides (CuS with q_{th} = 560 mAh g^{-1} and Cu$_2$S q_{th} = 337 mAh g^{-1}) are also well known as high capacity storage materials for LIBs and NIBs. Their high intrinsic electronic and ionic conductivity is a great advantage, but cycle life is poor in commonly used carbonate electrolytes.[14] Han et al. for example showed for a carbonate electrolyte a comparably high specific capacity of 582 mAh g^{-1} in the initial cycle, but only 13.8% after the first 10 cycles were retained for a Li half-cell.[15] Moreover, in another study from Debart et al. a similar high capacity value was achieved in the initial cycle, and they observed a drop to about 50 mAh g^{-1} after five cycles, explained by the dissolution of active material in the carbonate electrolyte.[16] Jache et al. could link this strong capacity fade to the electrolyte solvent and showed that the use of carbonates leads to short cycle life while ethers provide long cycle life. Bulk CuS and Cu$_2$S were used for this study, the latter showing the best cycle life.[14b] Using also an ether electrolyte, Wang et al. showed for nanostructured CuS that high capacities between 376 and 447 mAh g^{-1} are obtained for more than 100 cycles at C-rates up to 2C.[17] In case of sodium, Park et al. showed that the theoretical capacity of CuS can be almost reached after a longer activation period of around 100 cycles (0.2C).[18]

The combined use of copper, sulfur and phosphorous leads to the class of copper thiophosphates. Cu (6 $ kg^{-1})[19] and especially P (0.45 $ kg^{-1})[20] and S (0.1 $ kg^{-1})[21] are cost-effective and abundant elements, making them attractive for application. It is interesting to note that lithium/sodium thiophosphates such as Li$_3$PS$_4$ and Na$_3$PS$_4$ are currently highly studied as solid electrolytes (SE) for all solid state batteries thanks to their high room temperature ionic conductivity in the order of $\approx$10^{-4}–10^{-2} S cm^{-1} and their high ductility.[22] Recent results, however, showed that

the solid electrolytes easily decompose in contact with positive and negative electrodes as the theoretical electrochemical stability window is quite narrow.[23] Long-term use of these materials in high voltage batteries therefore requires the formation of suitable interphases that stabilize the electrode–electrolyte contact areas.[22b,e,23b] In analogy to conventional lithium-ion batteries, formation of a solid electrolyte interphase (SEI) is desired, yet this is not a trivial task. Decomposition products of the solid electrolyte, however, can also remain redox active during cycling, hence leading to excess capacity. While this is not necessarily a problem, it can lead to a continuous cell degradation and an overestimation of the storage capacity of the electrode material.[23b] Calculations predicted that the electrochemical stability window for thiophosphate electrolytes is limited by sulfur and by phosphorus redox activity (depending on the redox potential).[23b,24]

Here, we intentionally use a thiophosphate not as solid electrolyte, but instead as electrode material Cu$_3$PS$_4$ is taken as a study case. To the best of our knowledge, the intentional use of thiophosphates as electrode material for NIBs has not been reported yet. Nevertheless, it is important to mention a very recent study by Fan et al., who reported on iron thiophosphite (FePS$_3$) and related compound.[25] According to their results, a composite electrode with reduced graphene oxide was synthesized and showed an initial capacity of about 880 mAh g^{-1} (0.05 A g^{-1}) in a Na half cell, however the ICE was only 48%. After the first cycle the capacity was around 420 mAh g^{-1}. Cycling led to a capacity fade of 58% over 300 cycles leading to 243 mAh g^{-1}. Higher capacities and better cycle life were achieved for lithium with 843 mAh g^{-1} found after 120 cycles. The ICE value was only 59%, however. Similar findings were observed in a study by Edison et al. about tin thiophosphite SnPS$_3$ in a Li half cell.[26] They obtained capacity values >2300 mAh g^{-1} in the initial cycle, but the ICE was even only 38%. However, still a capacity of 532 mAh g^{-1} after 100 cycles (0.1 A g^{-1}) was retained. Although improvement is necessary, these findings are a clear motivation to study the behavior of thiophosphates as electrodes in batteries. An advantage of Cu$_3$PS$_4$ over FePS$_3$ and SnPS$_3$ is the possibility to synthesize the former by simple reactive ball milling, while for the latter two more complex synthesis routes were applied. The Cu$_3$PS$_4$ was first prepared in a ball mill and then subsequently mixed with carbon black in a second ball milling step to prepare a Cu$_3$PS$_4$/C composite. Electrodes of the active material were tested for their sodium storage behavior in half cells. A variety of analytical tools (scanning and transmission electron microscopy (SEM, TEM), X-ray photoelectron spectroscopy (XPS) as well as operando X-ray diffraction (XRD) are applied to study the reaction mechanism. Electrochemical results are compared with the analogue lithium half cells.

2. Results and Discussion

2.1. Materials Characterization

Cu$_3$PS$_4$ was synthesized in a planetary ball mill (PBM) for 24 h at 400 rpm from stoichiometric amounts of Cu, sulfur and P$_2$S$_5$ according to

$$6Cu + P_2S_5 + 3S \rightarrow 2Cu_3PS_4 \tag{1}$$

**ADVANCED
SCIENCE NEWS**
www.advancedsciencenews.com

*ADVANCED
FUNCTIONAL
MATERIALS*
www.afm-journal.de

The reaction product was confirmed by XRD, as shown in **Figure 1**. Cu_3PS_4 crystallizes in an orthorhombic structure and the pattern is well in line with the reference (ICSD: 98-041-2240). Rietveld refinement revealed lattice parameters of $a = 7.254(5)$ Å, $b = 6.305(5)$ Å, $c = 6.041(2)$ Å ($Pmn21$ space group) and a crystallite size of 21 nm, see Figure S1 in the Supporting Information.

Local analysis was done using TEM combined with selected area electron diffraction (SAED), presented in **Figure 2**. The images show that the as-prepared Cu_3PS_4 consisted of polycrystalline agglomerates with high phase purity. SAED pattern and bulk powder XRD pattern are compared in Figure S2 (Supporting Information), showing good agreement. High resolution TEM images in Figure 2c show an interplanar lattice spacing of 3.09 Å (red) corresponding to the (002) planes, i.e., half of the length of the c-axis of the Cu_3PS_4 unit cell. Moreover, 6.39 Å were measured for the interplanar distance of the (100) lattice plane, which is in good agreement with the length of the b-axis of the Cu_3PS_4 unit cell. These results are well in line with the results of the Rietveld refinement of the XRD analysis in Figure 1. Overall, the results confirm that phase pure Cu_3PS_4 was obtained by the ball milling process. An important difference

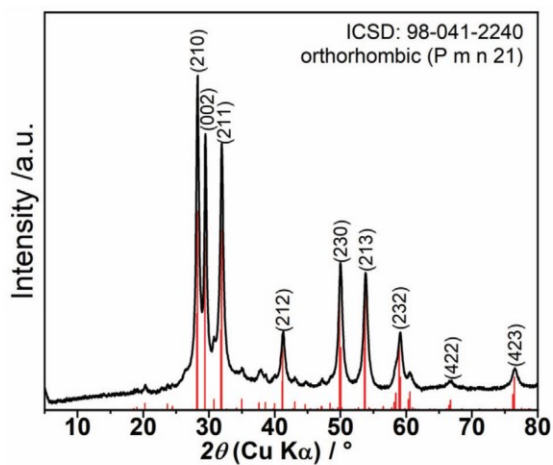**Figure 1.** X-ray diffraction pattern of Cu_3PS_4 powder synthesized by high energy ball milling for 24 h in a planetary ball mill (ICSD: 98-041-2240). The obtained pattern corresponds to an orthorhombic crystal lattice of the $Pmn21$ space group.
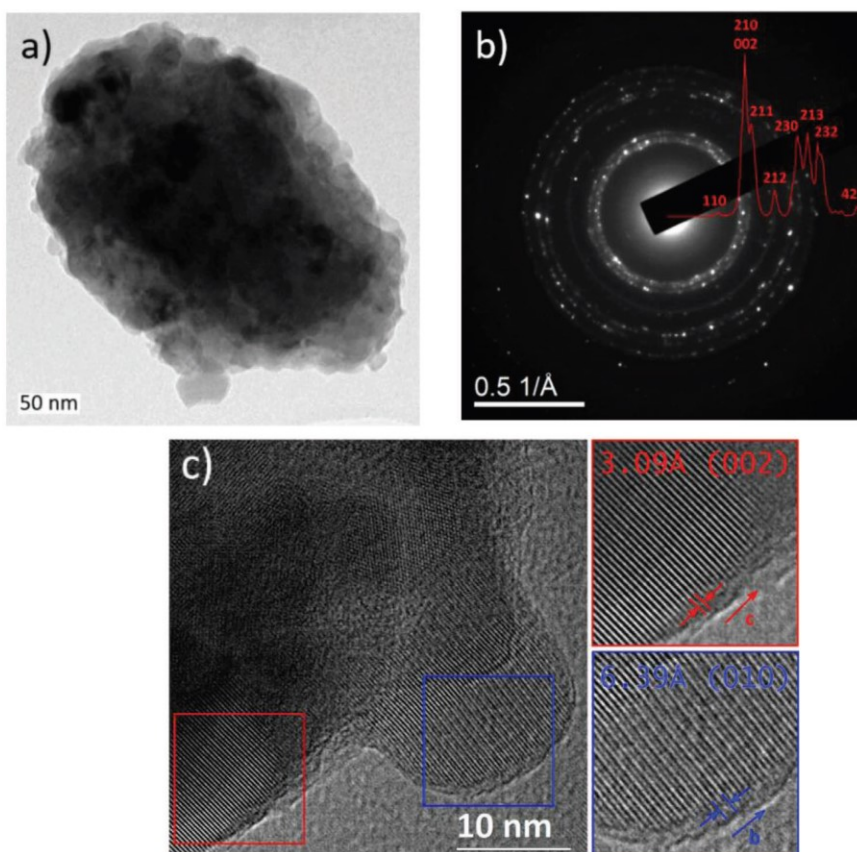

Figure 2. TEM analysis of the Cu_3PS_4 powder: a) single particle image; b) TEM/SAED pattern; c) HRTEM images of agglomerated Cu_3PS_4 crystals.
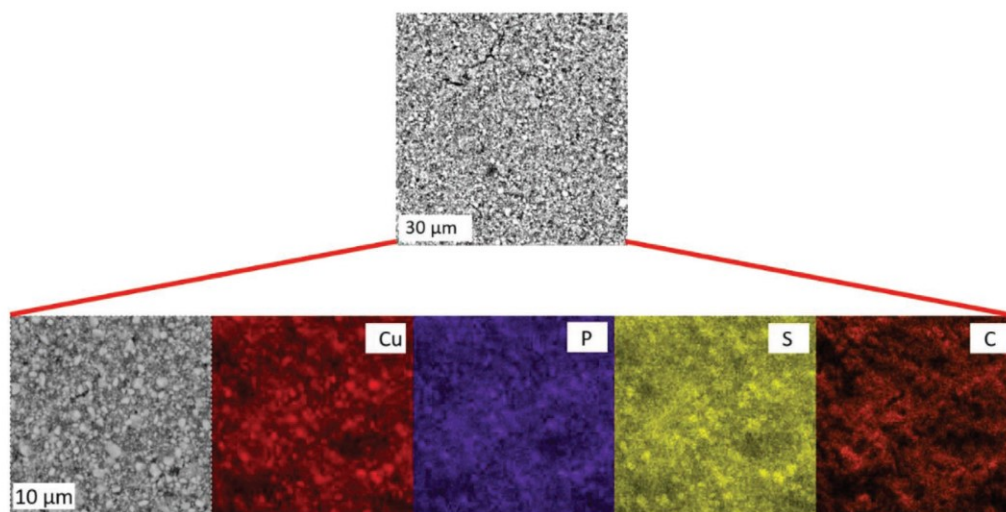
Figure 3. SEM images of the Cu_3PS_4/C composite electrode and EDS elemental mapping.

between Cu_3PS_4 and the thiophosphates Li_3PS_4 and Na_3PS_4 used for solid state batteries is that Cu_3PS_4 is air stable, while the latter compounds are highly hygroscopic, leading to immediate formation of H_2S upon air exposure. Cu_3PS_4 is also stable in ethanol as it was used in photo-electrochemical studies.[12e,27]

The synthesized Cu_3PS_4 was mixed with carbon black as conductive additive (7:3 by weight) in a swing ball mill (SBM) for 12 h (25 Hz) to form a Cu_3PS_4/C composite. Electrodes were then prepared by casting a slurry onto a copper current collector using PVDF as binder. The total composition of the electrode in weight fractions was Cu_3PS_4:C:PVDF = 0.66:0.29:0.05. SEM/EDS images of the electrodes shown in **Figure 3** reveal fine particles up to a few μm in size and a homogenous distribution of all elements suggesting that Cu_3PS_4 was intimately mixed with carbon. This observation is in line with the XRD results. A more detailed view on the particle size and the materials morphology can be seen in the TEM images shown in Figure S3a,b (Supporting Information). The particles presented in Figure S3a (Supporting Information) were captured directly after synthesis in the PBM. The synthesis leads to particles in different sizes ranging from around <100 nm up to about 1 μm. The embedment in the surrounding carbon matrix after the additional ball milling step with carbon can be seen in Figure S3b–d (Supporting Information). Herein, also larger aggregates >1 μm were observed. The particles show an irregular shape as expected, which can be seen with a more detailed view on Figure S3c,d (Supporting Information).

Thickness and loading of the electrodes were around 20 μm (without current collector) and between 1.5–2.2 mg cm^{-2}. Assuming an ideal and full conversion according to

$$Cu_3PS_4 + 11Na \rightleftarrows 3Cu + 4Na_2S + Na_3P \,|\, 843 \text{ mAh g}^{-1} \qquad (2)$$
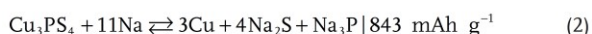
would correspond to a theoretical areal capacity between 2.5–3.7 mAh cm^{-2}. All experiments presented in this manuscript were performed at a current density of 120 mA g^{-1}, using a solution of $NaPF_6$ (1 M) in diglyme as electrolyte.

2.2. Electrochemical Characterization of Cu_3PS_4

Voltage profiles are shown in **Figure 4**a,b. The initial cycle shows a discharge capacity of more than 1030 mAh g^{-1} (1.49 mAh cm^{-2}), followed by a charge capacity of 817 mAh g^{-1}. Sloping voltages and a large hysteresis are observed, which are typical for conversion reactions. However, some distinct features can be seen, which will be discussed further below. The initial coulombic efficiency of 79% indicates an irreversible capacity loss within the initial desodation step. This is also typical for conversion reactions and a result of solid electrolyte interphase formation along with formation of a nanoscopic structure.[10b] The coulombic efficiency values were determined using $\eta_C = \frac{Q_{out}}{Q_{in}} \times 100\%$. As can be seen in **Figure 5**, the capacity further drops in the subsequent cycle by more than 200 mAh g^{-1}. This fading ends after around 25 cycles (≈400 mAh g^{-1}), after which the capacity increases again until the 150th cycle. The gradual activation of the electrode can be also seen from the derivative plots. Figure 4c shows that the peak positions shift during cycling for about 100 cycles after which the situation becomes stable (with a slight average increase of +0.35 mAh g^{-1} between the 100th and 200th cycle). Such a long-term activation over many cycles has been also reported by Park et al. for CuS by using the same electrolyte as in the present study.[18] It is important to note that carbon black also contributes to the storage capacity, see Figure S4 (Supporting Information). The maximum capacity of carbon black after the initial cycle is about 180 mAh g^{-1} in the applied voltage window. This means that the maximum contribution to the electrode is 54 mAh g(Cu_3PS_4)$^{-1}$, i.e., below 10% when considering stable cycling at capacities of around 600 mAh g(Cu_3PS_4)$^{-1}$. We therefore neglect the contribution of carbon black in the following discussion. The derivate plot accentuates voltage plateaus, i.e., the plateau at 1.42 V becomes clearly visible as a strong peak. This feature almost completely disappears upon cycling, being a first hint on some irreversible two-phase process taking place. It is unlikely that

**ADVANCED
SCIENCE NEWS**
www.advancedsciencenews.com

**ADVANCED
FUNCTIONAL
MATERIALS**
www.afm-journal.de
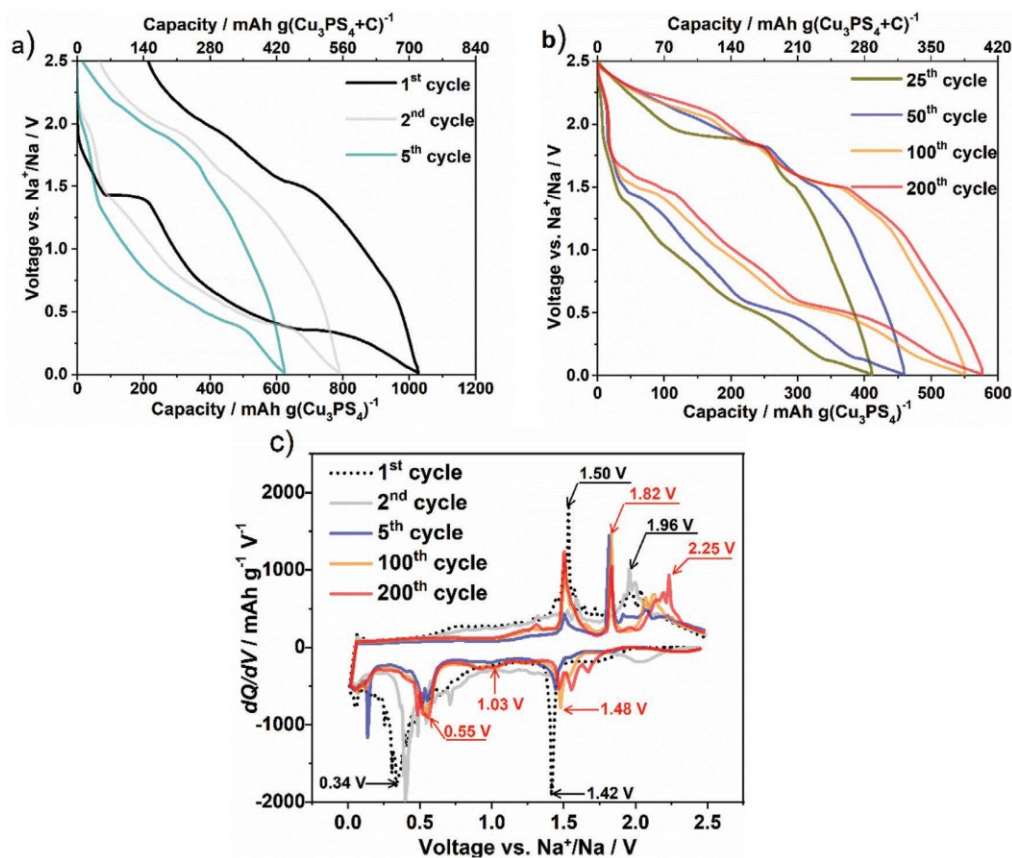
Figure 4. a) Voltage profiles of the 1st, 2nd, and 5th cycle. Cycling was performed with 1 M $NaPF_6$ in diglyme as electrolyte within a voltage window of 0.01–2.5 V versus Na^+/Na with a current density of 120 mA g^{-1}; b) voltage profiles of the 25th, 50th, 100th and 200th cycle; c) capacity derivative curves of the 1st, 2nd, 50th, 100th, and 200th cycle.

this feature relates to electrolyte decomposition as glymes are usually very stable at low potentials versus Na^+/Na. In the subsequent cycles, enhanced activity is found around 2 V. The intensity of the peaks increases upon cycling, indicating that the redox behavior changes. This is in line with the activation of the electrode seen from the galvanostatic measurements.
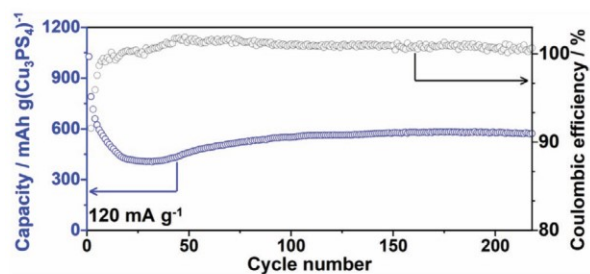
Figure 5. Discharge capacities versus cycle number and the corresponding Coulombic efficiencies for more than 200 cycles. Cycling was performed with 1 M $NaPF_6$ in diglyme as electrolyte within a voltage window of 0.01–2.5 V versus Na^+/Na with a current density of 120 mA g^{-1}.

Without further analysis, a redox activity around 2 V could be due to reduction/oxidation of sulfur and/or polysulfides.[28] The voltage profiles and corresponding derivate plots over 200 cycles show that, although the overall behavior is quite sloping, several steps repeatedly appear, indicating a multistep reaction process. According to the derivative plot, redox plateaus during reduction occur at around 1.5, 1.0, and 0.5 V. Plateaus during oxidation (desodiation) become more distinct during cycling, especially at higher cycling numbers (1.50 and 1.82 V). The third desodiation plateau is developing after around 100 cycles and shifts to voltages of about 2.25 V after 200 cycles. The combined overpotentials vary between about 0.6 to 1.0 V, being similar to many other sulfides/phosphides.[10a,b,18,29] Interestingly, the kinetics improve over cycling as the voltage gap of the hysteresis decreases. This decrease is likely the reason for the gradual increase in electrode capacity, as one can observe in Figure 5. In order to prove the reproducibility of the cycle life test, in total five cells were assembled being successfully cycled at least for 50 times. All of them showed the mentioned activation process reaching capacity values of at least 450 mAh $g(Cu_3PS_4)^{-1}$ so far. The capacities obtained for Cu_3PS_4 are higher than for CuS electrodes and enable enhanced cycling life in comparison

**ADVANCED
SCIENCE NEWS**
www.advancedsciencenews.com

**ADVANCED
FUNCTIONAL
MATERIALS**
www.afm-journal.de

to the well-known CuP_2 when not using complex synthesis methods in order to create composites.[12b,18,30]

We further used impedance spectroscopy to qualitatively follow changes of the electrode during cycling. Figure S5a,b (Supporting Information) shows impedance spectra over several cycles (desodiated state). The overall resistance increases during the early cycles, which is generally associated with an increase in the charge transfer resistance. After that, the total resistance decreases again reaching values of about 10–16 Ω. This observation is in line with the gradual activation of the electrode discussed above.

For comparison, the electrodes were also tested in lithium half cells and with different electrolyte compositions and voltage windows, see Figures S6 and S7 (Supporting Information). In a previous study, we found a very strong influence of the conductive salt on reactions in diglyme based electrolytes, with NaOTf and $NaPF_6$ being preferred for sodium and graphite electrodes.[31] Figure S6 (Supporting Information) shows that, for lithium, the best capacity retention was found for a voltage window between 1–2.5 V versus Li^+/Li, with a capacity of 170 mAh $g(Cu_3PS_4)^{-1}$ retained after 200 cycles at 50 mA g^{-1} using 1 M LiTFSI in diglyme. Figure S7 (Supporting Information) shows results for various electrolyte compositions at two different current densities (50 and 120 mA g^{-1}). It is important to mention that a one-to-one comparison between $NaPF_6$ and $LiPF_6$ in diglyme is not possible as $LiPF_6$ forms solid complexes with diglyme. A similar behavior is found for $LiClO_4$.[32] Moreover, a selected carbonate electrolyte was tested and showed to be not appropriate for the use in Li and Na half cells, concluded from Figure S8 (Supporting Information). Among the various compositions tested, stable cycling at high capacity as well as an activation of the electrode is only found for $NaPF_6$ when using diglyme as solvent. In case of other salts as well as for the lithium half cells, a much lower capacity and rapid fading was observed. While further explanations on this behavior are outside the scope of this manuscript, it is clear that the electrolyte composition is very important for cycling the Cu_3PS_4 electrodes. The differences in electrode performance for varying electrolyte compositions are usually linked to a different solid electrolyte interphase formation. Further optimization of the electrolyte composition may therefore even lead to better results. The improved behavior for diglyme compared to carbonates is well in line with reports on copper sulfides, which also suffer from rapid capacity for the latter solvents.[14b] Interestingly, the sodium cells show higher capacities compared to the lithium cells in the diglyme-based electrolyte. This is also found for conversion reactions with copper diimide (CuNCN)[33] though usually the opposite trend is found, i.e., experimentally determined capacities for conversion reactions with lithium are typically higher than for the analogue reaction with sodium.

2.3. Postmortem Analysis of Cu_3PS_4

The reaction mechanism was studied by X-ray photoelectron spectroscopy (XPS) and (operando) X-ray diffraction. For this, the best performing electrodes, i.e., the electrodes cycled in $NaPF_6$ (1 M) diglyme were chosen. Before discussing the results,

one has to realize that the redox chemistry of thiophosphates is very complex. Considering Cu_3PS_4, the formal oxidation states are Cu(+I), P(+V), and S(−II). During oxidation/reduction, all three elements can be redox active, e.g., Cu(+I) can be reduced to Cu(0) or oxidized to Cu(II), S(−II) can be oxidized to polysulfides S_x^{2-} or S(0), P(+V) may be reduced to P(+IV), P(0) or P(−III) and so on. P_2S_5 may also reappear as compound during the reaction. Moreover, a variety of thiophosphate anions exists, that may form during cycling as well. A discussion on the chemistry of lithium thiophosphates can be found in a review by Ghidiu et al.[34]

As conversion reactions are typically very complex in nature, it is generally difficult to clarify the redox chemistry. Part of the problem is that the reactions are often incomplete and, in many cases, amorphous and intermediate phases are formed. This becomes even more challenging for Cu_3PS_4 as all elements can be redox active. Moreover, the formation of often thick SEIs additionally aggravates the analysis of the bulk electrode. Nevertheless, in the following we attempt to at least confirm or exclude some of the possible reaction products using a more surface (XPS with depth profiling) and a bulk (XRD) sensitive technique. It is known that thiophosphates used as solid electrolytes react when exceeding their electrochemical stability window (≥2 V vs Li^+/Li), leading to excess capacity.[23b] During oxidation, S(0) formation is likely as well as the formation of P_2S_5 or anions like $P_2S_6^{2-}$, $P_2S_7^{4-}$, and $P_2S_8^{4-}$.[23a,c] Further side reactions with these decomposition products can occur during reduction at lower voltages of about 1.5 V, this way forming products like $Li_4P_2S_6$ as well as Li_3P and Li_2S.[23]

For the XPS studies, the pristine electrodes and the cycled electrodes after stabilization (50th cycle sodiated and desodiated state) were compared, see **Figure 6**. Ar^+-sputtering was applied to remove possible surface layers/SEI components (see the Characterization Methods for details). Figure 6a,b shows the high resolution S 2p and P 2p spectra for the pristine electrode. Results on Li_3PS_4 and Ag_3PS_4 served as reference for interpreting the data.[35] The spectra were in good agreement, which is reasonable considering that γ-Li_3PS_4, Ag_3PS_4 and Cu_3PS_4 share the same crystal structure and space group ($Pmn21$). Doublet peaks (energy separation = 1.2 eV) at binding energies (BE) of 162.0 eV for the S2p signal can be related to the transition metal-PS_4^{3-} bondings by comparison with literature data on Li_3PS_4 and Ag_3PS_4. A signal for PS_4^{3-} has been reported at 161.5 eV for Li_3PS_4,[35a] at 163.7 eV for crystalline Ag_3PS_4 and at 162.1 eV for amorphous Ag_3PS_4.[35b] The small deviations between the different thiophosphates are due to the different cations. Another peak at a BE of 163.5 eV was detected, corresponding to sulfur or other P–S compounds.[23c] Qiao et al. explain that amorphization leads to a shift of the P–S–P binding energies to lower values.[35b] Consequently, the overall broad peak related to the S2p signal may be also due to an overlay of crystalline and amorphous Cu_3PS_4. Note that there was no indication for other phases by XRD (Figure 1). Results for the cycled electrode are shown in Figure 6c–f. Figure 6c shows the S 2p spectrum of the electrode after sodiation. The peaks according to the S $2p_{3/2}$ and S $2p_{1/2}$ signals at 161.6 and 162.8 eV can be assigned to Na_2S,[36] which is an expected discharge end product according to Equation (2). This means that the tetrahedral coordinated P−S bonds cleave during sodiation.

**ADVANCED
SCIENCE NEWS**

www.advancedsciencenews.com

**ADVANCED
FUNCTIONAL
MATERIALS**

www.afm-journal.de
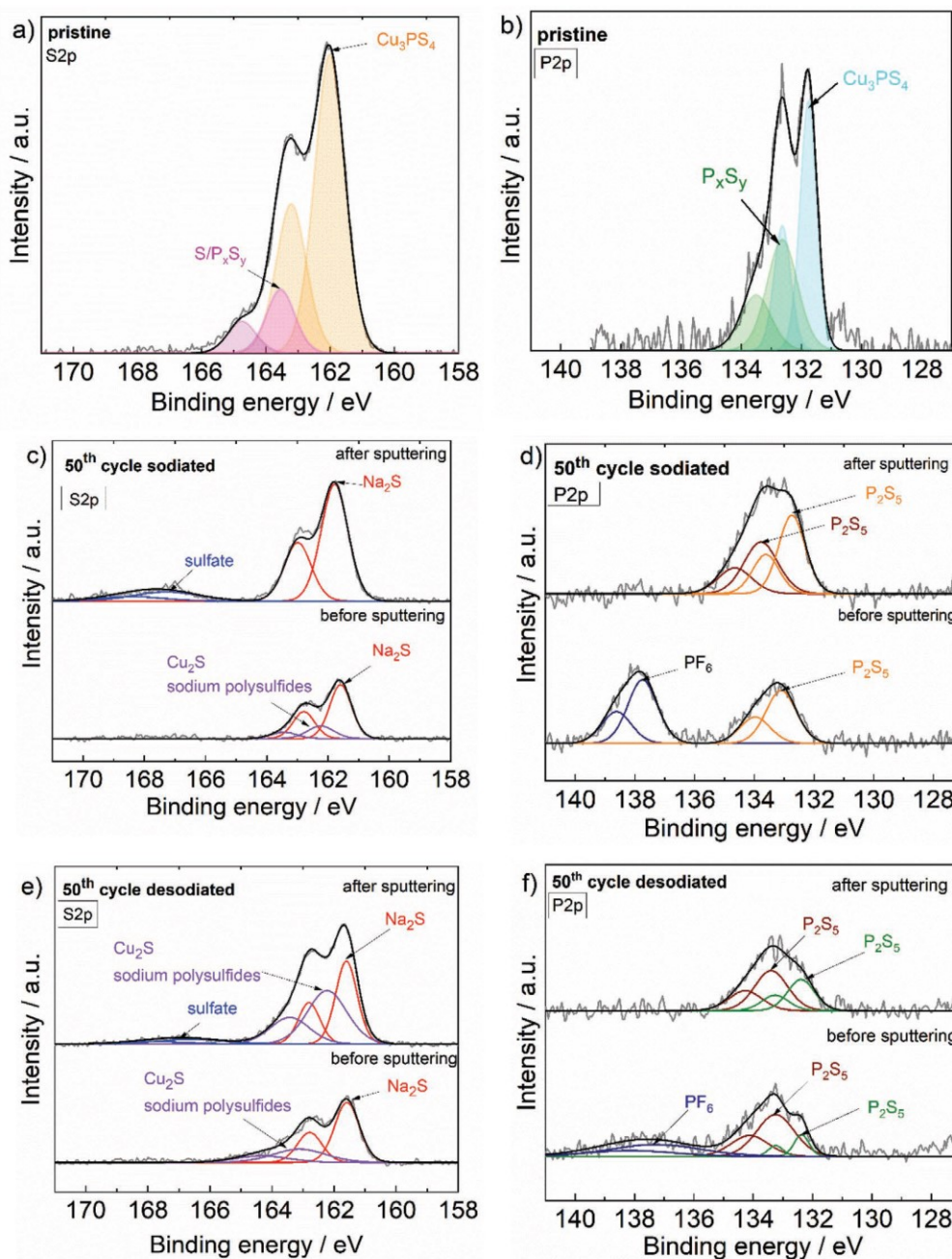
Figure 6. XPS analysis of the S 2p signal for a) pristine Cu_3PS_4; c) the sodiated state of the 50th cycle; e) the desodiated state of the 50th cycle. b,d,f) The corresponding P 2p signals are shown. The sputtering time was 30 min. Cycling was performed at 120 mA g^{-1} in a voltage window of 0.01–2.5 V versus Na$^+$/Na using 1 M NaPF$_6$ in diglyme as electrolyte.

Similarly, the P 2p signal has changed after sodiation, as can be seen in Figure 6d. The vanishing of the species marked in light blue at 131.8 eV (P2p$_{3/2}$) and 132.6 eV (P2p$_{1/2}$), indicates the P–S bond cleavage. This finding is in line with the results by Fan et al. and Edison et al. obtained for FePS$_3$ and SnPS$_3$.[25,26]

Figure 6e shows the S 2p spectrum after subsequent charging (50th cycle, desodiated state). Again, the signature of Na$_2$S can be found. However, the signal is broader, especially after removing the oxidic surface layer by sputtering with Ar$^+$-ions. This is an indication that residues of Na$_2$S remain inactive.[37]

1910583 (7 of 12)

**ADVANCED
SCIENCE NEWS**
www.advancedsciencenews.com

**ADVANCED
FUNCTIONAL
MATERIALS**
www.afm-journal.de

Moreover, more sodium polysulfide compounds might be formed. The occurrence of other charging products such as Cu_3PS_4 or Cu_2S could not be clearly evidenced as the signals from Na polysulfides (161.7 eV/163.3 eV for terminal and central sulfur), PS_4^{3-} (162.1 eV) and Cu_2S (162.6 eV) are overlapping each other.[36,37]

Overall, the S 2p spectrum provides at least proof for the formation and (partial) decomposition of Na_2S during discharging/charging. The XPS data could not be used to confirm formation of elemental copper since the signals of Cu (I) (932.4 eV) and elemental Cu (932.6 eV) in the Cu $2p_{3/2}$ spectrum are extremely close.[38] Nevertheless, the data is shown in Figure S9a,b (Supporting Information). Little evidence for the presence of a small amount of Cu^{2+} (933.8 eV) can be found in the charged electrode, as it can be observed in Figure S9b (Supporting Information). This indicates that some CuO might be present in the sample. However, this contribution can be also due to a CuO impurity that formed during the short air exposure during sample transfer or formed by a side reaction with the diglyme electrolyte.

Figure 6b,d,f shows the results for the P 2p spectra. The pristine material shows a doublet at a BE of 131.8 eV due to PS_4^{3-} (again by comparison with Li_3PS_4).[23c,35a] Furthermore, another P–S bonding species can be seen at 132.6 eV, being either a sign for a local P_xS_y residue which might not have fully reacted to Cu_3PS_4 during synthesis or being due to the above mentioned existence of some amorphous Cu_3PS_4. As sulfur formally remains in the –II state during discharging, phosphorous may be redox active. As the oxidation state of P in Cu_3PS_4 is +V, reduction to lower oxidation states during sodiation is expected. However, formation of Cu_3P could be excluded, because no signal at BEs around 129–130 eV was detected.[39] There was also no evidence for elemental phosphorous, which should show signals at a BE of around 128 eV. The signal at around 133 eV fits to phosphates and thiophosphates, which may have formed due do side reactions or reactions with the electrolyte. The formation of Na_3P as the most likely discharge product (see Equation (2)) could not be confirmed. However, the corresponding binding energy at around 127 eV overlaps with signals of the Cu 3s spectrum at 126 eV, therefore complicating the analysis. Due to this overlap, no data <127 eV were acquired. Nevertheless, substantial formation of Na_3P during discharging can be excluded from the XPS data. After sodiation, P_2S_5 could be detected at 133.7 eV.[40] However, as formation of P_2S_5 cannot account for the large capacity values determined, it is expected to be only a minor component of the electrode. Consequently, the redox activity of phosphorus cannot be clearly clarified via XPS, but phosphorus could be evidenced as oxidized species with an oxidation state larger than zero in the sodiated and in the desodiated state as well. Dietrich et al. demonstrated that the occurrence of Li_2S in presence of P_2S_5 influences the P–S–P binding energy due to acting polarization forces.[40] Thus, we may observe an analogue case for Na, i.e., an overlay of shifted binding energies between 132–134 eV derived from P_2S_5 due to the presence of Na_2S is likely.

Before sputtering, the spectra of F 1s (687.7 eV) and P 2p (137.7 eV) show presence of PF_6^-, which remains from the conductive salt. The signals disappear by sputtering, indicating the conductive salt residues are located close to the electrode surface. Figure S9c,d (Supporting Information) shows evidence for NaF at a BE of 684.7 eV in the F 1s spectrum, which is an expected product of SEI formation.

The analysis by XPS leads to the following conclusions for the redox reactions after electrode activation (50th cycle): a) After sodiation as well as after desodiation, the presence of Cu_3P, Na_3P, P(0) and S(0) can be excluded; b) sodiation leads to formation of Na_2S, but not all of it disappears during desodiation; c) PS_4^{3-} could not be observed, meaning that Cu_3PS_4 is not an active compound during cycling, so it is irreversibly decomposed during electrode activation. However, very little P_2S_5 may be present; d) small amounts of Cu_2S in overlay with Na polysulfides may be present.

2.4. Operando XRD Analysis of Cu_3PS_4

Figure 7a shows operando XRD results for the 1st cycle. Upon sodiation, the Cu_3PS_4 reflections immediately start to disappear. This process is clearly linked to the voltage plateau at 1.4 V versus Na^+/Na. This plateau only appears during the first sodiation process, see also Figure 4a indicating that the structure of Cu_3PS_4 is irreversibly converted. At the same time, reflections due to Na_2S and Cu become more intense, which can be more clearly seen from the patterns after complete discharge and charge, looking at Figure 7b. The Na_2S signal intensity continuously increases with the degree of sodiation, reaching its maximum at the end of the discharge at 0.01 V versus Na^+/Na. This indicates that Na_2S continuously forms during sodiation. During subsequent desodiation (charging), the intensity of the reflections continuously decreases, yet complete disappearance does not take place. This indicates a partial reversibility of the Na_2S conversion during cycling, well in line with the XPS findings. Charge products could be polysulfides or elemental sulfur (the former being confirmed by XPS). Formation and disappearance of Na_2S could be also found in the 2nd cycle (cf. Figure 7b). Only minor changes in the intensity of the Cu (111) reflection are observed within the 2nd cycle, indicating a very small, if any, redox activity of copper during cycling, looking at Figures S10 and S11 (Supporting Information). The results therefore indicate that the high storage capacity of the electrode is due to sulfur redox. Also phosphorous might contribute, but neither XPS nor XRD could provide any evidence for this.

Considering this, the first cycle is clearly very different from all the others. As sulfur in Cu_3PS_4 is already in its fully reduced state, the initial sodiation capacity is largely linked to reduction of Cu^+ to Cu(0). Sulfur then becomes redox active during the first desodiaton step. In view of the very good cycle life for an electrode based on sulfur redox, one may therefore speculate that the formed copper nevertheless plays a role in improving the behavior of the electrode. This might be because the formed copper improves the local electronic conductivity and because copper can trap polysulfides (by forming, e.g., CuS and Cu_2S) that would otherwise dissolve into the electrolyte. Copper sulfides could also reversibly store charge in this electrolyte;[14b,18] however, XRD clearly shows that most of the copper remains in its metal state during cycling. The dominant role of the sulfur redox can also be rationalized from the experimentally determined capacity values which reach about
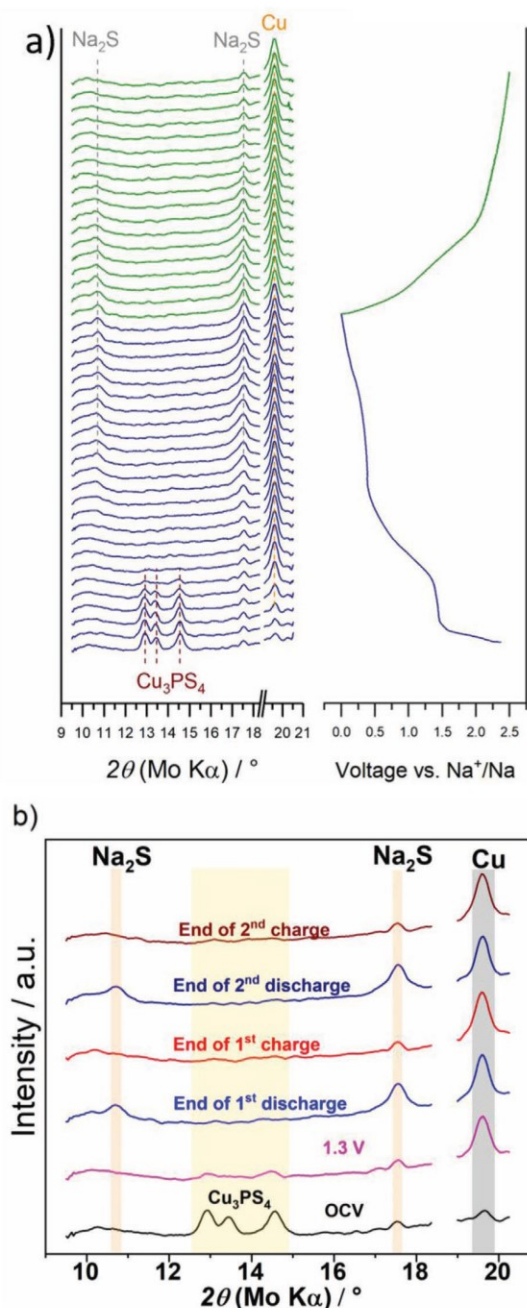
**ADVANCED
SCIENCE NEWS**
www.advancedsciencenews.com

**ADVANCED
FUNCTIONAL
MATERIALS**
www.afm-journal.de

Figure 7. Operando XRD analysis after a) the initial sodiation and desodiation step. The crystalline nature of Cu_3PS_4 vanishes and Cu as well as Na_2S signals increase during sodiation. The measurement was performed continuously during recording the diffraction patterns. b) XRD patterns after completed sodiation and desodiation of the initial 2 cycles. Following references were used: Cu_3PS_4: ICSD: 98-041-2240 with the (210), (002) and (211) plane; Na_2S: ICSD: 98-006-0436 with the (111) and (022) plane and Cu: ICSD: 98-005-3755 with the (111) plane. Cycling was performed at 120 mA g^{-1} in a voltage window of 0.01–2.5 V versus Na$^+$/Na using 1 M NaPF$_6$ in diglyme as electrolyte.

580 mAh g^{-1} after more than 200 cycles. Assuming solely sulfur redox between S^{2-} and S^0, the capacity of the electrode (with the formal composition of Cu_3PS_4) would be 613 mAh g(Cu_3PS_4)$^{-1}$, i.e., the values are close to each other.

Finally, it is also worth noting that the long cycle life shown in Figure 5 implies that dissolution of the electrode components does not take place. This is not necessarily expected, as for example Na_2S in combination with P_2S_5 shows a high solubility in diglyme (the individual compounds do not).[41] Dissolution of the active material would lead to a rapid capacity fading. As XPS and XRD both provide evidence for Na_2S formation, the long cycle life directly implies that P_2S_5 does not occur in larger amounts during cycling.

2.5. Rate Performance and High Current Stability

Rate capability measurements are shown in **Figure 8**a. Even at current densities as high as 5 A g^{-1}, values around 350 mAh g^{-1} were obtained. After decreasing the current density again to 120 mA g^{-1}, the capacity recovered to values of about 600 mAh g^{-1}. The voltage profiles at different current densities are shown in Figure S12 (Supporting Information). Figure 8b shows the cycling stability test at a current rate of 1 A g^{-1}. The storage capacity exceeded more than 400 mAh g^{-1} even after 1400 cycles, indicating that the redox processes (after stabilization of the electrode) are highly reversible. Coulombic efficiency values obtained were ≈100% over the whole study. Selected voltage profiles and derivative plots are compared in Figure 8c,d and show that the redox behavior remains nearly constant over the long term test. Overall, compared to FePS$_3$,[25] Cu_3PS_4 performs better with respect to rate capability, cycling stability as well as capacity when cycled toward sodium.

3. Conclusion

The use of copper thiophosphate (Cu_3PS_4) as electrode for sodium-ion batteries was explored. Cu_3PS_4 was synthesized by reactive ball milling from Cu, sulfur and P_2S_5 and tested in half cells between 0.01 and 2.5 V versus Na$^+$/Na. Different electrolytes were tested with NaPF$_6$ (1 M) in diglyme, showing the best behavior. At 1 A g^{-1}, capacity values of around 450 mAh g^{-1} were obtained for more than 1400 cycles, indicating excellent reversibility of the reaction. The redox behavior was analyzed using (operando) XRD and XPS with depth profiling. During initial sodiation, Cu_3PS_4 undergoes a conversion reaction including the formation of copper and Na_2S. The PS$_4^{3-}$ tetrahedrons are cleaved. During cycling, the redox activity is dominated by sulfur redox likely between S^{2-} and polysulfides S$_x^{2-}$. Some Na_2S seems to remain inactive during cycling, however. Copper seems to contribute to a minor degree during charge storage as Cu metal is found in the charged and discharged state; however, the intensities of the XRD reflections slightly vary during cycling. The role of phosphorous remains unclear so far. NMR spectroscopy may provide further information on this in the future. Overall, the processes appear highly reversible.
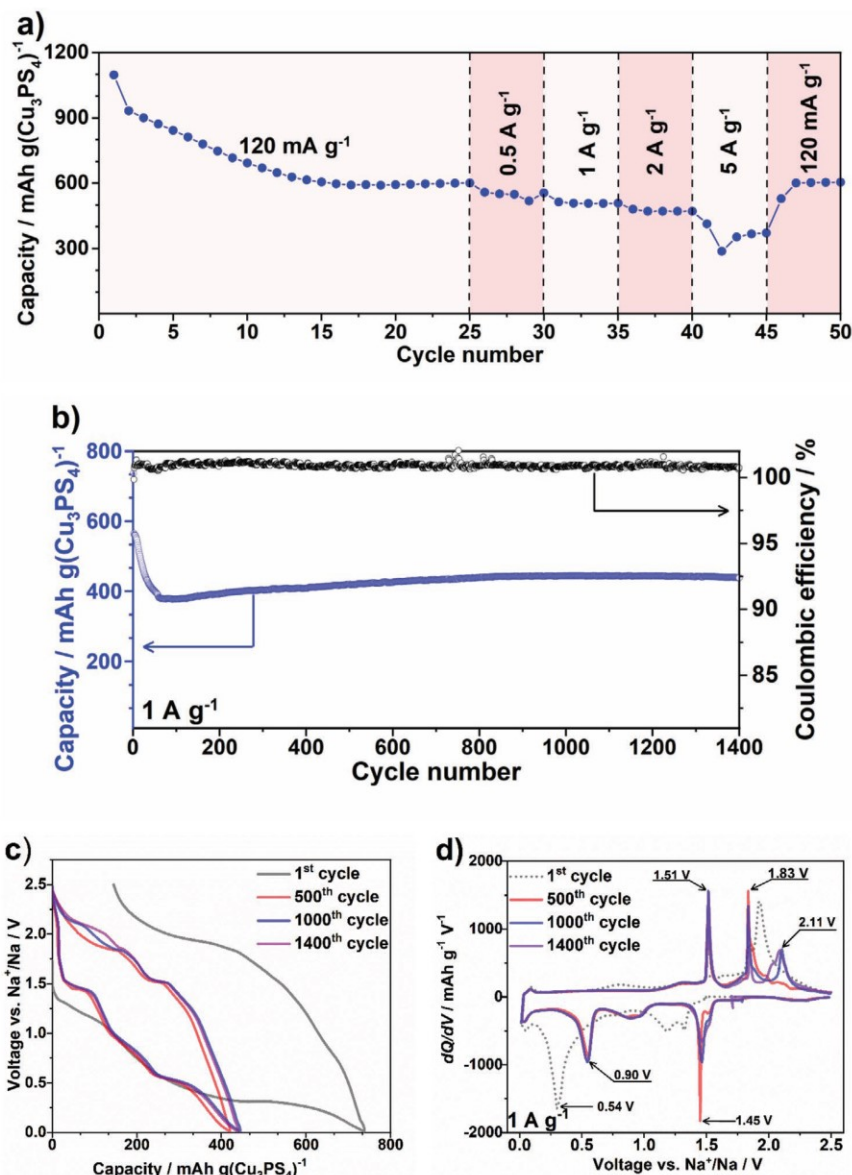
Figure 8. a) Rate capability for a Cu_3PS_4/C electrode with 1 M $NaPF_6$ in diglyme for a voltage window of 0.01–2.5 V; b) High current rate cycling performance test for a Cu_3PS_4/C electrode with 1 M $NaPF_6$ in diglyme for a voltage window of 0.01–2.5 V at 1 A g^{-1}; c) corresponding voltage profiles and d) capacity derivatives.

The remaining Cu metal may aid the electronic wiring of the electrode and act as a polysulfide trap, thereby improving cycle life. Reference experiments with the analogue lithium cell showed that the storage capacity of Cu_3PS_4 is higher for sodium. The lower voltage limit for achieving stable cycling is higher for Li ($\approx$1 V vs Li$^+$/Li) compared to sodium (0.01 V vs Na$^+$/Na). Finally, we also demonstrated that the storage capacity of Cu_3PS_4 electrodes is higher compared to Cu_2S, CuS, Cu_3P, and $FePS_3$ and shows better cycling stability than Cu_3P, $FePS_3$ and CuP_2 electrodes.

4. Experimental Section

Preparation of the Electrodes: Commercial Cu particles (<425 μm, 99.5% purity), P_2S_5 (99% purity), and sulfur (99.5% purity) from Sigma Aldrich were used as active materials and were put in appropriate stoichiometric ratios into zirconia jars. 5 g of the raw materials were ball milled in a planetary ball mill (PBM, Fritsch Pulverisette 7) for 24 h at 400 rpm with a jar volume of 80 mL as well as in a subsequent step in a swing ball mill (SBM, Retsch MM 400) for 12 h with a jar volume of 10 mL applying a frequency of 25 Hz, this way forming a composite with carbon. Cu_3PS_4 to carbon weight ratio was set to 7:3. For the use of both ball mills, the ball to powder weight ratio was set to 10:1.

1910583 (10 of 12)

Electrode Preparation: A slurry, using 5 wt% of PVDF binder related to the total weight of Cu_3PS_4 powder was prepared in an NMP solution in an MBraun Glovebox under Ar atmosphere. The slurry was casted with a doctor blade by hand onto a copper foil (Schlenk) under inert conditions and the electrodes were cut into spherical 12 mm diameter pieces and dried in a vacuum tube oven at 70 °C overnight. The finally obtained active mass loadings varied between 1.5–2.2 mg cm^{-2}.

Characterization Methods: XRD analysis of the Cu_3PS_4 electrodes and powders was performed with a Bruker Phaser D2 diffractometer using Cu Kα radiation (0.02° step width and 20 s step time). XPS of the Cu_3PS_4/C electrodes was performed using a multiprobe system (Scienta Omicron) with a monochromatic X-ray source (Al Kα) and an electron analyzer (Argus CU) with an 0.6 eV spectral energy resolution. The spectra were fitted using Voigt functions after background subtraction. In order to remove the thin surface layer, consisting of salt rests and oxidized species, the samples were sputtered in the same multiprobe system using Ar$^+$ ions (FOCUS FDG150, 1 keV, 10 mA) for 30 min. This corresponds to an approximate sputter depth of 15 nm. Longer sputter times did not change the spectra. TEM specimens were prepared by dispersing the powder in ethanol in an ultrasonic bath and placing onto a holey carbon copper grid. The structural features of the Cu_3PS_4 nanoparticles were studied by high-resolution transmission electron microscopy (HRTEM) and selected area electron diffraction in a JEOL JEM 3010HT operating at 300 kV that is equipped with a LaB$_6$ filament and a 1k × 1k GATAN multi scan CCD-camera. TEM investigations for getting information about the particle size (Figure S3a,b, Supporting Information) were carried out on a Philips CM200 LaB$_6$ operated at an acceleration voltage of 200 kV.

The operando XRD measurement was performed on an STOE Stadi MP diffractometer equipped with a Dectris Mythen 1K linear silicon strip detector and Ge(111) double-crystal monochromator (Mo Kα1 radiation) in a Bragg–Brentano geometry on a specifically developed operando half cell.[42] One XRD pattern was recorded every hour and the operando cell was cycled at C/20 in order to obtain one XRD pattern every 0.3 sodium atoms reacted per formula unit.

Electrochemical tests: Electrolytes were prepared by dissolving NaPF$_6$ (1 M) from Alfa Aesar in diglyme (Sigma Aldrich). Diglyme was dried over a molecular sieve (4 Å, Sigma Aldrich) to ensure the water content to be lower than 20 ppm, confirmed by Karl-Fisher titration. Other electrolyte solutions were prepared in the same way. Electrochemical measurements were performed in C2032 coin cells, using 2 pieces of glass microfiber filters (Whatman, GF/A) as separator and Na metal (BASF SE) as counter electrode. The electrochemical experiments were performed with a Biologic MPG2 and a BCS galvanostat/potentiostat. Reproducibility of the results was assured by cycling in total more than 20 cells. Impedance tests were carried out in beaker cells (two electrode system) and measured using a Biologic SP150 galvanostat/potentiostat.

Supporting Information

Supporting Information is available from the Wiley Online Library or from the author.

Conflict of Interest

The authors declare no conflict of interest.

[1] a) P. K. Nayak, L. Yang, W. Brehm, P. Adelhelm, *Angew. Chem., Int. Ed.* **2018**, *57*, 102; b) S.-W. Kim, D.-H. Seo, X. Ma, G. Ceder, K. Kang, *Adv. Energy Mater.* **2012**, *2*, 710; c) D. Kundu, E. Talaie, V. Duffort, L. F. Nazar, *Angew. Chem., Int. Ed.* **2015**, *54*, 3431; d) M. D. Slater, D. Kim, E. Lee, C. S. Johnson, *Adv. Funct. Mater.* **2013**, *23*, 947; e) N. Yabuuchi, K. Kubota, M. Dahbi, S. Komaba, *Chem. Rev.* **2014**, *114*, 11636; f) H. Pan, Y.-S. Hu, L. Chen, *Energy Environ. Sci.* **2013**, *6*, 2338; g) M. H. Han, E. Gonzalo, G. Singh, T. Rojo, *Energy Environ. Sci.* **2015**, *8*, 81.

[2] a) M. Li, Z. Du, M. A. Khaleel, I. Belharouak, *Energy Storage Mater.* **2020**, *25*, 520; b) H. Zhang, Y. Huang, H. Ming, G. Cao, W. Zhang, J. Ming, R. Chen, *J. Mater. Chem. A* **2020**, *8*, 1604.

[3] a) K. Kubota, S. Kumakura, Y. Yoda, K. Kuroki, S. Komaba, *Adv. Energy Mater.* **2018**, *8*, 1703415; b) B. Senthilkumar, C. Murugesan, L. Sharma, S. Lochab, P. Barpanda, *Small Methods* **2018**, *3*, 1800253; c) J. Qian, C. Wu, Y. Cao, Z. Ma, Y. Huang, X. Ai, H. Yang, *Adv. Energy Mater.* **2018**, *8*, 1702619.

[4] a) G. Piana, M. Ricciardi, F. Bella, R. Cucciniello, A. Proto, C. Gerbaldi, *Chem. Eng. J.* **2020**, *382*, 122934; b) J. Zhang, D.-W. Wang, W. Lv, L. Qin, S. Niu, S. Zhang, T. Cao, F. Kang, Q.-H. Yang, *Adv. Energy Mater.* **2018**, *8*, 1801361; c) J. Yang, H. Zhang, Q. Zhou, H. Qu, T. Dong, M. Zhang, B. Tang, J. Zhang, G. Cui, *ACS Appl. Mater. Interfaces* **2019**, *11*, 17109; d) F. Bella, F. Colo, J. R. Nair, C. Gerbaldi, *ChemSusChem* **2015**, *8*, 3668; e) J.-J. Kim, K. Yoon, I. Park, K. Kang, *Small Methods* **2017**, *1*, 1700219.

[5] a) Y. Li, Y. Lu, P. Adelhelm, M. M. Titirici, Y. S. Hu, *Chem. Soc. Rev.* **2019**, *48*, 4655; b) B. Jache, P. Adelhelm, *Angew. Chem., Int. Ed.* **2014**, *53*, 10169.

[6] M. Goktas, C. Bolli, E. J. Berg, P. Novák, K. Pollok, F. Langenhorst, M. v. Roeder, O. Lenchuk, D. Mollenhauer, P. Adelhelm, *Adv. Energy Mater.* **2018**, *8*, 1702724.

[7] a) W. Luo, F. Shen, C. Bommier, H. Zhu, X. Ji, L. Hu, *Acc. Chem. Res.* **2016**, *49*, 231; b) X. Dou, I. Hasa, D. Saurel, C. Vaalma, L. Wu, D. Buchholz, D. Bresser, S. Komaba, S. Passerini, *Mater. Today* **2019**, *23*, 87; c) C. Bommier, X. Ji, *Isr. J. Chem.* **2015**, *55*, 486.

[8] a) P. Senguttuvan, G. Rousse, V. Seznec, J.-M. Tarascon, M. R. Palacín, *Chem. Mater.* **2011**, *23*, 4109; b) L. Wu, D. Buchholz, D. Bresser, L. Gomes Chagas, S. Passerini, *J. Power Sources* **2014**, *251*, 379; c) S. K. Das, B. Jache, H. Lahon, C. L. Bender, J. Janek, P. Adelhelm, *Chem. Commun.* **2016**, *52*, 1428; d) X. Ma, K. An, J. Bai, H. Chen, *Sci. Rep.* **2017**, *7*, 162; e) F. Bella, A. B. Munoz-Garcia, F. Colo, G. Meligrana, A. Lamberti, M. Destro, M. Pavone, C. Gerbaldi, *ACS Omega* **2018**, *3*, 8440.

[9] a) W. Brehm, J. R. Buchheim, P. Adelhelm, *Energy Technol.* **2019**, *7*, 1900389; b) T. Palaniselvam, M. Goktas, B. Anothumakkool, Y. N. Sun, R. Schmuch, L. Zhao, B. H. Han, M. Winter, P. Adelhelm, *Adv. Funct. Mater.* **2019**, *29*, 1900790; c) L. Xiao, Y. Cao, J. Xiao, W. Wang, L. Kovarik, Z. Nie, J. Liu, *Chem. Commun.* **2012**, *48*, 3321; d) A. Darwiche, R. Dugas, B. Fraisse, L. Monconduit, *J. Power*

ADVANCED
SCIENCE NEWS
www.advancedsciencenews.com

ADVANCED
FUNCTIONAL
MATERIALS
www.afm-journal.de

Sources **2016**, *304*, 1; e) V. L. Chevrier, G. Ceder, *J. Electrochem. Soc.* **2011**, *158*, A1011; f) H. Xie, X. Tan, E. J. Luber, B. C. Olsen, W. P. Kalisvaart, K. L. Jungjohann, D. Mitlin, J. M. Buriak, *ACS Energy Lett.* **2018**, *3*, 1670.

[10] a) F. Klein, B. Jache, A. Bhide, P. Adelhelm, *Phys. Chem. Chem. Phys.* **2013**, *15*, 15876; b) J. Cabana, L. Monconduit, D. Larcher, M. R. Palacin, *Adv. Mater.* **2010**, *22*, E170; c) K. Cao, T. Jin, L. Yang, L. Jiao, *Mater. Chem. Front.* **2017**, *1*, 2213.

[11] F. Klein, R. Pinedo, P. Hering, A. Polity, J. Janek, P. Adelhelm, *J. Phys. Chem. C* **2016**, *120*, 1400.

[12] a) C. Kim, H. Kim, Y. Choi, H. A. Lee, Y. S. Jung, J. Park, *ACS Omega* **2018**, *3*, 7655; b) F. Zhao, N. Han, W. Huang, J. Li, H. Ye, F. Chen, Y. Li, *J. Mater. Chem. A* **2015**, *3*, 21754; c) S. Liu, X. He, J. Zhu, L. Xu, J. Tong, *Sci. Rep.* **2016**, *6*, 35189; d) J. Zhu, Q. He, Y. Liu, J. Key, S. Nie, M. Wu, P. K. Shen, *J. Mater. Chem. A* **2019**, *7*, 16999; e) E. J. Sheets, W.-C. Yang, R. B. Balow, Y. Wang, B. C. Walker, E. A. Stach, R. Agrawal, *J. Mater. Res.* **2015**, *30*, 3710.

[13] M. C. Stan, R. Klöpsch, A. Bhaskar, J. Li, S. Passerini, M. Winter, *Adv. Energy Mater.* **2013**, *3*, 231.

[14] a) Z. Hu, Q. Liu, S. L. Chou, S. X. Dou, *Adv. Mater.* **2017**, *29*, 1700606; b) B. Jache, B. Mogwitz, F. Klein, P. Adelhelm, *J. Power Sources* **2014**, *247*, 703.

[15] Y. Han, Y. Wang, W. Gao, Y. Wang, L. Jiao, H. Yuan, S. Liu, *Powder Technol.* **2011**, *212*, 64.

[16] A. Débart, L. Dupont, R. Patrice, J. M. Tarascon, *Solid State Sci.* **2006**, *8*, 640.

[17] Y. Wang, X. Zhang, P. Chen, H. Liao, S. Cheng, *Electrochim. Acta* **2012**, *80*, 264.

[18] J. Y. Park, S. J. Kim, J. H. Chang, H. K. Seo, J. Y. Lee, J. M. Yuk, *Nat. Commun.* **2018**, *9*, 922.

[19] Deutsche Rohstoffagentur, Preistrendmonitor, https://www.deutsche-rohstoffagentur.de/DE/Themen/Min_rohstoffe/Produkte/Preistrendmonitor/Preistrendmonitor-2019_06.pdf?__blob=publicationFile&v=4 (accessed: February 2020).

[20] Bildungsministerium fuer Bildung und Forschung, Phosphor-recycling–Abwasser und Klärschlamm als Quelle eines wert-vollen Stoffs, http://ressourcewasser.fona.de/reports/bmbf/annual/2010/nb/German/401050/-2_1_05-phosphorrecycling-abwasser-und-klaerschlamm-als-quelle-eines-wertvollen-stoffs.html (accessed: February 2020).

[21] E. Sesay, TFI '19: Sulphur sentiment dampened by weak down-stream demand, high stocks, https://www.icis.com/explore/resources/news/2019/09/20/10420493/tfi-19-sulphur-sentiment-dampened-by-weak-downstream-demand-high-stocks (accessed: February 2020).

[22] a) K. Xu, *Chem. Rev.* **2014**, *114*, 11503; b) T. Famprikis, P. Canepa, J. A. Dawson, M. S. Islam, C. Masquelier, *Nat. Mater.* **2019**, *18*, 1278; c) Z. Liu, W. Fu, E. A. Payzant, X. Yu, Z. Wu, N. J. Dudney, J. Kiggans, K. Hong, A. J. Rondinone, C. Liang, *J. Am. Chem. Soc.* **2013**, *135*, 975; d) Z. Ma, H.-G. Xue, S.-P. Guo, *J. Mater. Sci.* **2018**, *53*, 3927; e) Ö. U. Kudu, T. Famprikis, B. Fleutot, M.-D. Braida, T. Le Mercier, M. S. Islam, C. Masquelier, *J. Power Sources* **2018**, *407*, 31; f) T. Famprikis, J. A. Dawson, F. Fauth, O. Clemens, E. Suard, B. Fleutot, M. Courty, J.-N. Chotard, M. S. Islam, C. Masquelier, *ACS Mater. Lett.* **2019**, *1*, 641; g) A. L. Santhosha, P. K. Nayak, K. Pollok, F. Langenhorst, P. Adelhelm, *J. Phys. Chem. C* **2019**, *123*, 12126.

[23] a) R. Koerver, F. Walther, I. Aygün, J. Sann, C. Dietrich, W. G. Zeier, J. Janek, *J. Mater. Chem. A* **2017**, *5*, 22750; b) G. F. Dewald, S. Ohno, M. A. Kraft, R. Koerver, P. Till, N. M. Vargas-Barbosa, J. Janek, W. G. Zeier, *Chem. Mater.* **2019**, *31*, 8328; c) D. H. S. Tan, E. A. Wu, H. Nguyen, Z. Chen, M. A. T. Marple, J.-M. Doux, X. Wang, H. Yang, A. Banerjee, Y. S. Meng, *ACS Energy Lett.* **2019**, *4*, 2418; d) T. Hakari, M. Nagao, A. Hayashi, M. Tatsumisago, *J. Power Sources* **2015**, *293*, 721; e) N. Tanibata, M. Deguchi, A. Hayashi, M. Tatsumisago, *Chem. Mater.* **2017**, *29*, 5232.

[24] a) F. Han, Y. Zhu, X. He, Y. Mo, C. Wang, *Adv. Energy Mater.* **2016**, *6*, 1501590; b) B. V. Lotsch, J. Maier, *J. Electroceram.* **2017**, *38*, 128; c) Y. Zhu, X. He, Y. Mo, *ACS Appl. Mater. Interfaces* **2015**, *7*, 23685; d) Y. Zhu, X. He, Y. Mo, *J. Mater. Chem. A* **2016**, *4*, 3253.

[25] C.-Y. Fan, X.-H. Zhang, Y.-H. Shi, H.-Y. Xu, J.-P. Zhang, X.-L. Wu, *J. Mater. Chem. A* **2019**, *7*, 1529.

[26] E. Edison, A. Chaturvedi, H. Ren, S. Sreejith, C. T. Lim, S. Madhavi, *ACS Appl. Energy Mater.* **2018**, *1*, 5772.

[27] X. Yin, S. A. McClary, Z. Song, D. Zhao, B. Graeser, C. Wang, N. Shrestha, X. Wang, C. Chen, C. Li, K. K. Subedi, R. J. Ellingson, W. Tang, R. Agrawal, Y. Yan, *J. Mater. Chem. A* **2019**, *7*, 4604.

[28] L. Medenbach, P. Adelhelm, *Top. Curr. Chem.* **2017**, *375*, 81.

[29] M. Fan, Y. Chen, Y. Xie, T. Yang, X. Shen, N. Xu, H. Yu, C. Yan, *Adv. Funct. Mater.* **2016**, *26*, 5019.

[30] a) J. Li, D. Yan, T. Lu, W. Qin, Y. Yao, L. Pan, *ACS Appl. Mater. Interfaces* **2017**, *9*, 2309; b) S. Kaushik, J. Hwang, K. Matsumoto, Y. Sato, R. Hagiwara, *ChemElectroChem* **2018**, *5*, 1340.

[31] M. Goktas, C. Bolli, J. Buchheim, E. J. Berg, P. Novak, F. Bonilla, T. Rojo, S. Komaba, K. Kubota, P. Adelhelm, *ACS Appl. Mater. Interfaces* **2019**, *11*, 32844.

[32] J. Grondin, *Solid State Ionics* **2004**, *166*, 441.

[33] A. Eguia-Barrio, E. Castillo-Martínez, F. Klein, R. Pinedo, L. Lezama, J. Janek, P. Adelhelm, T. Rojo, *J. Power Sources* **2017**, *367*, 130.

[34] M. Ghidiu, J. Ruhl, S. P. Culver, W. G. Zeier, *J. Mater. Chem. A* **2019**, *7*, 17735.

[35] a) A. Kato, H. Kowada, M. Deguchi, C. Hotehama, A. Hayashi, M. Tatsumisago, *Solid State Ionics* **2018**, *322*, 1; b) A. Qiao, H. Tao, Y. Yue, *J. Non-Cryst. Solids* **2019**, *521*, 119476.

[36] C.-H. Kuo, Y.-T. Chu, Y.-F. Song, M. H. Huang, *Adv. Funct. Mater.* **2011**, *21*, 792.

[37] M. Fantauzzi, B. Elsener, D. Atzei, A. Rigoldi, A. Rossi, *RSC Adv.* **2015**, *5*, 75953.

[38] A. V. Naumkin, A. Kraut-Vass, S. W. Gaarenstroom, C. J. Powel, NIST Standard Reference Database 20, Version 4.1, https://doi.org/10.18434/T4T88K (accessed: December 2019).

[39] Y.-C. Chen, Z.-B. Chen, Y.-G. Lin, Y.-K. Hsu, *ACS Sustainable Chem. Eng.* **2017**, *5*, 3863.

[40] C. Dietrich, R. Koerver, M. W. Gaultois, G. Kieslich, G. Cibin, J. Janek, W. G. Zeier, *Phys. Chem. Chem. Phys.* **2018**, *20*, 20088.

[41] L. Medenbach, P. Hartmann, J. Janek, T. Stettner, A. Balducci, C. Dirksen, M. Schulz, M. Stelter, P. Adelhelm, *Energy Technol.* **2020**, https://onlinelibrary.wiley.com/doi/full/10.1002/ente.201901200.

[42] J.-C. Jumas, M. T. Sougrati, A. Perea, L. Aldon, J. Olivier-Fourcade, *Hyperfine Interact.* **2013**, *217*, 107.

6. Conclusion and outlook

The main aim of this Ph.D. thesis was to find new aspects of conversion electrodes for Li and Na cells. On the one handside, an alloy electrode was investigated for its use in Na cells related to the influence of ball milling time on the electrochemical performance. On the other side, a comparison for transition metal compounds related to their use in Li as well as in Na half cells was performed. For the first major project, the ball milling time was varied and a variety of electrochemical characterization and analytical methods was used. In the second major project transition metal compounds were investigated. Therefore, in one study, a copper phosphide was compared for its use in Li and Na cells in terms of its electrochemical properties. In another study, a thiophosphate was investigated as an electrode material for its use in Li and Na cells as well. For all these studies, a variety of analysis and characterization tools was used, including *in situ* methods. XRD (and *in situ* XRD), XPS, TEM, SEM and others were used for the material characterization before, after and during cycling.

GCPL, EIS and CV measurements were applied for the investigation of the electrochemical performance of the electrodes. Moreover, *in situ* dilatometry was applied in order to study the electrode breathing during cycling. The most important conclusions from the obtained results are listed below.

Findings for Sn+Sb/C and SnSb/C composite electrodes:

- Reactive and non-reactive ball milling influence the voltage profiles and the redox activity of the elements Sn and Sb dependent on the electrolyte.
- Sb becomes redox inactive in diglyme upon cycling when not being bond with Sn as SnSb.
- The use of diglyme delivers appropriate conditions for excellent capacities and good cycle life.
- The capacity retention is dominated by the composite formation with carbon due to prolonged ball milling in the swing ball mill over the formation of the intermetallic phase or the mixture, which can be understood from *in situ* dilatometry studies.

However, despite a couple of questions are answered, following discussion points should be considered in futural studies:

- The effect of reactive and non-reactive ball milling onto the crystallite size, crystallinity and amount of percentage of the desired reaction product should be monitored via *in situ* XRD measurements during ball milling in order to optimize the synthesis conditions. Associated with that, lattice strain and contraction effects could be analyzed as well as their influence onto the electrochemical performance.

- The influence of other ball milling parameters, like jar volume or amount of material in the jar, may be varied in order to further optimize the efficiency of the electrode fabrication.

Findings for Cu₃P as a conversion electrode:

- Cu$_3$P as a conversion electrode in Li cells shows improved properties in comparison to the use of Na in all cases. Overpotentials are also smaller in Li half cells.

- The use of diglyme shows outperforming properties in comparison to selected carbonate electrolytes.

- *In situ* dilatometry shows that breathing in the initial discharge/charge cycle is larger for carbonate electrolytes, which may be correlated with a more excessive SEI formation as rapid capacity fading occurs upon further cycling.

- In contrast, diglyme electrolytes enable constant breathing after the initial cycle without any notable capacity decay within the initial five cycles.

The following aspects require additional studies in the future:

- In the study on Cu$_3$P, XRD and XPS investigations could not show expected charge and discharge products when comparing the reaction mechanisms between their use in LIBs and SIBs in detail. Hence, NMR studies or a larger active mass loading for improved detection of signals when using XRD should be applied for post mortem studies.

- The influence of the glyme length for the herein investigated transition metal compounds might show effects on the electrochemical behavior and should be proven.

Findings for Cu₃PS₄ as a conversion electrode:

- Herein, a thiophosphate (Cu$_3$PS$_4$) is used as an electrode material mainly in SIBs which is found to be largely redox active and shows much better battery performance in comparison to its use in Li cells.

- The use of a NaPF$_6$ dissolved in diglyme as an electrolyte in Na cells was found to be most appropriate in order to obtain excellent cycle life and very large capacities without any remarkable capacitiy decay.

- The redox mechanism was found to be dominated by sulfur via *in situ* XRD and XPS including the reversible formation of Na$_2$S, but, however, only in the initial cycle, copper is redox active while being reduced to its elemental state. Cu remains redox inactive upon further cycling, but it still can act as a trap for polysulfides.

Open remaining questions/studies about Cu$_3$PS$_4$ are proposed as follows for the future:

- It is important to clarify the reason for the inapplicability of carbonate electrolytes with the thiophosphate Cu$_3$PS$_4$ in detail. Moreover, the strong influence of the appropriate conducting salt should be clarified. A post mortem SEI investigation via XPS might reveal information about the enhanced cycle life when using NaPF$_6$ in diglyme in comparison to the use of other conducting salts like NaOTf. Since the reaction mechanism seems to be rather complicated

and the role of phosphorus remains unclear so far, an NMR study should be conducted. Moreover, the role of copper as polysulfide trap should be better understood by further studies.

- Cu_3PS_4 should be studied in full cell measurements in order to check its applicability for industrial application.

- The use of Cu_3PS_4 together with a solid state thiophosphate electrolyte should be investigated as it may lead to faster diffusion between electrode and electrolyte, because of the same crystal structures.

- Is the application of Cu_3PS_4 in solid state batteries different as when being compared with the use of liquid electrolyte? A detailed comparison for application in LIBs and SIBs might show different results and therefore needs to be studied.

- Are there other thiophosphates which also show large redox activity when being used as an electrode material?

7. Experimental methods and characterization techniques

7.1. Cell assembly and setup

Cell assembly was performed in an Argon filled glovebox in order to avoid oxidation and wetting of the electrode materials. Within this thesis two-electrode and three-electrode measurements were performed. Galvanostatic cycling experiments were carried out by using coin cells (two-electrode measurements, CR2032 Coin Cells by MTI Corp.), see **Figure 29**. Coin cells are usually fabricated by applying pressure onto the cell parts through a special coin cell press, resulting in very good sealing and contacting. Further, impedance measurements were performed in beaker cells (two-electrode measurements), see **Figure 30**. These cells show a similar setup like coin cells, but they are larger in size and thus allow the use of larger electrode diameters and larger amount of electrolyte. The cell pressure is enabled by screws, pressing on the central spring being fixed on the top of the cell. Air leakage is avoided by the use of rubber sealing rings. Three electrode measurements were carried out in t-shaped Swagelok type cells for cyclic voltammetry (CV) as well as impedance measurements, see **Figure 31**. These cells contain an additional reference electrode which is set close to the working electrode in order to reach a higher accuracy of the potential measured at the working electrode. The battery materials are therefore put into the t-shaped cell housing. Screws, springs and silicone sealing rings enable reasonable cell pressure and sealing of the cell, respectively. The reference electrode, which is typically the same alkali metal as being used for the counter electrode for half cell measurements, is connected vertically to the cell by an additional separator stripe through a small slit.
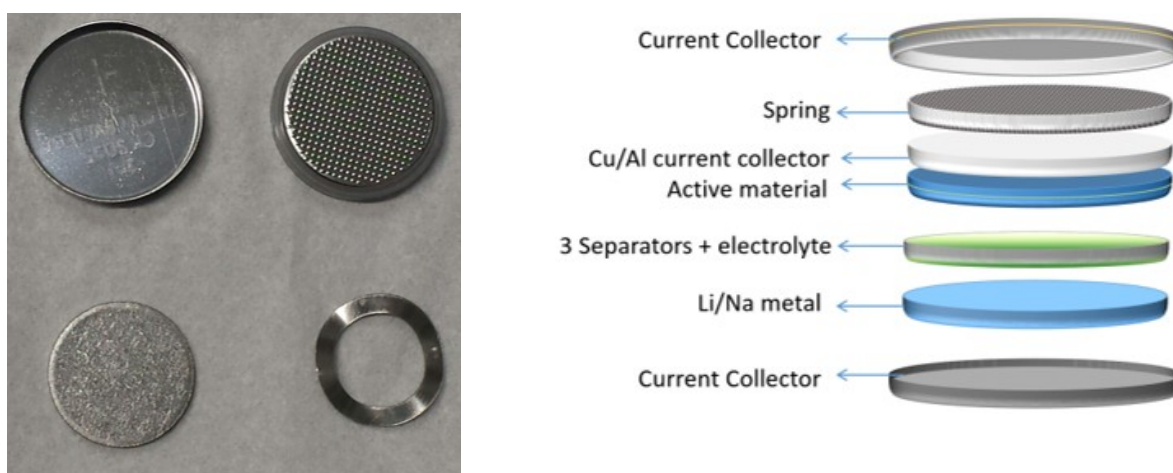

Figure 29: Left: Coin cell parts. Right: Schematic setup of a coin cell used for Li/Na half cells, which was used for galvanostatic cycling and rate performance tests.

Figure 30: *Two electrode setup in a beaker cell used for impedance measurements.*
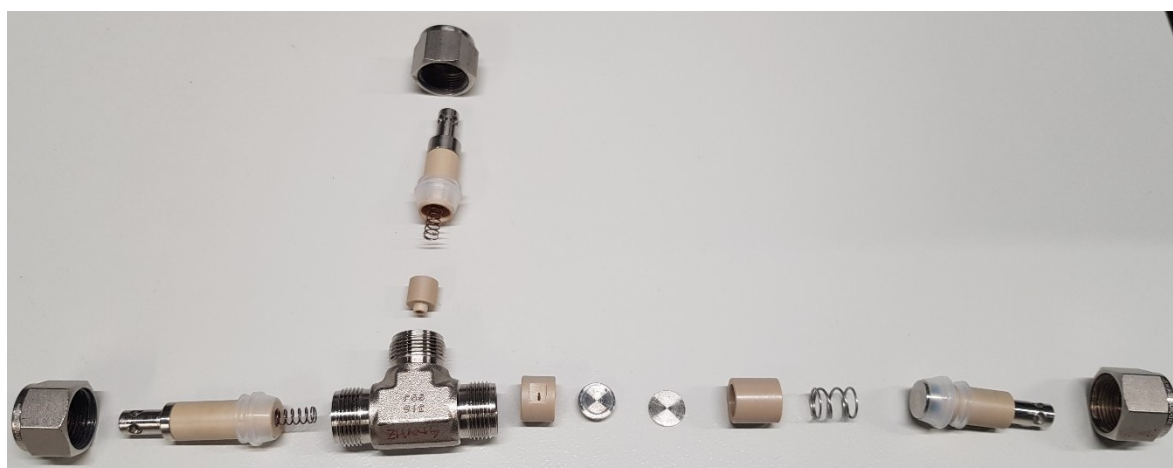

Figure 31: *Swagelok cell components for three electrode measurements.*

7.2. Electrochemical measurements

Galvanostatic cycling with potential limitation (GCPL)

GCPL is the most convenient method in the battery community for characterizing electrode materials in terms of their electrochemical properties. Within a defined voltage window, voltage is recorded over time while a constant current is applied. LIBs and SIBs this way can be continuously discharged/charged. The current direction is thereby alternately changed after reaching a potential limit. The resulting voltage profiles supply information about phase transitions indicated by voltage steps or sloping profiles, see **Figure 32**a. Moreover, capacities, energy densities and efficiencies, overpotentials as well as Coulomb efficiencies can be determined. The voltage profiles can be further used to create capacity derivative plots, which provide a detailed information about redox potentials and reversibility of a cell reaction as shown in **Figure 32**b. GCPL is also used for testing the rate

performance of a cell when applying different currents and cycle life tests, see **Figure 32**c,d. GCPL was used in publications 1-3 as the main electrochemical characterization tool.
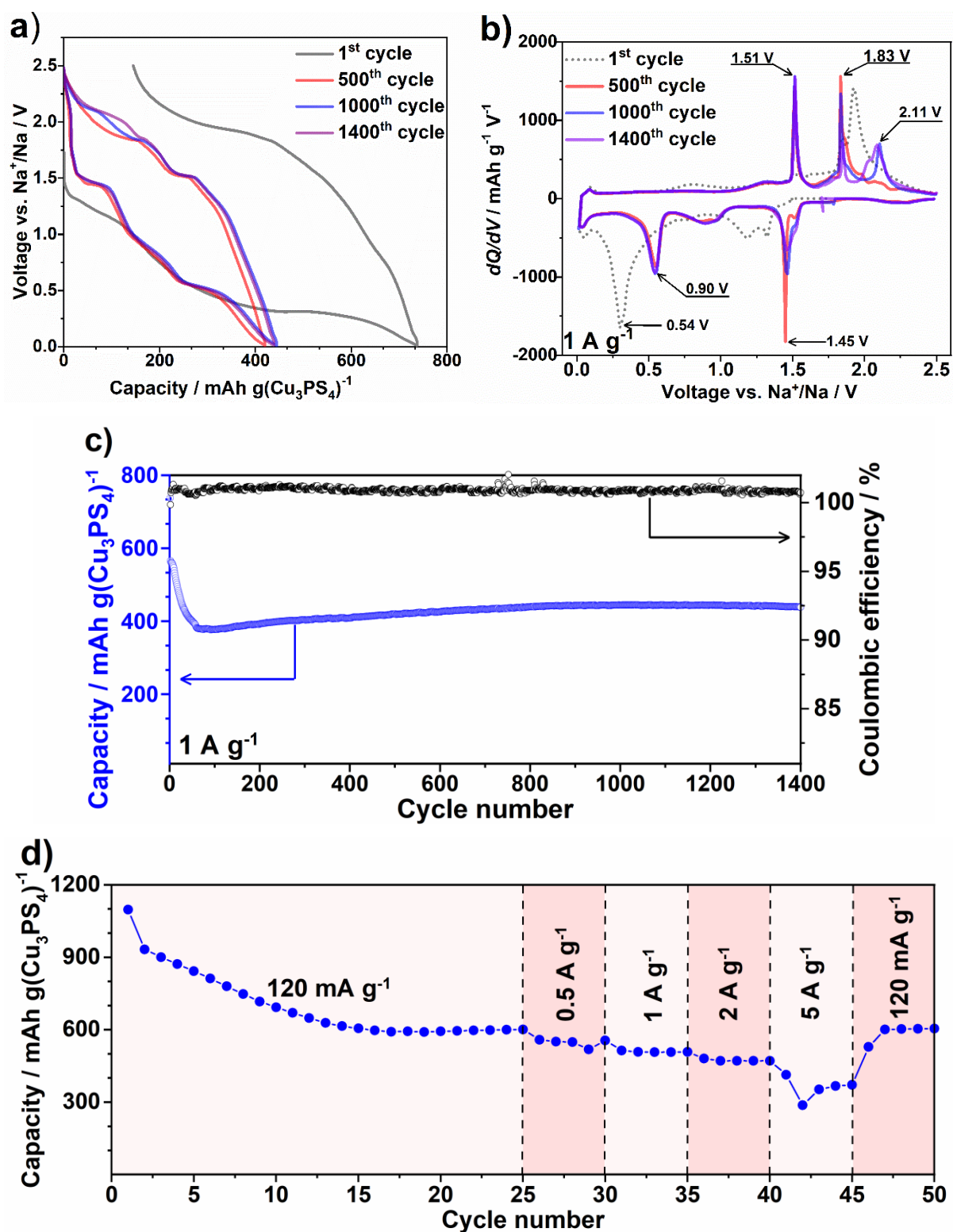

Figure 32: *a) Voltage profiles; b) capacity derivatives; c) cycle life test; d) Rate capability for a Cu₃PS₄/C electrode with 1 M NaPF₆ in diglyme for a voltage window of 0.01 V - 2.5 V. Reproduced with permission from Wiley.* [11b]

7.2.1. Galvanostatic intermittent titration technique (GITT)

A typical GITT profile is shown in **Figure 33**. For this method current pulses are applied onto a battery followed by a relaxation period under a predefined relaxation condition, typically reaching an equilibrium (voltage change per time unit ~ 0). In practice however, the equilibrium cannot be reached, thus only an approximated equilibrium curve can be determined. This method delivers an insight about the equilibrium voltage in the dependency of the state of discharge/charge. GITT was used in order to discuss the equilibrium discharge voltages of Cu_3P in Li- and Na half cells in publication 2.
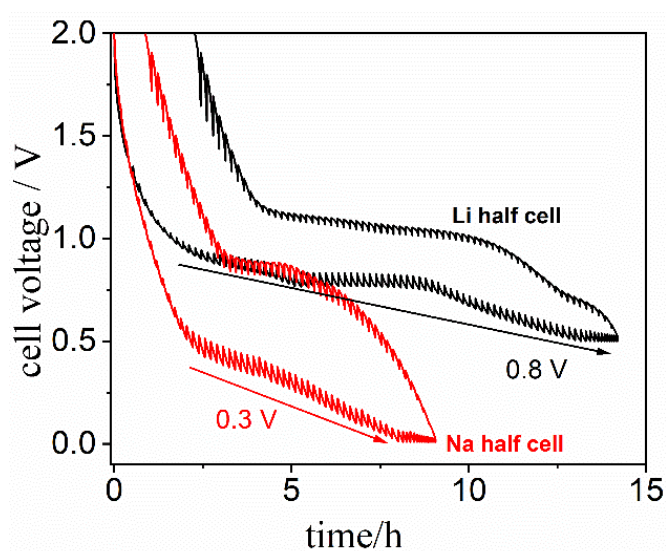

Figure 33: *GITT profiles of the second cycles of Cu_3P/C electrodes in Li and Na half cells.* [11b]

7.2.2. In situ electrochemical dilatometry (ECD)

During a conversion reaction the electrode undergoes a huge volume change due to changes in the crystal structure and the formation of a nanoscopic structure (for transition metal compounds) within the initial discharge process. This usually leads to contact losses which result in rapid capacity fading. However, to circumvent this issue, usually conducting agents are used which make it impossible to determine the overall volume change by standard methods like *in situ* X-ray diffraction. The shrinking and expansion of the whole electrode can be directly reliable measured by *in situ* dilatometry under use of a sensor contacting the electrode surface during the cell reaction. The dilatometry cell setup is schematically shown in **Figure 34**. *In situ* dilatometry directly provides information about the height change in dependency of the electrochemical storage capacity of the electrode. This method was used to investigate the electrode thickness changes during cycling in publications 1,2.
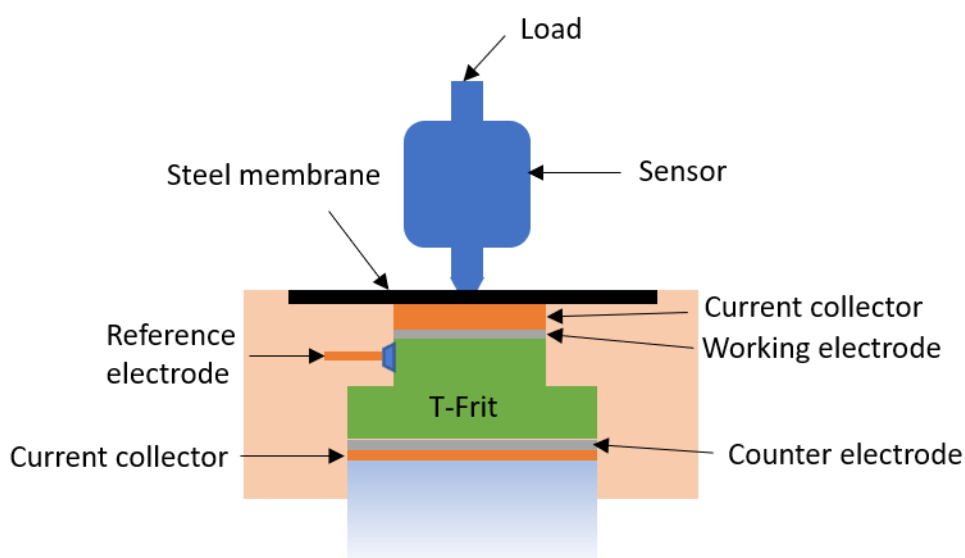

Figure 34*: Schematic in situ dilatometry cell setup.*

7.2.3. Cyclic voltammetry (CV)

Cyclic voltammetry is a common method to clarify the redox behavior of an active material. A typical CV scan profile is screened in **Figure 35**. For a CV scan, the applied potential E is continuously changed with a constant scan rate v within a predefined voltage window which is defined by a vertex upper potential limit and vertex lower potential limit in a saw tooth shape (see inlay in **Figure 35**). The resulting current response I can be negative (reduction) or positive (oxidation). By this method, redox potentials of a redox active species and moreover, the reversibility of a cell reaction may be determined. When looking at the I vs. E diagram, the current response follows the Butler-Volmer kinetics, beginning on its onset until reaching a current maximum or minimum. After reaching such a peak, the absolute current usually decreases as diffusion limitation takes place, i.e. diffusion of the ions towards an electrode limits the current response.
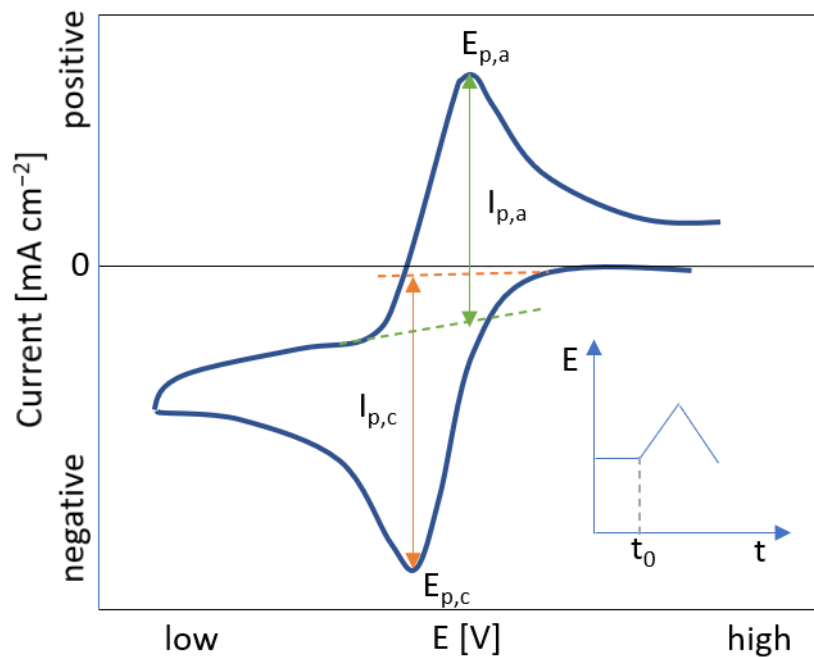

Figure 35: *Schematic illustration of a cyclic voltammogram: The small inlay shows the applied voltage as function of the time in a peak shape.*

7.2.4. Potentiostatic electrochemical impedance spectroscopy (PEIS)

Potentiostatic electrochemical impedance spectroscopy is a complex method being used for understanding dielectric properties of a material in dependency of the frequency. Therefore, a sinus form alternating potential E is applied to the system.

$$E = E_0 \sin(\omega t) \qquad \text{(eq. 9)}$$

The current response is measured in dependency of the frequency. From that one obtains a phase shifted sinus form current about the phase angle φ

$$I = I_0 \sin(\omega t + \varphi) \qquad \text{(eq. 10)}$$

$$\text{with } \omega = 2\pi f \qquad \text{(eq. 11)}$$

The impedance Z of an electrochemical system then can be determined by

$$Z = \frac{E}{I} = \frac{E_0 \sin(\omega t)}{I_0 \sin(\omega t + \varphi)} \qquad \text{(eq. 12)}$$

Eulers relationship: $e^{i\varphi} = \cos\varphi + i\sin\varphi \qquad \text{(eq. 13) leads to}$

$$E = E_0 e^{i\omega t} \qquad \text{(eq. 14)}$$

$$I = I_0 e^{i\omega t - \varphi} \qquad \text{(eq. 15)}$$

The complex notation of the impedance consequently can be illustrated as:

$$Z(\omega) = \frac{E}{I} = Z_0 e^{i\varphi} = Z_0(\cos\varphi + i\sin\varphi) \qquad \text{(eq. 16)} \qquad \text{with } Z_0 = \frac{E_0}{I_0} \qquad \text{(eq. 17)}$$

This relationship then can be used in the so called Nyquist plot, being explained below in order to obtain information about resistances and kinetics at interphases.

The complex impedance $Z(\omega)$ is composed of a real and an imaginary part. The plot of the negative imaginary part on the y-axis vs. the real part on the x-axis is named as Nyquist plot. It is worth to mention that each measurement point is related to one frequency value for the Nyquist plot.

Low frequency data is located at high resistances on the x-axis, while high frequency processes take place at lower resistances under assumption of the presence of only ohmic and capacitive effects. In the battery community electrochemical impedance spectroscopy (EIS) is often used to receive information about charge transfer resistance (high frequencies) and diffusion kinetics (lower frequencies) when considering electrode processes. A typical impedance spectrum of a Li or Na half cell in a three electrode arrangement is shown in **Figure 36**. [44] Herein, bulk resistance R_b is only

contained in the real part on the x-axis and contains the resistance of the inner cell parts like separator, electrolyte and electrodes. R_{sei} is the resistance of the solid electrolyte interphase layer (SEI) while R_{ct} is the charge transfer resistance of the electrode. These processes can be better understood by applying equivalent circuits, see inlay in **Figure 36**. Impedances of the SEI and the charge transfer are usually illustrated as parallely connected resistance and capacitance equivalents, for example. Diffusion processes of the alkali ion at the interface between electrode material and electrolyte are indicated by a straight sloping line at lower frequencies (identified by a Warburg impedance in an equivalent circuit). PEIS was used in order to discuss the charge transfer kinetics of Cu_3P and Cu_3PS_4 electrodes in publications 2 and 3.
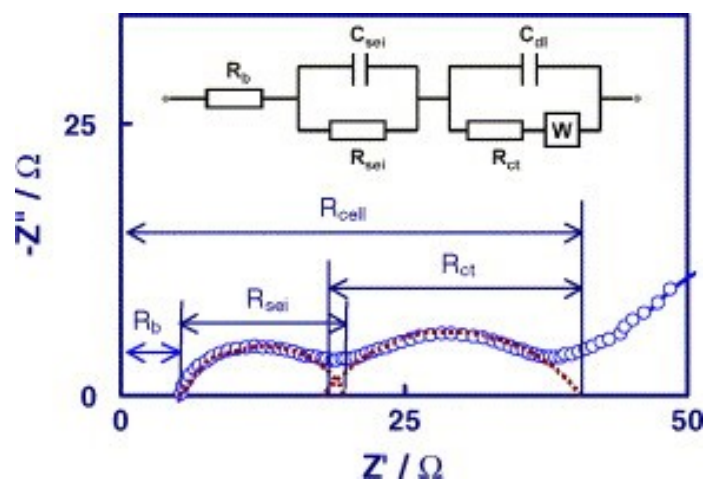

Figure 36: *Typical EIS of a Li- or Na-ion cell and the equivalent circuit used to fit the EIS. Reproduced with permission from Elsevier.* [44]

7.3. Characterization methods

7.3.1. X-ray diffraction (XRD)

X-Ray diffractometry is a convenient method to characterize crystalline materials. It provides information about crystal structures, crystal orientations, crystallite size, crystallinity as well as strain effects of the lattice parameters. X-rays are created by beaming electrons onto a metal source, often copper (Cu) or molybdenum (Mo), which releases X-rays. An XRD signal is created by constructive interference of a monochromatic X-ray beam being scattered from lattice planes at specific angles. Hence, an XRD pattern enables visualization of a periodic atomic arrangement in a material. Scattering follows according to Bragg's law as follows:

$$n \cdot \lambda = 2d \cdot \sin(\theta) \qquad\qquad\qquad (eq.\ 18)$$

n represents the resonance order, λ the characteristic wave length, d the distance between the lattice planes and θ is the diffraction angle.

XRD was used in publications 1-3 in order to discover crystal structures, lattice parameters and crystallite sizes of the electrode materials.

7.3.2. In situ XRD

In situ XRD is useful to analyze the development, decomposition and/or maintenance of crystalline phases during a running chemical or electrochemical reaction. Within the thesis, it was used in order to identify the phase development during the sodiation/desodiation of Cu_3PS_4. For this kind of measurement a special cell setup with an X-ray transparent window is used.

7.3.3. X-ray photoelectron spectroscopy (XPS)

While XRD is dependent on the crystallinity of a material, XPS can be also applied for non-crystalline materials which is useful for the determination of surface binding characteristics and the elemental composition of a material's surface. XPS is based on the irradiation of a material with X-rays while detecting the energy for the excitation and release of electrons in order to characterize the binding energies. Due to the strong surface sensitivity of about 10 nm, one carefully needs to judge whether the results being discussed are representative or not. Hence, XPS is often used together with other characterization techniques. Herein, XPS was used in order to support the understanding of the reaction mechanism for the use of Cu_3P/C and Cu_3PS_4/C electrodes in Li and Na cells.

7.3.4. Scanning electron microscopy (SEM)

SEM is a common imaging method for the characterization of the materials morphology. The working principle of SEM is based on an electron beam scanning the surface of a material. The electrons impinging on the sample are backscattered, while additionally secondary electrons of the sample are emitted. These backscattered electrons and/or the secondary electrons are detected and can be converted into an image. Thereby, the electron beams' focus may be controlled by several magnetic lenses analogue to an optical microscope working with optical lenses. Herein, imaging was processed for all projects directly after ball milling to get an insight to the particles morphology and particle sizes without the influence of additives like binder materials.

7.3.5. Transmission electron microscopy (TEM)

TEM is another imaging technique for morphological characterization of a material. It enables higher resolution imaging and is therefore a much more local method in comparison to SEM. TEM allows even to visualize structural properties on atomic level. This technique enables predictions about particle size and shape and furthermore, the local crystal structure. The working principle of TEM thereby is analogue to a light microscope permitting electrons instead of light. The TEM electron source is usually a tungsten filament or a LaB_6 single crystal, which is connected to a high voltage source, enabling the emission of electrons by thermionic or field electron emission into the vacuum. A high voltage difference of a few hundred kV is required in order to sufficiently accelerate the electrons for receiving a high resolution image. When the electron beam targets a very thin sample or particle, the electrons undergo a diffraction according to Bragg's law. These electrons are collected by a detector, this way converting the information into a high resolution image. Herein, TEM was processed in order to discuss crystal sizes and shapes, lattice parameters as well as the particle morphology of the as synthesized Cu_3P and Cu_3PS_4 particles in publication 3.

7.3.6. Energy dispersive X-ray spectroscopy (EDS)

SEM and TEM use an electron beam impinging on a sample. In this process, electrons of the atoms contained in the sample become excited. During the relaxation of the electrons, element specific X-rays are emitted with a certain wave length which can be detected. This method allows to specify the amount of atoms contained in a local surface area of the investigated material. EDS is suitable for heavy elements contained in the sample, since they enable a more intense scattering. This method was used in order to prove the homogeneity of the considered materials in publications 1-3.

7.3.7. Particle size distribution (PSD) by light scattering

Particle sizes can be determined by diffracting laser light through a dispersion of particles in a liquid. This technique allows measuring the particle size by the angular variation with the light intensity of light. The angular scattering intensity is recorded and being used to calculate the particle sizes for creating a light scattering pattern by means of the Mie theory or Fraunhofer approximation. As the diffraction angle increases with decreasing particle size, particle sizes between 0.1 and 3 μm can be reliable analyzed with this method. Analysis of the PSD was used in publication 1 in order to prove the change particle sizes by influence of the ball milling time.

8. Appendix

8.1 Supporting information on publication 1

Supporting Information on

Reactive and non-reactive ball milling of tin-antimony (Sn-Sb) composites and their use as electrode for sodium-ion batteries with glyme electrolyte

Wolfgang Brehm[a,b], Johannes R. Buchheim[a,b], Philipp Adelhelm[a,b]*

[a] Institute of Technical Chemistry and Environmental Chemistry, Friedrich Schiller University Jena, Philosophenweg 7a, 07743 Jena, Germany

[b] Center for Energy and Environmental Chemistry (CEEC Jena), Friedrich Schiller University Jena, Philosophenweg 7a, 07743 Jena, Germany

* correspondence: philipp.adelhelm@uni-jena.de

a)

b)

c)
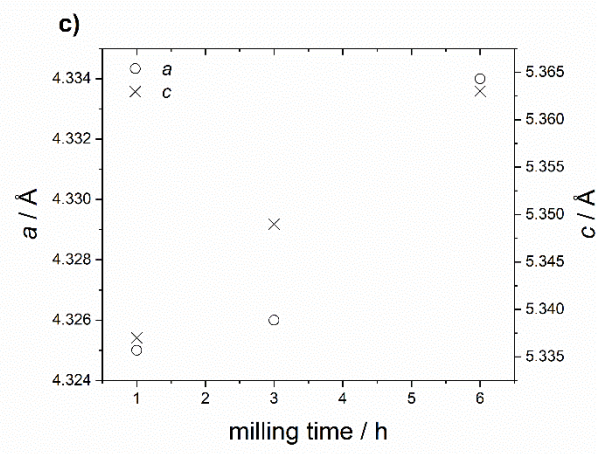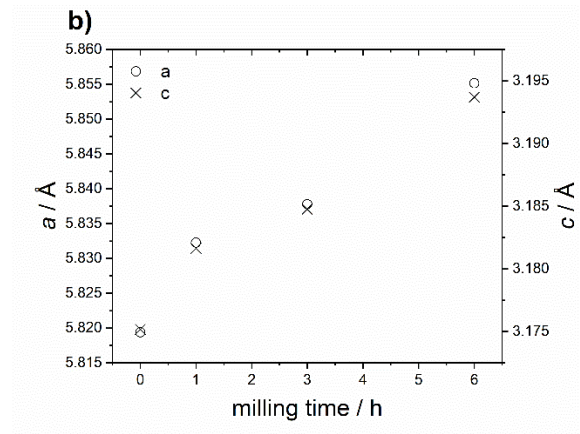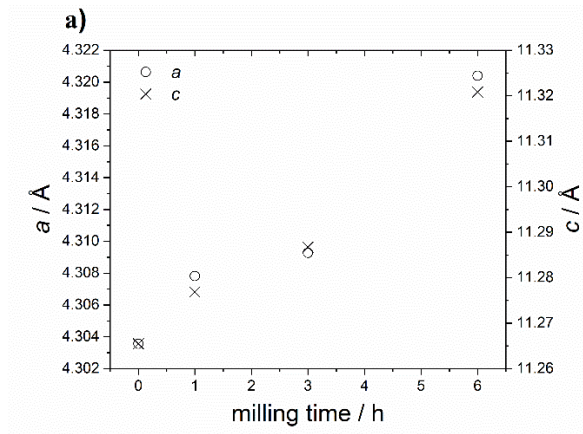
Figure S1: Changes of the lattice parameters a and c of a) Sb, b) Sn and c) β-SnSb with the ball milling time in the SBM with carbon black.

Table S1: Results of the Rietveld refinement of the prapered samples (Sn: ICSD 98-004-0037; Sb: ICSD 98-000-9859;SnSb: ICSD 98-005-2294).

Sample	Composition [wt%]	Lattice parameters [Å]	D [nm]	R-values
Sn+Sb/1h	Sn 49 %	a = 5.8322 c = 3.1816	100	R_{wp} 0.2488
	Sb 49 %	a = 4.3078 c = 11.2769	99	R_{exp} 0.1851
	SnSb 2 %	a = 4.3250 c = 5.3375 α = 89.3	100	χ^2 1.344
Sn+Sb/3h	Sn 47 %	a = 5.8377 c = 3.1847	122	R_{wp} 0.1238
	Sb 44 %	a = 4.3093 c = 11.2867	137	R_{exp} 0.0996
	SnSb 9 %	a = 4.3261 c = 5.3490 α = 89.6	119	χ^2 1.243
Sn+Sb/6h	Sn 36 %	a = 5.8551 c = 3.1937	45	R_{wp} 0.1031
	Sb 44 %	a = 4.3204 c = 11.3208	137	R_{exp} 0.0821
	SnSb 20 %	a = 4.3340 c = 5.3631 α = 89.6	69	χ^2 1.255

$$R_{wp} = \sqrt{\frac{\sum_{i=1}^{N}[w_i(I_i^{exp}-I_i^{calc})]^2}{\sum_{i=1}^{N}[w_i I_i^{exp}]^2}} \ldots\text{weighted-profile R value}$$

$$R_{exp} = \sqrt{\frac{(N-P)}{\sum_{i=1}^{N}[w_i I_i^{exp}]^2}} \ldots\text{statistically expected R value}$$

$$w_i = \frac{1}{\sqrt{I_i^{exp}}} \ldots\text{weighting factor}$$

$$\chi^2 = \frac{R_{wp}}{R_{exp}} \ldots\text{goodness of fit}$$

N …number of points

P …number of parameters

Table S2: Results of the Rietveld refinement of β-SnSb-synthesized by ball milling for 24h in a PBM and further ball milling with C65 for 1h and 6h. (SnSb: ICSD 98-005-2294)

Parameter	SnSb	SnSb/1h	SnSb/6h
R_{wp}	0.1395	0.0505	0.0443
R_{exp}	0.0690	0.481	0.3586
χ^2	2.021	0.105	0.123
a [Å]	4.321(2)	4.319(9)	4.323(0)
c [Å]	5.340(2)	5.328(8)	5.334(4)
D [nm]	50	50	56
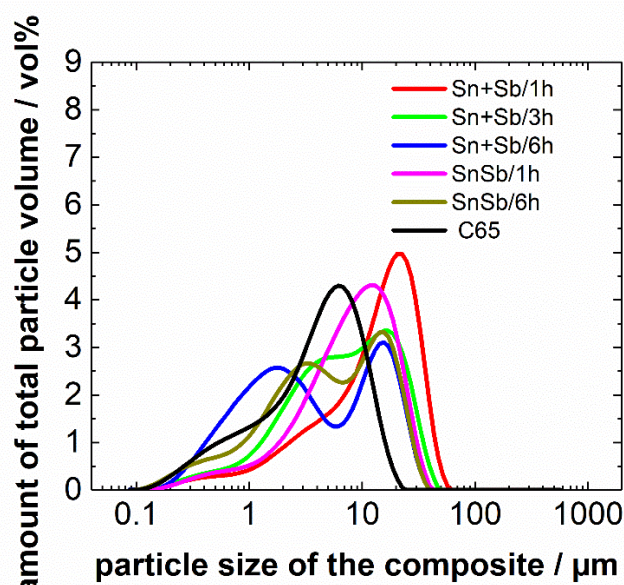
Fig. S2: Particle size distribution measurement based on a light scattering technique of wet dispersions of Sn+Sb/C, SnSb/C and carbon black C65.
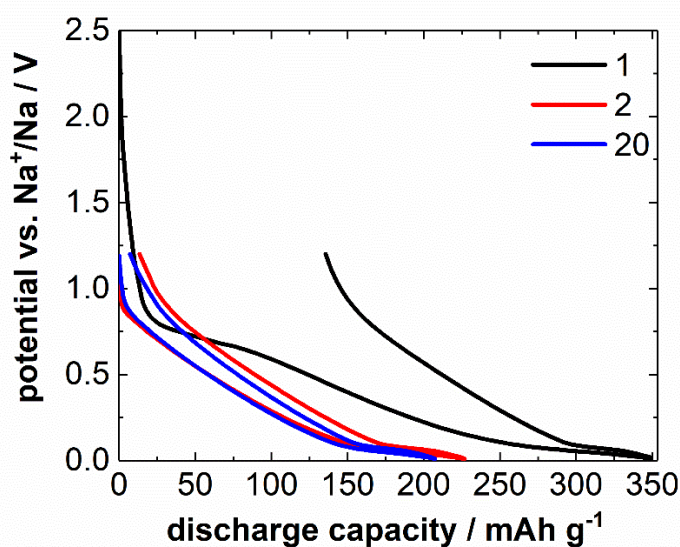
Fig. S3: Voltage profiles for carbon black C65 in a voltage range from 0.01-1.2 V vs. Na⁺/Na at same current density conditions of the herein considered composite electrodes (100 mA g⁻¹).

107
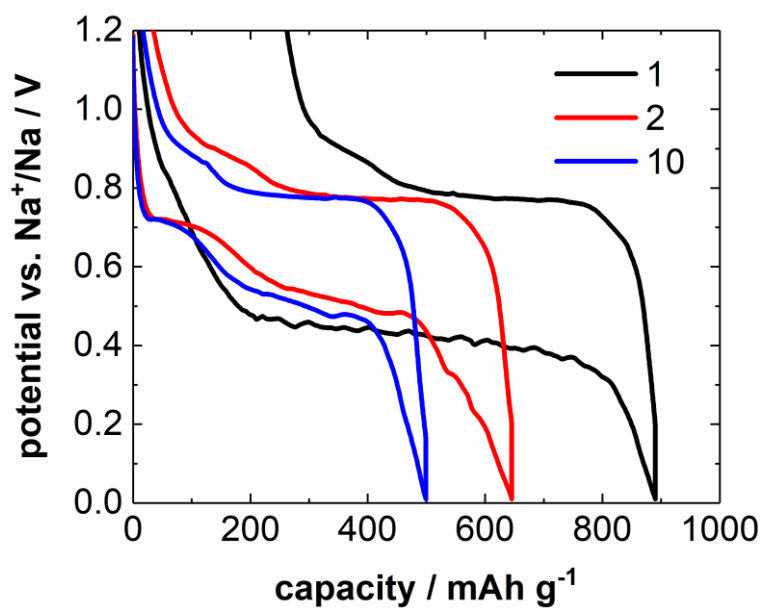
Fig. S4: Voltage profiles for Sb/C in a voltage range from 0.01-1.2 V vs. Na+/Na at same current density conditions of the herein considered composite electrodes (100 mA g^{-1}).
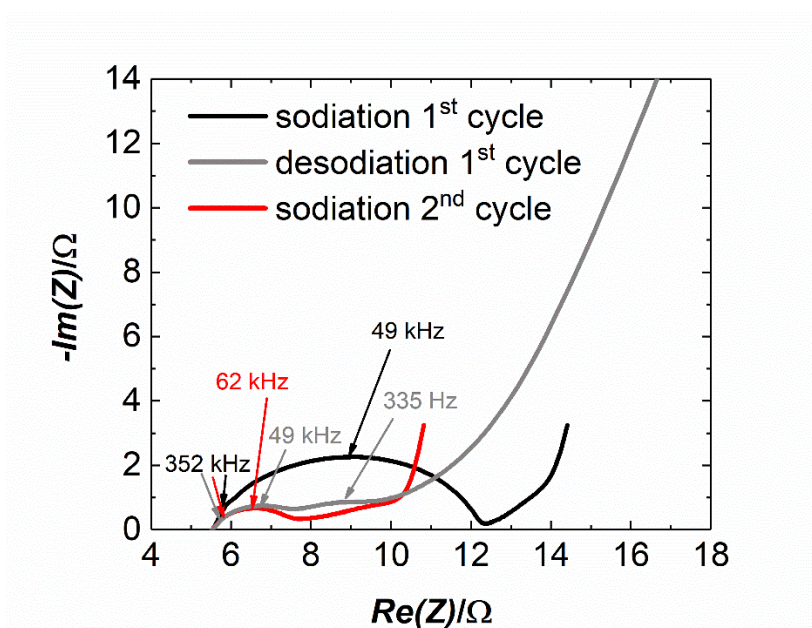

Fig. S5: Impedance analysis for a two-electrode cell with Sb/C as working electrode and sodium metal as counter electrode. Spectra were collected after the 1st sodiation and desodiation as well as after the 2nd sodiation. The frequency range was 1 MHz to 100 mHz and the amplitude 10 mV. The electrolyte used was NaPF$_6$ dissolved in diglyme (1M). Cells were cycled in a voltage window between 0.01-1.20 V vs. Na+/Na.
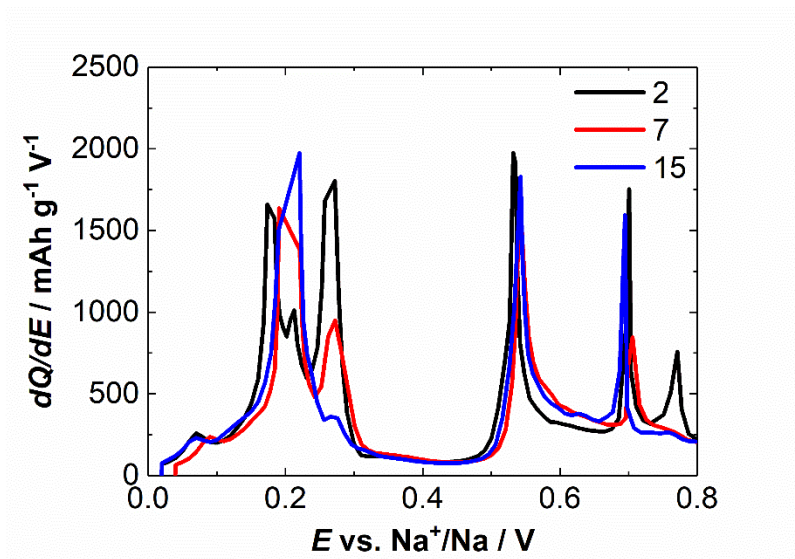
Fig. S6: Derivative curves of Sn+Sb/1h: The change of the desodiation mechanism can be seen by formation of an uniform signal at 0.2 V within the initial 15 cycles. The little peak at around 0.77 V vs. Na$^+$/Na, vanishing after the 2nd cycle, correlates with SEI formation.

Table S3: Literature overview about the electrochemical performance of Sn and SnSb electrodes prepared by ball milling (containing carbon as additive)

| Source	Weight ratio	Binder type and content / wt%	Active load / mg cm^{-2}	Electrolyte	Voltage window / V vs. Na$^+$/Na	C-Rate / h^{-1}	Cryst. size / nm	Particle size	Cycles	Specific capacity / mAh g^{-1}
Liu et al., Chem. Commun. 2012	SnSb/C=7:3	n.a.	n.a.	n.a.	0.01-1.2	~0.1	10	few 100 nm	50	453
Zhang et al., Electrochimica Acta 2017	SnSb/C=10:1.25	CMC 10	0.78	PC/NaClO$_4$	0.01-2	0.59	n.a.	50-100 nm	200	100
Darwiche et al., Electrochem. Com. 2013	SnSb/C = 6:1	CMC 12	1.9	FEC content	0.02-1.5	0.06 ?	n.a.	n.a.	125	525
Our study	SnSb/C = 7:3	CMC 10	1.3	2G NaPF$_6$	0.01-1.2	0.13	56	0.1-40 µm	190 (50)	408 (680)
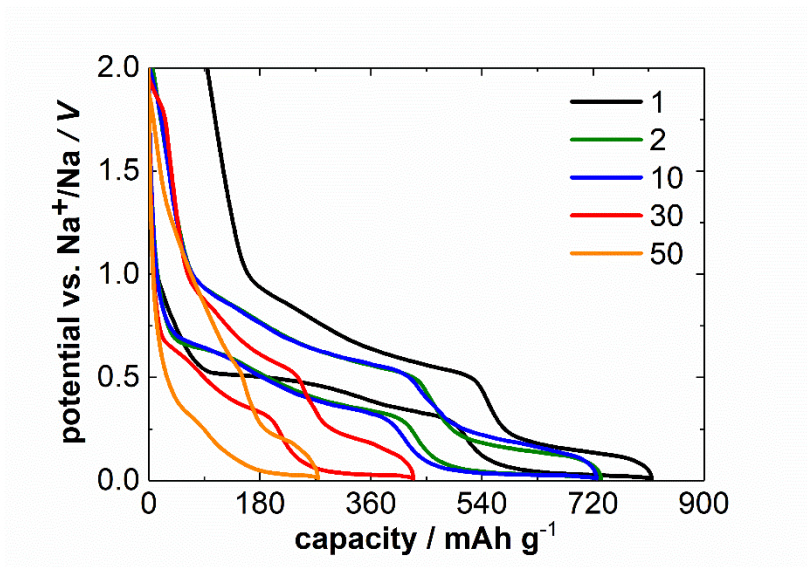
Fig. S7: Voltage profiles for SnSb/6h in a voltage range from 0.01-2.0 V vs. Na^+/Na at 0.13 C. The increase of the upper cutoff voltage from 1.2 V to 2 V vs Na^+/Na leads to rapid capacity fading. This observation can be explained by the SEI becoming more instable, when reaching higher voltages.

8.2 Supporting information on publication 2

Supporting Information on

Mechanochemically synthesized Cu₃P/C composites as a conversion electrode for Li-ion and Na-ion batteries in different electrolytes

Wolfgang Brehm[a], Aggunda L. Santhosha[a,c], Zhenggang Zhang[a,c], Christof Neumann[b], Andrey Turchanin[b], Martin Seyring[d], Markus Rettenmayr[a,d], Johannes. R. Buchheim[a] and Philipp Adelhelm[a,c]*

[a] Institute of Technical Chemistry and Environmental Chemistry, CEEC Jena, Friedrich Schiller University Jena, Philosophenweg 7a, 07743 Jena, Germany

[b] Institute of Physical Chemistry, CEEC Jena, Friedrich Schiller University Jena, Lessingstraße 10, 07743 Jena, Germany

[c] Department of Chemistry, Humboldt-University Berlin, Brook-Taylor-Str. 2, 12489 Berlin, Germany

[d] Otto-Schott-Institute of Materials Research, Friedrich Schiller University Jena, Löbdergraben 32, 07743 Jena, Germany

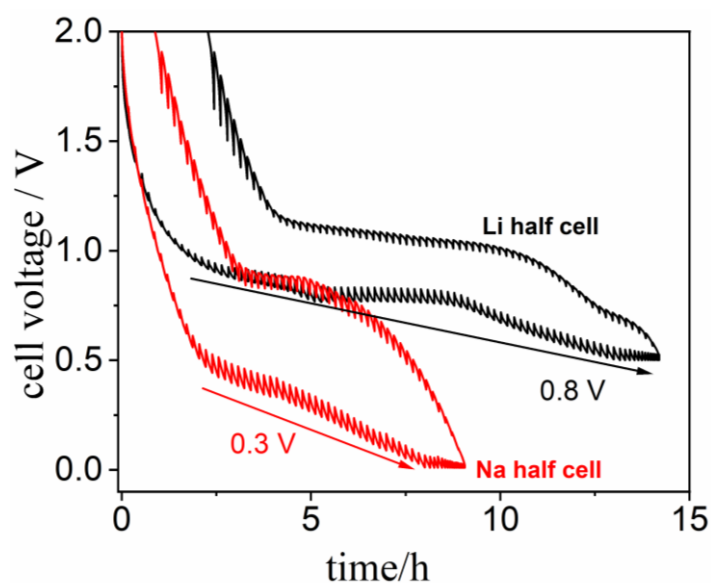** correspondence: philipp.adelhelm@hu-berlin.de*

Figure S1 Galvanostatic intermittent titration technique (GITT): GITT profiles of the second cycle with consecutive current pulses of 8 min at 0.1C. The relaxation condition for each step was set to dE/dt = 10 mV/h for lithiation/sodiation and delithiation/desodiation. The used electrolytes were 2G LiTFSI and 2G NaOTf in lithium and sodium half cells, respectively. Although the electrochemical equilibrium was not achieved under the given conditions, the results give an estimate of the average discharge voltage derived from these measurements. The average discharge voltages of 0.8 V vs. Na$^+$/Na and 0.3 V vs. Li$^+$/Li were determined by taking the voltage values after relaxation.
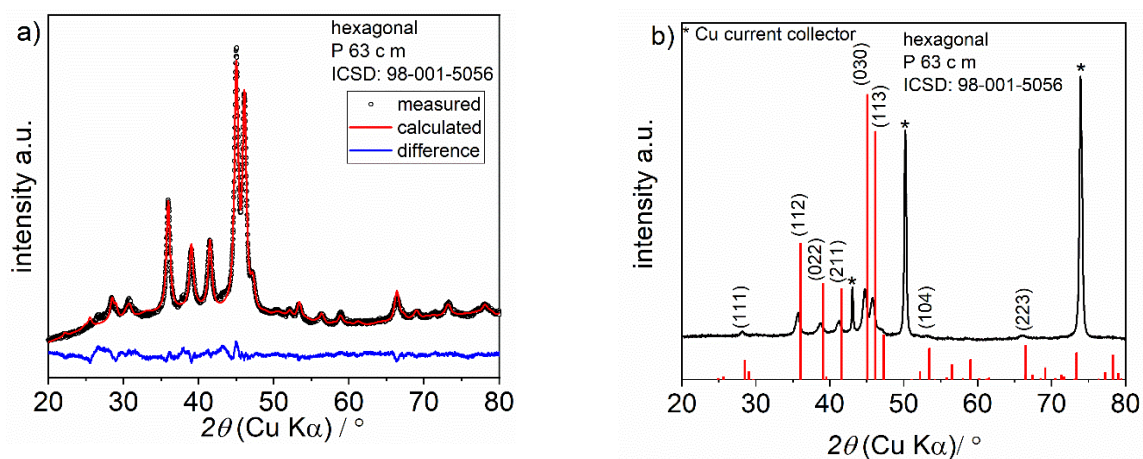

Figure S2: a) Rietveld refinement analysis of Cu$_3$P; b) XRD analysis of the Cu$_3$P/C (7:3) electrode on a current collector (Reference: ICSD: 98-001-5056).

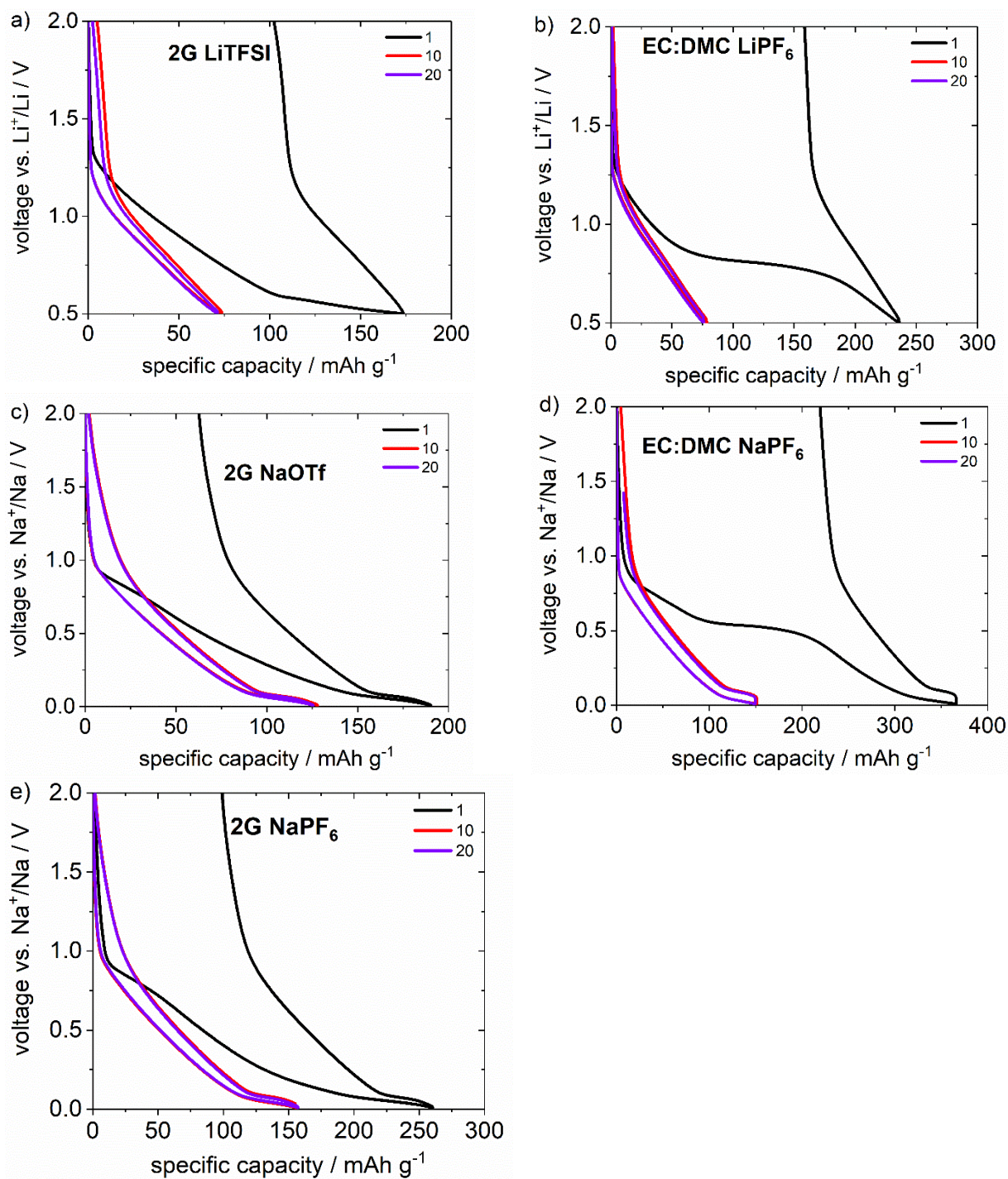*Figure S3: Voltage profiles of carbon black at 36 mA g⁻¹ for different electrolytes. It is of note, however, that the preparation of carbon black electrodes is difficult as the material is very fluffy, which causes problems during electrode preparation. The mass loadings are typically very small (in our case about 0.7-1.0 mg cm⁻²). Overall, an exact deconvolution of the individual contributions of Cu₃P and carbon black to the capacity of the Cu₃P electrode is not possible, but the contribution of carbon black is discussed in the main manuscript. The herein used carbon black was Carbon Super P.*

Table S1: Literature overview about Cu_3P/C composites as electrode material in Li and Na ion half cells

| Type	Reference	Weight ratio	Binder type and content / wt%	Cu_3P loading / mg cm^{-2}	Electrolyte	Voltage window / V vs. A$^+$/A	Current / mA g^{-1}	Cryst. size / nm	Particle size / µm	Cycles	Specific capacity / mAh g^{-1}
Li	Stan et al., doi: 10.1002/aenm.201200655	Cu_3P/C=8:1	PVDF 10	n.a.	EC:DEC+LiPF$_6$.	0.5-2	24.2	20	10	50	220
Li	Bichat et al., doi:10.1016/j.jpowsour.2004.05.024	Cu_3P/C = 85:15	n.a.	10-12 mg	EC:DMC+LiPF$_6$.	0.02-2	6.1	n.a.	3	39	~273
Li	Bichat et al., doi: 10.1149/1.1815156	Cu_3P/C = 85:15	n.a.	10-12 mg	EC:DMC+LiPF$_6$.	?	C/8 ?	n.a.	0.1-0.2	16	~440 ?
Li	Crosnier et al., doi: 10.1149/1.1736592	Cu_3P/C = 9:1	PVDF 5		EC:DMC+LiPF$_6$	0.01-2.5	C/10	300	20	30	~120
Li	Our study	**Cu_3P/C=7:3**	**PVDF 5**	**3.3**	**2G+LiTFSI**	**0.5-2**	**36.6**	**17**	**0.1-40**	**120**	**210**
Na	Zhu et al., doi: 10.1039/C9TA04035H	Cu_3P@C5/C = 8:1	PVDF 10	1.17 (incl. C)	EC:DMC+NaClO$_4$	0.01-3	100		~100	300	~286
Na	**Our study**	**Cu_3P/C=7:3**	**PVDF 5**	**3.3**	**2G+NaOTf**	**0.01-2**	**36.6**	**17**	**0.1-40**	**120**	**124**
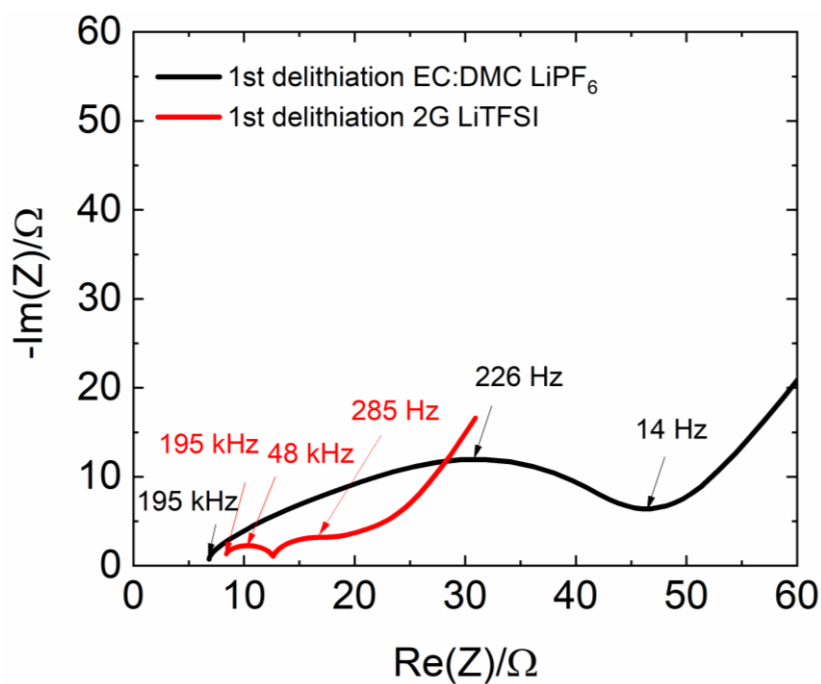
Figure S4: Impedance analysis of Cu₃P electrodes in a frequency range of 1 MHz to 10 mHz after the first delithiation/desodiation cycle in a Li cell. Results were obtained using a cell in three electrode geometry using 1M LiPF₆ in EC:DMC and 1M LiTFSI in 2G in Li cells. Galvanostatic cycling was performed in a voltage window of 0.5-2 V.
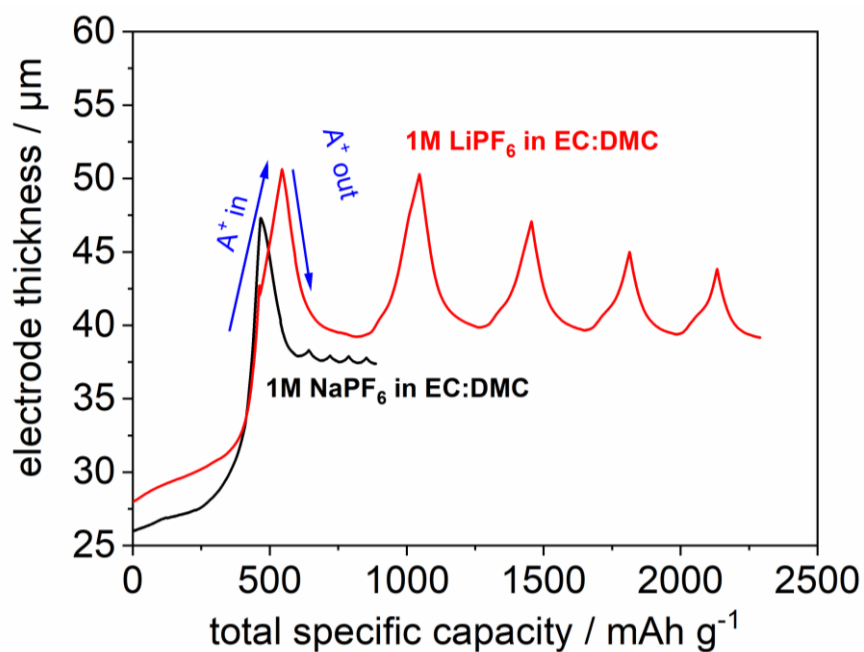

Figure S5: In situ dilatometry studies of Cu₃P in Li and Na half cells with carbonate electrolytes a) 1M LiPF₆ in EC:DMC (1:1); b) 1M NaPF₆ in EC:DMC (1:1). Cycling was performed with a current rate of 0.1 C (36.6 mA g⁻¹) in a voltage window of 0.5-2.5 V vs. Li⁺/Li for the use of Li and 0.01 -2.5 V vs. Na⁺/Na for the use of Na.

Table S2: Parameters of the Cu$_3$P/C electrodes: Electrode thicknesses and the height change during the first sodiation measured by ECD at 0.1 C (36.6 mA g^{-1}). The porosity P was calculated based on the real electrode volume and the volume of the components with their crystalline densities. The following density values were used: ρ_{Cu3P} = 7.34 g cm^{-3} (space group P 63 cm), $\rho_{(carbon\ black)}$ = 2.00 g cm^{-3}, $\rho_{(PVDF\ binder)}$ = 1.78 g cm^{-3}. q$_{th,vol}$ and q$_{th,areal}$ are the theoretical volumetric and areal capacities of the electrode including the porosity.

Electrode	Initial electrode thickness / μm	Cu$_3$P loading / mg cm^{-2}	$q_{th,\ areal}$ / mAh cm^{-2}	P / %	$q_{th,\ vol}$ / mAh cm^{-3}	Height change 1st discharge / μm	Height change 1st discharge / %
Li/2G:LiTFSI	36	3.49	1.27	62	530	10	28
Li/EC:DMC LiPF$_6$	28	3.28	1.18	54	642	23	82
Na/2G:NaPF$_6$	22	2.52	0.91	55	627	16	73
Na/2G:NaOTf	39	3.23	1.17	67	577	17	44
Na/EC:DMC NaPF$_6$	20	2.30	0.83	54	630	20	100

8.3 Supporting information on publication 3

ADVANCED FUNCTIONAL MATERIALS

Supporting Information

Copper Thiophosphate (Cu$_3$PS$_4$) as Electrode for Sodium-Ion Batteries with Ether Electrolyte

Wolfgang Brehm, Aggunda L. Santhosha, Zhenggang Zhang, Christof Neumann, Andrey Turchanin, Andréa Martin, Nicola Pinna, Martin Seyring, Markus Rettenmayr, Johannes R. Buchheim, and Philipp Adelhelm*

Supporting Information on

Copper thiophosphate (Cu₃PS₄) as electrode for sodium-ion batteries with ether electrolyte

Wolfgang Brehm[a,c], Aggunda L. Santhosha[a,c,d], Zhenggang Zhang[a,c,d], Christof Neumann[b], Andrey Turchanin[b,c], Andréa Martin[d], Nicola Pinna[d], Martin Seyring[e], Markus Rettenmayr[e], Johannes. R. Buchheim[a] and Philipp Adelhelm[a,c,d]*

[a] *Institute of Technical Chemistry and Environmental Chemistry, CEEC Jena, Friedrich Schiller University Jena, Philosophenweg 7a, 07743 Jena, Germany*

[b] *Institute of Physical Chemistry, Friedrich Schiller University Jena, Lessingstraße 10, 07743 Jena, Germany*

[c] *Center for Energy and Environmental Chemistry Jena (CEEC Jena), Philosophenweg 7a, 07743 Jena, Germany*

[d] *Institut für Chemie, Humboldt-Universität zu Berlin, Brook-Taylor-Str. 2, 12489 Berlin, Germany*

[e] *Otto-Schott-Institute of Materials Research, Friedrich Schiller University Jena, Löbdergraben 32, 07743 Jena, Germany*

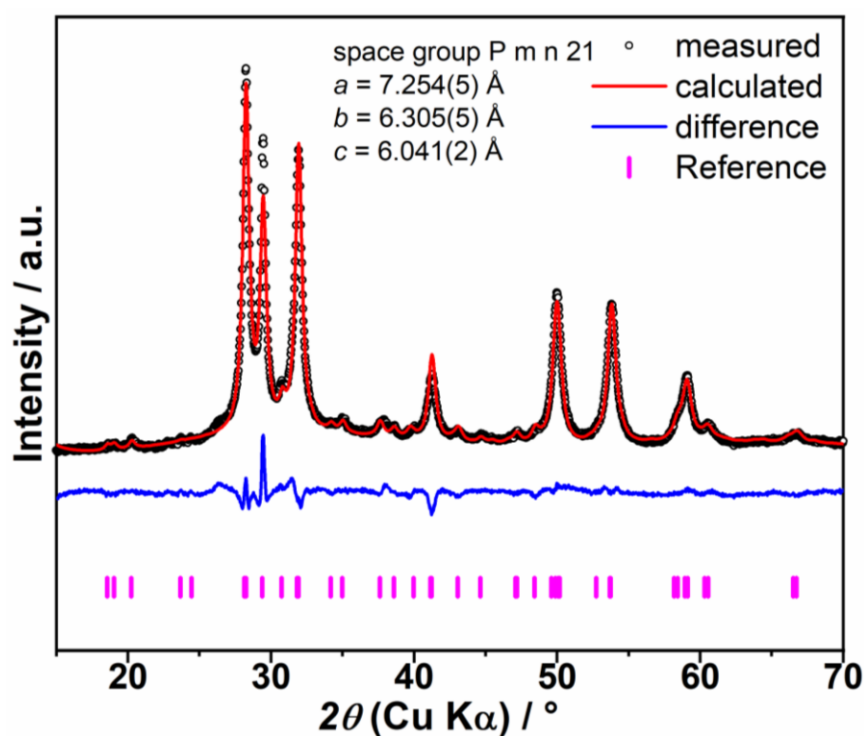** correspondence: philipp.adelhelm@hu-berlin.de*

Figure S1: Rietveld refinement of Cu₃PS₄ raw powder after mechanochemical synthesis in a PBM. Crystal sizes of 21 nm were obtained. The lattice parameters were determined to: a = 7.254(5) Å, b = 6.305(5) Å, c=6.041(2) Å.
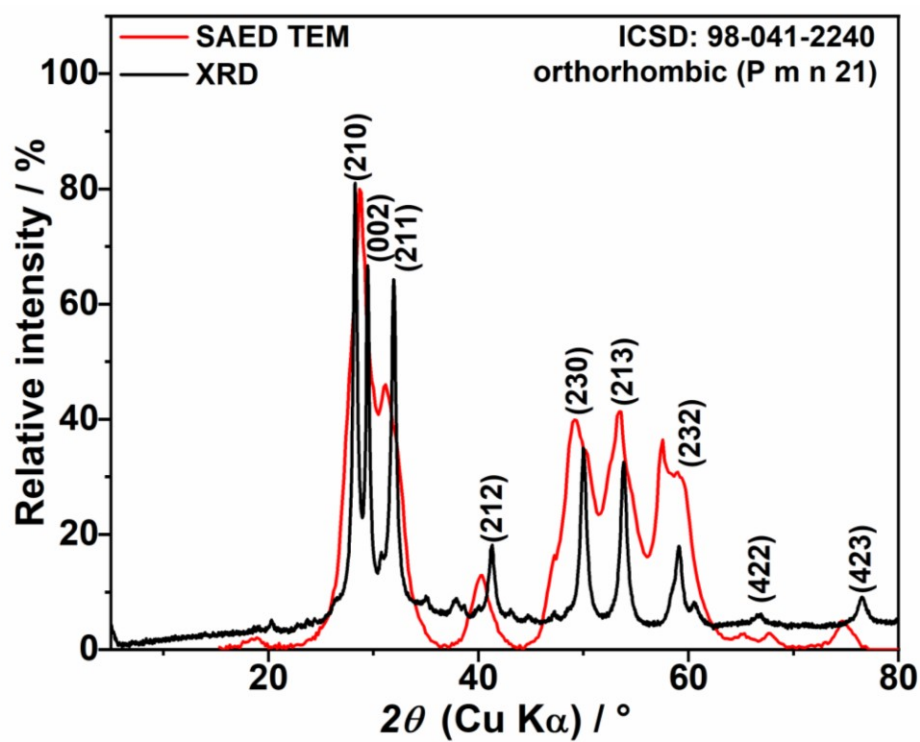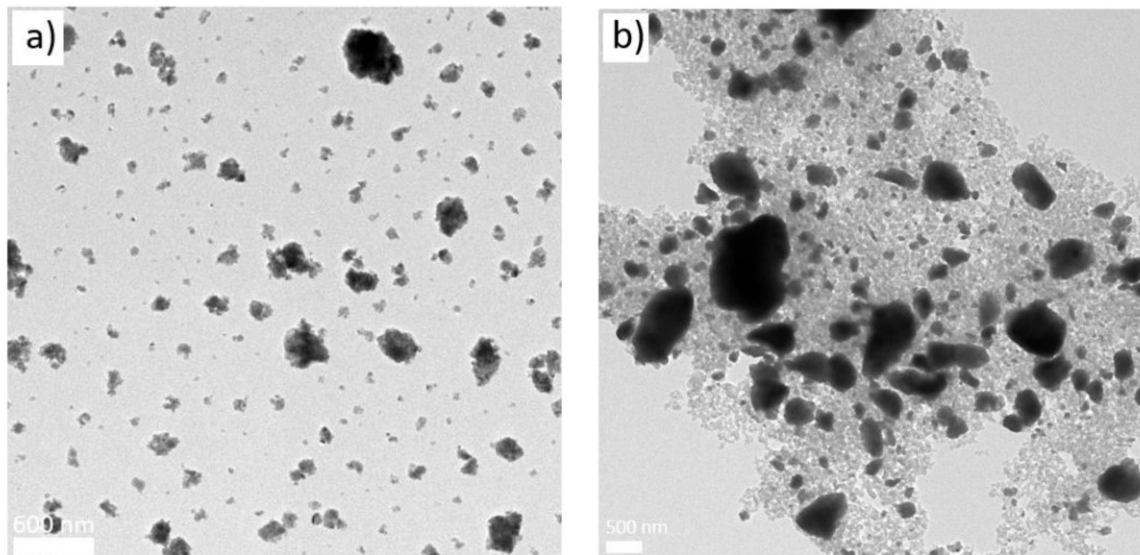
1

Figure S2: Results from TEM/SAED and XRD for the synthesized Cu$_3$PS$_4$ in comparison. Both methods evidence formation of Cu$_3$PS$_4$ through the ball milling process.
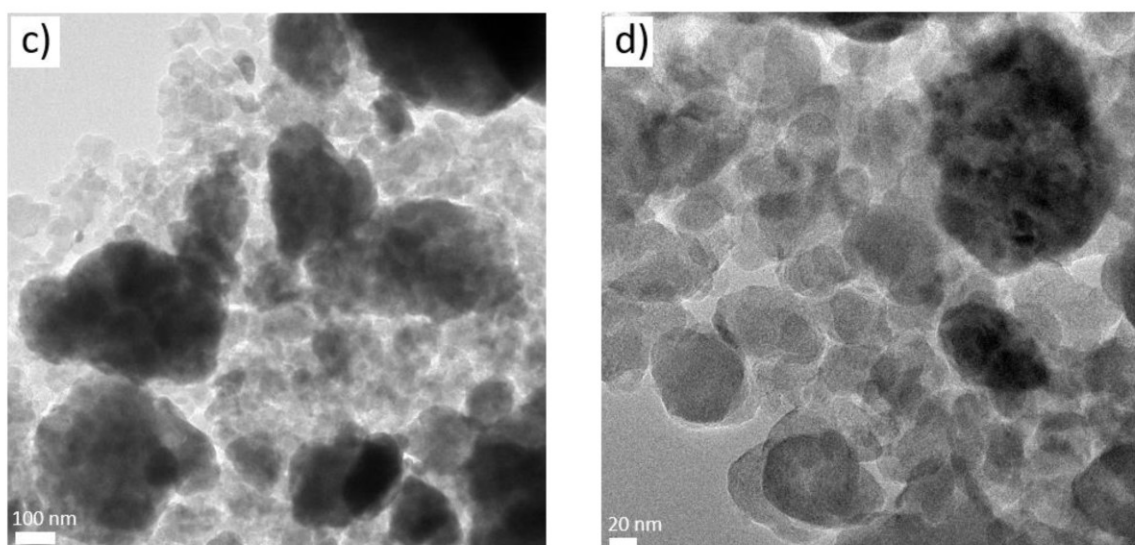
Figure S3: TEM images of a) Cu_3PS_4 particles after their synthesis by ball milling in the PBM for 24 h @ 400 rpm and b),c),d) after an additional milling step with carbon black for another 12 h at a frequency of 25 Hz.
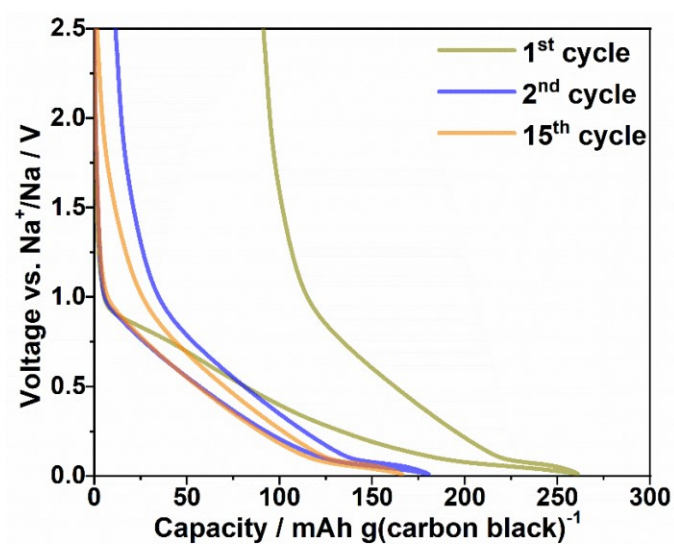

Figure S4: Voltage profiles of carbon black at 36 mA g^{-1} using 1 M $NaPF_6$ in diglyme as electrolyte. It is of note, however, that the preparation of carbon black electrodes is difficult as the material is very fluffy, which causes problems during electrode preparation. The mass loadings are typically very small (in our case about 0.7-1.0 mg cm^{-2}). This might explain the difference from the results reported by Zhang et al. (155 mAh g^{-1}) and an own previous study[1] for the same carbon black. Moreover, the obtainable capacity of carbon black in the composite might differ from pure carbon black electrodes. Overall, an exact deconvolution of the individual contributions of Cu_3PS_4 and carbon black to the capacity of the Cu_3PS_4/C electrode is not possible, but the contribution of carbon black is small enough to be neglected for the discussion in the main manuscript.
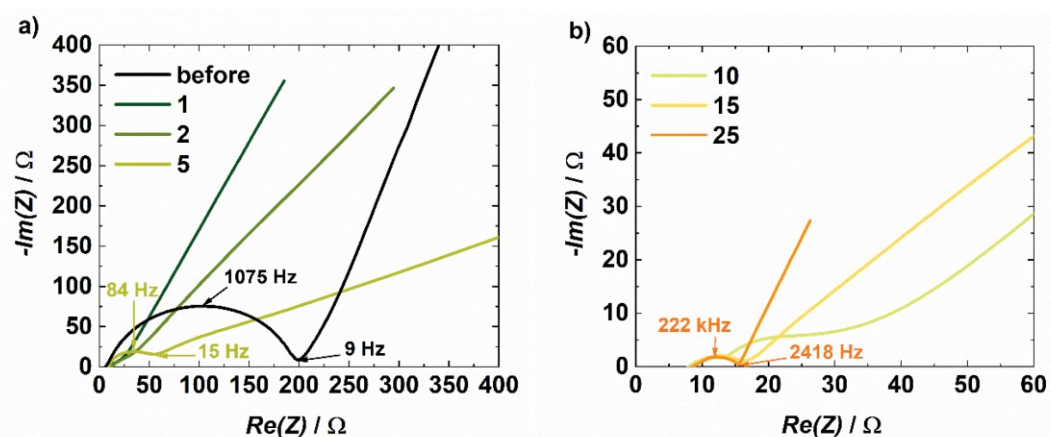
3

Figure S5: Impedance measurement of the a) pristine electrode and the desodiated states of the 1st, 2nd and 5th cycle and b) the 10th, 15th and 25th cycle for a voltage amplitude of 10 mV applied in a frequency range from 1 MHz to 100 mHz, when being cycled between 0.01 – 2.5 V with a current density of 120 mA g^{-1}. The used electrolyte was 1 M NaPF$_6$ in diglyme.
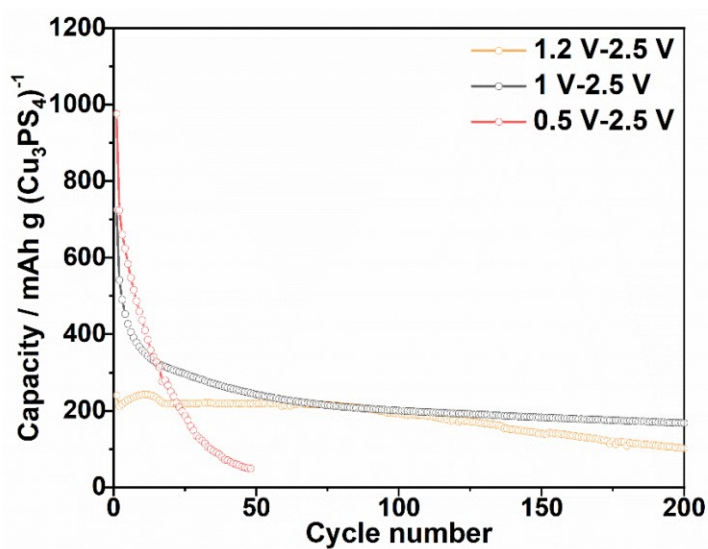

Figure S6: Discharge capacities vs. cycle number with a current rate of 50 mA g^{-1} using Li with 1°M LiTFSI dissolved in diglyme as electrolyte.
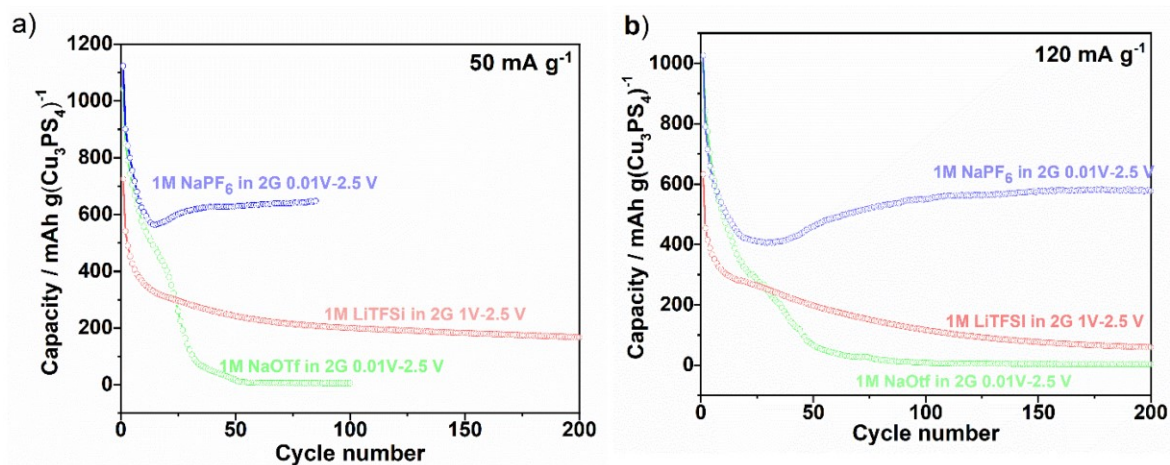
4

Figure S7: Discharge capacities vs. cycle number with a current rate of a) 50 mA g^{-1} and b) 120 mA g^{-1} for Na and Li with different electrolytes using diglyme (abbreviation 2G) as a solvent.
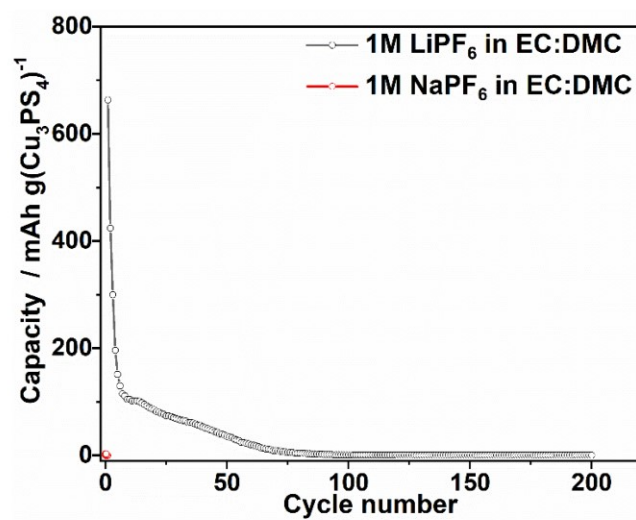

Figure S8: Discharge capacities vs. cycle number with a current rate of 120 mA g^{-1} for Na and Li with different electrolytes using EC:DMC as a solvent. The applied voltage window was 0.01-2.5 V vs. Na$^+$/Na for the Na half cells and 1 V-2.5 V vs. Li$^+$/Li for the half cells with Li.
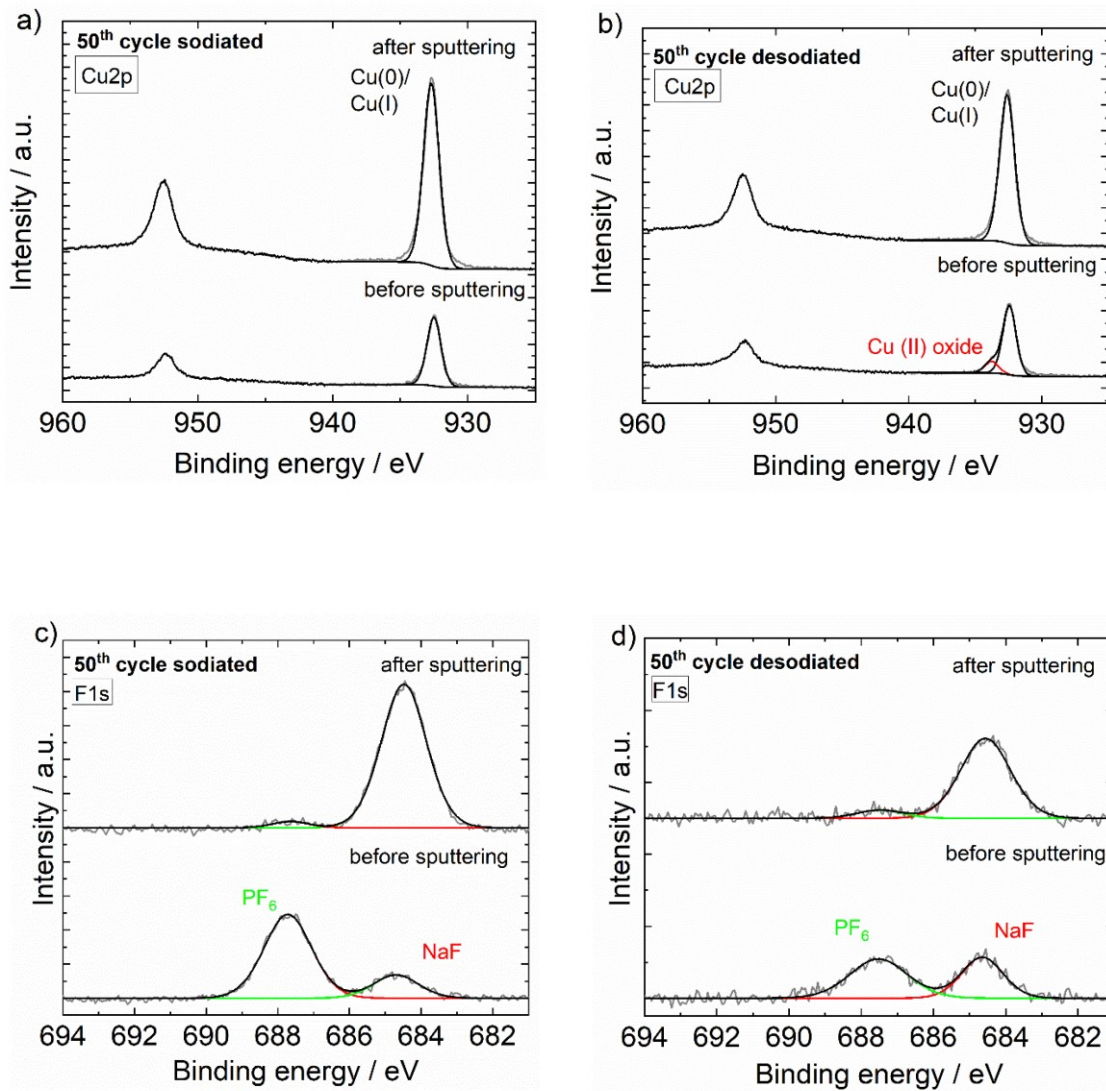
5

Figure S9: XPS analysis of the sodiated and desodiated Cu₃PS₄/C for a,b) Cu 2p and c,d) F 1s species before and after sputtering the surface layer. The measurements were performed after 50 cycles. The cycling experiment was performed with a current density of 120 mA g⁻¹ within a voltage window of 0.01 V-2.5 V vs. Na⁺/Na.
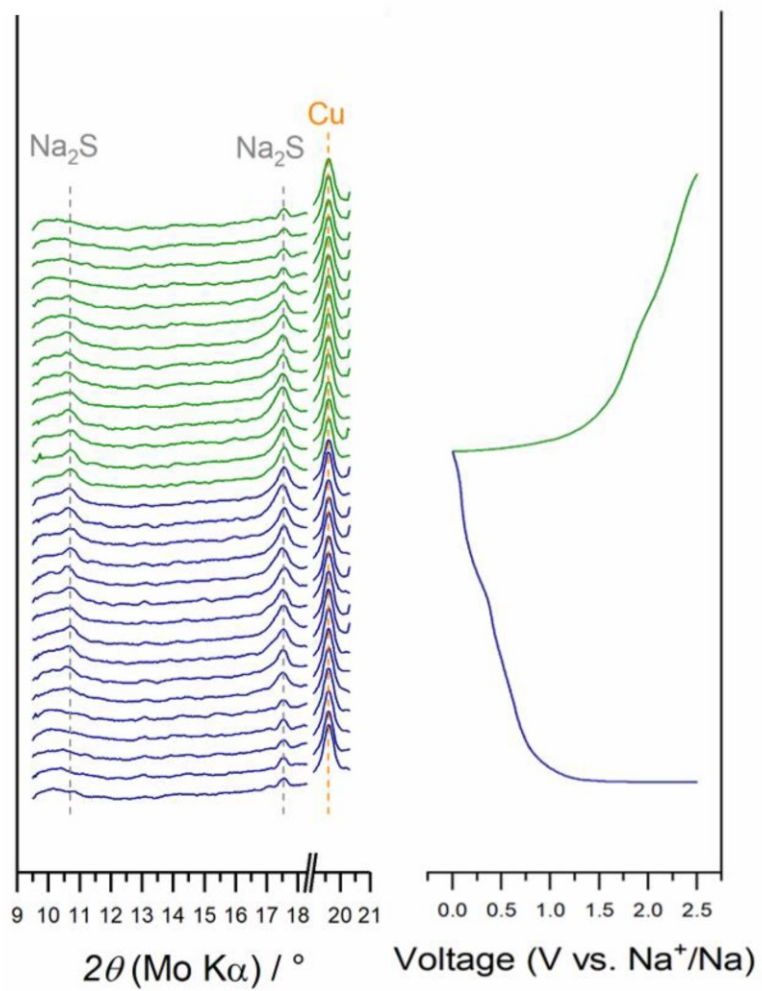
6

Figure S10: Operando XRD analysis after the 2nd sodiation and desodiation step (Cu$_3$PS$_4$: ICSD: 98-041-2240; Na$_2$S: ICSD: 98-006-0436; Cu: ICSD: 98-005-3755).

7
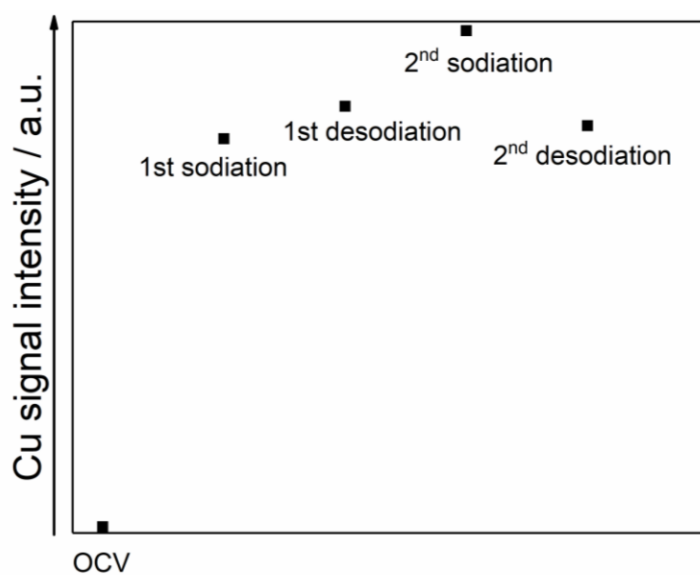
Figure S11: Cu signal intensity change measured by in operando XRD before and after the first two sodiation and desodiation cycles (Cu: ICSD: 98-005-3755).
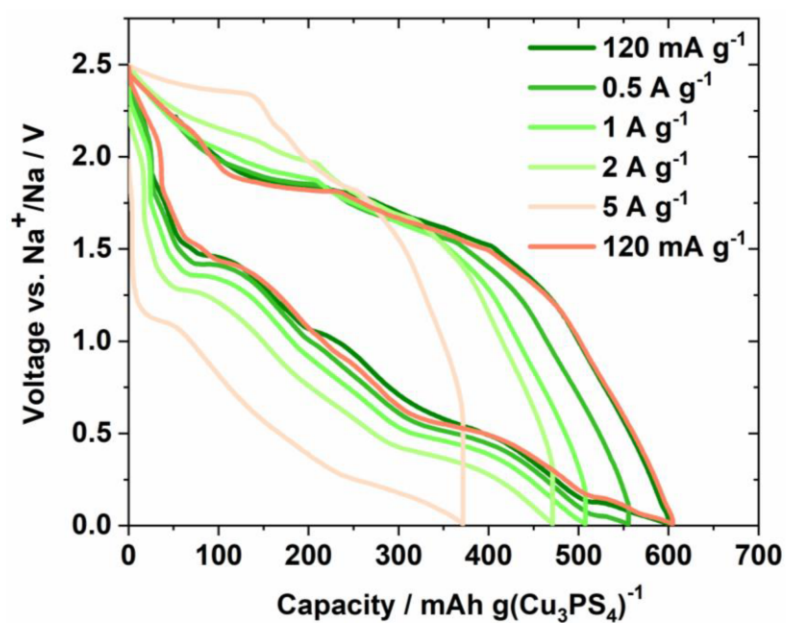
Figure S12: a) Voltage profiles of the rate capability test for a Cu_3PS_4/C electrode with 1 M $NaPF_6$ in diglyme cycled in a voltage window of 0.01 V - 2.5 V.

[1]   a) B. Zhang, G. Rousse, D. Foix, R. Dugas, D. A. Corte, J. M. Tarascon, Adv Mater 2016, 28, 9824; b) W. Brehm, J. R. Buchheim, P. Adelhelm, Energy Technology 2019, DOI: 10.1002/ente.2019003891900389.

9. References

[1]   https://www.umweltbundesamt.de/en/indicator-ghg-emissions-avoided-through-the-use-of#assessing-the-development, **access 11/2020**.

[2]   S. Kulandaivalu, Y. Sulaiman, *Energies* **2019**, 12.

[3]   a) J. P. Brett Ammundsen, *Adv Mater* **2001**, 13; b) Y. K. Sun, Z. Chen, H. J. Noh, D. J. Lee, H. G. Jung, Y. Ren, S. Wang, C. S. Yoon, S. T. Myung, K. Amine, *Nat Mater* **2012**, 11, 942; c) J. Yan, X. Liu, B. Li, *RSC Adv.* **2014**, 4, 63268; d) H. Z. Zhang, Q. Q. Qiao, G. R. Li, X. P. Gao, *J. Mater. Chem. A* **2014**, 2, 7454; e) S. S. Zhang, *Energy Storage Materials* **2020**, 24, 247.

[4]   a) P. K. Nayak, E. M. Erickson, F. Schipper, T. R. Penki, N. Munichandraiah, P. Adelhelm, H. Sclar, F. Amalraj, B. Markovsky, D. Aurbach, *Advanced Energy Materials* **2018**, 8; b) X. Zeng, M. Li, D. Abd El-Hady, W. Alshitari, A. S. Al-Bogami, J. Lu, K. Amine, *Advanced Energy Materials* **2019**, 9; c) P. K. Nayak, L. Yang, W. Brehm, P. Adelhelm, *Angew Chem Int Ed Engl* **2018**, 57, 102.

[5]   E. Peled, *J. Electrochem. Soc.* **1979**.

[6]   a) A. Wang, S. Kadam, H. Li, S. Shi, Y. Qi, *npj Computational Materials* **2018**, 4; b) X. B. Cheng, R. Zhang, C. Z. Zhao, F. Wei, J. G. Zhang, Q. Zhang, *Adv Sci (Weinh)* **2016**, 3, 1500213; c) P. Verma, P. Maire, P. Novák, *Electrochimica Acta* **2010**, 55, 6332; d) K. Edström, M. Herstedt, D. P. Abraham, *Journal of Power Sources* **2006**, 153, 380; e) S. Leroy, F. Blanchard, R. Dedryvère, H. Martinez, B. Carré, D. Lemordant, D. Gonbeau, *Surface and Interface Analysis* **2005**, 37, 773; f) A. Augustsson, M. Herstedt, J. H. Guo, K. Edström, G. V. Zhuang, J. P. N. Ross, J. E. Rubensson, J. Nordgren, *Phys. Chem. Chem. Phys.* **2004**, 6, 4185.

[7]   a) S.-W. Kim, D.-H. Seo, X. Ma, G. Ceder, K. Kang, *Advanced Energy Materials* **2012**, 2, 710; b) D. Kundu, E. Talaie, V. Duffort, L. F. Nazar, *Angew Chem Int Ed Engl* **2015**, 54, 3431; c) M. D. Slater, D. Kim, E. Lee, C. S. Johnson, *Advanced Functional Materials* **2013**, 23, 947; d) N. Yabuuchi, K. Kubota, M. Dahbi, S. Komaba, *Chem Rev* **2014**, 114, 11636; e) H. Pan, Y.-S. Hu, L. Chen, *Energy & Environmental Science* **2013**, 6, 2338; f) M. H. Han, E. Gonzalo, G. Singh, T. Rojo, *Energy & Environmental Science* **2015**, 8, 81; g) M. Li, Z. Du, M. A. Khaleel, I. Belharouak, *Energy Storage Materials* **2020**, 25, 520; h) H. Zhang, Y. Huang, H. Ming, G. Cao, W. Zhang, J. Ming, R. Chen, *Journal of Materials Chemistry A* **2020**, 8, 1604.

[8]   D. R. Lide, *CRC Handbook of Chemistry and Physics, 84th ed.*, CRC, Boca Raton, **2004**.

[9]   M. Okoshi, Y. Yamada, A. Yamada, H. Nakai, *Journal of The Electrochemical Society* **2013**, 160, A2160.

[10]   B. Jache, P. Adelhelm, *Angew Chem Int Ed Engl* **2014**, 53, 10169.

[11]   a) K. Chayambuka, G. Mulder, D. L. Danilov, P. H. L. Notten, *Advanced Energy Materials* **2018**, 8; b) W. Brehm, A. L. Santhosha, Z. Zhang, C. Neumann, A. Turchanin, A. Martin, N. Pinna, M. Seyring, M. Rettenmayr, J. R. Buchheim, P. Adelhelm, *Advanced Functional Materials* **2020**, DOI: 10.1002/adfm.201910583.

[12]   a) Y. You, A. Manthiram, *Advanced Energy Materials* **2018**, 8; b) K. Kubota, S. Kumakura, Y. Yoda, K. Kuroki, S. Komaba, *Advanced Energy Materials* **2018**, 8.

[13]   F. Klein, B. Jache, A. Bhide, P. Adelhelm, *Phys Chem Chem Phys* **2013**, 15, 15876.

[14]   a) Y. Li, Y. Lu, P. Adelhelm, M. M. Titirici, Y. S. Hu, *Chem Soc Rev* **2019**, 48, 4655; b) S. Mariyappan, Q. Wang, J. M. Tarascon, *Journal of The Electrochemical Society* **2018**, 165, A3714; c) M. Sathiya, K. Hemalatha, K. Ramesha, J. M. Tarascon, A. S. Prakash, *Chemistry of Materials* **2012**, 24, 1846; d) M. Goktas, C. Bolli, E. J. Berg, P. Novák, K. Pollok, F. Langenhorst, M. v. Roeder, O. Lenchuk, D. Mollenhauer, P. Adelhelm, *Advanced Energy Materials* **2018**, 8, 1702724.

[15]   L. Croguennec, M. R. Palacin, *Journal of the American Chemical Society* **2015**, 137, 3140.

[16]   a) C. F. a. P. H. C. Delmas, *Physica* **1980**, 99B 81; b) L. Viciu, J. W. G. Bos, H. W. Zandbergen, Q. Huang, M. L. Foo, S. Ishiwata, A. P. Ramirez, M. Lee, N. P. Ong, R. J. Cava, *Physical Review B* **2006**, 73.

[17]   a) M. Goktas, C. Bolli, J. Buchheim, E. J. Berg, P. Novak, F. Bonilla, T. Rojo, S. Komaba, K. Kubota, P. Adelhelm, *ACS Appl Mater Interfaces* **2019**, 11, 32844; b) M. Goktas, B. Akduman, P. Huang, A. Balducci, P. Adelhelm, *The Journal of Physical Chemistry C* **2018**, 122, 26816.

[18]   a) P. Senguttuvan, G. Rousse, V. Seznec, J.-M. Tarascon, M. R. Palacín, *Chemistry of Materials* **2011**, 23, 4109; b) L. Wu, D. Buchholz, D. Bresser, L. Gomes Chagas, S. Passerini, *Journal of Power Sources* **2014**, 251, 379; c) X. Ma, K. An, J. Bai, H. Chen, *Sci Rep* **2017**, 7, 162.

[19]   a) M. Ashuri, Q. He, L. L. Shaw, *Nanoscale* **2016**, 8, 74; b) T. Ramireddy, N. Sharma, T. Xing, Y. Chen, J. Leforestier, A. M. Glushenkov, *ACS Appl Mater Interfaces* **2016**, 8, 30152; c) B. Zhang, G. Rousse, D. Foix, R. Dugas, D. A. Corte, J. M. Tarascon, *Adv Mater* **2016**, 28, 9824; d) G. Wang, X. Xiong, Z. Lin, C. Yang, Z. Lin, M. Liu, *Electrochimica Acta* **2017**, 242, 159.

[20]   S. C. Jung, D. S. Jung, J. W. Choi, Y. K. Han, *J Phys Chem Lett* **2014**, 5, 1283.

[21]   C.-H. Lim, T.-Y. Huang, P.-S. Shao, J.-H. Chien, Y.-T. Weng, H.-F. Huang, B. J. Hwang, N.-L. Wu, *Electrochimica Acta* **2016**, 211, 265.

[22]   a) L. D. Ellis, T. D. Hatchard, M. N. Obrovac, *Journal of The Electrochemical Society* **2012**, 159, A1801; b) W. Brehm, J. R. Buchheim, P. Adelhelm, *Energy Technology* **2019**, DOI: 10.1002/ente.2019003891900389; c) T. Palaniselvam, M. Goktas, B. Anothumakkool, Y. N. Sun, R. Schmuch, L. Zhao, B. H. Han, M. Winter, P. Adelhelm, *Advanced Functional Materials* **2019**, 29, 1900790; d) L. Xiao, Y. Cao, J. Xiao, W. Wang, L. Kovarik, Z. Nie, J. Liu, *Chem Commun (Camb)* **2012**, 48, 3321; e) A. Darwiche, R. Dugas, B. Fraisse, L. Monconduit, *Journal of Power Sources* **2016**, 304, 1; f) V. L. Chevrier, G. Ceder, *Journal of The Electrochemical Society* **2011**, 158, A1011; g) H. Xie, X. Tan, E. J. Luber, B. C. Olsen, W. P. Kalisvaart, K. L. Jungjohann, D. Mitlin, J. M. Buriak, *ACS Energy Letters* **2018**, 3, 1670.

[23]   a) M. Lao, Y. Zhang, W. Luo, Q. Yan, W. Sun, S. X. Dou, *Adv Mater* **2017**, 29; b) T. Palaniselvam, M. Goktas, B. Anothumakkool, Y.-N. Sun, R. Schmuch, L. Zhao, B.-H. Han, M. Winter, P. Adelhelm, *Advanced Functional Materials* **2019**, DOI: 10.1002/adfm.2019007901900790.

[24]   J. Wang, C. Eng, Y. C. Chen-Wiegart, J. Wang, *Nat Commun* **2015**, 6, 7496.

[25]   L. D. H. Ellis, T.D.; Obrovac, M.N., *Journal of The Electrochemical Society* **2012**, 159, A1801.

[26]   J. W. Wang, X. H. Liu, S. X. Mao, J. Y. Huang, *Nano Lett.* **2012**, 12, 5897.

[27]   J. M. Stratford, M. Mayo, P. K. Allan, O. Pecher, O. J. Borkiewicz, K. M. Wiaderek, K. W. Chapman, C. J. Pickard, A. J. Morris, C. P. Grey, *J Am Chem Soc* **2017**, 139, 7273.

[28]   J. Qian, Y. Chen, L. Wu, Y. Cao, X. Ai, H. Yang, *Chem Commun (Camb)* **2012**, 48, 7070.

[29]   P. K. Allan, J. M. Griffin, A. Darwiche, O. J. Borkiewicz, K. M. Wiaderek, K. W. Chapman, A. J. Morris, P. J. Chupas, L. Monconduit, C. P. Grey, *J Am Chem Soc* **2016**, 138, 2352.

[30]   A. Darwiche, C. Marino, M. T. Sougrati, B. Fraisse, L. Stievano, L. Monconduit, *J Am Chem Soc* **2012**, 134, 20805.

[31]   C. H. Mathewson, *Z. Anorg. Allg. Chem.* **1906**, 50, 192.

[32]   M. Walter, S. Doswald, M. V. Kovalenko, *Journal of Materials Chemistry A* **2016**, 4, 7053.

[33]   H. Okamoto, *Journal of Phase Equilibria and Diffusion* **2012**, 33, 347.

[34]   a) K. Cao, T. Jin, L. Yang, L. Jiao, *Materials Chemistry Frontiers* **2017**, 1, 2213; b) F. Klein, R. Pinedo, P. Hering, A. Polity, J. Janek, P. Adelhelm, *The Journal of Physical Chemistry C* **2016**, 120, 1400; c) X. Wei, X. Wang, X. Tan, Q. An, L. Mai, *Advanced Functional Materials* **2018**, 28, 1804458.

[35]   J. Cabana, L. Monconduit, D. Larcher, M. R. Palacin, *Adv Mater* **2010**, 22, E170.

[36]   a) S. O. Kim, A. Manthiram, *ACS Appl Mater Interfaces* **2017**, 9, 16221; b) J. Li, D. Yan, T. Lu, W. Qin, Y. Yao, L. Pan, *ACS Appl Mater Interfaces* **2017**, 9, 2309; c) S. O. Kim, A. Manthiram, *Chem Commun (Camb)* **2016**, 52, 4337; d) W. Brehm, A. L. Santhosha, Z. Zhang, C. Neumann, A. Turchanin, M. Seyring, M. Rettenmayr, J. R. Buchheim, P. Adelhelm, *submitted in Journal of Power Sources Advances* **2020**.

[37]   a) X. Wang, H.-M. Kim, Y. Xiao, Y.-K. Sun, *Journal of Materials Chemistry A* **2016**, 4, 14915; b) M. S. Chandrasekar, S. Mitra, *Electrochimica Acta* **2013**, 92, 47.

[38]   a) ; b) F. Zhao, N. Han, W. Huang, J. Li, H. Ye, F. Chen, Y. Li, *Journal of Materials Chemistry A* **2015**, 3, 21754; c) M. C. Stan, R. Klöpsch, A. Bhaskar, J. Li, S. Passerini, M. Winter, *Advanced Energy Materials* **2013**, 3, 231.

[39]   J. Grondin, *Solid State Ionics* **2004**, 166, 441.

[40]   a) Y. Yang, Q. Wu, Y. Cui, Y. Chen, S. Shi, R. Z. Wang, H. Yan, *ACS Appl Mater Interfaces* **2016**, 8, 25229; b) C. Dietrich, R. Koerver, M. W. Gaultois, G. Kieslich, G. Cibin, J. Janek, W. G. Zeier, *Phys Chem Chem Phys* **2018**, 20, 20088; c) M. Ghidiu, J. Ruhl, S. P. Culver, W. G. Zeier, *Journal of Materials Chemistry A* **2019**, 7, 17735; d) G. F. Dewald, S. Ohno, M. A. Kraft, R. Koerver, P. Till, N. M. Vargas-Barbosa, J. Janek, W. G. Zeier, *Chemistry of Materials* **2019**, DOI: 10.1021/acs.chemmater.9b01550; e) Z. Liu, W. Fu, E. A. Payzant, X. Yu, Z. Wu, N. J. Dudney, J. Kiggans, K. Hong, A. J. Rondinone, C. Liang, *J Am Chem Soc* **2013**, 135, 975; f) S. Wenzel, T. Leichtweiss, D. A. Weber, J. Sann, W. G. Zeier, J. Janek, *ACS Appl Mater Interfaces* **2016**, 8, 28216.

[41]   C.-H. Kuo, Y.-T. Chu, Y.-F. Song, M. H. Huang, *Advanced Functional Materials* **2011**, 21, 792.

[42]   a) R. Koerver, F. Walther, I. Aygün, J. Sann, C. Dietrich, W. G. Zeier, J. Janek, *Journal of Materials Chemistry A* **2017**, 5, 22750; b) D. H. S. Tan, E. A. Wu, H. Nguyen, Z. Chen, M. A. T. Marple, J.-M. Doux, X. Wang, H. Yang, A. Banerjee, Y. S. Meng, *ACS Energy Letters* **2019**, 4, 2418.

[43]   T. Hakari, M. Nagao, A. Hayashi, M. Tatsumisago, *Journal of Power Sources* **2015**, 293, 721.

[44]   S. S. Zhang, K. Xu, T. R. Jow, *Electrochimica Acta* **2004**, 49, 1057.